Predicting Melt Pool Behaviour in LPBF through High Fidelity Modelling

William Joe Reynolds

Thesis

Submitted to University of Nottingham

for the degree of

Doctor of Philosophy

Department of Engineering

Submitted December 2021

Abstract

Empirical process parameter optimisation for laser powder bed fusion (LPBF) is a long, arduous process that inefficiently locates process parameters that may or may not be optimal. It is often circumstantial; meaning it is dependent on the thermodynamic regime at a given location within a component. In order to obtain mastery of this process we must control the energy distribution delivered to the melt pool.

Reducing the porosity and cracking of components made through LPBF is still the largest barrier for entry in high integrity applications. Optimising laser power and speed are considered two of the most influential factors in LPBF, which drive track consolidation, reducing porosity. These parameters though, are difficult to link to desirable melt pool properties, without extensive experimental testing. Controlling the process via surface temperature has been shown to substantially improve processing, as well as provide a more direct link with the process. However, no literature examines which melt pool temperatures are optimal in producing highly dense components.

The primary novelty in this work is the derivation and validation of a novel optimisation method that monitors and modulates peak melt pool temperatures by varying the laser power administered to the melt pool through computational modelling. Understanding optimal melt pool peak temperatures is a valuable approach since increasingly, machine tools are able to monitor surface temperature and, in the future, attenuate energy density accordingly. This work provides a framework in which porosity and cracking defects can be eliminated through optimal process parameter calculations. This process parameter optimisation utilises high performance computing facilities to simulate LPBF at small time durations, with high resolution. This aspect has been shown to be critical in providing detailed information for the evaluation of cracking behaviours and the prediction of optimal processing conditions.

This work makes use of a 'high fidelity model' to accurately and precisely measure and evaluate conditions within LPBF, in addition to providing a platform for the process optimisation to run from. Model fidelity here describes the exactness of the degree to which something is copied or produced. For this model, this involves including fundamental physics that describe how photons in the laser beam are reflected and absorbed into the metal surface, rather than using approximations to generalise the heat input. For example, a low fidelity heat source would use a volumetric approach to heat the metal powder particles. This includes assumptions as to the absorptivity of the powder bed, how deep that particular laser would heat the powder bed, and therefore

would have a larger error when comparing the temperature on the powder surface to experiments. A high fidelity heat source, that will be used in this work, replicates reality to a higher degree, so that temperatures can be modelled with greater accuracy. In this instance, ray tracing has been proven in literature to accurately reflect the behaviour of photons interacting with the metal surface, so that the absorptivity of the metal is not approximated, but calculated using the Fresnel equations [1]. A high fidelity model does not have to be non-linear, but often is due to temperature dependant properties. In this work, complex physical phenomena such as: melting and solidification, buoyancy effects, surface tension, temperature dependant surface tension (Marangoni flow), vaporisation phenomena including recoil pressure and evaporation flux, melt pool flow and variable absorptivity from the Fresnel equations, and a stochastic powder bed are used to replicate LPBF through numerical modelling. The model is designed to be flexible and user friendly, to allow the modification of every aspect of the laser, powder and other process conditions.

Three main research chapters are presented in this work, along with an extensive literature review covering the complex nature of LPBF, combined with a methodology to create a high fidelity model to simulate this process. Results have been validated with four different validation experimental to model comparisons. These validations include;

- Validation against a continuous laser system for 316L stainless steel in conduction mode
- Validation against a continuous laser system for 316L stainless steel in keyhole mode
- Validation against a ramp up laser profile for 316L stainless steel
- Validation against a pulsed laser system for AA204 for two different parameter sets.

These results include validation with a variable pulsed laser system for 316L stainless steel, to ensure that the model can be used with variable laser conditions, as well as a more typical continuous wave laser. In order to replicate LPBF single track deposition of high strength aluminium alloy AA2024, a revised refractive index was tailored to experimental conditions. Literature shows how literature values of absorptivity of aluminium do not represent the measured behaviour in LPBF. For the first time, this work combines a revised refractive index to simulate absorptivity of AA2024, whilst keeping a high fidelity ray tracing heat source. This allows for detailed analysis of the development of porosity, which is vital in determining track consolidation.

The main body of this work comprises of a predictive framework for LPBF parameter optimisation. This framework has been proven for two different material systems, 316L stainless steel and AA2024. Using an inverse solution, a link is created between laser power and melt pool temperature, allowing for stable melt pools to be established and maintained throughout a single track deposition. Links have been established with surface temperature and common LPBF defects, such as a lack of fusion defects and keyhole porosity. A new parameter, P-ratio, has been derived and shown to work as a single processing variable that LPBF can be optimised too. P-ratio has proven to be independent of laser speed, and provides a constant recoil pressure to the surface of a melt pool to ensure track consolidation. This work uses a case study on AA2024, to validate the inverse solution with a second material system. The inverse solution correctly identifies a laser power at a set point distance and exposure time that gives the highest density, compared to samples validated in experimental conditions.

Additionally, the model has successfully demonstrated its use in measuring and evaluating cracking for high strength aluminium alloy, AA2024. Data generated by the model clearly shows differences between cracked and crack free parameter sets. Large differences in cooling rates and temperature gradients show that the main drivers for cracking in LPBF can be evaluated with the high fidelity model. Results from this work will be used to predict and eliminate cracking in high strength aluminium alloys.

Acknowledgments

I am happy that at last I can write this section of my thesis, as it signals a major milestone in my life, one that I am very thankful and grateful to achieve. I am also slightly nervous, as I am not sure what people who are not writing up do on evenings and weekends. This must also mean that my student discount will end soon.

Without a doubt this has been the hardest four years of my nine year long stint as a student. I can definitively say that I could and would not have achieved it without an enormous amount of help and support from my supervisory team, family and friends. Thank you to Mum and Dad and my brothers and sisters who have helped and supported me every day during this long project.

I would like to individually thank my supervisory team, Adam, Marco, David, Alper and Simon, for providing countless hours of support during my PhD. Thank you Alper and Simon, for providing me with invaluable feedback and experience during our monthly progress meetings and making me feel so welcome during my visits to Oerlikon in Munich. Thank you David for providing me with support and guidance with my project. It is a shame that the PVD coating work did not progress, but the effort that Matt Wadge has put into the barrel coater has not gone to waste. Thank you also Matt for your time and effort spent teaching me PVD. I also thank you for your support with my thesis. Thank you Marco for being the technical voice of reason throughout my project. Without your keen eye and dedication to find the reasons why, I would have not progressed technically as far during my PhD. A huge appreciation goes to Adam, who has devoted an extraordinary amount of time to my PhD project, and who has been very patient with me throughout my time at the University of Nottingham. I am extremely grateful for the effort you have put into my project, and I can safely say that I would not be employed at Rolls-Royce if it wasn't for the lessons I have learnt from you during my PhD. Thank you.

I would like to thank Mark, Mark and Adam, who keep the lab running smoothly every day consistently throughout my entire PhD. Special thanks goes to Mark Hardy, I would not be in the position I am today without the knowledge I have gained through listening to your advice and guidance.

A very special thanks goes to Giuseppe, your effort in supporting me with the aluminium part of this project has been huge. Thank you. An additional thanks goes to Alex, Eva, George, Alex, Simon, Richard, Alice, Tim, Matt, Kieran, Chris, James, and everyone at CfAM who has made my time during my PhD so enjoyable.

My biggest thank you goes to Jess. I would not have been able to do any of this without your support, guidance and patience throughout these four long years. Thank you.

Publications

Publications as a co-author.

A. Speidel et al, Matthew D. Wadge, Leonidas Gargalis, Timothy P. Cooper, William J. Reynolds, David Grant, Richard Hauge, Adam T. Clare, James W. Murray, "The interaction of volatile metal coatings during the laser powder bed fusion of copper," Journal of Materials Processing Technology, vol. 299, p. 117332, Jan. 2022, doi: 10.1016/j.jmatprotec.2021.117332.

M. S. Knieps, W. J. Reynolds, J. Dejaune, A. T. Clare, and A. Evirgen, "In-situ alloying in powder bed fusion: The role of powder morphology," Materials Science and Engineering: A, vol. 807, p. 140849, Mar. 2021, doi: 10.1016/j.msea.2021.140849.

A. T. Clare, William J. Reynolds, James W. Murray, Nesma T. Aboulkhair, Marco Simonelli, Mark Hardy, David M. Grant, Chris Tuck, "Laser calorimetry for assessment of melting behaviour in multi-walled carbon nanotube decorated aluminium by laser powder bed fusion," CIRP Annals, vol. 69, no. 1, pp. 197–200, 2020, doi: 10.1016/j.cirp.2020.04.053.

Giuseppe Del Guercio, William J. Reynolds, Marco Simonelli, Adam Clare, "Mechanisms to measure, evaluate, predict and eliminate cracking in high strength aluminium alloys", To be submitted to Nature, 2022

Publications as first author.

William J. Reynolds, Marco Simonelli, Giuseppe Del Guercio, Ali Gökhan Demir, Adam T. Clare, "Temperature regulation in laser powder bed fusion", (under review by Journal of Materials Processing and Technology). 2021

Order

Table of contents

Contents

Abstract i

Acknowledgments iv

Publications vi

Order vii

Table of contents vii

List of figures xi

List of tables xxvi

Abbreviations xxvii

Nomenclature xxviii

1 Introduction 1

1.1 Background 1

1.2 Aim and objectives 2

1.3 Significance and novelty 3

1.4 Research methodology 4

1.5 Thesis layout 5

Chapter 2 8

2 Literature review 8

2.1 Introduction 8

2.2 Overview of AM techniques for the production of metal components 8

2.2.1 Overview 8

2.2.2 Powder bed fusion 9

2.2.3 Laser powder bed fusion 10

2.3 Laser material interaction for laser powder bed fusion 11

2.3.1 Laser metal interactions 11

2.3.2 Laser metal interactions for laser powder bed fusion 16

2.3.3 Initial laser powder bed interaction 18
2.3.4 Experimental measurement of Absorptivity 21
2.3.5 Laser-powder-meltpool interactions 22
2.4 Defects generated in laser powder bed fusion 37
2.4.1 Overview 37
2.4.2 Lack of fusion defects 37
2.4.3 Keyhole porosity 40
2.4.4 Spatter 41
2.4.5 Residual stress 44
2.5 Tailoring material consolidation in laser powder bed fusion 45
2.5.1 Overview 45
2.5.2 Solidification concepts 46
2.5.3 Solidification in laser powder bed fusion 47
2.5.4 Solidification cracking 49
2.5.5 Microstructure control 51
2.6 Process parameter optimisation and defect elimination strategies 56
2.6.1 Traditional process parameter optimisation 56
2.6.2 Feed forward control in laser powder bed fusion 58
2.7 Representing LPBF through Computational modelling 64
2.7.1 Meso-scale modelling 65
2.7.2 Macro-scale modelling 69
2.8 Shortfalls in the literature 70
Chapter 3 72
3 Combined discrete element model with computational fluid dynamics for simulating laser powder bed fusion 72
3.1 Overview 72
3.2 Discrete element modelling for a stochastic powder bed 72
3.3 Computational fluid dynamics for a high fidelity meso-scale model of LPBF. 74
3.3.1 Basic fluid flow 75

3.3.2 Multiphase flows 77
3.3.3 Solidification and melting model 78
3.3.4 Modelling of the heat source 80
3.3.5 Solver theory 85
3.3.6 Implementation within ANSYS Fluent 2021R1 85
3.4 High performance computing (HPC) 86
3.5 Thermophysical material properties 87
3.6 Laser micro calorimetry (LMC) 89
3.6.1 Overview 89
3.6.2 LMC working calculations 91
Chapter 4 93
4 Evaluation of Model Performance 93
4.1 Introduction 93
4.2 Methodology 94
4.2.1 Continuous and variable pulsed 316L stainless steel validation 94
4.2.2 Aluminium validation 96
4.3 Results 99
4.3.1 316L Stainless Steel validation results 99
4.3.2 Aluminium 2024 validation results 109
4.4 Discussion 116
4.4.1 316L stainless steel validation 116
4.4.2 Aluminium Alloy 2024 validation 119
4.5 Summary 123
Chapter 5 124
5 Model Informed Temperature regulation in laser powder bed fusion 124
5.1 Introduction 124
5.2 Methodology 125
5.2.1 Inverse solution for melt pool temperature control 125
5.3 Results 128

5.3.1 Demonstration of inverse solution 128
5.4 Discussion 134
5.4.1 The Inverse Solution 134
5.4.2 Melt Pool Manipulation via Tailored Recoil Pressure 135
5.4.3 Melt pool manipulation via a constant $\boldsymbol{Pratio}$ 141
5.4.4 Practical Implications 145
5.5 Summary 146
Chapter 6 147
6 Model informed strategy for the processing of a high strength aluminium alloy. 147
6.1 Introduction 147
6.2 Methodology 148
6.2.1 AA2024 cracking analysis method 148
6.2.2 Cracking model parameters 149
6.2.3 AA2024 process prediction framework 150
6.3 Results 151
6.3.1 AA2024 cracking analysis framework 152
6.3.2 AA2024 behaviour prediction 162
6.4 Discussion 168
6.4.1 AA2024 cracking analysis framework 168
6.4.2 AA2024 process prediction framework 171
6.5 Summary 175
Chapter 7 176
7 Conclusions 176
Chapter 8 179
8 Recommendations for future work 179
9 References 181
10 Appendices 200
10.1 Discrete element modelling script used for generating the initial powder bed configuration in LIGGGHTS 200

10.2 ANSYS Fluent custom user defined functions 203
10.2.1 Heat source model 203
10.2.2 Momentum equations 206
10.2.3 Define Adjust 206
10.2.4 Patching 210
10.2.5 Submission of HPC Job 212
10.3 Matlab post processing script for plotting ANSYS Fluent data 213

List of figures

Figure 1-1 shows how the thesis is structured around the different elements of the model and how the optimisation framework fits within the core high fidelity model. The numbers in this image represent the chapter that the information is contained in. The model can be used to model 'standard' inputs to output precise temperature, velocity and pressure data. The optimisation framework receives temperature inputs that can be chosen or calculated. These are then fed into the inverse solution, that interfaces with the core high fidelity model. 5

Figure 2-1 Metal Additive Manufacturing Market sector size 2020 [14] 9

Figure 2-2 Schematic of a Renishaw AM400 machine. The laser is generated at a laser source, and passed through a collimator which allows the focus of the beam to be changed. The beam then travels through a beam expander and hits the XY galvanometer. These two sets of mirrors direct the laser beam over the powder bed to coordinates defined by the on board processor. The laser finally travels through the f-theta lens where it impacts the powder bed. Powder is spread over the substrate with a recoater blade, to spread the powder and achieve the desired layer thickness. Bottom left shows a plan view of the powder bed, showing the gas flow that provides the inert atmosphere and carries away any spatter particles. The powder particles are not to scale. 11

Figure 2-3 shows the timeline for event timescales in LPBF, for time and distance..... 12

Figure 2-4 Incident light impacting a metal surface. Here an incident light particle is reflected by a metallic material. A portion of the energy of the particle is absorbed by the metal surface. 13

Figure 2-5 Plot showing how absorptivity varies as a function of the angle of incidence of a photon 14

Figure 2-6a Surface absorptivity for AA1100 against surface temperature b) shows the effect of surface roughness on the reflectivity for copper and aluminium [32]..... 15

Figure 2-7a) shows the instantaneous initial absorptivity of the powder bed b) shows initial stage of melting, with the materials temperature below its boiling point c) shows the melt pool as it rises above the boiling temperature at atmospheric pressure, with a keyhole forming, trapping photons within it d) shows the absorptivity at the stages a), b) and c) respectively 17

Figure 2-8 2D illustration of the ray tracing model [48]..... 18

Figure 2-9a) shows the absorption (α) calculated along the beam path for the ray tracing simulation over the Gaussian distributed stainless steel powder layer. B) shows the absorption calculated along the beam bath for the bimodal distribution [52] 19

Figure 2-10 shows a schematic of the calorimetric measurement system [56] 21

Figure 2-11 show images from an X-Ray synchrotron of the cross section of a keyhole during laser powder bed fusion. The images show a keyhole pore being formed from keyhole instability [58]..... 23

Figure 2-12 shows the effect of scanning direction and pump speed on the vapour plume generated during a single layer of magnesium processed by laser powder bed fusion. The top row shows the scan vector with the gas flow, the middle row shows the scan vector against the gas flow, with the bottom row showing the scan direction perpendicular to the gas flow. The columns represent different pump speeds. This figure shows that at high pump speeds all vapour is efficiently removed, whilst at low pump speeds more vapour is present in the chamber [74]..... 24

Figure 2-13 Shows the dependence of the contact angle (between the mid-level of the single track) with the substrate can dictate whether the track is in a stable or instable track formation zone [5] 27

Figure 2-14 shows illustrations for the relationships between the surface tension gradient and the temperature on the flow direction in the melt pool. Figure 2 13 shows how the flow in a melt pool can change, depending on the sign of the surface tension gradient. A negative surface tension over the entire temperature range of the melt pool, results in a lower surface tension in the high temperature regions. This results in outward flow, from the centre to the outer edge of the melt pool. With the surface tension having a positive value and then changing to a negative value, the melt pool can be in a situation where there is an outward flow in the centre of the melt pool, and an inward

flow at the outermost edges. Total inward flow occurs if the surface tension gradient is positive [90]..... 29

Figure 2-15 a) shows an image of the direct calorimetry setup inside the process chamber. B) shows a schematic of the disc holder and attached thermocouples. C) shows the disc, with a machined recess of 100 μm to hold the powder layer [39] 30

Figure 2-16 a) shows the absorptivity curve for 316L stainless steel. Shown are three modes, I – conduction mode, II – conduction – keyhole transition zone, III – keyhole mode. B) shows the absorptivity as a function of laser power for 316L stainless steel, tungsten and aluminium 6061 [39]..... 31

Figure 2-17 shows the experimental absorptivity as a function of wavelength for incident light on aluminium at room temperature. The blue results are from the handbook of optical solids [101] and the red results are from S. Krishnan and P. C. Nordine [102].. 32

Figure 2-18 shows laser power as a function of time, for a continuous wave laser (CW - Blue) and a Pulsed wave (PW – Red) laser..... 33

Figure 2-19 shows the effect of a positive (Divergent) and a negative (Convergent) beam defocus on the melt pool width and depth. The focus position is at the narrowest beam size [129] 36

Figure 2-20 shows a circular gaussian (CG), longitudinal elliptical beam(LE) and a transverse elliptical beam (TE). [130]..... 37

Figure 2-21 shows a defect structure process map for a range of laser powers and scan speeds for Ti6Al4V. [140] 38

Figure 2-22 Samples made by Gordon et al. use Tang et al.'s criterion for elimination of LOF pores. [140] 39

Figure 2-23a) shows the Marangoni convection in the melt pool b) shows how the Marangoni flow can disrupt the oxide formation during the solidification of the melt pool [152] 39

Figure 2-24 shows the three separate zones for the transport of pores within a melt pool. The circulation zone, the transition zone and the laser interaction zone [154] 40

Figure 2-25 shows the computational modelling results, demonstrating the four different modes in powder-gas interactions. Images a-d show the laser absorption distribution on the 2D powder layer. E-h show the temperature and velocity fields i-l

Show the pressure distribution on the highlighted powder particle. M-p shows the resulting force on that particle due to the pressure exerted from vaporisation [164] .. 42

Figure 2-26 shows the sequence of events leading to a particle becoming entrained in the vapour jet, and then due to significant recoil pressure, the particle hits the right side of the melt pool edge, causing massive melt pool instability [164]. 43

Figure 2-27 shows a schematic on the temperature gradient mechanism that results in the generation of residual stresses in the HAZ [166] 44

Figure 2-28 shows the temperature, thermal gradient, longitudinal and transverse stresses formed during a single track deposition [169]. 45

Figure 2-29 shows how G and R can affect the solidification modes [174] 46

Figure 2-30 Shows how epitaxial growth nucleates from the base material from a melt pool. The grains grow in the opposite direction the heat flow as can be seen in the image on the right. The image to the right shows how grains can nucleate in the mushy zone [174] 48

Figure 2-31 shows the effect of supercooling on the solidification mode. Supercooling increases from a through to d. The size of the mushy zone increases with the degree of supercooling, promoting equiaxed dendritic microstructure [174]. 49

Figure 2-32a) shows how AlSi10Mg and Al7075 solidify over a temperature range. B) shows how the dendritic growth occurs for an alloy that is susceptible to solidification cracking, and one that is not. The solidification for AlSi10Mg is different because the channels in between the dendritic arms can be backfilled [183] 49

Figure 2-33 shows the pulse power as a function of time. The pulses are compromised of the main welding pulse, and then subsequent ramp down pulses of different gradients [117] 51

Figure 2-34 shows how the elastic modulus varies with the angle in which the part is printed on the build plate. [189] 52

Figure 2-35 a) shows the dimensions of the chevron shaped laser beam. B) shows the direction of the laser scan for SP1, SP2 and SP3. C and D show the growth of grains from the chevron shaped beam. E, F and G show the grain boundaries and orientation for the different directions of the chevron shaped beam, in addition to effect of power [192] 54

Figure 2-36a and b show the grain structure from a low Δt_i and a high Δt_i . E shows the G and R values for the different regions, showing a low GR for region 1 and a high GR for region 2. F shows how the distribution of Δt_i splits the two microstructures [196] 55

Figure 2-37 shows normalised melt pool depth vs normalised enthalpy for 316L stainless steel. Conduction mode and keyhole modes can be seen from gradient changes [6] 58

Figure 2-38 shows how a camera voxelises the powder bed into individual areas. Each individual area is given a GCF value and then a subsequent scan matches the GCF constant to the previous one. GCF values vary dynamically as the print progresses, due to the GCF constant changes due to residual heat [222] 59

Figure 2-39a) shows a melt pool during a turn in LPBF. Overheating during the turn creates two keyholes, creating porosity. B) shows the pore after the laser has passed the turn. C) Shows how the stability criterion can generate a stable keyhole and eliminate porosity in the turn. D) shows the power modulation that was generated through the stability criterion [78] 63

Figure 2-40 shows the multiscale modelling strategy from LLNL for LPBF [43] 64

Figure 2-41 shows full laser ray tracing. C) shows laser ray tracing in conduction mode, with the colours representing how many reflections the ray has undergone . D) shows laser ray tracing for a keyhole mode track. This clearly shows the multiple reflections inside the keyhole formed in the cavity [78] 67

Figure 3-1 shows the particle size distribution which was adopted into the DEM model. Here, a PSD of 15 – 45 μm is adopted for the PSD of the model, after the measured distribution of powder from the experimental study. 74

Figure 3-2 shows the interface capturing method used in the VOF scheme, to model the free surface. Blue cells show the metal volume fraction of 1, the green cells show a volume fraction for the gas phase which equals 0, and then red cells are the interface cells, which are between 0 and 1. 78

Figure 3-3 shows the boundary conditions for LPBF model. The model has two boundary conditions. One is the metal boundary condition (side solid boundary and bottom boundary condition). These are modelled as 'Wall' boundary conditions within fluent where the zero normal derivative is used. The other is the pressure outlet boundary condition, which is applied to any boundary that is argon. These are the top boundary condition and the side gas boundary condition..... 79

Figure 3-4 showing a typical domain for the LPBF model. The metal phase is highlighted in orange, whilst the gas phase is highlighted in green. The convention used throughout this thesis is shown in the top left. 80

Figure 3-5 shows a schematic of the spawning locations and direction of travel of the initial DPM step. Grey regions in the image represent powder at ambient temperature, blue regions represent previously melted powder, orange shows melted powder, and the red region represents the keyhole cavity. 82

Figure 3-6 shows a flowchart of the pressure-based solver order of operations 86

Figure 3-7 shows the temperature dependant properties for density (a), thermal conductivity (b), Heat capacity (c), and the dependence on the angle of incidence for the absorptivity from the refractive index (d). Properties taken from [244], [255], [256] . 89

Figure 3-8 shows the LMC setup, inside the Renishaw AM400 machine with the key constituents labelled. The design is easily adapted for other systems and can be integrated with other instruments as necessary. 90

Figure 3-9a shows the temperature trace captured by the pyrometer, with the fitted cooling curve. b) shows the temperature dependant heat capacity, with the integration area shown for the points T0 and T1. 91

Figure 4-1 shows the laser profile for the continuous and variable (Ramp up) profiles. 96

Figure 4-2 shows the difference between the two different representation of a pulsed laser. The first image shows laser power vs distance for both the PW laser in Milan (Blue) and the PW laser in Nottingham (Red). The second image shows laser power vs time for both PW lasers. With respect to time, both lasers have exactly the same laser on and off times throughout the track length (Green). However, with respect to distance, they both differ. The PW laser in Nottingham, acts in stationary spots during its laser pulse, whereas the PW in Milan constantly moves, applying its power over its point distance. 97

Figure 4-3 shows the literature value and the revised value of the refractive index. The plot shows how the absorptivity changes depending on the angle of incidence of the incoming photon. 99

Figure 4-4 shows the validation for the 316L stainless steel 200 W CW single track with a laser velocity of 0.3 m/s. The left portion of the image, is an SEM image of the YZ cross section of the experimental track. The black line denotes the melt pool boundary. The

right portion of the image represents the simulation result. Here, the red region represents the material that has melted during the process, mimicking the melt pool. The images are aligned so the substrate is the same height in both images at the same scale. 100

Figure 4-5 shows the melt pool boundary line 101

Figure 4-6 shows the longitudinal XZ cross section of both the experiment and the model for 316L stainless steel. Both XZ cross sections are cut in the middle of the track. Top left of the image shows the longitudinal XZ cross section of the experimental single track. Here, the undulating black line represents the melt pool boundary. The top right image shows the simulation melt pool boundary, with the red region representing the amount of material that has been melted during the simulation. Marked at the end of the CW track is a pore. The bottom image shows the experimental XZ cross section with the simulation result overlayed. The white dotted line represents the substrate level, with the red line denoting the model XY depth, as shown in Figure 4-4, and the black line showing where the XY melt pool depth for the experimental track lies. The images are aligned so the substrate is the same height in all three images at the same scale. 102

Figure 4-7 shows the YZ cross sections of the Ramp Up experimental and simulation single track results for 316L stainless steel. The left image shows the XZ cross section of the experimental track, viewed in a SEM. The blue line represents the melt pool boundary for the experimental XZ cross section. The right image shows the XZ cross section of the simulation single track. Here, the red region is the region that has gone above the melt pool temperature during the simulation. The white space represents Argon that has been trapped in the melted region during the single track deposition. The images are aligned so the substrate is the same height in both images at the same scale. 103

Figure 4-8 shows the XZ cross section for the Ramp Up experimental and simulation single track depositions for 316L stainless steel. Both XZ cross sections are cut in the middle of the track. The top left image shows the XZ cross section of the experimental single track, viewed on an SEM. The black line denotes the melt pool boundary. The black regions at the bottom of each melt pool peak are porosity. The top right image shows the simulation XZ cross section of the deposited single track. The simulation result shows the regions in red that have been above the melting temperature during the deposition. Again, the white regions labelled in the image, is porosity. These appear in the same region as the porosity in the experimental sample. The bottom images are both experimental and simulation overlayed atop one another. This image shows how well

these two single track measurements match. Porosity is also shown to be produced in the same location for both model and experiment. The images are aligned so the substrate is the same height in all three images at the same scale. The jagged edges of the SEM images are from multiple SEM images stitched together. 104

Figure 4-9 shows the validation to Yadroitsev et al for 316L stainless steel. No comparison image was produced in the extant paper by Yadroitsev et al, so the simulation image is presented here only. The red region in the image shows cells that have gone above the melt pool temperature during the single track deposition. 105

Figure 4-10 shows absorptivity as a function of time for the 316L stainless steel validations on the primary axis, and Laser Power as a function of time on the secondary axis. The Red traces are for the Ramp Up, and the black traces for the Continuous laser power. The Ramp Up profile consists of two peaks, one at 500 μs and one at 1000 μs. The total track length for both profiles is 300 μm. 106

Figure 4-11 shows 3 sequential images during a crucial phase of the Ramp Up power profile for 316L stainless steel. The peak distance for the Ramp Up profile is 500 μs. Therefore these three images show the Ramp Up profile from the peak power, to the lowest power, and shows how the porosity is formed during this change. The first image at 450 μs, shows a near maximum laser power of 260 W, the second image a laser power of 100 W, and the third a laser power od 120 W. The colours shown on the simulation represent temperature, the amounts given by the scale bar on the left side of the images. The column of rays show each individual ray tracing DPM particle and their trajectories. The colours of the DPM particles are the power (W/m^2) carried by each particle. The scale bar on the bottom of the image shows the values for the DPM particle power values. 108

Figure 4-12 Left: shows the YZ cross section of the melt pool produced with the parameters for PD60 for AA2024. The literature value shows a melt pool depth of 3 μm, against the dotted white line, which is the melt pool depth for the average experiment, at 46.9 μm. Right: The revised version of the refractive index is shown, with an average melt pool depth of 40.47 μm. 109

Figure 4-13 shows a plot of the validation study for AA2024. Melt pool dimensions from the LMC are compared with that of the model, both using 50 μm layer thickness with no preheat at the same laser conditions. Two laser parameter cases are used for the validation, PD15 and PD60. The results for the LMC are shown in black, and the model results shown in red. Error bars represent the +/- standard deviation for the results,

measured at 3 different locations along the track length for the model, and across 3 different tracks for the LMC. Melt pool depth and width values are shown here. 111

Figure 4-14 shows XZ SEM cross sections from the LMC experiment (top row) and the XZ cross sections of the model (bottom row) for PD15 for AA2024. The bottom row shows the XZ cross sections from the model. Here, the red region shows cells that have been melted during the single track deposition. Blue shows cells that have not melted. Multiple images are shown for the LMC experiment to showcase the variation in measured melt pool dimensions. To mimic the semi-random sectioning of the LMC tracks over several mm, the model has been sectioned at 3 different points along the track length.....112

Figure 4-15 shows XZ SEM cross sections from the LMC experiment (top row) and the XZ cross sections of the model (bottom row) for PD60 for AA2024. The bottom row shows the XZ cross sections from the model. Here, the red region shows cells that have been melted during the single track deposition. Blue shows cells that have not melted. Multiple images are shown for the LMC experiment to showcase the variation in measured melt pool dimensions. To mimic the semi-random sectioning of the LMC tracks over several mm, the model has been sectioned at 3 different points along the track length.....112

Figure 4-16 shows the top view in the YX plane, and also the longitudinal view of the track in the XZ plane for PD60 for AA2024. The top view shows the track width variation along the single track length. Overspills at periods of 60 μm match to the point distance. The locations of the validation XZ slices are shown at arbitrarily chosen positions of 160 μm, 368 μm and 533 μm. The bottom image shows the XZ cross section of the track, also showing where slice locations are taken from.....113

Figure 4-17 shows the top view in the YX plane, and also the longitudinal view of the track in the XZ plane for PD15 for AA2024. The top view shows the track width variation along the single track length. The locations of the validation XZ slices are shown at arbitrarily chosen positions of 134 μm, 335 μm and 488 μm. The bottom image shows the XZ cross section of the track, also showing where slice locations are taken from. 113

Figure 4-18 show a top SEM view of the PD15 (top) and PD60 (bottom) tracks for AA2024. Much more variability can be observed in the PD15 track. PD60 shows cracking at the left side of the track. Tracks were deposited in the LMC using a Renishaw AM400. 114

Figure 4-19 shows the absorptivity as a function of distance for PD15 and PD60. Here, the top plot shows the absorptivity vs distance of PD15, the black solid line representing the average absorptivity from the track length. The bottom plot shows absorptivity vs distance for PD60, with the red solid line showing the average absorptivity across the track length. This plot only shows the first 1250 μs, in addition to being smoothed, taking an average of 1 μs to aid in readability. The blue dotted line represents the absorptivity measured from the LMC. 115

Figure 4-20 shows a plot of the absorptivity results for both the LMC and the model. The results for the LMC show the average absorptivity value that the experiment generates as the average absorptivity for the entire track length. In contrast, the model generates a 'live' absorptivity value that varies throughout the entire track length. Therefore, the absorptivity results for the model have been plotted with error bars showing the standard deviation throughout the live absorptivity trace..... 116

Figure 5-1 shows an example of the methodology behind the inverse solution process. Each timestep evaluates dT, and if the temperature is below $Ttarget$ (dT is positive) then the solution calculates the power required to raise the temperature to the target. If dT is negative, where the temperature is above $Ttarget$, no power is inputted. 126

Figure 5-2 shows how the power is changed to keep the peak temperature of the melt pool at the target temperature of 3700 K, while maintaining a constant traverse speed of 1.5 m/s. b) shows an image of the melt pool track at 150 μs. The black line denotes the melt pool boundary (cells which exceeded the melt temperature of SS 316L). The temperature measurement point corresponds to the power calculation cell. c) shows a cross section of the powder before the laser is turned on. The image is aligned so that each power fluctuation can be matched with a powder level change. An identical powder bed is used in each simulation e) The inverse solution process is validated, by taking the average of the power from a). Using this constant predicted power of 106W, the melt pool temperature is shown to average out to an average temperature of 3716 K. d) shows the cross section of the melt pool from 106W, showing a similar profile to b). 129

Figure 5-3 a) and c) show how the power is changed to keep a constant temperature of 2200 K and 2500 K, below the boiling point of the metal, at 0.3 m/s. b) shows how a constant peak surface temperature of 2200 K is insufficient at creating a large enough melt pool to produce a consolidated track. d) shows how a 300 K higher surface temperature is sufficient to create a melt pool large enough to prevent balling..... 131

Figure 5-4 a), b) and c) Side, and top view of the melt pools created with a constant peak surface temperature of 3300 K, 3700 K and 4100 K, at 1.5 m/s. a) Underpowered melt pool, with an insufficient peak temperature to achieve consolidation at 1.5 m/s. b) Consolidated track, on the edge of the keyhole transition, with a peak surface temperature of 3700 K. c) Overpowered melt pool, with a peak surface temperature of 4100 K, which has created a keyhole cavity. d), e) and f) show the YZ plane through the centre of the laser spot. The arrows indicate the direction of the force generated by the recoil pressure. g) Power given over the length of the track for the 3300 K, 3700 K and 4100 K targets.....133

Figure 5-5 shows a plot of temperature vs recoil pressure for 316L stainless steel 136

Figure 5-6 a) shows a schematic of the melt pool, with the surface temperature above the boiling point, but with the ratio Pr/Pi + Po below 1. The recoil pressure is insufficient to overcome the internal pressure. b) shows this with a peak surface temperature of 3300 K. c) shows how a surface temperature of 3700 K, has enough force to overcome the internal pressure, creating a depression in the melt pool. Here Pr / Pi + Po is greater than 1, and so a depression is created. This is demonstrated in d), where the recoil pressure is strong enough to start pushing the melt pool surface downwards. e) shows how if Pr / Pi + Po is large enough, the melt pool surface can be pushed substantially downwards. f) shows this with a surface temperature of 4100 K, where the whole surface of the newly created cavity has a force acting on the surface.....138

Figure 5-7 a) shows how the normalised boiling temperature (T/Tb) varies with Pr / Pi + Po for the 3 popular LPBF metals/alloys, aluminium, titanium and 316L stainless steel. Note, the logarithm of both axis is taken here. b) shows how the calculated peak temperature, tends towards the same value, regardless of R or speed. Each bounding box represents a Pr / Pi + Po value of 5, 9 and 18 respectively. c) shows us that the calculated temperature T_cpk is not dependant on speed, as each speed tends to the same temperature value. T_cpk only depends on the value of Pr / Pi + Po. (i) shows the dependence of the calculated temperature on the radius of the melt pool. 140

Figure 5-8 a-i show an XZ cross section through the domain. a), b) and c) show a Pr / Pi + Po of 5, 9 and 18, at the speed of 0.3 m/s. d), e) and f) show a Pr / Pi + Po of 5, 9 and 18 with a speed of 1.5 m/s. g), h) and i) shows the 3 different Pr / Pi + Po 5, 9 and 18 with a speed of 2.5 m/s. j), k) and i) show the maximum force generated by the recoil pressure over the melt pool area in mN for Pr / Pi + Po = 5, 9 and 18 at 1.5 m/s respectively..143

Figure 5-9 a depth vs laser scan speed for a P value of 9. This plot shows how different melt pool depths can be obtained through different laser scan speeds. For a speed of 2.5 m/s heat conduction is very limited, resulting in the lowest melt pool depth. 1.5 m/s and 0.3 m/s show how through a reduction in speed, larger melt pool depths can be obtained, without entering into keyhole mode. b) shows how using a P value of 9, results in a temperature target of 3860 K. The inverse solution is then used to keep the melt pool surface at this target while varying the laser power. An average of 161 W gives this surface temperature.....144

Figure 6-1 shows an explanatory figure showing the different aspects of each figure presented in this results chapter.....151

Figure 6-2 shows XZ cross sections of PD60 and PD15, showing the temperature field in the XZ plane. The contour bars show temperature, with the top limit set to the boiling temperature of AA2024 (2743 K). The left column shows PD60, and the right column shows PD15. Rows represent different time series of both PD60 and PD15. Each row is matched so that the corresponding PD15 pulse impacts in the same location. The upper right corner of each plot shows the pulse at each snapshot. 1.0 represents the end of the first pulse, so therefore 0.4 represents the snapshot at 48 μs through the pulse duration. 152

Figure 6-3 shows a magnified image of the last row in figure 6-1, for both PD60 and PD15. The contour bars show the temperature field in the window between x position 200 μm and 400 μm. The contour bars show temperature, with the top limit set to the boiling temperature of AA2024 (2743 K). Here, the white line represents the interface between argon and metal cells. The outside black line shows the solidus temperature boundary, whilst the inner black line denotes the liquidus temperature boundary. 154

Figure 6-4 shows a magnified image of the last row in Figure 6-1, for both PD60 and PD15. The contour bars show the temperature gradient field in the window between x position 200 μm and 400 μm with the top limit set to 1.5e7 K/m. Here, the white line represents the interface between argon and metal cells. The outside black line shows the solidus temperature boundary, whilst the inner black line denotes the liquidus temperature boundary.....155

Figure 6-5 shows a magnified image of the last row in Figure 6-1, for both PD60 and PD15. The contour bars show the solidification speed in the window between x position 200 μm and 400 μm with the top limit set to 0.5 m/s, close to the maximum speed for PD60. Here, the white line represents the interface between argon and metal cells. The

outside black line shows the solidus temperature boundary, whilst the inner black line denotes the liquidus temperature boundary. 156

Figure 6-6 shows a magnified image of the last row in Figure 6-1, for both PD60 and PD15, but showing sequential images showing the transition from 0.4 of a pulse, though 0.7, 0.8 and 0.9. Images a – b show PD60 and images c – d show PD15. The images show that when the laser is turned off at 0.85 of a laser pulse, how the melt pool cools. The contour bars show the cooling rate in the window between x position 200 μm and 400 μm with the limit between 7e6and -4e6 K/s. A negative cooling rate shows cooling, whilst a positive cooling rate shows heating. Here, the white line represents the interface between argon and metal cells. The outside black line shows the solidus temperature boundary, whilst the inner black line denotes the liquidus temperature boundary. ... 157

Figure 6-7 shows a magnified image of the last row in Figure 6-1, for both PD60 and PD15, but showing sequential images showing the transition from 0.4 of a pulse, though 0.7, 0.8 and 0.9. Images a – d show PD60 and images e – h show PD15. The images show that when the laser is turned off at 0.85 of a laser pulse, how the melt pool cools. The contour bars show the cooling rate in the window between x position 200 μm and 400 μm with the limit between 7e6and -4e6 K/s. A negative cooling rate shows cooling, whilst a positive cooling rate shows heating. Here, the white line represents the interface between argon and metal cells. The outside black line shows the solidus temperature boundary, whilst the inner black line denotes the liquidus temperature boundary. ... 158

Figure 6-8 shows a magnified image of the last row in Figure 6-1, for both PD60 and PD15. The contour bars show the strain rate in the window between x position 200 μm and 400 μm with the top limit set to 100 Hz and the bottom limit set to -100 Hz. Here, the white line represents the interface between argon and metal cells. The outside black line shows the solidus temperature boundary, whilst the inner black line denotes the liquidus temperature boundary. 160

Figure 6-9 shows the volume of the mushy zone, for PD15 (in black) and PD60 (in red). As the two different parameter sets use different point distances (and therefore different effective speeds), this plot depicts the volume of the mushy zone as a function of distance and not time. The top plot shows the volume of the mushy zone as a function of the entire track length. The lower plot shows the plot PD15 subtracted by PD60, showing the amount that PD15 is under/over PD60. 161

Figure 6-10 shows the XZ cross section of P-ratio 5 and P-ratio 3. The left column shows P-ratio 5 and the right column shows P-ratio 3, with the rows increasing sequentially

from 112 μs, 784 μs, 1584 μs. The contour bars show temperature, with the top limit set to the boiling temperature of AA2024 (2743 K). The images show the effect of different power inputs on the temperature fields experienced at different sections of the track. 162

Figure 6-11 shows calculated power and the peak temperature as a function of time for P-ratio 5 and P-ratio 3. The red line denotes temperature and is measured off the secondary axis (right). The black line is the calculated power and is measured off the primary axis (left). Average values of power for P-ratio 5 are 268 W and 216 W for P-ratio 3. 164

Figure 6-12 shows plots of the error throughout the inverse solution for P-ratio 3, of the peak melt pool temperature and the calculated temperature by Tpk. The bottom plot shows this percentage error over a period of 1200 μs, whilst the top plot shows a magnified view between 0 and 280 μs (the duration of 2 pulses). The image is overlayed with labels displaying periods where the is laser on and laser off. 166

Figure 6-13 shows the maximum force (in mN) generated by the recoil pressure over the melt pool area for P-ratio 5 and P-ratio 3, shown with the force needed to be equal to the internal pressure of the melt pool. The black line represents the maximum force, and the grey line shows the force needed to match the internal pressure of the melt pool. 167

Figure 6-14 shows XZ cross sections of 10 x 10 x 10 mm cubes printed on the Renishaw AM400 for the inverse solution validation study. Cubes progress from low density to high density (at a peak between 200 – 220 W), and then back down to low density. The red text and dotted lines denote at which point in the scale (from 180 W to 240 W) the inverse solution has predicted the laser power. P-ratio 5 shows porosity in its single track, and predicts a power of 268 W. P-ratio 3 shows a consolidated track with a predicted power of 216 W, which falls in the middle of the highest density region between 200 – 220 W. 168

Figure 6-15 shows the main differences in PD60 compared to PD15 through the dendrite growth. PD60 shows long, closely spaced dendrites, that cannot back fill easily, causing high strain rate areas. PD15 shows shorter dendrites spaced further away, with a larger tendency to back fill. Additionally PD15 shows low melting point eutectic fluid from microsegregation at the dendrite roots. 171

Figure 6-16 shows the XZ cross section of the optimisation run for 316L stainless steel and AA2024 with a P-ratio of 5. Both images are aligned to the melt pool centres, and show an image halfway along the single track. The images show the difference between

a continuous optimisation (top) and a pulsed optimisation (below), with respect to the melt pool depths. The cooling time for the speed of the pulse needed for AA2024 resulted in identical small melt pools of this size, that are not affected by track length. These melt pools were captured half way along its length.....174

List of tables

Table 2-1 Table showing an example of software and numerical methods used in the literature. 68

Table 3-1 showing the thermophysical properties for the 316L stainless steel, AA2024 and aluminium..... 88

Table 4-1 shows the laser parameters for both continuous and variable (Ramp up) laser profiles. * Average laser power is the average laser profile over the length of the track. 95

Table 4-2 shows the laser input parameters for the aluminium validation. 98

Table 4-3 shows the validation results for 316L stainless steel. Shown is the three validation cases, along with the respective melt pool widths and depths for both the model and the experimental single track. Errors presented are the percentage error between measured experimental measurements (of which 3 different measurements were taken in 3 different locations) and measurements from the model results. The melt pool depth and width value for the Ramp Up single track, are taken from the second peak. 99

Table 4-4 Table shows the individual validation results from the AA2024 validation study. Here the PD15 parameter represents a laser power of 200 W with a 15 μm point distance, a exposure time of 120 μs and a delay time of 20 μs. The PD60 parameters are a mirror of AA2024, the only difference being the point distance is increased to 60 μm. Therefore the effective speed of PD15 is 0.107 m/s, and PD60 is 0.429 m/s..... 110

Table 5-1 shows the properties of the tracks produced at different surface temperatures. The average peak temperature is the average peak melt pool temperature measured across the track length, whilst trying to stay at the target peak temperature. The average power to achieve target is the average power value across the length of the track, to achieve the average peak temperature. 134

Table 6-1 shows the laser input parameters for the aluminium validation. 149

Table 6-2 shows the melt pool dimensions of P-ratio 5 and P-ratio 3. 163

Abbreviations

AA2024	Aluminium Alloy 2024
AM	Additive Manufacturing
CAD	Computer Aided Manufacturing
CAE	Computer Aided Engineering
CFD	Computational Fluid Dynamics
CFL	Courant-Friedrich-Lewy
DED	Direct Energy Deposition
EBPBF	Electron Beam Powder Bed Fusion
FEA	Finite Element Analysis
FV	Finite Volume
HPC	High Performance Computing
LBM	Lattice Boltzmann Method
LPBF	Laser Powder Bed Fusion
Nd:YAG	Neodymium-doped Yttrium Aluminium Garnet
PDE	Partial Differential Equation
SEM	Scanning Electron Microscopy
SLM	Selective Laser Melting
VOF	Volume of Fluid
UDF	User Defined Function

Nomenclature

p	Density
U	Velocity
t	Time
μ	Dynamic viscosity
S_m	Momentum source term
T	Temperature
k	Thermal conductivity
C_p	Specific heat capacity
S_T	Energy equations
S_b	Buoyancy source term
S_d	Melting and solidification source term
S_{sf}	Surface tension source term
S_{rp}	Recoil pressure source term
α_1	Volume fraction gradient
σ	Surface tension
κ	Curvature
$\vec{n}$	Surface normal vector
∇_t	Tangential gradient operator
∇T	Temperature gradient
L_{vap}	Latent heat of vaporisation
M	Molar mass
T_b	Boiling temperature
R	Avogadro's number
$\vec{u}$	Flow velocity
$\bar{\rho}$	Volume averaged density
$\overline{\Phi}$	Any material property
C_p	Heat capacity
h_{ref}	Reference Enthalpy
T_{ref}	Reference temperature
P	Laser power
r	Laser beam radius
v	Laser speed
Q_{init}	Initial energy of DPM particle
n	Complex refractive index

$\vec{I}$	Incident DPM particle direction
$\vec{R}$	Reflected DPM particle direction
Q_{end}	Irradiance at each cell
Ab	Absorptivity
Q_{laser}	Laser power per unit volume
V	Cell volume
Q_{rad}	Heat loss through radiation
Q_{evap}	Heat loss through evaporation
Q_{melt}	Heat loss through melting
P_0	Chamber pressure
L_{melt}	Latent heat of melting
G	Thermal gradient
R	Solidification speed
T_x	X component of temperature gradient
C	CFL condition
$\frac{d\sigma}{dT}$	Temperature coefficient of surface tension
C_{p0}	Heat capacity at 0 °
α	Temperature coefficient of heat capacity
E_c	Calculated energy
P_c	Calculated laser power
t_s	Solver timestep
A	Cell surface area of surface normal
A_G	Global absorptivity
Q_{inv}	Inverse solution power
P_i	Internal pressure of a melt pool
P_{ratio}	Ratio of recoil pressure to internal pressure
T_{cpk}	P_{ratio} calculated temperature
$\dot{T}$	Cooling rate
$\dot{\varepsilon}$	Strain rate
λ_1	Primary dendrite arm spacing
I_c	Cellular dendritic length
T^*	Cell tip temperature
T_s'	Dendrite root temperature

1 Introduction

1.1 Background

Laser powder bed fusion (LPBF) is the most prominent metal Additive Manufacturing (AM) technique and is disrupting diverse fields of high-value manufacturing [2]. LPBF is conceptually simple as a single (or multiple) laser beam(s) that selectively melts metallic powder sequentially, adding continuous single tracks into layers to form 3D objects of various geometrical complexity. Central to the development of this technology has been the quest of so-called 'optimised laser beam parameters'. These are parameters that minimise porosity through excessive or insufficient energy input, or eliminate material specific defects like hot tearing (cracking) during the LPBF process, in addition to promoting favourable microstructures. However, optimising process parameters can be an arduous process, that is time consuming, costly and reliant on user expertise. The method of optimising process parameters can also be blocked by material specific defects, that cannot always be solved through a quick parameter optimisation study. Phenomena such as hot tearing in aluminium alloys, prohibits the use of some alloy systems being used in LPBF.

Reducing the likelihood of defects created during the LPBF process can be achieved by establishing a melt pool that is thermodynamically stable throughout the process [3]. Porosity defects, aside from powder feedstock issues, stem predominantly from undesirable melt pool characteristics, dependant on the power density delivered into the melt pool [4]. In-sufficient power density leads to lack of fusion defects. These defects have been shown to arise from a small melt pool volume, that does not melt the top surface of the previous layer [5]. On the other hand, excessive delivery into the melt pool, results in a large recoil pressure, generated from the surface temperature of the material greatly exceeding the materials boiling point [6]. This causes a large cavity to be formed in the melt pool, accompanied by a marked increase in absorptivity, that can destabilise the melt pool. The volatile liquid metal at the bottom of the cavity can capture a volume of gas, creating a keyhole pore. Stable melt pools have been shown to reduce lack of fusion and keyhole defects, as well as reduce spatter. Some defect mechanisms have been proven theoretically and measured post process, such as hot tearing within aluminium alloys processed by LPBF [7], [8]. However, the elimination of the effects of hot tearing through combined empirical and numerical process parameter studies alone, have not been demonstrated.

The energy delivery method of LPBF makes it difficult to process all metallic materials without verifying an absence of defects in a component. Defect inclusion within LPBF components is the main limiting factor of the acceptance of LPBF in industry [9]. The importance of this fact underpins most research published in the LPBF and AM communities.

The method of process parameter selection has progressed in recent years. The advent of dynamic, model informed, feed forward control in LPBF is the future of process parameter control [10]. In-situ methods can use sensors to adjust processing parameters on the fly, and model based methods use computational techniques to optimise strategies in a digital environment before the part is built [11], [12]. These methods offer even more control over the LPBF process, and provide some automation into how these process parameters are calculated. In addition to this, high fidelity modelling of the LPBF process, have been shown to be compulsory for providing sufficient information to capture the complexity of the process, and provide accurate optimisations.

This work is funded by the Engineering Physical Science Research Council (EPSRC) and by Oerlikon AM, to reduce cost, complexity and reduce timescales associated with the use of new materials in LPBF. Current process parameter optimisation needs to progress further from trial and error approaches that are commonly used within industry and research environments.

1.2 Aim and objectives

To supersede trial and error approaches commonly used in LPBF, this work aims to provide a framework by using computational modelling to provide an optimised set of parameters, through a high fidelity model. This novel framework optimises process input conditions, by stabilising the process through the regulation of peak melt pool temperatures. Peak melt pool temperature has been chosen as the objectives of this study are to control the melt pool temperature above and below the boiling point. In addition, one cannot rely solely on the boiling temperature of the metal to naturally limit the peak temperature, as peak melt pool temperatures can exceed the boiling temperature of the metal [13].

Two materials, 316L stainless steel and a high strength aluminium alloy, AA2024 are used to validate the framework. In addition, AA2024 will be used to showcase how high fidelity modelling in LPBF can be used to measure and evaluate cracking in high strength aluminium alloys, by providing visualisation into material cracking mechanisms and

driving forces. The temperature driven optimisation framework will then be used to provide an optimal set of parameters for AA2024.

Ultimately, this framework will reduce the cost, complexity and timescale of optimising process parameters. This framework has been achieved by meeting the following objectives:

- Create a high fidelity model, that replicates the LPBF process
- Validate the model fidelity to two different LPBF materials
- Create a material agnostic framework to optimise process parameters for LPBF
- Using the high fidelity model to investigate hot tearing in AA2024
- Using the high fidelity model to optimise a difficult to print alloy, AA2024

1.3 Significance and novelty

In this work, two significant and novel pieces of research are presented. Firstly, the high fidelity model is used to investigate the hot tearing defect mechanism in AA2024. AA2024 is a high strength to weight ratio material, offering good fatigue resistance and is often used in the aerospace industry. The alloy, in addition to most aluminium alloys, suffers from hot tearing during LPBF processing. These cracks prevent AA2024 from being used in a structural component after being processed via LPBF. In this work, the model is used to demonstrate how this type defect can be eliminated through correct process parameter optimisation, without changing the alloy composition. The investigation into the mechanism of hot tearing in AA2024 has not been explored by computational methods in the literature. This chapter is part of a larger body of research to measure, evaluate, predict and eliminate cracking in high strength aluminium alloys at the University of Nottingham. This work presents an initial part of the project to measure and evaluate the cracking behaviour of a high strength aluminium alloy. The second part of this project is being performed by a second student at the University, to predict and eliminate this cracking behaviour, the mechanisms of which are uncovered in this initial research.

Secondly, and the primary focus of this research, shows how temperature should be used as the primary process parameter that is optimised in LPBF, so that melt pool stability is prioritised. Stability of the melt pool is controlled by a novel inverse solution driven framework, that via a high fidelity model, controls laser power to keep melt pool temperatures near constant during a laser track deposition. This framework considers what peak melt pool temperatures should be used for the most proficient processing

during LPBF. In addition, this framework is demonstrated to be viable for all users of LPBF technology, not only those with a feed forward capable LPBF machines.

1.4 Research methodology

To achieve the objectives outlined above, a high fidelity model is needed to replicate the LPBF process. In addition to the core of the LPBF simulation, additional modules have been added to provide the framework needed to optimise the LPBF process parameters.

The core of the model uses computational fluid dynamics (CFD) to simulate the metal hydrodynamics in the melt pool, and a ray tracing sub routine to simulate the laser and subsequent heat transfer to a stochastic powder bed. This is further detailed in Chapter 3. The model is then validated against 316L stainless steel and AA2024, by providing a novel 316L stainless steel validation study through a variable laser, and using a revised refractive index for AA2024. This is further detailed in Chapter 4. This base model is then used to simulate LPBF, and investigate a novel visualisation of the cracking mechanism in AA2024. This is further detailed in Chapter 6. The material agnostic stable melt pool for LPBF is implemented through a novel algorithm created in this research, based upon an inverse solution. This is further detailed in Chapter 5 and 6. This algorithm is the foundation for a framework created to reduce the cost, complexity and timescales associated with process parameter optimisation for the 'perfect part' to be manufactured through LPBF. The framework for the model, in addition to the inverse solution module, is shown in Figure 1-1.

The framework can be used with common processing parameter inputs such as fixed laser power and laser speed. However, it is the aim of this work that these inputs shall be replaced with a parameter that is based upon the surface temperature of the melt pool. This parameter will be inputted into the high fidelity model, and used to predict the laser process parameters. Figure 1-1 shows how the optimisation framework fits within the core high fidelity model. The model can be used to model 'standard' inputs to output precise temperature, velocity and pressure data. The optimisation framework however, receives temperature inputs that can be chosen or calculated. These are then fed into the inverse solution, that interfaces with the core high fidelity model. The output of the optimisation framework gives predicted laser process parameters that can be used on either pulsed or continuous wave systems, that are either standard or feed forward capable.

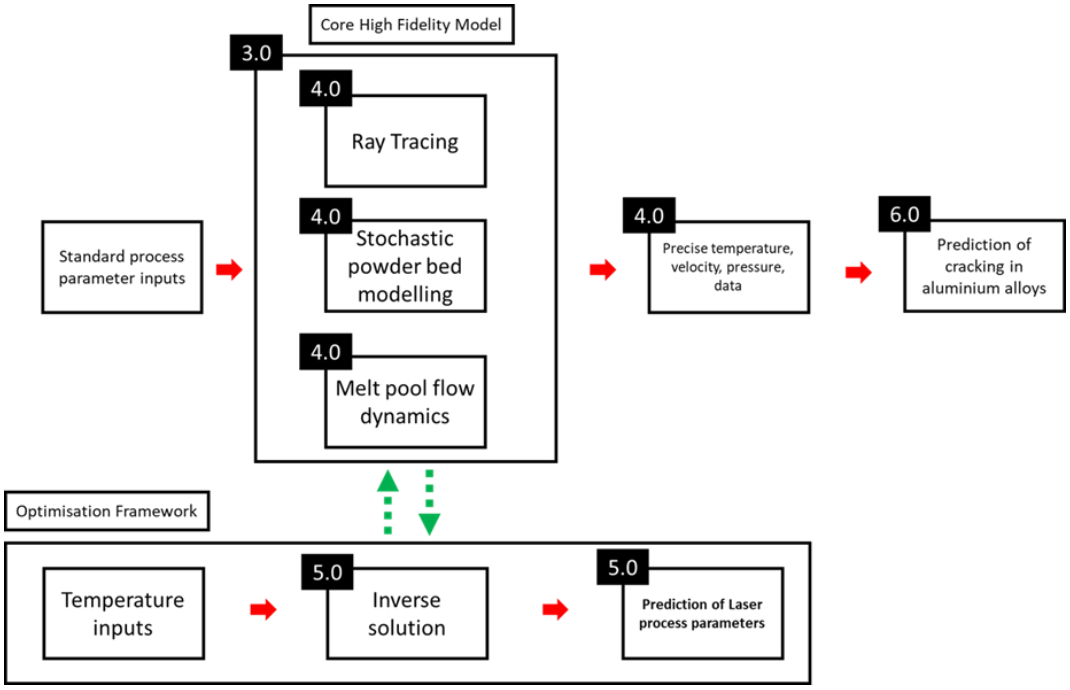

Figure 1-1 shows how the thesis is structured around the different elements of the model and how the optimisation framework fits within the core high fidelity model. The numbers in this image represent the chapter that the information is contained in. The model can be used to model 'standard' inputs to output precise temperature, velocity and pressure data. The optimisation framework receives temperature inputs that can be chosen or calculated. These are then fed into the inverse solution, that interfaces with the core high fidelity model.

1.5 Thesis layout

A description of the content of each chapter is presented below.

Chapter 2

Literature review

In this chapter, a literature review was performed to identify, critique and evaluate the literature for LPBF. A general overview for AM is provided, briefly outlining the different methods for processing metals using AM powder bed fusion. Then, a specific review of LPBF is presented, detailing laser metal interactions and the types of melt pool characteristics and geometry that can be achieved with different laser beam parameters. An overview of defects generated in LPBF is also included. A section is dedicated to solidification in LPBF, specifically focussing on metal solidification in a LPBF environment, and how cracks are formed during the LPBF process. Literature has then been reviewed for process optimisation, including extant methods often used in industry and research, in addition to state of the art optimisation methods, such as in-situ and model based feed forward modelling methods. The remainder of the chapter examines in detail the different techniques employed for the modelling the LPBF process. Lastly, the chapter is summarised by identifying gaps in the literature.

Chapter 3

Combined discrete element model with computational fluid dynamics for simulating laser powder bed fusion

In this chapter, the methods are presented for the core aspects of the model. The first section of this chapter details the creation of the stochastic powder bed, through discrete element modelling (DEM). The second section address the creation of the CFD model using ANSYS Fluent 2021 R2, and how custom user defined functions (UDFs) are used in the creation of the ray tracing representation of the laser heat source, and the implementation of the physics associated with melting and solidification, buoyancy effects, surface tension, temperature dependant surface tension (Marangoni flow), vaporisation phenomena including recoil pressure and evaporation flux.

Chapter 4

Evaluation of Model Performance

In this chapter, the model is validated against results obtained through empirical measurements. The model is validated against two materials, AA2024 and 316L stainless steel. This chapter contains novel results from the modelling of aluminium using a revised refractive index, and the validation against longitudinal cross sections of single tracks. This novel validation method shows how the model can validated against variable laser power parameters and shows excellent agreement with simulation results. . In addition, this chapter showcases the use of a laser micro calorimeter (LMC), built to empirically measure the absorptivity of the LPBF process.

Chapter 5

Model Informed Temperature regulation in laser powder bed fusion

In this chapter, a framework is established that allows for process parameters to be optimised via surface temperature, and shows the benefits of doing so. The chapter covers how the inverse solution algorithm works, and is applied into the model. Test cases are demonstrated, showing how the algorithm is apt in controlling the temperature of a melt pool above and below the materials boiling point. Additionally the chapter also outlines how laser power and laser speed are consolidated into one parameter, that can be adjusted in-situ to create a thermodynamically stable melt pool for LPBF.

Chapter 6

Model informed strategy for the processing of a high strength aluminium alloy

The aim of this chapter is to provide a case study on how a high fidelity model can be used to evaluate and visualise precise time and space dependant information for LPBF, in addition to using this information to predict process parameters based upon a surface temperature. This chapter uses AA2024 as a case study material. Here, the inverse solution correctly identifies a laser power at a set point distance and exposure time that gives the highest density of samples validated in experimental conditions. This work also raises important differences in modelling pulsed and continuous laser systems. The results show that whilst the P-ratio parameter is material agnostic, lower P-ratio values must be used in pulsed laser strategies as opposed to continuous wave strategies.

Chapter 7

Conclusions

This chapter provides a summary of the significant and novel conclusions obtained through this research work.

Chapter 8

Future work

This chapter provides recommendations for future work based upon on the conclusions brought forward by this research work.

Chapter 2

2 Literature review

2.1 Introduction

This chapter will review the literature for laser power bed fusion (LPBF), and show how computational modelling is used to represent and optimise this complex manufacturing process. This chapter will review, critique and identify the gaps in literature for the computational optimisation of LPBF.

The main objective of this study is to understand how feed forward control via surface temperature distribution management can lead to optimised components for LPBF. An optimised component would have a consolidated structure with high density, in addition to a crack free structure. The aim is to achieve this within a computational framework, so that process parameter optimisation can be material agnostic, faster, and operate with a greater degree of control than traditional methods. In order to contextualise the framework presented in this work, an overview of laser powder bed fusion will first be presented. This review will encompass the dynamic transfer of energy from a laser beam to a component, the growth mechanism of crucial microstructures, and how this process is currently optimised, by analysing the state of the art literature.

2.2 Overview of AM techniques for the production of metal components

2.2.1 Overview

The additive manufacturing of metals can be achieved using any of the seven AM processes, with six of these processes used in industry. Figure 2-1 shows the distribution of the metal AM machine market, with powder bed fusion, direct energy deposition and material/binder jetting being the most popular metal AM machines manufactured in 2020 [14]. The growth of the AM market is also demonstrated by a 7.5 % growth in 2020 to £9.6 Billion, despite the COVID-19 pandemic [15].

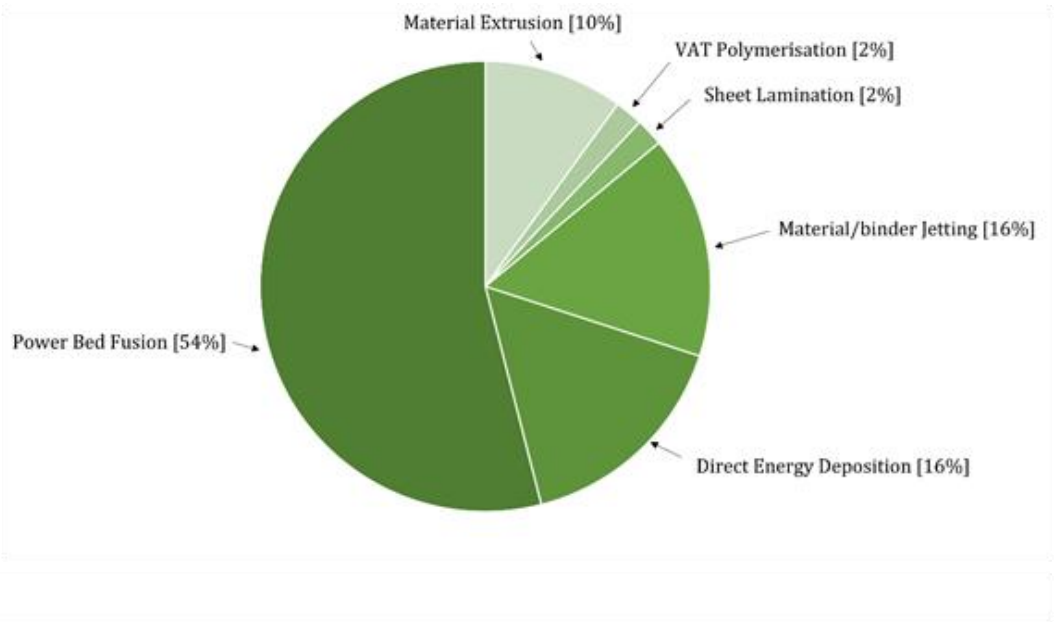

Figure 2-1 Metal Additive Manufacturing Market sector size 2020 [14]

2.2.2 Powder bed fusion

Powder bed fusion techniques are the most popular manufacturing method of metals in AM. Powder is spread over a substrate with a pre-determined layer thickness whereby a heat source will then selectively melt the powder. A new layer is then spread over the previous one, and the process repeats itself until the 3D component has been produced [16], [17]. Metal powder bed fusion processes are split into two types based on the heat source used to melt the metal powder particles [18]. Laser powder bed fusion (LPBF) uses a laser that transfers energy from high energy photons that are absorbed onto the metal surface, heating the metal to above its melting point. Electron beam powder bed fusion (EBPBF/EBM) however, needs an electrically conductive powder bed, as high energy electrons transfer heat into the powder through kinetic energy [19]. LPBF operates within an inert atmosphere with a galvanometer controlled laser beam, whereas EBPBF operates in a vacuum, with the direction of electrons controlled by electromagnets [3]. EBPBF can operate at high speeds of up to 1000 m/s. This allows EBPBF to pre-heat the powder bed to very high temperatures, reducing thermal gradients and high thermal stresses commonly seen in LPBF [20]. LPBF operates much slower, with maximum speeds of up to 3 m/s. Recently, in LPBF, manufactures have used multiple lasers to boost part production speeds. SLM solutions now produce a machine which has 12 1kW lasers, claiming to decrease build times by 20x over a single laser machine [21]. While boosting speed, this adds another layer of complexity to the

selection of process parameters. Currently, LPBF is a much more widely studied technology.

2.2.3 Laser powder bed fusion

Laser powder bed fusion (often called selective laser melting (SLM) or direct metal laser sintering (DMLS)) is the most popular powder bed fusion technique. Manriquez-Frayre and Bourell created the first part produced by LPBF in 1990 from 95% Cu and Pb-Sn solder with 5% $ZnCl_2$ [22]. The part was created with a 1060 nm Nd:YAG laser with a beam size of 500 μm and nominal power of 100 W. The authors used a parametric study with a constant laser power of 26 W using scanning speeds from 0.068 to 0.027 m/s to optimise parameters for part density. Today, the usual choice for industrial systems is a single mode ytterbium fiber laser due to their higher brilliance than older Nd:YAG systems[23], [24]. However, the method of finding process parameters remains relatively unchanged since the conception of LPBF.

A current schematic of a LPBF system based upon a commercially available Renishaw AM400 is presented in Figure 2-2. The laser train contains all of the laser generation and optical components needed to shape and direct the beam to the powder bed. Starting at the laser source, the beam enters the collimator. The collimator reduces the divergence of the beam and also allows for the focus of the beam to be changed. For a gaussian laser beam, the focus position can affect the beam radius size and intensity. From the beam expander the beam enters the X-Y galvanometer. The galvanometer is made up of two mirrors that can be controlled precisely with electromagnets [25]. These mirrors then deflect the beam through an f-theta lens, which focuses the beam at the surface of the powder bed. The powder is stored in a large hopper. During the recoating cycle the hopper allows a volume of powder to be released, which is then spread over the substrate by a recoater blade to a desired layer thickness. During the process a constant gas flow travels across the part as shown in Figure 2-2.. As well as reducing the oxygen content in the atmosphere, the gas flow also carries away spatter particles that are generated during the process [26].

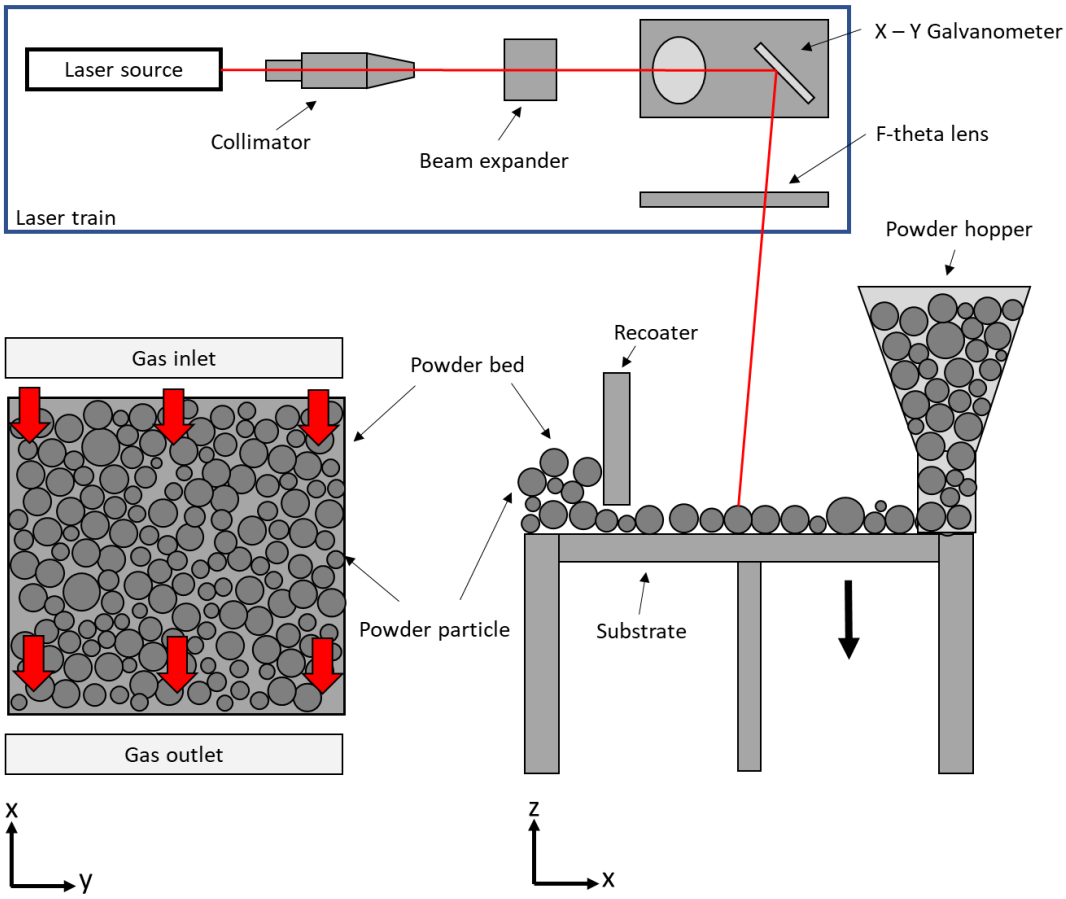

Figure 2-2 Schematic of a Renishaw AM400 machine. The laser is generated at a laser source, and passed through a collimator which allows the focus of the beam to be changed. The beam then travels through a beam expander and hits the XY galvanometer. These two sets of mirrors direct the laser beam over the powder bed to coordinates defined by the on board processor. The laser finally travels through the f-theta lens where it impacts the powder bed. Powder is spread over the substrate with a recoater blade, to spread the powder and achieve the desired layer thickness. Bottom left shows a plan view of the powder bed, showing the gas flow that provides the inert atmosphere and carries away any spatter particles. The powder particles are not to scale.

2.3 Laser material interaction for laser powder bed fusion

2.3.1 Laser metal interactions

In order to optimise the process of LPBF one must understand the physical complexity involved in the dynamic transfer of energy from a laser beam to a component. LPBF operates over a huge range of timescales and length scales. Initial laser material interactions can happen within nano-seconds, and melt pool solidification can occur in the milli-second range. This is then repeated over the course of a build that could take hours or even days to complete. Melt pool sizes are of micron size whilst part dimensions can measure 10s of cm across, made up of thousands of layers with hundreds of kms of laser travel. This is shown in Figure 2-3.

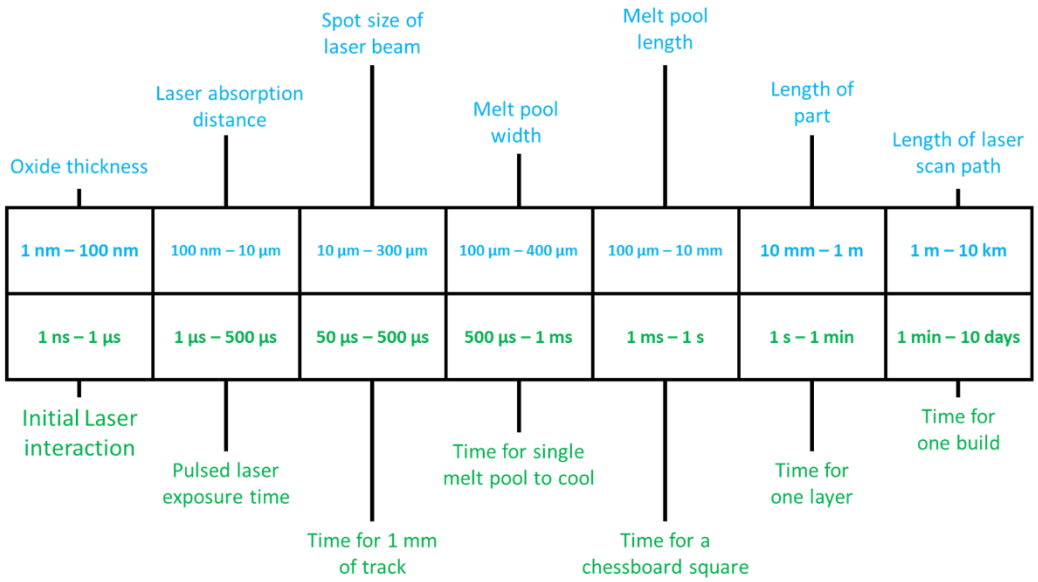

Figure 2-3 shows the timeline for event timescales in LPBF, for time and distance.

Control over this intricate process is done through process parameter selection. According to Yadroitsava et al. there are approximately 130 possible process parameters for LPBF [27]. All of these parameters have some effect on the produced components properties. Attributing the effect of each process parameter type on the final component properties has been the focus of most of the LPBF literature to date [23]. Laser power, laser velocity, beam size and shape, and layer thickness have large effects on conditions in the powder bed/melt pool and will be considered more closely in this literature review.

The transfer of energy from the laser beam to the metal powder bed is the most critical interaction in LPBF processing. This interaction governs the transformation from a raw powder feedstock to a component. This energy delivery has to consolidate the powder into a solid layer and to also bond with the layer beneath. This energy delivery can be achieved in many ways, with a variety of different customisable parameters to choose from. Key to this, is the consistent and predictable coupling of the incoming beam energy and the material surface. Precise energy control can also tailor solidification conditions and therefore the mechanical properties of the component.

The five main process parameters all directly change the amount of energy that is absorbed on the metal surface. To understand the effect of process parameters on this transfer of energy, one must understand first how the energy is imparted from the laser beam to the metal. The absorption or absorptivity represents the portion of energy that is absorbed into the metals surface from the total energy delivered by the laser. This is dependent on multiple factors such as; laser wavelength, the angle in which the incident photon hits the metal material, material composition, surface characteristics, powder bed/melt pool geometry and powder bed/melt pool temperature. In order to optimise the energy delivery to the material, a metal materials response to laser irradiation must be understood.

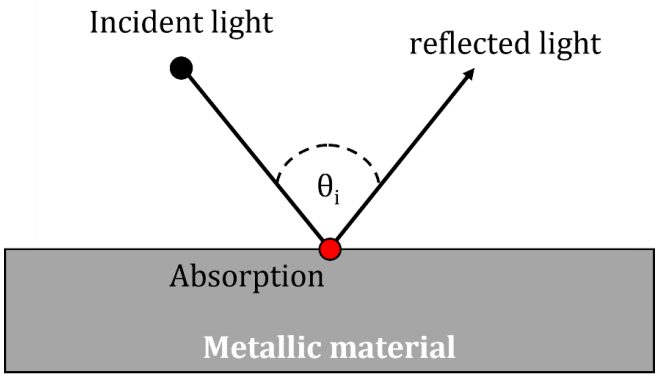

Figure 2-4 Incident light impacting a metal surface. Here an incident light particle is reflected by a metallic material. A portion of the energy of the particle is absorbed by the metal surface.

To understand this process, the problem must be simplified. Consider one photon of light hitting a flat metallic surface as shown in Figure 2-4. The photon hits the metal and interacts with the electrons within the first 10 – 100 nm into the metal surface. The electron-phonon collision imparts energy into the atomic lattice structure of the metal. This heats up the metals surface. This energy transfer happens due to the atomic structure of the metal taking the energy from the photon, in addition to excitations of electrons from the valence band to the conduction band. Different material lattice structures, electron configurations, photon wavelength and photon incident angles determine how much energy is imparted onto the metals surface [28]. To calculate the amount of light that will be absorbed by the material in this instance, optical constants n (refractive index) and k (extinction coefficient) must first be determined from the complex dielectric permittivity, as shown in the following equations.

$$n^2 = \left(\epsilon_1 + \sqrt{\varepsilon_1^2 + \varepsilon_2^2}\right) \div 2 \qquad \textit{Equation 2-1}$$

$$k^2 = \left(-\epsilon_1 + \sqrt{\varepsilon_1^2 + \varepsilon_2^2}\right) \div 2 \qquad \textit{Equation 2-2}$$

Where ε_1 is the permittivity of free space, and ε_2 is the relative permittivity of free space. Optical constants *n* and *k* form the complex refractive index and can be used to describe the absorptivity of metals at different angles of incidence. To calculate the absorptivity we can use Fresnel's equations which shows the dependence of absorptivity on the angle of incidence(θ) [29]:

$$Ab_s = 1 - \left|\frac{\cos\theta - (n^2 - \sin^2\theta)^{1/2}}{\cos\theta + (n^2 - \sin^2\theta)^{1/2}}\right|^2 \qquad \textit{Equation 2-3}$$

$$Ab_p = 1 - \left|\frac{n^2\cos\theta - (n^2 - \sin^2\theta)^{1/2}}{n^2\cos\theta + (n^2 - \sin^2\theta)^{1/2}}\right|^2 \qquad \textit{Equation 2-4}$$

For laser light, these two polarisation terms S and P are averaged together. The angle of natural or unpolarised electromagnetic radiation varies rapidly all the time, therefore the reflection is simplified to the average value of S and P polarisations. Therefore [1];

$$Ab = 0.5Ab_s + 0.5Ab_p \qquad \textit{Equation 2-5}$$

Where *Ab* is the absorptivity for a given angle of incidence. Figure 2-5 shows this absorptivity as a function of the angle of incidence for a range of common elements used in LPBF. The optical constants *n* and *k* are difficult to find for metal alloys and are hence only listed for pure elements or well-studied alloys such as 316L stainless steel. These optical material properties are also only measured for clean and flat surfaces, free from any surface oxides, that change with wavelength.

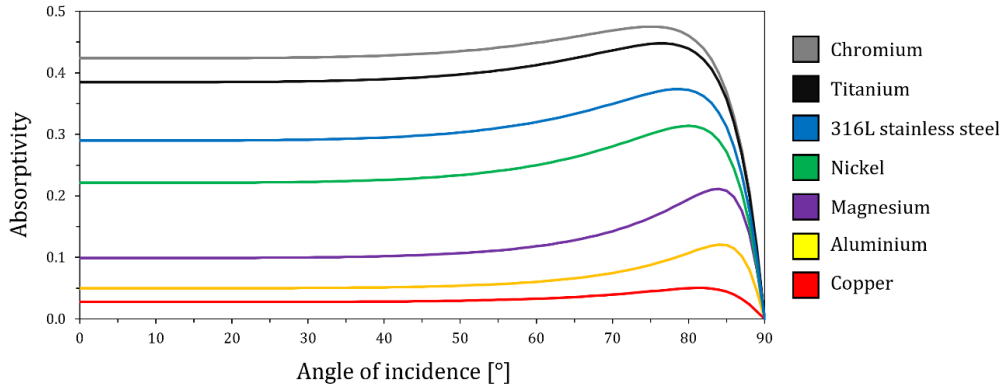

Figure 2-5 Plot showing how absorptivity varies as a function of the angle of incidence of a photon

This fact presents problems for the LPBF community, as the majority of materials being processed are alloys, and are a mixture of elements which do not have a clean and smooth, oxide free surface. Factors such as surface roughness and oxide coating can modify the absorptivity beyond literature values [30].

These effects have been studied in the literature. Kaplan studies the effect of laser irradiation on the surface of steel through empirical and modelling methods. His study found that strong surface waviness enhances the local absorptivity on a surface. At some

wavelengths from a $C0_2$ laser beam, high areas of absorptivity contributed to high temperature hotspots leading to local boiling of the steel surface [31]. Wang et al. used AISI 1045 steel and a AA1100 aluminium alloy to show the effect on surface absorptivity for different surface treatments. They concluded that surface treatments have a significant effect on the absorptivity, as shown in Figure 2-6a. Polishing the surface of a aluminium alloy significantly decreases the absorptivity as there are less reflections from photons on the surface of the material. Pitting the surface of the aluminium with an acid however, increases the surface roughness and therefore the absorptivity. Temperature also has an effect on absorptivity. Figure 2-6a shows the absorptivity of all the treated surfaces as a function of temperature. Once the temperature reaches the melting temperature of the alloy the surface of the material melts, and due to surface tension forces, the surface is flattened. All surface treatments have now been effectively removed from the surface, converging the absorptivity values [32]. Temperature can also affect the absorptivity of metals below the melting point. However, for the wavelengths of light often used for LPBF, these changes are small [28]. Bang et al. also showed that in continuous wave (CW) machining of ceramic materials, material removal rates could be increased up to 70% with the addition of grooves in the materials surface prior to laser irradiation [33]. These grooves increase the number of photon reflections, allowing a higher overall transfer of energy to the metal.

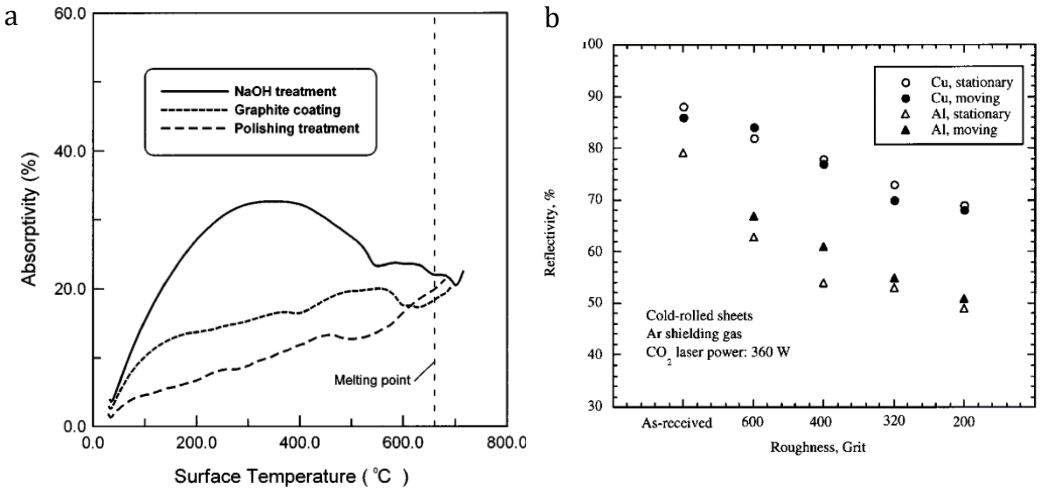

Figure 2-6a Surface absorptivity for AA1100 against surface temperature b) shows the effect of surface roughness on the reflectivity for copper and aluminium [32]

Xie and Kar examined the role of surface roughness and oxidation on the absorptivity and mechanical properties of laser welds for steel, copper and aluminium [34]. For copper and aluminium, increasing the surface roughness showed a 15 – 30 % decrease

in the reflectivity (increase in absorptivity), as shown in Figure 2-6b. Their findings also concluded that for a C02 laser, absorptivity increased by 30% from surface oxidation.

LPBF primarily uses spherical metallic powders as its feedstock material. Zhou et al. showed the effect that oxide coatings have on the absorptivity of LPBF powders in particular [35]. Their results showed that surface oxides from multiple oxide layers significantly improved the absorptivity of the powder layer. They found that the first and last oxide layer affected the absorptivity the most, with oxide thickness having little affect. They attributed this to the extinction coefficient (k) being zero for ceramic materials, meaning that little additional energy is transferred to the lattice from a thicker oxide layer. They also showed that intentional oxidation of copper led to higher absorptivity values [35]. Increasing the absorptivity of copper is important as the absorptivity at common wavelengths (1080nm) for LPBF is low, as shown in Figure 2-5 [36]. Researchers from Grenoble in France used physical vapour deposition to coat copper powder with CrZr. Using this surface coating method, they increased the surface absorptivity from 39% to 81.8%, however this was measured using a UV-VIS spectrometer, and would not represent the absorptivity during the process [37]. Literature from Speidel et al. shows a PVD coating of copper with zinc promotes a similar absorptivity increase, demonstrating this in LPBF [38].

From these studies it is clear that the absorptivity during LPBF is heavily dependent on the surface features and chemical composition of the surface. It also clear that the absorptivity cannot be represented as a single number, but one that changes dynamically to different conditions. This is especially important if the LPBF process is to be replicated through computational modelling and the process then optimised for a predictable transfer of energy from laser to powder.

2.3.2 Laser metal interactions for laser powder bed fusion

The absorptivity can vary by as much as 50% during the LPBF process [39]. Absorptivity depends heavily on surface geometry, and photons can become 'trapped' on the rough surface of the material, increasing absorptivity through multiple reflections. Each reflection gives a portion of the photons energy to the metal. Multiple reflections greatly increases the energy exchanged by the laser beam, and hence increases the absorptivity. This is especially prevalent for LPBF as the surface of the powder bed/melt pool are constantly changing throughout each stage of LPBF processing.

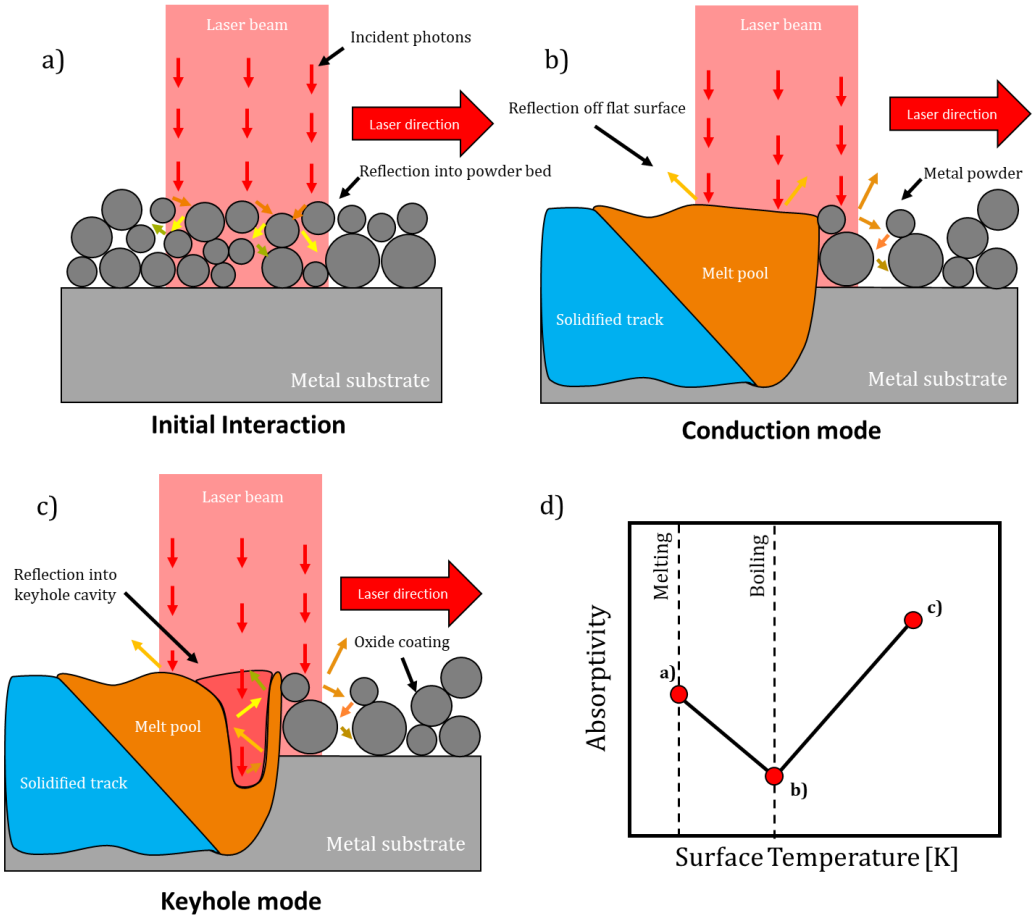

Figure 2-7a) shows the instantaneous initial absorptivity of the powder bed b) shows initial stage of melting, with the materials temperature below its boiling point c) shows the melt pool as it rises above the boiling temperature at atmospheric pressure, with a keyhole forming, trapping photons within it d) shows the absorptivity at the stages a), b) and c) respectively

Being able to understand the absorptivity at each stage of the process is crucial to understanding the effect that each process parameter has on the process [40]–[43]. Figure 2-7 shows how different stages of LPBF processing can affect the absorptivity as a function of surface temperature. Figure 2-7a shows the initial stage of the laser interacting with the powder bed. Here, photons get trapped within the powder bed structure, increasing the absorptivity (Figure 2-7d). Figure 2-7b shows the powder surface temperature increasing to above the materials melting point, creating a melt pool. As shown in Figure 2-6a, the surface of the material has melted, and the melt pool surface is relatively flat. The absorptivity at this stage is at its lowest for the 3 different processing modes (Figure 2-7d). Figure 2-7c shows the melt pool when the surface temperature has gone above the materials boiling temperature – defined here at atmospheric pressure. In reality the vapour pressure increases the materials boiling temperature beyond its atmospheric value. Due to this localised recoil pressure from evaporation of the molten metal, a cavity is created, increasing the absorptivity though multiple reflections. At this point, the absorptivity is at its highest of all the processing

modes. LPBF can switch between these 3 modes, depending on the lasers position and the processing parameters that are used.

In an ideal world, a user would input the desired component properties into the machine directly. Past literature needs to be understood and interpreted to make links between process parameters, melt pool dynamics, solidification conditions to achieve the desired material properties.

2.3.3 Initial laser powder bed interaction

The effect of the powder bed on absorptivity has been of interest since 1995, as it would allow users of LPBF to find a suitable processing window for consolidation without evaporation[44]–[46]. The first known work measuring the absorptivity of metallic powders for LPBF was done by Nikolay K. Tolochko et al. in 2000 [47].

The instant in which the laser is turned on for a new layer in LPBF, photons hit a dense powder bed full of near spherical particles. As shown in Figure 2-7, the photons can become trapped within the powder bed structure. For a deep powder bed, the absorptivity of the powder bed can approach the absorption of a black body [47]. Gusarov et al. studied the absorptivity of metal powders from 1060 nm and 10.6 µm wavelength using Nd:YAG and $C0_2$ lasers. Their findings show that powder layer thickness has a substantial effect on the absorbed energy from the laser. However, this changes with the material used. Materials such as iron and tungsten carbide have a large decrease in absorptivity with an increase in the layer thickness.

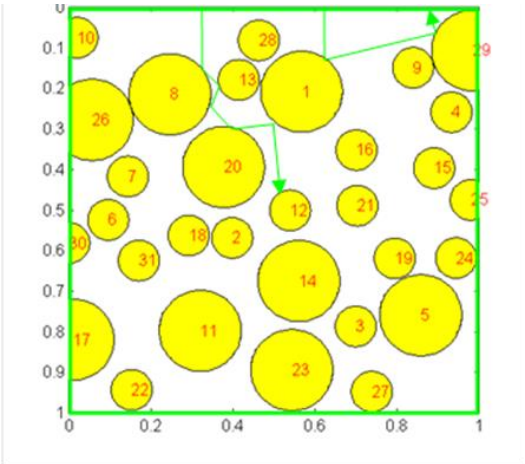

Figure 2-8 2D illustration of the ray tracing model [48]

Whereas, materials that have a low absorptivity such as copper, increase absorptivity with an increase in layer thickness. Materials with a low absorptivity give less energy per 'hit' of a particle, and can reflect and give more energy to lower levels of powder in

a layer thickness. They also found that deposited energy distribution for a thin layer can sharply decline or have a local maximum depending on the layer thickness. This can be explained through the interference of the substrate at the bottom of the power layer. Backwards reflection of light from the substrate can increase the deposited energy at thin layer thicknesses [49]. During processing above the machines substrate material, the previous melted layer would act as the 'substrate'. Additionally, McVey et al. provided initial insight into the absorptivity dependency on the powder size distribution. Their results found absorption coefficients for copper and iron powders for different powder layer thickness and powder size distributions[50]. These results are supported by the work of two early ray tracing simulations[48], [51]. These supporting works by Wang et al. and Van der Schueren are important as experimental absorptivity testing can be costly and time consuming. Early ray tracing models however, assume diffuse radiation transport, which is not applicable for thin, low porosity metal powder layers used in LPBF (Figure 2-8). Additionally, these first calculations were done in 2D with only a small number of rays modelled. A small number of rays can introduce error into the ray tracing calculation by packing the same amount of energy into a smaller number of particles. One particle has more of an effect with more energy, and can influence the energy distribution.

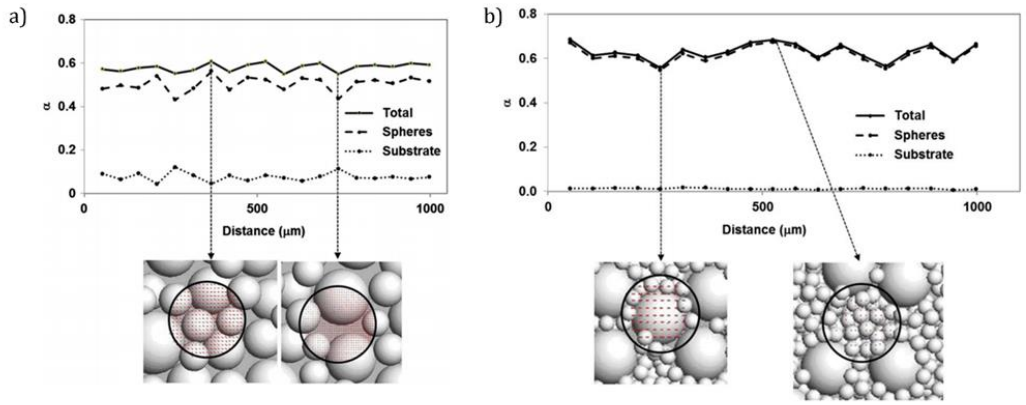

Figure 2-9a) shows the absorption (α) calculated along the beam path for the ray tracing simulation over the Gaussian distributed stainless steel powder layer. B) shows the absorption calculated along the beam bath for the bimodal distribution [52]

Further work by Boley et al. in 2015 built upon these earlier studies [52]. Using an optical commercial software, FRED, they model three sets of powder types and study the effect on absorptivity. The three powder distributions used are; i) an ideal powder array of spheres with the same radius, ii) a gaussian distributed powder with an average radius of 13.5 μm and iii) a bio-modal powder with a 20% addition fines added. The software uses ray tracing calculations from the Fresnel equations to model the 3D ray scattering within the powder bed. The number of rays used in the simulation varied from 50,000

to a few million so that results were insensitive to the number of rays. For a realistic array of powder commonly used in LPBF, a particle packing program was used (ParticlePacker) to randomly populate spheres with a gaussian distribution of radii. Bi-modally distributed powders have been shown to enhance process performance through dense particle packing[53]. Here the results vary as seen in Figure 2-9a and b. The gaussian distributed powder has a stochastic nature compared to the ordered particles, and the absorptivity varies across the powder bed. The two insets in Figure 2-9 show absorptivity peaks, attributed to different powder radius inside the laser spot.

Smaller powder particles in the laser spot, increase the absorptivity through multiple reflections that are constrained though the smaller powder particles. Local minimums in the absorptivity plot are from large particles that allow gaps through to the substrate. This allows rays to be backscattered without interacting with the powder. Local absorptivity distributions can contribute towards defect generation during the process either through excessive or insufficient laser power delivery. Figure 2-9b shows the bi-modal distribution of the powder. For this powder distribution, local minimums come from rays striking a large sphere. Local maximums come from finer particles distributed inside the powder bed, similar to the gaussian distributed powder. The denser powder bed from the bi-modally distributed powder also increases the total absorptivity over the gaussian distributed powder. This is due to rays being trapped within the denser structure, imparting a higher proportion of the energy available.

As observed in earlier works, materials with low absorptivity (high reflectance) respond differently to materials that have a high absorptivity. In these results, powders with high reflectance and low absorptivity such as silver and gold, increase absorptivity by a factor of 2 for the bi-modally distributed powders. For highly absorbing materials such as stainless steel, the increase was only a few percent. Results from this work correlate well with the work of Gusarov and Kruth for highly reflective materials[49]. Materials that have a higher absorptivity and lower thermal diffusivity however differed from Gusarov's work. This work shows that powder layer thickness and size distribution must be accounted for when optimising process parameters. Fine powder in this aspect increases absorptivity, but must be kept between a range in order to not detrimentally effect processing[53]–[55]. Knieps et al. also shows that there exists a critical range of between 21 – 30 % of fines in order to improve processability and also density.

2.3.4 Experimental measurement of Absorptivity

Despite the progress of computational modelling, there still exists a need for experimental validation and testing. Previous methods of measuring absorptivity used an integrating sphere to collect all reflected light from the laser and subsequently calculate the absorptivity. However, the equipment was complex and expensive, and absorption from the measurement device itself complicated the measurement process. A technique devised by Rubenchik et al. uses a calorimetric measurement to measure the powder absorptivity [56]. The technique is shown in Figure 2-10. The measurement system compromises of a tantalum disc, with a recess cut into the surface with height, *h* (intended to simulate a layer height) as shown in Figure 2-10. Laser irradiation with a wavelength of 1000 nm is then directed to the powder surface. As the laser irradiates the powder, the tantalum disc heats up. The temperature evolution can be shown by the following equation:

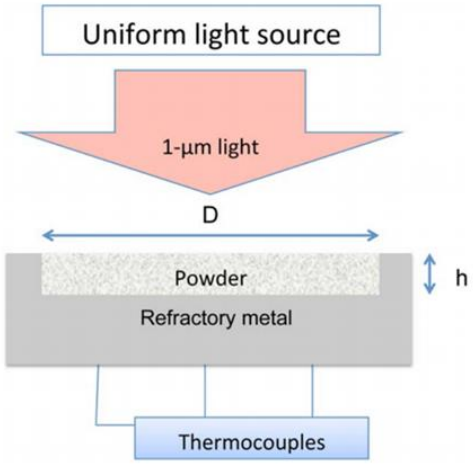

Figure 2-10 shows a schematic of the calorimetric measurement system [56]

$$(\rho_1 c_1 d_1 + \rho_2 c_2 d_2)\frac{dT}{dt} = A(T)I - Q(T) \qquad \textit{Equation 2-6}$$

Where *T* is temperature, *A(T)* is absorptivity, *Q(T)* are thermal losses, ρ is the density, *c* is the specific heat and *d* is the thickness. Subscript 1 and 2 refers to the powder and the substrate respectively. In order to find the absorptivity of the powder, equation 6.6 is multiplied by the disc area S. Therefore equation 6.6 is rewritten to equation 6.7, where *m* is the mass and *P* is the total power on the discs surface.

$$(m_1 c_1 + m_2 c_2)\frac{dT}{dt} = A(T)P - Q(T)S \qquad \textit{Equation 2-7}$$

The results from this experiment match well with ray tracing calculations for 316L stainless steel from Boley et al.. Though, experimental measurements for Ti6Al4V differ by 5% from calculated and measured values. Rubenchik et al. attribute this to refractive index values used for the ray tracing calculations being the value for pure Ti, where

values differ to the alloy. The values for aluminium however show a large difference from ray tracing to experimental results. Textbook values for the absorptivity of aluminium (AA6061), and those predicted by ray tracing calculations show an absorptivity of 5%. Experimental measurements show this value at 20% for a 1000 nm wavelength laser, both measured on a powder structure. This suggests a large influence from oxide layers and surface structure on the absorptivity of the aluminium powder layer but wasn't experimentally verified in their study.

2.3.5 Laser-powder-meltpool interactions

2.3.5.1 Overview

During the LPBF process, the laser is generally in a 'steady' state. After the initial interaction with the powder bed, with sufficient irradiance, the surface of the metal powder will begin to melt. Depending on the absorptivity, laser power, laser velocity and beam size the process will operate in either conduction or keyhole mode. When the laser irradiation reaches a certain intensity, the temperature on the surface of the metal will increase past the vaporisation temperature. Further increase of this intensity will result in the ionisation of the gas, creating a plasma. The plasma will strongly absorb the laser light, affecting the energy deposited into the newly created keyhole cavity. This newly formed cavity enables the laser to penetrate deep into the melt pool, and increase the absorptivity through multiple reflections[57] (Figure 2-11[58]).

If the processing conditions are not sufficient to raise the surface temperature past the boiling point, then the LPBF process will operate in conduction mode. In this mode, the dominant heat transfer mechanism is through conduction. The cross section of melt pools made in conduction mode are normally shaped so that the depth is less than or equal to half its width, in a semi-circle profile[59].

2.3.5.2 Keyhole mode processing

The literature for keyhole formation stems from laser welding. Laser welding was first demonstrated in the 1960/70s, when lasers were first used in industry [60]. Laser welding is advantageous as it requires less weld preparation than conventional arc welding, and unlike electron beam processing, does not require a vacuum. However, for high thermally conductive materials such as aluminium, power requirements for achieving deep welds from early industrial lasers were extremely high. Early analytical modelling research from Swift-Hook and Gick suggested that moving to a narrower beam profile would result in higher peak temperatures and would subsequently greatly improved the efficiency (absorptivity) of the welding operation, even for highly

conductive materials. They correlated penetration depths with various process parameters such as laser power and speed. They also noted that while a narrow molten zone should be sought after, and resulted in higher absorptivity, this was not necessarily desirable [61].

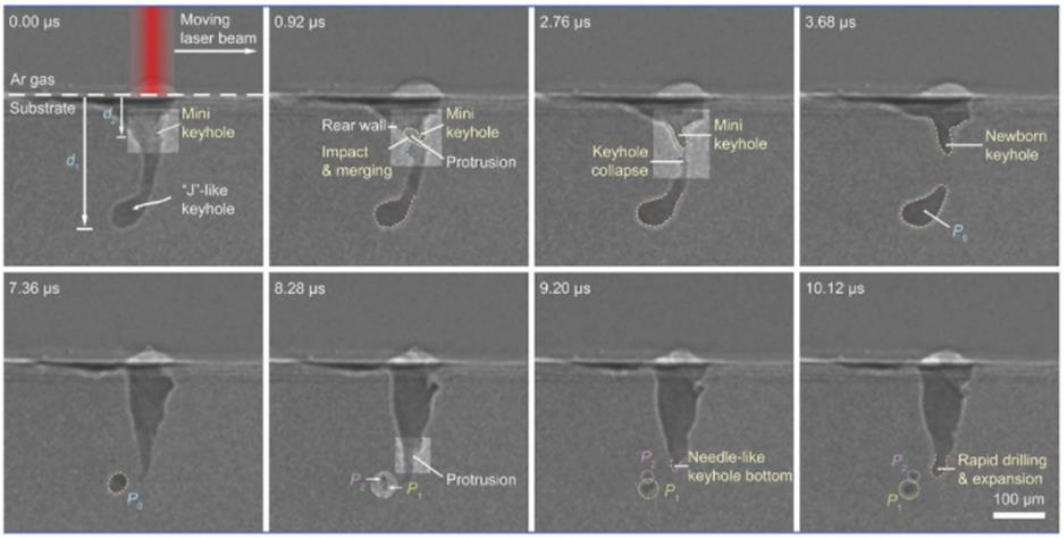

Figure 2-11 show images from an X-Ray synchrotron of the cross section of a keyhole during laser powder bed fusion. The images show a keyhole pore being formed from keyhole instability [58]

This so coined 'keyhole' effect was then investigated with early analytical modelling[62]–[67].

The evaporation of metal from a liquid melt pool is a probabilistic process and is a function of the equilibrium recoil pressure described by an Arrhenius relationship shown below:

$$p_s = p_0 exp\left\{\frac{L_{vap}(T - T_b)}{R(T - T_b)}\right\} \qquad \textit{Equation 2-8}$$

Where p_s is the recoil pressure formed on the surface through evaporation, p_0 is the ambient pressure, L_{vap} is the latent heat of vaporisation, R is the universal gas constant, T is the temperature and T_b is the boiling temperature. This recoil pressure is responsible for the creation of the cavity, or the keyhole. The force pushes down anti-parallel to the surface normal, and once it has overcome the materials surface tension, begins to move the melt pool surface. This recoil pressure can then be substituted into the Langmuir equation to calculate the rate of evaporation J_i:[68]

$$J_i = \frac{M_i p_s p_i}{\sqrt{2\pi M_i RT}} \qquad \textit{Equation 2-9}$$

Where M_i is the atomic mass and p_i is the partial recoil pressure for the alloy. Juechter et al. also showed that by varying the scan speed in electron beam melting, the composition of the final alloy of Ti6Al4V could be changed. Due to the preferential

evaporation of aluminium, the element evaporates under high energy densities, leading to their recommendation of avoiding overboiling to prevent changes to the chemical composition [69]. This formula therefore can also include the constituent components of the alloys as some alloys may have substantial different partial pressures, that lead to preferential evaporation [70]–[73].

$$J_i = \frac{\gamma_i p_s^0 C_i^s}{\rho_m \sqrt{2\pi M_i R_0 T}} \qquad \textit{Equation 2-10}$$

Where γ_i is the activity coefficient, p_s^0 is the recoil pressure C_i^s is the volumetric concentration at the surface and ρ_m is the molar density of the alloy. Additionally, the negative evaporation flux (heat taken away by the liquid metal evaporating) can also be calculated on the surface of the metal by:

$$-Q_{flux} = \sum J_i L_{vap} \qquad \textit{Equation 2-11}$$

The evaporation flux is the main self-limiting factor for the surface temperature during laser irradiation, and scales exponentially with the recoil pressure.

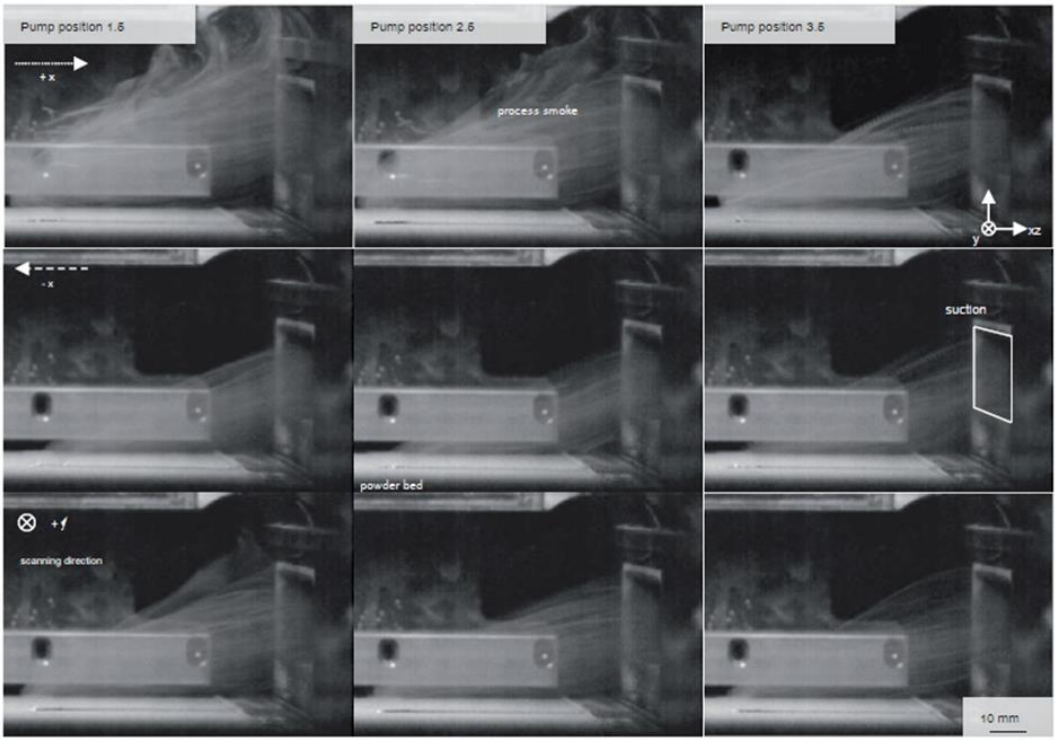

Figure 2-12 shows the effect of scanning direction and pump speed on the vapour plume generated during a single layer of magnesium processed by laser powder bed fusion. The top row shows the scan vector with the gas flow, the middle row shows the scan vector against the gas flow, with the bottom row showing the scan direction perpendicular to the gas flow. The columns represent different pump speeds. This figure shows that at high pump speeds all vapour is efficiently removed, whilst at low pump speeds more vapour is present in the chamber [74]

Metal vapour that is generated as a result of the high surface temperatures can also pose a problem during processing. The vapour that is generated, forms above the keyhole cavity, and depending on the speed of the laser and the protective gas flow can interact

with the laser beam[75]. Greses et al. also showed that small particles are generated in the plume that can attenuate the beam between 10 – 70% depending on the particle size and particle size ratio produced. This attenuation can significantly decrease the combined energy of photons interacting with the keyhole cavity, limiting the depth of the keyhole [76]. Additionally, the ionisation of the vapour plume creates a plasma. Szymanski et al. experimentally measured the temperatures of a plasma generated by a $C0_2$ laser. They found that temperatures inside the plasma reached 11,500K, also speculating that peak temperatures could reach between 15,000 – 19,000K. However, they also found that the absorption of the laser radiation in the plasma plume was about 6% during the course of the experiments, and these high temperatures were extremely localised. But since the plasma bursts could last up to 100 μs (the experiment lasted 200 ms) the effect on the keyhole could be seriously affected [77]. Recent results from Khairallah et al. however, show that reducing the absorptivity by 3% in their computational modelling work, compared well enough to experimental data, to not account for this physical mechanism in the modelling during deep keyhole processing regimes [78].

The effect of plume/plasma attenuation can be addressed with the selection of process parameters. By increasing the speed of the laser, increasing the gas flow speed and volume and controlling the scan vector direction respective to the gas flow, this affect can be reduced [79]. However, these challenges are escalated for some materials due to low boiling temperatures, high vapour pressure and oxidation tendencies[80], [81]. To combat this for magnesium, Jauer et al. used a custom Aconity MINI LPBF machine with a purpose built gas flow system. The system was able to flood the chamber with 5 l/min of high purity argon to take away the magnesium vapour. Additionally, they studied the effect on the scanning direction to the amount of vapour carried away with the gas flow. They found that the flow was sufficiently powerful to take away vapour in any scan direction (Figure 2-12). Furthermore, the researchers also introduced a pause in between each laser pulse. This allowed any excess vapour to be removed by gas flow so the laser did not reduce the energy supplied to the powder bed through attenuation [74], [82].

One of the first works to identify the presence of keyholes in laser powder bed fusion was from King et al. In their work they identified that to keep the molten metal out of the cavity formed by the keyhole, the pressure must exceed the pressure produced by the surface tension. The experimental work used a synchrotron to visualise the pores left from the keyhole post process[6]. Literature from 2019 uses a synchrotron, but to

measure the keyhole during the LPBF process. Figure 2-11 shows the images that can obtained through the use of the high powered X-Ray source, with temporal resolution great enough to see real time melt dynamics and pore formation [58], [83]. Shevchik et al. also used synchrotron analysis of laser welding to analyse keyhole porosity in situ. They used this equipment to monitor the laser back reflected (LBR) and acoustic emissions (AE), the results of which matched to significant events during keyhole development[84]. Using machine learning, they hope to match these signals with events to deepen understanding of keyhole welding physics.

Cullom et al. experimentally measure the recoil pressure through vibrations in the LPBF structure being printed [85]. The experiments print tuning forks built at an angle on the build plate. Post powder removal, an accelerometer is fixed to the tuning fork, and a new layer of powder spread on top of the tuning fork structure. During the single track deposition, the force generated from the laser impacting the powder surface is measured. The results show that conduction mode printing results in a recoil pressure force of < 0.5 mN, the transition zone shows a recoil pressure of between 0.8 and 8 mN, and keyhole mode shows a recoil pressure of 10 mN. The force measurements are crucial in validating computational models, where forces can be calculated at different processing conditions.

It is obvious that processing conditions are effected considerably through the variability that is introduced through the keyhole mechanism. This must be taken into account when modelling the LPBF process, otherwise large errors will accumulate between simulation and experimental results.

2.3.5.3 The role of surface tension

Surface tension has a significant effect on the melt pool behaviour. This behaviour governs the maximum speed that the laser can traverse across the powder bed at a certain laser powers. During steady state processing, the melt pool is subject to complex thermo-fluid physical phenomena, such as buoyancy, gravity, surface tension and capillary forces. However, at the length scales of LPBF, surface tension forces dominate [86].

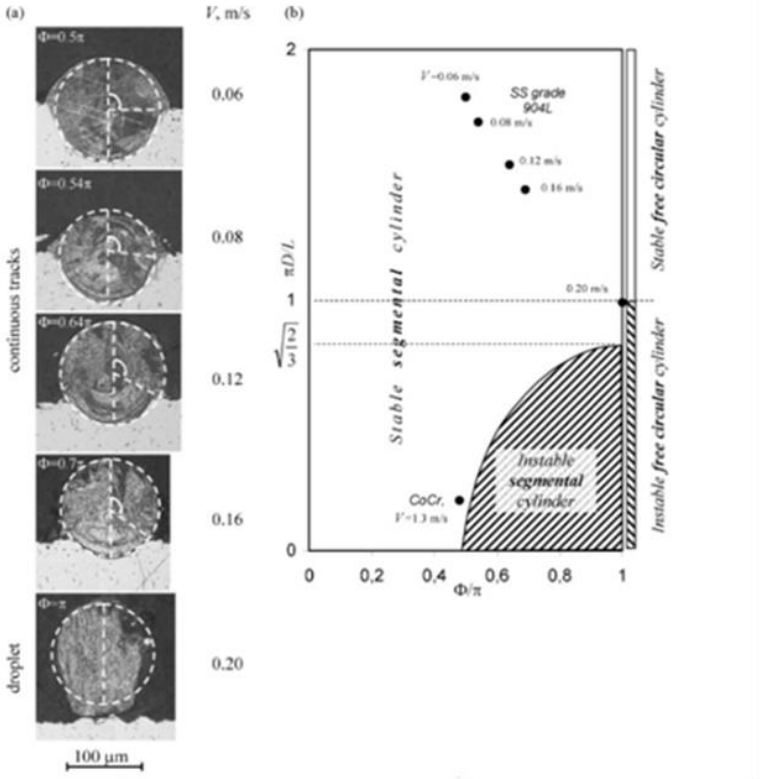

Figure 2-13 Shows the dependence of the contact angle (between the mid-level of the single track) with the substrate can dictate whether the track is in a stable or instable track formation zone [5]

Yadroitsev et al. experimentally showed how surface tension can affect the formation of a single track, the most basic of structures fabricated with LPBF. With insufficient laser power, there exists a critical speed where the track will not form a continuous line, but droplets on the substrate surface form. The upper stability limit of the laser velocity is when the molten pool loses contact with the substrate as shown in Figure 2-13. The authors found that when the energy was insufficient to melt the substrate in addition to the powder layer, the powder did not wet to the substrate, causing the surface tension forces to lower the surface energy to form a sphere of powder on the substrate, breaking the continuous track[5]. This shows that heating of the immediate substrate layer underneath the powder is critical for forming a stable track. They also discovered that the penetration into the substrate layer was linearly dependant on the scan velocity and the thermal conductivity. This means that the range of optimal scanning speeds is larger for higher powers. Materials with a higher thermal conductivity also have a narrow window of laser speeds at fixed laser powers. This balling effect was also shown by other researchers, showing that balling happens more often at high aspect ratio melt pool geometries. This means as the melt pool becomes larger than an equivalent sphere of the same volume, balling is more likely to occur[87], [88].

Surface tension also has a temperature dependence, called the Marangoni flow. The melt pool flow is predominantly driven by Marangoni convection due to the surface tension gradients, and control the distribution of the heat in the melt pool. The Marangoni flow is also a main factor for limiting the free surface of the melt pool[71]. This will ultimately affect the thermal gradients and therefore the final properties of the part. In addition to the temperature dependence, the surface temperature has a strong dependence on the active surface elements on the melt pool surface.

The Marangoni flow acts upon the melt pool with a shear force from the following formula[89]:

$$\tau = -\mu\frac{\partial u}{\partial z} = -\mu\frac{\partial \gamma}{\partial T}\frac{\partial T}{\partial r} \qquad \textit{Equation 2-12}$$

Whereby μ is the metal viscosity and $\frac{\partial \gamma}{\partial T}$ is the surface tension gradient. Using this equation, the vector of the flow can be found using the non-dimensional Marangoni number Ma:

$$Ma = \frac{\partial \gamma}{\partial T}\frac{\partial T}{\partial r}\frac{L}{2\mu\alpha} \qquad \textit{Equation 2-13}$$

Where L is a characteristic length scale and the sign of the number dictating the direction. Figure 2-14 shows how the flow in a melt pool can change, depending on the sign of the surface tension gradient. A negative surface tension over the entire temperature range of the melt pool, results in a lower surface tension in the high temperature regions. This results in outward flow, from the centre to the outer edge of the melt pool. With the surface tension having a positive value and then changing to a negative value, the melt pool can be in a situation where there is an outward flow in the centre of the melt pool, and an inward flow at the outermost edges. Total inward flow occurs if the surface tension gradient is positive [90].

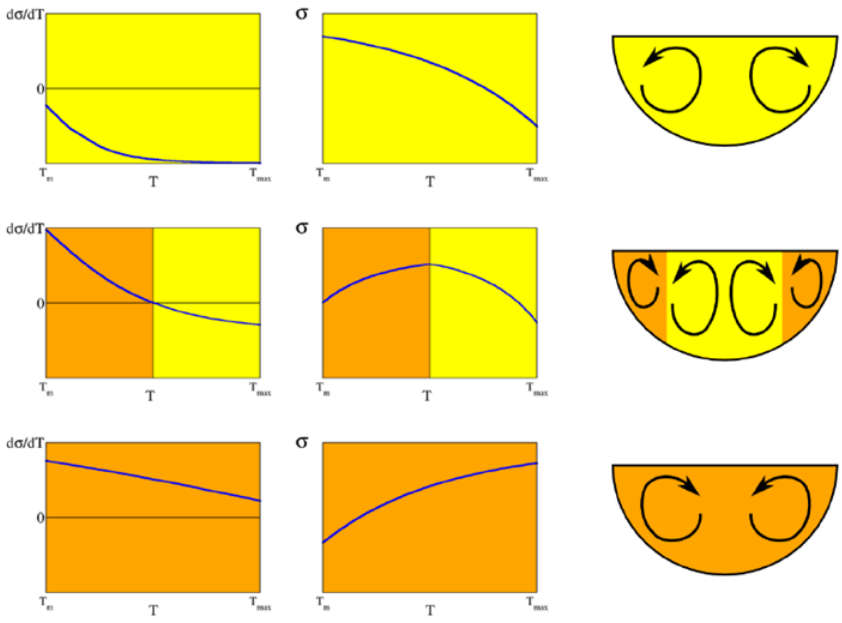

Figure 2-14 shows illustrations for the relationships between the surface tension gradient and the temperature on the flow direction in the melt pool. Figure 2 13 shows how the flow in a melt pool can change, depending on the sign of the surface tension gradient. A negative surface tension over the entire temperature range of the melt pool, results in a lower surface tension in the high temperature regions. This results in outward flow, from the centre to the outer edge of the melt pool. With the surface tension having a positive value and then changing to a negative value, the melt pool can be in a situation where there is an outward flow in the centre of the melt pool, and an inward flow at the outermost edges. Total inward flow occurs if the surface tension gradient is positive [90]

During flows where Marangoni convection becomes dominant at high Peclet numbers (ratio of advective transport rate and the diffusive transport rate), the effect of alloying elements and oxygen can become significant. Le and Lo showed that increasing the sulphur content in stainless steel can increase the melt pool depth of a laser processing. An increased sulphur content puts an inward flow on the melt pool, driving the melt pool deeper. In contrast, a lower sulphur content, increase the width of the shallower melt pool with an outward flow[91], [92]. Zhao and Richardson also looked more closely at the hydrodynamics of melt pools from the effect of oxygen in aluminium. Even small concentrations of oxygen between 100-1000 ppm increased the surface tension at lower temperatures[89], [93]. This shows the sensitivity of aluminium properties to oxygen.

2.3.5.4 Absorptivity for conduction-keyhole mode processing

As discussed previously in this chapter, the mode of processing (keyhole, conduction, initial) has a substantial effect on the absorptivity of the laser beam to the metal. Also discussed is the effect that process parameters, namely energy density, can have on the surface of the melt pool. In order to optimise process parameters, it is important to be able to calculate these different absorptivity changes as a function of energy density. Rubenchik et al. first proposed a calorimetric experimental process to measure absorptivity. However, this test was conducted below the powders melting point and so

only considered the first initial laser-powder phase [56]. Trapp et al. from the same research group at Lawrence Livermore National Laboratory (LLNL) developed this process, measuring absorptivity over a single track length in-situ [39].

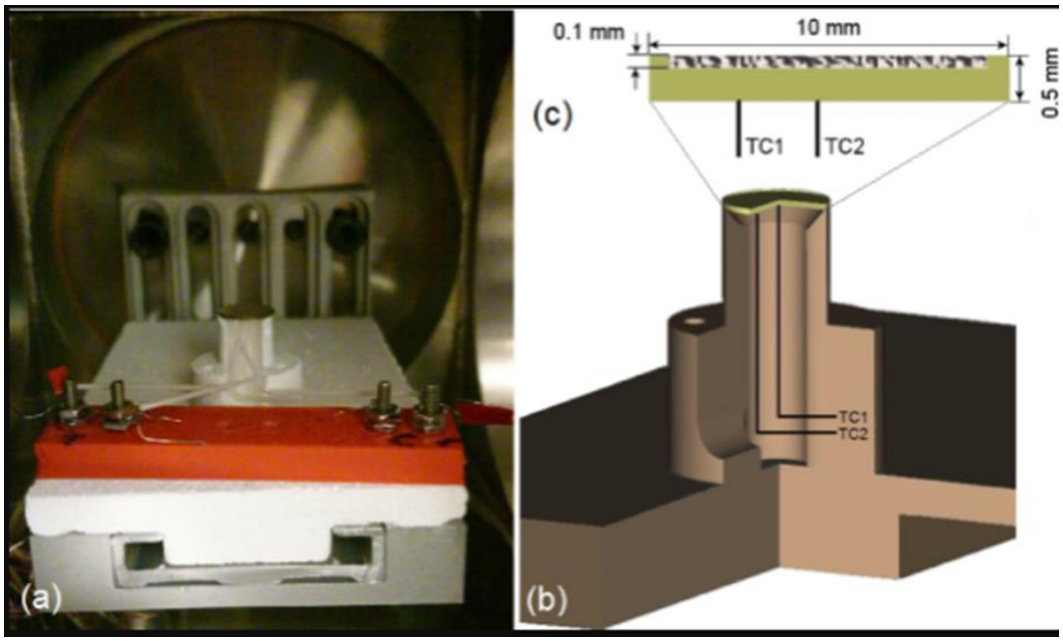

Figure 2-15 a) shows an image of the direct calorimetry setup inside the process chamber. B) shows a schematic of the disc holder and attached thermocouples. C) shows the disc, with a machined recess of 100 µm to hold the powder layer [39]

Their experimental setup uses a disc made from the same alloy as the powder material, machined to disc with a 10 mm diameter, 0.5 mm thickness and a 100 µm recess machined from the top surface, to create a well for the power to sit in simulating the layer height. The difference to this experimental configuration to 2.3.4 is these experiments melt the powder, rather than just irradiate them to temperature below their melting point. This is shown in Figure 2-15. The disc holder is made from low conductivity porous alumina to minimise the thermal losses from the disc. Two thermocouples are spot welded to each disc to measure the temperature of the disc during processing. The experiment melted a single track in a line of powder on top of the metal disc. During the experiment, the disc heats up, which is measured by the thermocouple. Equation 6.1 shows the formula needed to calculate the absorptivity:

$$Ab = \frac{E_{out}}{E_{in}} = \frac{\int_{T_0}^{T_1} mC_p(T)dT}{\frac{l}{vP}} \qquad \textit{Equation 2-14}$$

Where m is the mass of the disc, C_p is the heat capacity, l is the single track length, v is the laser velocity and P is the power. The temperature dependant heat capacity, is from the T_1 temperature to T_0 temperature from the function:

$$C_p(T) = C_{p,0}(1 + \alpha T) \qquad \textit{Equation 2-15}$$

With $C_{p,0}$ being the heat capacity at 273K and α being the temperature coefficient of C_p.

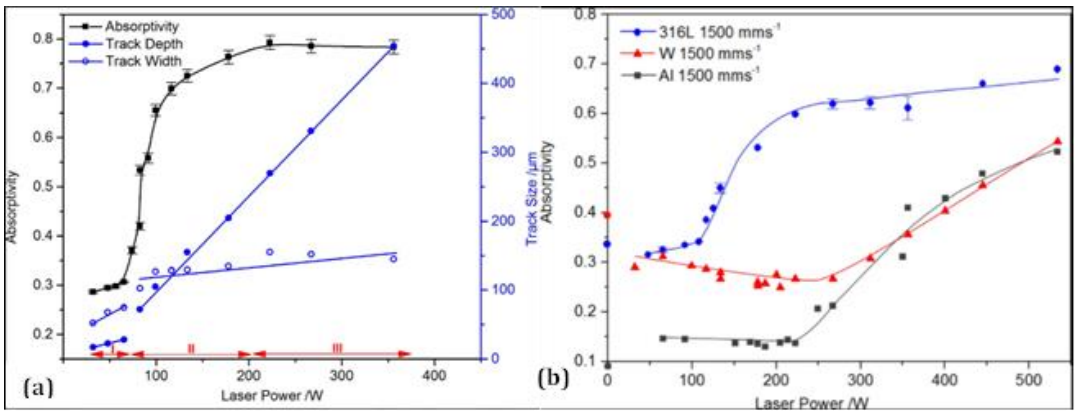

Figure 2-16 a) shows the absorptivity curve for 316L stainless steel. Shown are three modes, I – conduction mode, II – conduction – keyhole transition zone, III – keyhole mode. B) shows the absorptivity as a function of laser power for 316L stainless steel, tungsten and aluminium 6061 [39]

The results can be summarised in Figure 2-16a and b. Figure 2-16a introduces a fourth mode to LPBF processing, the conduction to keyhole transition zone (C-K transition)(Mode II in Figure 2-16a). The transition from conduction mode to keyhole is not instantaneous, as shown in Figure 2-16. As the temperature of the melt pool surface rises to above the boiling point, a recoil pressure acts on the surface, however, this does not result in an immediate keyhole cavity. This recoil pressure has to first overcome the surface tension, in order to push the surface downwards. As it starts to do this, the absorptivity increases sharply due to the multiple reflections inside the newly forming cavity. This has the effect of increasing the surface temperature well above the boiling temperature (at atmospheric pressure), increasing the recoil pressure, as well as increasing the absorptivity; [83] until at a certain laser power, the absorptivity reaches a maximum threshold, and starts to plateau [94], [95].

Interestingly, the plateau level for the powdered samples is lower than that of the bare disc for some laser scanning speeds. This is due to powder entrapment in the beam causing a reduction in the absorptivity, balanced by the addition of the powder geometry. Also, powder particles are interacting with the melt pool surface, causing an imperfect keyhole with a powdered layer – compared to a plane surface [39], [96].

This C-K transition zone is different for each material. Aluminium for example has a low surface tension at its boiling temperature (0.28 Nm^{-1} [97]). This means that with a reduced temperature, less recoil pressure is required to push the material down into a keyhole cavity. Materials with high thermal conductivity show a lower dependency on laser velocity and a higher dependency on the laser power. Due to high thermal transport through the melt pool into the substrate, the C-K transition zone is more power

dependant [98]. Temperature gradients have to be pushed much higher than in materials with a low thermal conductivity materials such as 316L stainless steel to get a larger melt pool [99]. Due to the high thermal transport, a limit exists that prevents very low scan speeds being used in conjunction with low laser powers. The low laser powers cannot provide sufficient energy to melt the material, before the energy is conducted away [99].

2.3.5.5 Absorptivity of Aluminium

For some materials with a high absorptivity on a flat surface (316L stainless steel), in-situ absorptivity measurements match well with predicted values. Figure 2-16b shows the literature value for the absorptivity of 316L stainless steel (red dot on the y axis) that matches the absorptivity seen at lower laser powers. For this material, the Fresnel equations can be used with the alloys refractive index, to get an accurate description of the materials absorptivity during LPBF. However, for aluminium, the refractive index values poorly describe the materials absorptivity during LPBF [39], [100].

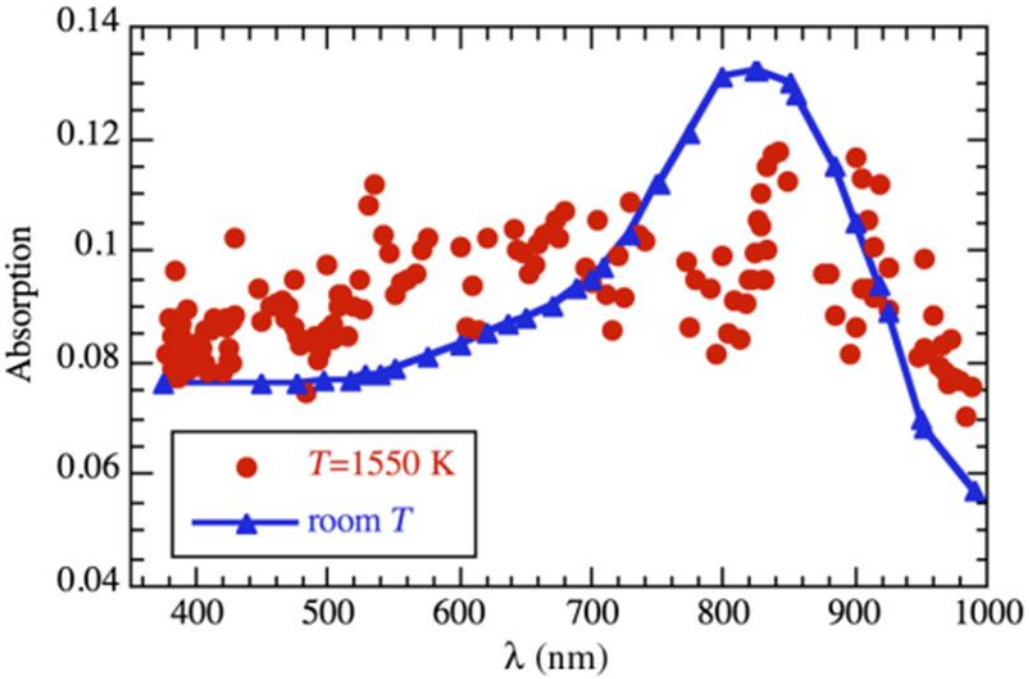

Figure 2-17 shows the experimental absorptivity as a function of wavelength for incident light on aluminium at room temperature. The blue results are from the handbook of optical solids [101] and the red results are from S. Krishnan and P. C. Nordine [102]

Aluminium is classified as a near-free-electron metal, where the electrons on the surface of the metal can be treated as a free-electron gas, with the addition of interband transitions [103]. Figure 2-17 shows the absorption of aluminium at wavelengths from 350 nm to 1000 nm. The figure shows a peak in absorption at 820 nm due to an interband

transition[102]. The absorptivity drops to 5.5% for wavelengths similar to most laser beams in LPBF. Also seen in Figure 2-17 is that the absorption of liquid aluminium (red dots [104]) seems to be insensitive to wavelength. However, from the results seen in Figure 2-16b), the absorptivity of aluminium once melted (representing a flat surface) has an absorptivity of about 15%. While these absorptivity results are useful for computation modelling that requires one value of absorptivity, modelling that requires a refractive index value for modelling absorptivity of metals are not catered for. While researchers discuss this topic, there is currently no literature on the modification of refractive indexes to match experimental data for ray tracing analysis.

2.3.5.6 Temporal and spatial laser beam shaping

2.3.5.6.1 Laser beam pulsing

The energy delivery from the laser is significantly affected by temporal and spatial laser beam shaping. Laser systems can be divided into categories for how they deliver energy as a function of time, in the 'temporal' domain. Continuous (CW) systems use a constant delivery of energy as a function of time, whereas pulsed lasers (PW) can modulate the amount of power delivered (Figure 2-18). Whilst these are fundamentally the same laser type, the energy delivery mechanism between pulsed and continuous lasers systems are significantly different.

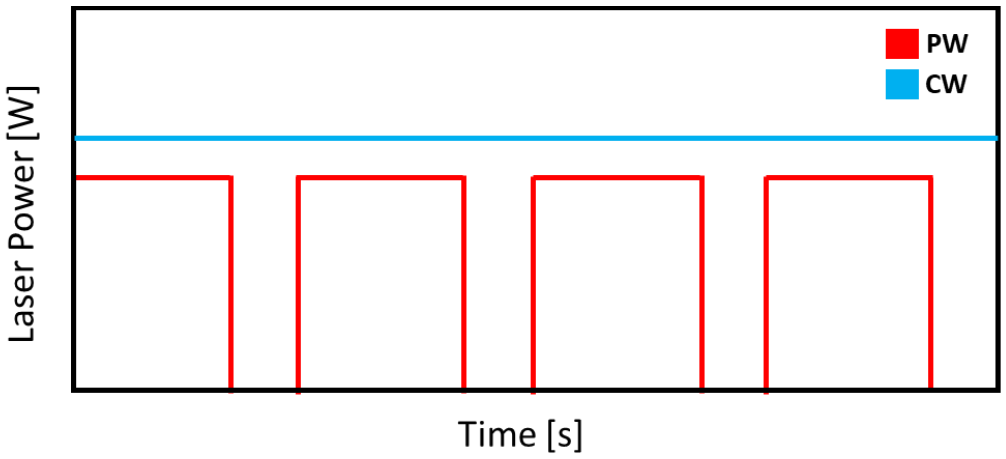

Figure 2-18 shows laser power as a function of time, for a continuous wave laser (CW - Blue) and a Pulsed wave (PW – Red) laser.

Pulsed fibre lasers achieve the pulsed emission by modulating the laser through fast switching of the electrical current injected to the pumping diodes. Fibre lasers have fast response times, allowing for kHz level repetition rates. Generally pulsed lasers have been attributed with higher porosity as the melt pool is more unstable than a melt pool from a continuous laser[105]. CW lasers are favoured in industry with all (EOS GmbH, Trumpf GmbH, GE Additive, SLM solutions GmbH, Realizer GmbH and Sisma SpA) the major

industry LPBF manufactures using CW lasers and leaving only Renishaw plc that uses PW lasers[24]. Recently however, the Renishaw AM500 series comes with the option of using CW or PW laser emission modes [106]. Recently, work by Demir and Previtali has shown that PW emission can be better for finer features in the LPBF process [107]–[109]. However, work from Caprio et al. from the same group also shows that CW emission showed a larger deposited track volume (2-3x) than PW with a much higher melt pool stability [110]. Further work from Caprio et al. also commented that process resolution through track width measurements, was noticeably increased with modulated emission, leading to much thinner tracks than CW. This could decrease the strut size for lattice components, decreasing the scale in which these parts can be printed by LPBF. Finally Caprio et al. showed that a mixture of CW and PW processing could benefit part production [111]. CW lasers can be used in the bulk of a part, whereas PW can be used in areas of geometry that require a high resolution finish, such as borders.

More advanced temporal control of the laser has been demonstrated by Mumtaz and Hopkinson, and Sparks et al. [109], [112]. Sparks et al. showed that ramp down pulses (initially high energy pulsed that drops in power during the duration of one pulse) influences grain growth. Mumtaz and Hopkinson used ramp up and ramp down pulses on thin-walled sections in LPBF, to evaluate the surface roughness. Their findings suggested that ramp up processes reduced spatter through gradual heating of the powder, in addition to reducing distortion due to shrinkage and improved the accuracy of parts. Ramp down profiles gave an improved surface roughness, due to a higher overall melt pool temperature, thus giving more time for thermocapillary forces to smoothen out the surface of the melt pool, rather than 'freezing' small discontinuities in the track. The tracks were also wider, as the increased melt pool size and duration during one pulse, allowed for greater heat conduction [108], [109]. The use of ramp up profiles has also been commented on by Khairallah et al. when introducing high laser powers to the powder bed, the extremely high temperatures delivered in a short timescale resulted in porosity and spatter. Introducing a ramp up profile for the start of the tracks, reduced these defects by a gradual heating cycle, reducing the ratio of inertial pressure to surface tension [78]. Khairallah also showed that a ramp down laser profile was beneficial to reducing pores formed at the end of tracks and decreased surface roughness on the outside surface of the part [86].

Laser welding also shows benefits to using temporal designed laser pulses. These have been shown to be beneficial to reducing spatter, porosity, hot cracking and general improvement of weld surface finishes[113]–[116]. One particular area of interest in the

welding literature uses ramp down pulses to eliminate solidification cracking from a 6061 aluminium alloy[117]–[121]. Longer solidification times from the ramp down pulses, allowed liquid to flow back into cellular-dendrites and reduce the solidification cracking susceptibility, in addition to lowering strain rates critical to cracking [117]. This is explored in section 2.5.4 in more detail.

2.3.5.6.2 Spatial laser beam shaping

Laser beams can also be varied spatially as well as temporally. Changes to the beam shape can be relatively simple, for example defocussing the laser beam so that intensity is reduced but beam diameter is increased. Laser beams can also be passed through additional optical elements so that the laser beam distribution can be changed [122].

The simplest of spatial variation of the beam is through defocussing. The practise stems from laser welding, where defocussed beams can produce wider welding beads for keyhole mode processing [123]–[126]. However, laser welding will use laser powers of 2 – 10kW over large spot sizes, whereas generally the laser beam power for LPBF never exceeds 1kW and spot sizes are smaller than 200 μm. For LPBF, beam focussing can be used to reduce the peak power output and increase the beam size. Jauer et al. used beam defocussing to manufacture magnesium components, by reducing the beam intensity by a factor of 2 to limit vaporisation [82]. Heeling and Wegener used a beam offset in a multi-laser strategy for pre/post-heating[127]. Bean et al. studied the effect of defocussing on the surface quality and density of LPBF parts with Inconel 718[128]. A comprehensive review on defocussing in LPBF was completed by Metelkova et al [129]. Using high powers (up to 800 W) they examined the effect of beam defocussing on the melt pool width and depth. Figure 2-19 shows how the beam width can vary if the focus position is either above or below the substrate level. With an above position (divergent beam) the melt pool often operates in conduction mode due to the same laser power distributed over a larger area. As the beam diameter is larger, the peak temperatures are lower, and the melt pool does not transition to keyhole mode. However, with a focus position below the substrate (convergent beam), an interesting effect occurs. Due to the in-focus plane now being in the material irradiated, the beams intensity is in an interesting position. Due to the in-focus position now below the substrate level, heating is intensified when at the focus position, creating a wide keyhole melt pool profile (Figure 2-19), that concentrates below the surface. However, the authors do not comment on how this affects the conduction-keyhole transition, or how a convergent beam is affected by lower powers. The work showed that using defocussed beams can

increase productivity by up to 840% through a larger track volume melted with an out of focus high powered laser[129].

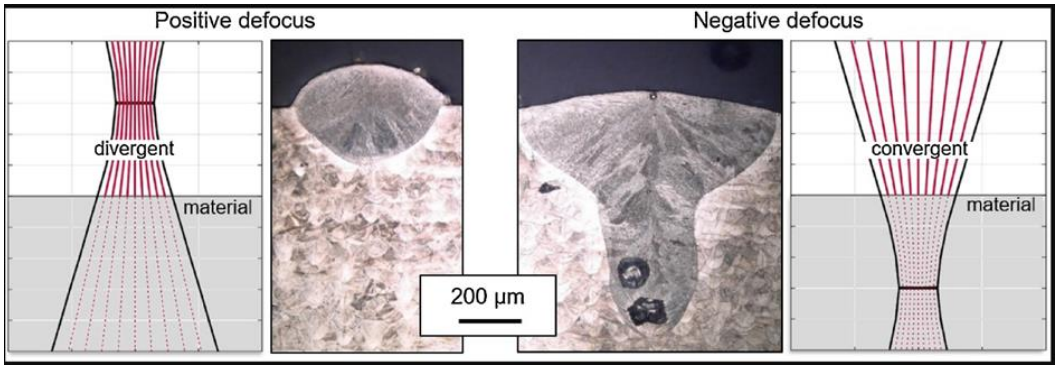

Figure 2-19 shows the effect of a positive (Divergent) and a negative (Convergent) beam defocus on the melt pool width and depth. The focus position is at the narrowest beam size [129]

Roehling et al., Matthews et al., Shi et al., have published results on the development of an elliptical beam at LLNL [130]–[133]. Through anamorphic prism pairs, a circular beam can be converted into an elliptical beam. The studies cover longitudinal elliptical (LE) and transverse elliptical (TE) beams. The different beam types are shown in Figure 2-20 as modelled by the ALE3D multi-physics code. The studies found that for consolidation, LE and TE beams at lower laser powers resulted in discontinuous and balled tracks, while moving to higher powers improved the track morphology over circular gaussian (CG) tracks. Interestingly, TE and LE beams produced much higher fluid velocities in the transition region between the recoil depression and the back of the melt pool. This high velocity flow can cause dendrite tip fragmentation and redistribution, allowing fragments to act as nucleation sites [130]. Shi et al. also concluded that TE beam profiles have a wider supercooled zone (small thermal gradients and low solidification speed) that contributes to a high number of beneficial equiaxed grains. The effects of a TE beam on the microstructure of components will be discussed more in section 2.5.5.1 [133].

Oscillating beams or 'wobble' lasers have also been studied in laser welding literature and are becoming popular in metal additive manufacturing. The use of an oscillating beam in laser welding has been shown to improve the process stability and the surface weld quality [134], [135]. Due to large overlaps between the melt pools in the oscillating laser beam, the melt pool behaviour has been shown to much more stable, and produces very little spattering events, in addition to reducing the surface texture [136]. Oscillating beams have also been shown to introduce equiaxed microstructure, through lower thermal gradients, due to the much larger area and melt pool size [137]. For LPBF, oscillating lasers have been shown to have effects similar to as has been shown in laser

welding such as the improvement of surface roughness and changes to thermal gradients [138], [139].

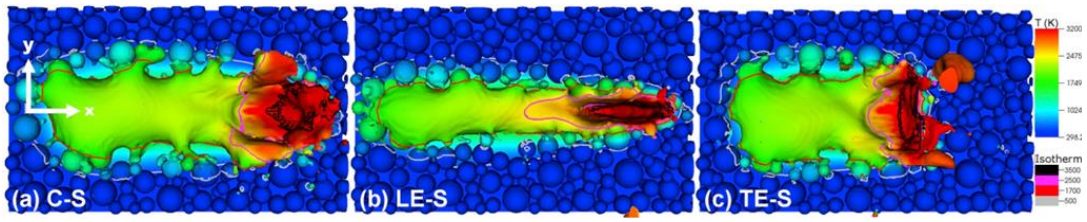

Figure 2-20 shows a circular gaussian (CG), longitudinal elliptical beam(LE) and a transverse elliptical beam (TE). [130]

2.4 Defects generated in laser powder bed fusion

2.4.1 Overview

If control over the process parameters in LPBF is not consistent, or optimised properly, then defects can occur in the component during processing. Naturally, defects generated through the LBPF process have been studied extensively in literature [3], [4]. Apart from microstructural factors (that can be tailored within the processing parameter window), they can represent how 'optimised' a set of process parameters are for particular a given LPBF machine, material or component. Experimental trial and error analysis can derive defect structure process maps as shown in Figure 2-21 [140]. The geometrical marker for this optimisation is often porosity. The aim is to reduce porosity as much as possible, as porosity is one of the main causes of failure in LPBF parts [2], [9], [41], [141], [142]. Porosity can be split into three main types; gas porosity, lack of fusion (LOF) defects, and keyhole porosity.

Gas porosity often occurs from moisture on the powder during process, but can be reduced from proper powder drying cycles, or be contained within the powder feedstock [143], [144]. Gas porosity will not be discussed in further detail, as this defect type is controlled mostly from powder preparation, not process parameter optimisation which is the focus of this study. Lack of fusion porosity occurs when there is insufficient energy to melt a continuous track. Keyhole porosity is formed due to excessive energy at the keyhole, forming porosity at the bottom of the cavity due to large melt pool fluctuations[145]–[147].

2.4.2 Lack of fusion defects

Lack of fusion defects are normally characterised post process from their large irregular shapes, which often act as stress concentrations within the bulk material, that can lead to component failure. Lack of fusion defects arise from incorrect process parameters, such as insufficient energy delivery from a high laser velocity[141], [142], [148]. This is

shown in Figure 2-21, with lack of fusion defects occupying the low laser power, high laser velocity region of the defect structure map[140]. However, they can also be attributed to spatter particle inclusion into the melt pool, as will be discussed in section 2.4.4 [149].

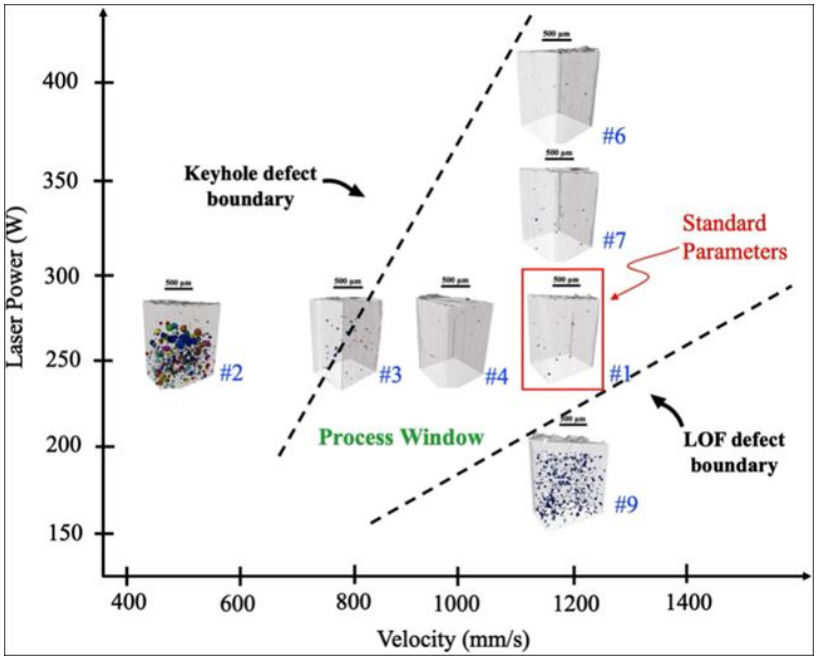

Figure 2-21 shows a defect structure process map for a range of laser powers and scan speeds for Ti6Al4V. [140]

Energy density can be used as an indicator to predict porosity in laser powder bed fusion. But, due to the energy density being a poor indicator of different process parameters used (multiple process parameter combinations can give the same energy density), geometrical models are a better gauge[150], [151]. Tang et al. produced a criterion based upon the melt pool dimensions as shown below[150], [151]:

$$\left(\frac{H}{W}\right)^2 + \left(\frac{L}{D}\right)^2 \leq 1 \qquad \textit{Equation 2-16}$$

Where H is the total track height above the substrate, W is the track width, L is the layer thickness and D is the total melt pool depth. As shown in Figure 2-22, samples produced with melt pool dimensions near the criterion are subject to LoF defects.

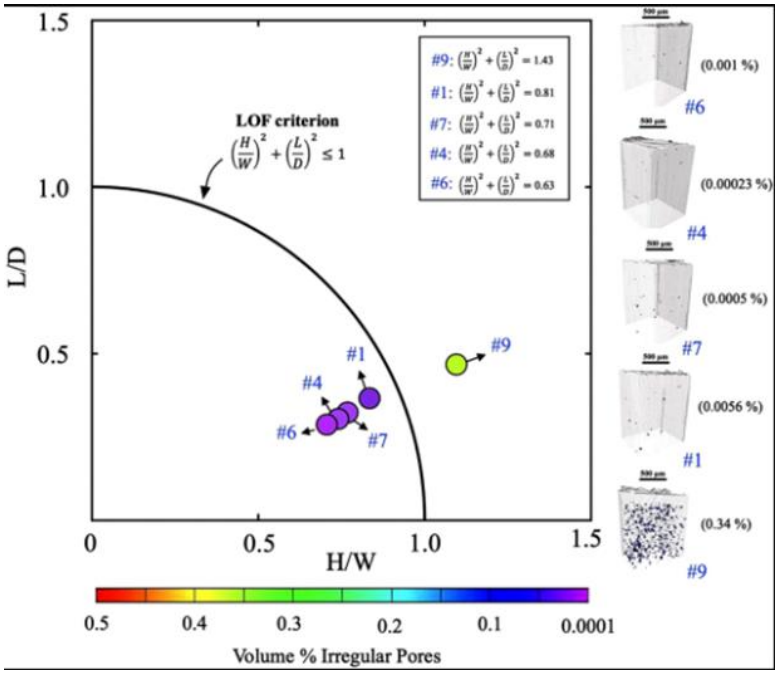

Figure 2-22 Samples made by Gordon et al. use Tang et al.'s criterion for elimination of LOF pores. [140]

Additionally, surface oxides can have a detrimental effect on lack of fusion defects in aluminium alloys. During processing above the boiling point, the top surface of the meltpool will vaporise, causing a change in the surface tension gradient from the change in surface tension due to the presence of oxygen, and the higher temperatures. This will cause oxides to be present on the melt pool sides, but not at the bottom. Due to the high Marangoni flow, oxides at the bottom of the melt pool will be disrupted. The oxides lining the wall of the meltpool, can reduce wetting (due to the low wettability between aluminium and aluminium oxide) causing lack of fusion defects as shown in Figure 2-23[152], [153].

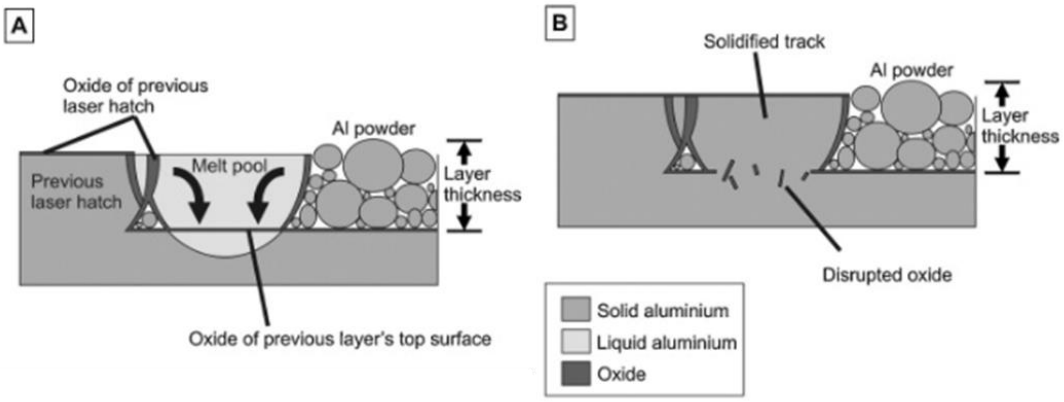

Figure 2-23a) shows the Marangoni convection in the melt pool b) shows how the Marangoni flow can disrupt the oxide formation during the solidification of the melt pool [152]

2.4.3 Keyhole porosity

Keyhole porosity has been extensively studied since the origins of laser welding in the 1960s and 1970s [61], [62]. Operating in keyhole mode has distinct advantages over conduction mode processing, such as increase melt pool mixing, better consolidation, higher absorptivity and better interlayer connections [23]. However, operating in keyhole mode can also give keyhole porosity from a narrow and deep weld profile. If the energy input into the keyhole is too much, then fluctuations at the bottom of the cavity create instability. Reflections from the laser, hit the front wall of the keyhole, heating up the bottom of the back side of the keyhole. The increase in recoil pressure pushes the back side of the keyhole back into the melt pool. If the conditions are correct, then variations in reflections can impact the 'pushed back' region and the surface temperature drops. Liquid movement caused by Marangoni flow can cause the collapse of the back wall of the keyhole, enveloping a portion of gas that is sitting in the cavity [6], [58], [66], [95]. The flow engulfing the gas now transports the pore to the back of the melt pool [154].

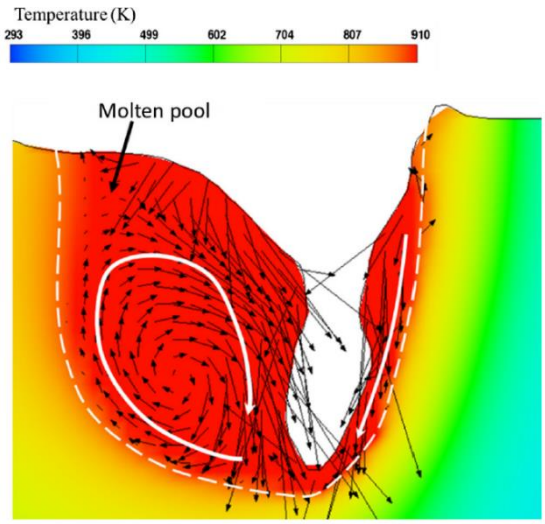

Figure 2-24 shows the three separate zones for the transport of pores within a melt pool. The circulation zone, the transition zone and the laser interaction zone [154]

The movement of pores within LPBF was demonstrated with an experimental study using high resolution X-Ray synchrotron experiments. Hojjatzadeh et al. observed keyholes and with the three main forces associated with the transport of pores within a melt pool; Drag forces, thermocapillary forces and buoyancy forces[155]. Using tungsten particles distributed in a AlSi10Mg melt pool, they tracked the velocities of each different region of the melt pool by monitoring the high melting temperature tungsten particles. In the circulation region of the domain (Figure 2-24), the average melt pool velocity is 0.6 ±0.2 m/s, in the laser interaction zone, melt pool velocities reached an average of 1.9

±0.6 m/s and in the transition zone, melt pool velocities reached 1.45 ±0.5 m/s. From these measurements they calculated that buoyancy forces will have limited to no effect on the transport of pores during LPBF, contrary to other works [156], [157]. They found that optimal processing conditions resulted in a high temperature gradient in the laser interaction zone, which needs to be higher than the induced drag force. They also suggested that a larger laser interaction zone is beneficial, as pores are much more likely to be transported to the surface of the melt pool, so that the gas can escape, due to density differences [155].

To stop the formation of keyhole porosity, users must operate in the 'stable' region of keyhole mode processing, i.e. the C-K transition zone[39]. Operating in this zone means that during steady state processing, the amount of energy entering the melt pool is not excessive, and does not lead to keyhole porosity. However, during the LPBF process, this is not always a simple exercise. While melting the main bulk of a component the laser can scan over the geometry in a raster pattern, leading to many sections where the raster patterns overlap. This leads to overheating in overlapping areas such as turn points – resulting in keyhole porosity at these corners. Due to the deceleration and acceleration of the XY galvanometer scanning mirrors during the turn, the melt pool overheats due to a drop in the scanning speed. This results in the formation of keyhole pores at turning points [78], [158]. This limitation can be partially solved by 'Skywriting', a method which reduces the power during the acceleration and deceleration phases of the turn, limiting overboiling [159]. The acceleration of the laser beam from stationary during a turn in the laser strategy can cause overboiling, creating keyhole porosity at corners. Skywriting decreases the power at these corners, reducing the amount of energy and therefore reducing the keyhole depth, reducing the likelihood of keyhole porosity.

2.4.4 Spatter

The most obvious defect causing mechanism that can arise during processing are spatter particles. During the LPBF process, bright streaks can be visibly seen by the naked eye to fly out of the melt pool and land in the surrounding powder bed, or be taken away by the gas flow. These particles are called spatter particles, and happen as a result of the chaotically driven powder dynamics happening near the melt pool. This occurs due to a high velocity vapour jet that flows as the opposite reaction of the recoil pressure acting on the surface of the melt pool. This vapour jet can entrain powder particles that are not melted by the laser beam, causing 85% of the spatter seen by the naked eye [96]. Spatter particles can be detrimental to processing, as large agglomerated particles landing back into the powder bed can cause lack of fusion defects[160]–[162], as well as wide

denudation zones to either side of the track which effects consolidation to adjacent tracks [86], [163].

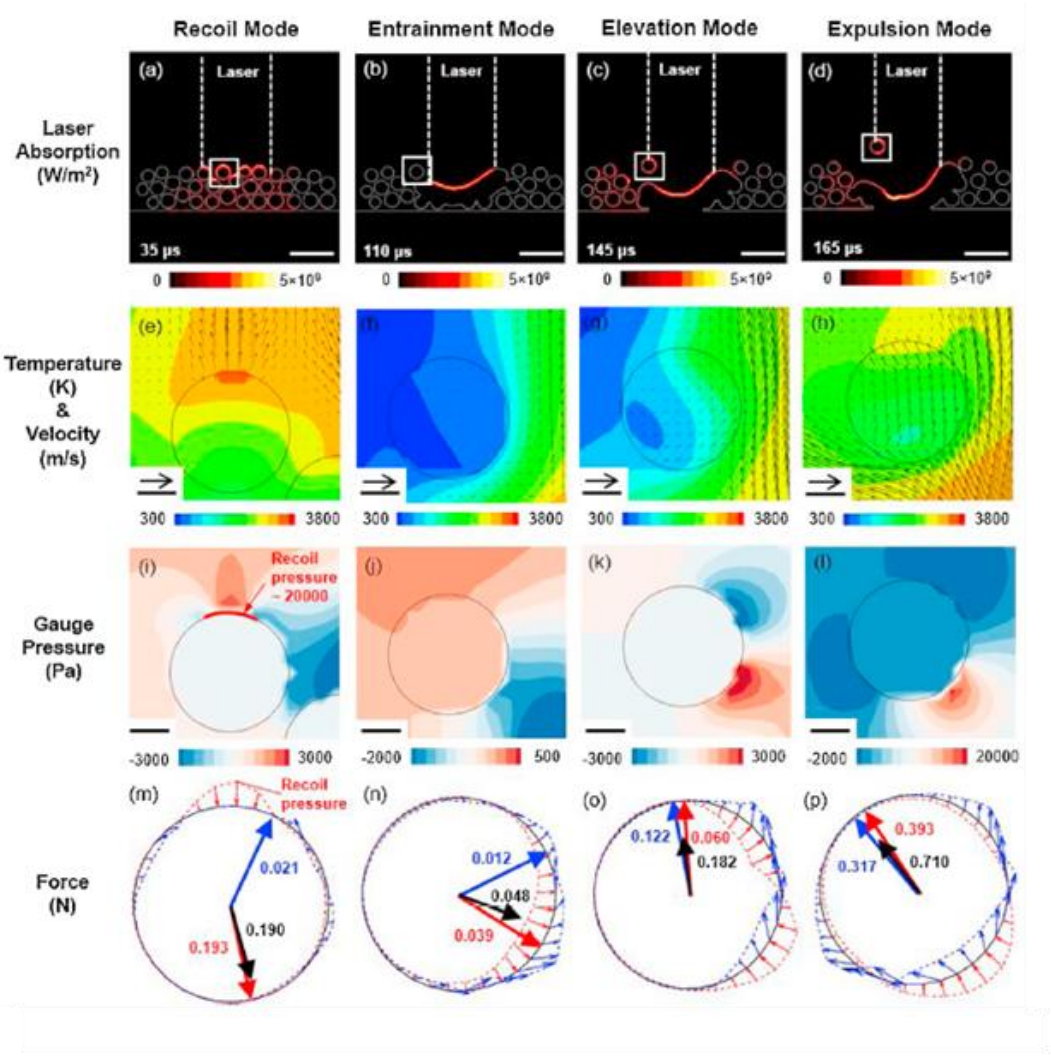

Figure 2-25 shows the computational modelling results, demonstrating the four different modes in powder-gas interactions. Images a-d show the laser absorption distribution on the 2D powder layer. E-h show the temperature and velocity fields i-l Show the pressure distribution on the highlighted powder particle. M-p shows the resulting force on that particle due to the pressure exerted from vaporisation [164]

The other 15% of spatter particles that are produced are from perturbations from the front of the melt pool. Ly et al. explored this through experimental and modelling studies. Spatter forms from this method due to strong recoil pressure in between the protuberance at the front of the melt pool and the main depression zone. This squeezes the liquid metal, and due to the laser velocity spurts a liquid droplet from the melt pool[96].

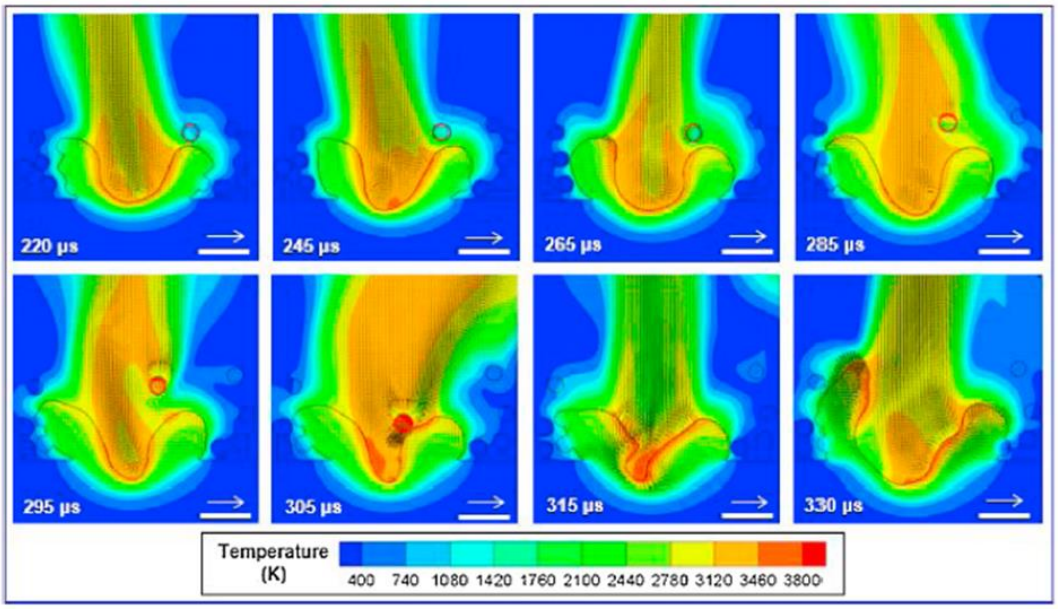

Figure 2-26 shows the sequence of events leading to a particle becoming entrained in the vapour jet, and then due to significant recoil pressure, the particle hits the right side of the melt pool edge, causing massive melt pool instability [164].

Li et al. uses computational fluid dynamics to model the powder-gas interaction in laser powder bed fusion, with computational results experimental validated with high speed synchrotron X-Ray imaging. Their results impressively captured four different modes of powder-gas dynamics during laser powder bed fusion that can be experienced once, or multiple times by the same particle [164]. An image of the four different modes can be seen in Figure 2-25. Recoil mode normally happen to powder particles directly beneath the laser beam, and are pushed downwards into the melt pool becoming molten. Entrainment mode acts on powder particles nearest the edge of the laser beam width. The entrainment of these particles causes the denudation zones. Entrained in the argon gas flow, they are pulled towards the melt pool, and then can then be subject to an elevation and expulsion mode. Elevation mode happens when the particle is caught in the vapour jet, and is expelled when the vapour jet force dominates the particle over a recoil pressure. Particles have also been seen to detonate in this mode [165]. Powder particles were also seen to experience a variety of different modes such as the diving particle in Figure 2-26.

This 'diving' phenomena happens when the recoil pressure interrupts the elevation of a particle after entrainment[164]. As seen in Figure 2-26, the entrained particle enters the vapour jet, and is then subject to a large recoil pressure from the elevated surface temperature. This force pushes the particle down onto the right side of the melt pool, significantly disrupting the melt pool shape and flow, as well as shadowing the melt pool

underneath. This effect could lead to increased surface roughness or defects in the produced part.

This shadowing effect has also been studied by Khairallah et al. who artificially introduced spatter into the domain, to examine the effects of large spatter particles on melt pool and track formation [78]. A large agglomeration of particles was introduced beneath the laser beam during a single track deposition. At higher laser powers, the recoil pressure on the surface of the agglomerate was sufficient to expel the particle away at 5 m/s within 40 μs. This caused the track depth to be decreased by 15% without causing a lack of fusion defect. At lower laser powers, the result was similar to Li et al. where the agglomerate particle was pushed down into the melt pool, causing a 90% melt pool depth decrease and distorting the track dimensions. Additionally, the large particle causes a significant shadowing effect, resulting in a pore being formed due to the reduction in laser power. These results show that large spatter particles lead to temperature fluctuations within the melt pool that result in the formation of defects. Temperature fluctuations (and therefore spatter events) must also be decreased for the melt pool quality to remain constant, to reduce the chance of defects arising during processing.

2.4.5 Residual stress

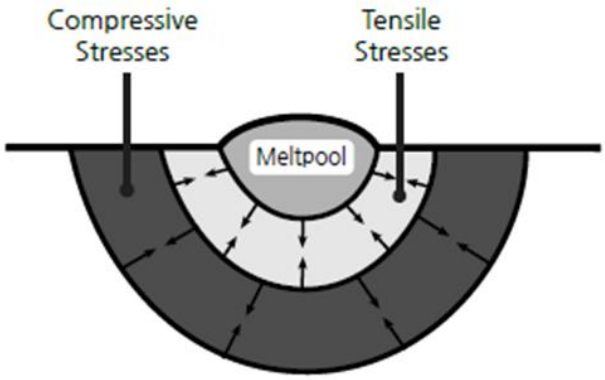

Figure 2-27 shows a schematic on the temperature gradient mechanism that results in the generation of residual stresses in the HAZ [166]

Another significant weakness that can be generated through LPBF processing is the inclusion of residual stress within a component due to the high thermal gradients and localised heating during the process [166]. The mechanism for the generation of residual stress comes from the temperature gradient mechanism [166], [167]. Due to restricted thermal shrinkage beneath the melt pool (Figure 2-27) tensile stresses are created, with opposite compressive stresses generated by material heating up rapidly and thermally expanding in the melt pool. These differences in thermal shrinkage causes the build-up

of thermal stresses. This can be especially prevalent during the production of larger components, and can result in build failure. Additionally, deformation and warping of the part can occur, leading to the dimensional accuracy being compromised. Furthermore, tensile stresses can develop at the surface of parts produced from LPBF, reducing the effective structural loads that the parts can carry [168]. This stress generation is seen in Figure 2-28 during a single track deposition. Longitudinal stress in the σ_{yy} direction is produced as the material behind the melt pool cools and contracts.

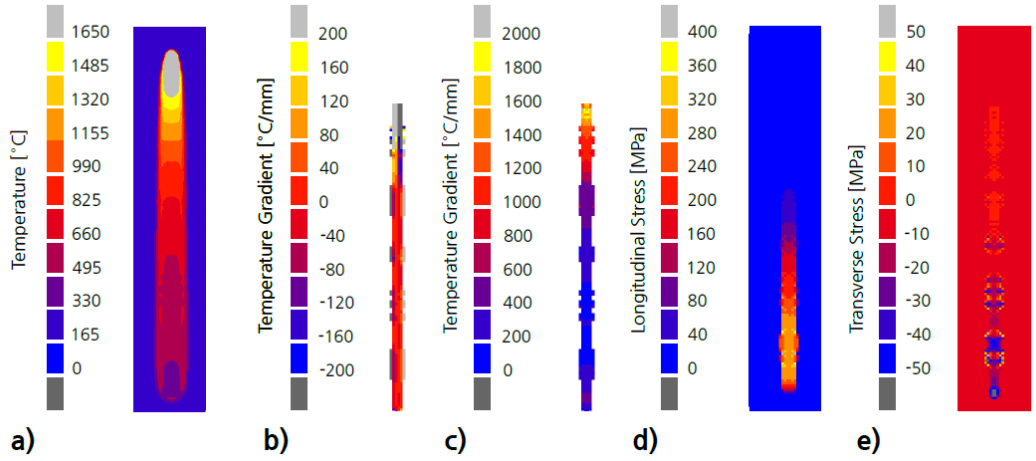

Figure 2-28 shows the temperature, thermal gradient, longitudinal and transverse stresses formed during a single track deposition [169].

Contradictory results exist for the effect of process parameters on the residual stress of components produced with LPBF [170]–[172]. Xiao et al. put this down to a complex relationship between the effect of the final stress on laser power, scanning speed and hatch spacing. Due to a layer experiencing multiple heating and reheating events, establishing a relationship between them can be difficult. However, the results of finite element modelling showed that the influence from scanning speed is stronger than that of laser power, which is stronger than that of the hatch spacing [173]. This was also confirmed by Parry et al. who through thermo-mechanical analysis showed that laser scan sped and scan strategy had the most influence on residual stresses formed in LPBF [169].

2.5 Tailoring material consolidation in laser powder bed fusion

2.5.1 Overview

This section addresses the physics of material solidification optimisation in the LPBF process. As discussed in section 2.4.1, the first goal of the LPBF optimisation is that of material consolidation. Controlling porosity is key to increasing the performance of the material for the intended application. However, within this window of 'optimal'

processing parameters, there exists a second window, for the optimisation of the microstructural conditions.

2.5.2 Solidification concepts

2.5.2.1 Solidification of metals

After laser irradiation, the melt pool cools and the liquid metal solidifies. Depending on solidification conditions, the solidification mode can either be planar, cellular, dendritic or equiaxed dendritic. The conditions of each mode are based upon G (the thermal gradient [K/m]), R (the solidification front velocity) [m/s]), ΔT (ΔT = T_L – T_S where T_L and T_S are the liquidus and solidus temperatures) and D_L (the diffusion coefficient). While ΔT and D_L are material constants, G and R can be changed by the process parameters during LPBF. Different processing conditions can affect G and R, which in turn will change the solidification mode. A high G/R ratio will leave the material in the planar solidification mode, whilst a low G/R ratio will lead to a equiaxed dendritic microstructure. The cooling rate (GR [K/s]) dictates the size of the solidification structure, a high cooling rate moves the graph towards the top right portion of Figure 2-29, leading to a finer structure.

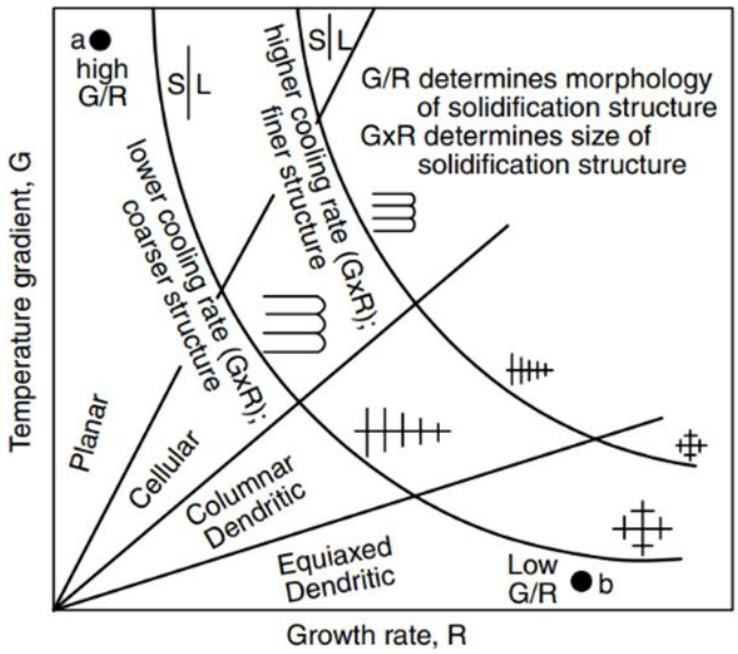

Figure 2-29 shows how G and R can affect the solidification modes [174]

A low cooling rate moves to the bottom left of the G and R graph, leading to coarser microstructure. The minimum G/R that is needed for planar solidification is 7000 K s/mm^2 for Inconel 718. Therefore LPBF will most likely have an unstable solidification front, meaning the solidification will be either cellular or dendritic[175]. In order to model these microstructural transitions using values of G and R, one must know what

values of G and R one is aiming for. This will change for different alloys and different alloy compositions. Hunt modelled the different grain growth mechanisms (Columnar dendritic, columnar to equiaxed transition (CET) and equiaxed dendritic) using approximations for the nucleation happening ahead of the solidification front. This relates dendritic/eutectic growth as a function of the local supercooling [176]. Kurz, Giovanola and Trivedi then developed this function to take into account non-equilibrium effects for fast solidification[177] . This allowed G and R maps to be constructed, with regions of columnar, equiaxed and CET which are likely to occur under the conditions of G and R. This model has been even further customised towards LPBF by Prasad et al. [178]. This allows users to target values for G/R and GR, that will give them a certain microstructure.

2.5.3 Solidification in laser powder bed fusion

Solidification during LPBF occurs initially at the interface with the substrate material, and grain growth nucleates from the existing grains on the substrate material [179]. Grain nucleation from previously solidified microstructure is called epitaxial growth [174]. Foundational work from Gäumann et al. shows that grain growth in powder bed fusion happens epitaxially from the substrate material, with the direction of the grain anti-parallel with the vector G, with a <001> crystal orientation for Inconel 718 [180]. In his work, this was used to their advantage, as the methodology was used for local repairs on single crystal turbine blades [179]. However, this epitaxial growth from dendrites nucleating from previously solidified grain structures, gives LPBF components trademark anisotropic properties from large columnar grains growing in the build direction. Figure 2-30 shows how epitaxial growth occurs during laser welding and LPBF.

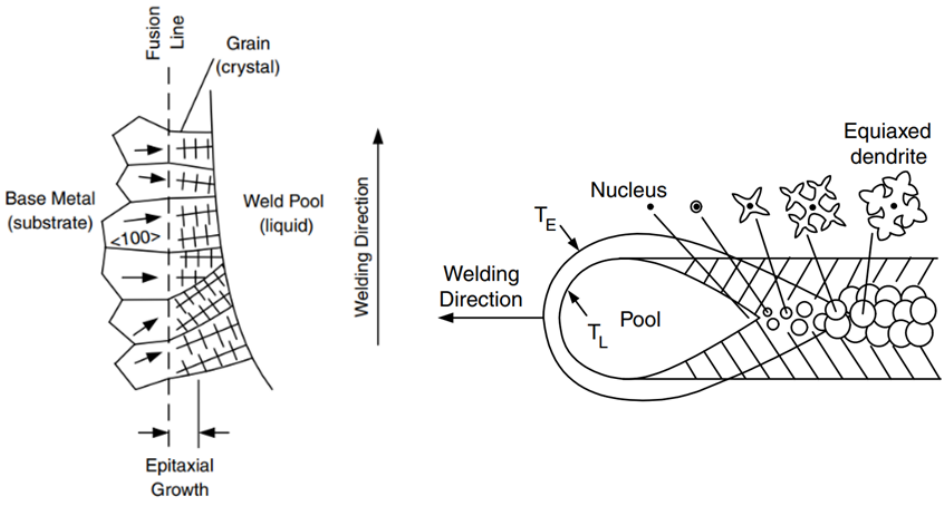

Figure 2-30 Shows how epitaxial growth nucleates from the base material from a melt pool. The grains grow in the opposite direction the heat flow as can be seen in the image on the right. The image to the right shows how grains can nucleate in the mushy zone [174]

Though, epitaxial growth does not proliferate unimpeded. New grains can nucleate in the melt pool where the temperature is between the solidus and liquidus. This is often referred to as the mushy zone. This can happen by three different mechanisms; dendrite fragmentation, grain detachment and heterogenous nucleation, and will promote equiaxed dendritic growth leading to an equiaxed grain structure [174], [181]. Dendrite fragmentation can be caused through strong melt pool flow. Strong flows in the melt pool from thermocapillary forces, cause dendritic fragments to be carried away to act as grain nuclei. Partially melted grains can also detach themselves in the mushy zone and act as grain nuclei elsewhere in the melt pool. Heterogenous nucleation occurs when foreign particles in the mushy zone promote are arranged in a crystalline form and act as heterogenous nuclei.

The amount of supercooling (constitutional supercooling) also has an effect on the size of the mushy zone. Constitutional supercooling occurs when the temperature of the liquid is below the liquidus temperature, and is constitutional due to it being caused by composition changes. As supercooling increases, the size of the mushy zone increases and the solidification mode can change to equiaxed dendritic. This nucleation is increased with the addition of heterogenous nucleation. Figure 2-31 shows the relationship between the supercooling and the size of the mushy zone. Additionally, due to G and R varying across the melt pool, different solidification modes can be seen in the same melt pool upon solidification.

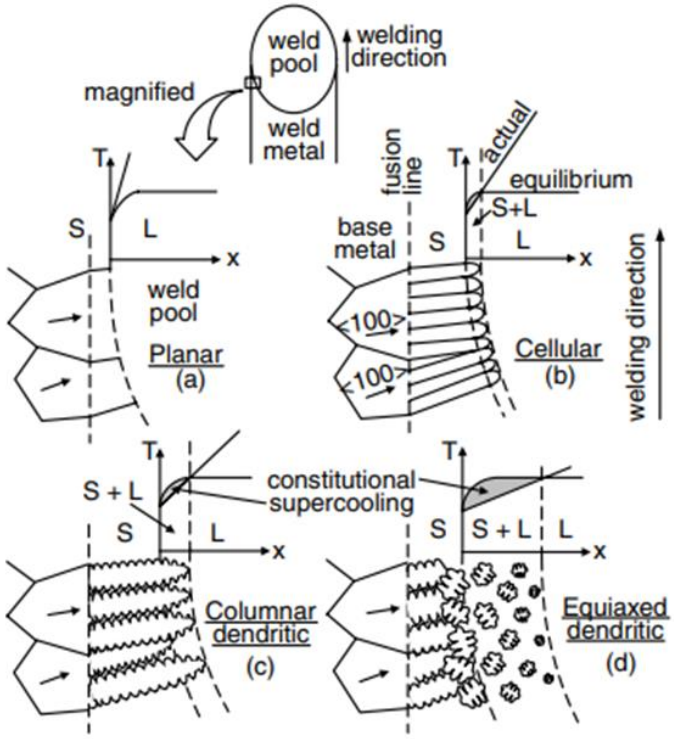

Figure 2-31 shows the effect of supercooling on the solidification mode. Supercooling increases from a through to d. The size of the mushy zone increases with the degree of supercooling, promoting equiaxed dendritic microstructure [174].

2.5.4 Solidification cracking

Laser powder bed fusion processing of certain materials can be hindered through cracking that occurs during solidification. During the final stages of solidification, shrinkage and thermal contraction occurs. While the dendrites are solidifying, long channels of inter-dendritic fluid can get trapped between the dendritic arms. The coupling of these two factors produces cavities and hot tearing cracks[182]. These cracks reduce the strength of the material considerably and limit the use of certain high strength aluminium alloys processed by LPBF [23].

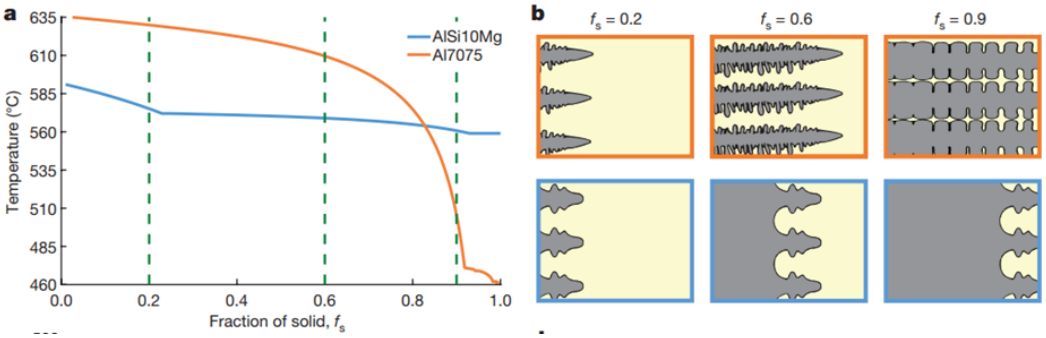

Figure 2-32a) shows how AlSi10Mg and Al7075 solidify over a temperature range. B) shows how the dendritic growth occurs for an alloy that is susceptible to solidification cracking, and one that is not. The solidification for AlSi10Mg is different because the channels in between the dendritic arms can be backfilled [183].

Figure 2-32 shows the difference between two aluminium alloys, one susceptible to hot tearing, and one not. Figure 2-32a shows the solidification curve for the two alloys. The components of the alloy constituents drive the shape of the curve and can be described using a Scheil-Gulliver solidification model. Al7075 has a large solidification range and a sharp decrease near the solid fraction of 1. The AlSi10Mg has an almost flat curve, translating to a high percent of inter-dendritic fluid present at the last stages of solidification. This can backfill the dendrite arms and decrease hot tearing [174].

Martin et al. showed how equiaxed dendritic growth could be used to accommodate strain in the material and eliminate hot tearing in LPBF processing of Al7075 and Al6061 [183]. Their method, originally conceived by Gourlay and Dahle, states that strain can be better overcome in equiaxed dendritic growth, rather than through purely dendritic growth [184]. As stated in section 2.5.3, this requires either: a significant amount of supercooling, grain/dendritic tip fragmentation or heterogenous nucleation from a foreign particle in the melt pool. Martin et al. claim that producing this amount of supercooling for an aluminium alloy would be difficult to achieve with a high thermal conductivity material like aluminium. Instead they use a software to select grain refiners that had similar lattice parameters to the target material. These grain refiners provide a low energy barrier heterogeneous nucleation sites ahead of the solidification front, changing the predominant nucleation mechanism to equiaxed dendritic. The equiaxed dendritic growth accommodates strain in the material better, and so the hot tearing was eliminated. As a result, the mechanical properties were 80% higher than AlSi10Mg and comparable to wrought Al7075. The study commented how these values could be improved with proper process parameter optimisation, as the sample had a low amount of porosity. These results present a significant step in the processing of high strength aluminium alloys through LPBF. However, the resultant chemistry of the Al7075 had been changed with the addition of nano Zr and working with nano-particles can increase the danger associated with the preparation process. Additionally, the pre-processing and mixing of nano-particles is difficult. This work is also supported by Yang et al. who modelled the heterogenous grain nucleation in 316L stainless steel with TiB2 particles through multiple layers [185].

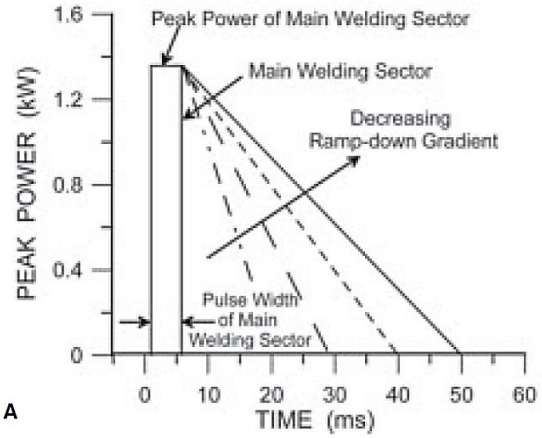

Figure 2-33 shows the pulse power as a function of time. The pulses are compromised of the main welding pulse, and then subsequent ramp down pulses of different gradients [117]

Zhang et al. showed how temporal pulse shaping could be used to eliminate solidification cracking in Al6061 in laser welding [117]. As shown in Figure 2-33 the initial pulse is used as the main welding portion, with the ramp down gradients being used to control the solidification. Crack free welds were achieved using a ramp down power profile of 100 kW/s at the end of the main power pulse (Figure 2-33). The two different peak powers density of 8.1 GW/m^2 and 11.5 GW/m^2 both showed regions of no cracking, however this zone was wider in the lower peak power density. For both power densities the results showed that solidification cracking restarted again when the ramp down profile was decreased further. This behaviour can be explained due to effects of the solidification time, interface velocities, cellular dendrite length and the cooling and strain rate. Solidification time was significantly increased with the ramp down profile, leading to more time for fluid to flow back and heal the dendrites. The interface velocities were lower, leading to increased primary dendrite arm spacings. This allowed a larger gap for fluid to flow back and solidify the structure. Additionally, a narrower mushy zone and smaller strain rates decreased the tendency for cracking. While these techniques have been proven to be successful in eliminating hot tearing in high strength Al alloys in laser welding, they have yet to be proved in LPBF.

2.5.5 Microstructure control

2.5.5.1 Microstructure manipulation in LPBF

The ability to control microstructure and therefore influence the mechanical properties of materials processed by LPBF is one of the largest areas of interest for AM. Typically, microstructures for LPBF consist of large columnar grains, spanning several layers, which are the result of epitaxial growth from predominantly dendritic grain growth [186]. The direction of the columnar grain growth follows the opposite direction to the heat flow inside the material during processing. This can lead to strong texture in the

build direction of LPBF components [187]. This texture can vary in inclination, depending upon the scan strategy used in the process. This has been demonstrated by Wei et al. who shows how different process parameters can affect the inclination of the columnar grains [175]. This preferential growth direction causes anisotropy in a large number of components made by LPBF [148], [188]. This can be seen in Figure 2-34 where anisotropy due to the growth direction of grains affects the elastic modulus of Inconel 718 when a print is angled upon the build bed [189].

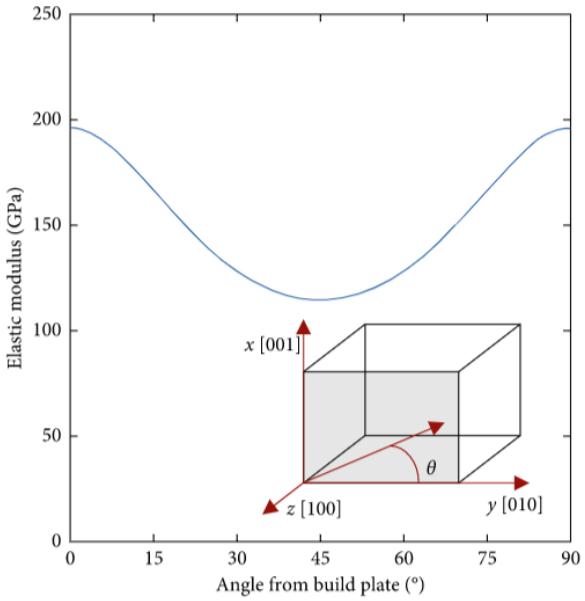

Figure 2-34 shows how the elastic modulus varies with the angle in which the part is printed on the build plate. [189]

These microstructures can be altered using either: the LPBF processing parameters or modifying the materials composition, through G and R changes, changes to modify the solidification range ($T_L - T_S$) or the introduction of heterogenous nucleation into the melt pool through inoculants (section 2.5.4)[187], [190]. To manipulate the solidification conditions through process parameters alone, one must change the values of G and R in the melt pool, and most crucially in the mushy zone.

The tailoring of microstructure for AM splits into two rough categories. The first is capitalising on the epitaxially dominant growth mechanism in LPBF, with the aim of creating single crystal materials. The second, wants to promote equiaxed dendritic growth in the melt pool, so that an equiaxed grain structure becomes dominant.

Single crystal or highly directionally solidified materials are advantageous due to a low number grain boundaries (or no grain boundaries in single crystals) leading to better creep resistance and thermal fatigue behaviour. Metal AM can be used to either manufacture, or repair single crystal components. Gäumann first demonstrated this

work with Inconel 718, a high strength nickel superalloy [179]. Dinda et al. furthered this work by developing a strong texture over several layers in a DED process [191]. They proposed that if the laser scanning velocity is tailored so that the heat flow direction is at angle of 45° to the substrate, then a highly textured directionally solidified structure can be formed. In order to achieve the large columnar growth, a large thermal gradient (G) is needed at a low solidification speed (R) with a scan rotation of 180°. Pham et al. studied the effect of beam shape on the grain solidification in thin Al films for microelectronics. A reduction in grain boundaries is needed so that parts do not suffer from conductivity deterioration and electromigration failure [192]. By using a micron sized, chevron shaped, laser beam, they were able to change the growth mechanism from the laser spot shape. Figure 2-35c and d show the two different orientations of the chevron and its effect on the grain growth. With the chevron shaped as in Figure 2-35c, the grain growth follows a typical dendritic growth to the centre of the melt pool. However, when the chevron is in the opposite direction (Figure 2-35d), a single grain crystal with multiple orientations grows in the centre of the track. Though the authors do not comment on this, the single grain growth is probably due to R varying across the melt pool width. The inverted shape of a 'normal' tear drop could mean that R drops to very low values across the melt pool. This could transition the melt pool solidification to a planar mode, causing the single grain to grow. Pure aluminium was used for this work, so the liquid would transition to solid without any supercooling. Therefore, this method applied to an alloy in LPBF might not give the same results. However, this has not been tested yet in LPBF and provides a good opportunity for further research.

Beam shaping in LPBF has been proved to alter the solidification conditions. Shi et al. varied the beam ellipticity for LPBF and through computational modelling, examined the grain growth behaviour. Spatially varying the beam with a transverse elliptical (TE) shape, resulted in 1.5x more nucleation events than a circular beam. Due to competitive growth, the higher nucleation propensity of the TE beam reduced the texture of the grain growth. The higher number of nucleation events happened much earlier in the track formation than the circular beam. The elliptical beam showed a much wider supercooled zone, leading to low G and high R values, leading to equiaxed dendritic growth[133].

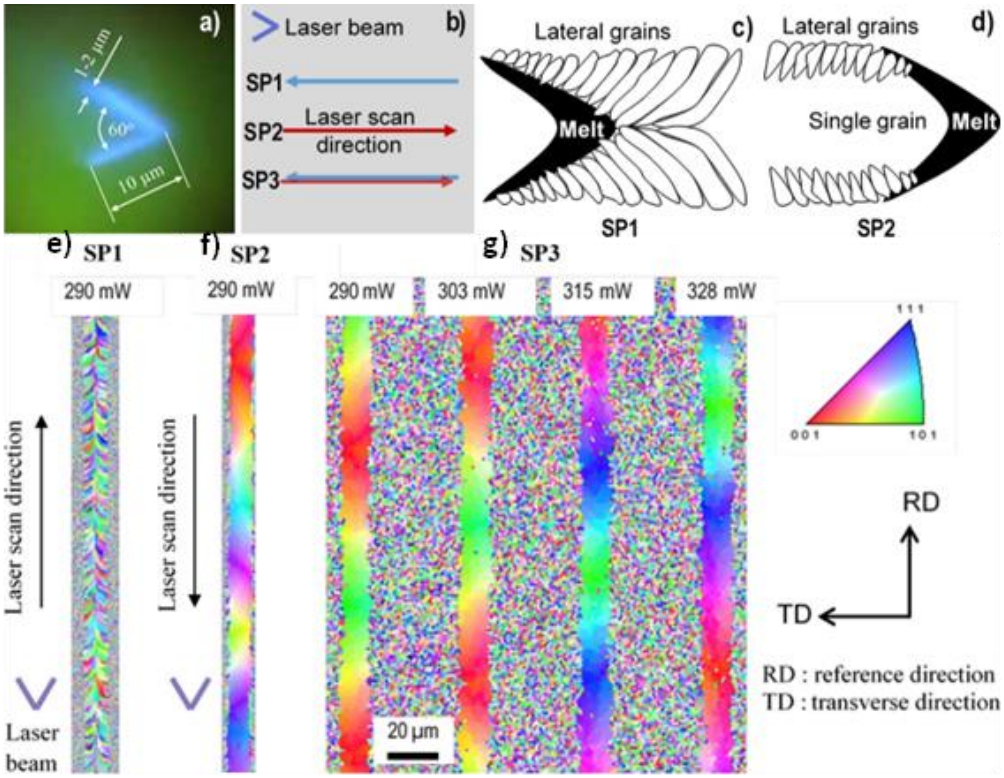

Figure 2-35 a) shows the dimensions of the chevron shaped laser beam. B) shows the direction of the laser scan for SP1, SP2 and SP3. C and D show the growth of grains from the chevron shaped beam. E, F and G show the grain boundaries and orientation for the different directions of the chevron shaped beam, in addition to effect of power [192]

Complete control over Inconel 718 microstructure has been achieved over the last 6 years by the University of Tennessee-Knoxville and Oak Ridge National laboratory [193]–[197]. The researchers take advantage of the extreme speeds of electron beam powder bed fusion (EBPBF). What makes their work interesting, is that they stipulate that the *heat flow direction* is crucial in achieving the equiaxed grain structure in EBPBF. Their concept is divided into two sections. Using a raster scan strategy (commonly used in LPBF) the grain growth will grow through the dendritic mode. However, whilst using a point melt strategy, they can achieve equiaxed dendritic growth. This phenomenon is explained through the grain growth competition between <001> grains growing with the thermal gradient vector and heterogenous nucleation at the dendrite tips. Large misorientations in crystal structure result in higher dendrite tip velocities. This increases the undercooling and increases the propensity for nucleation. For a raster scan strategy, there is a high volume of grains growing with the thermal gradient vector, leading to high competition for grain growth. This results in columnar growth, due to easy growth directions winning over heterogenous nucleation. For the point melt scan strategy, the large misorientations coupled with large deviations in the thermal gradient result in an equiaxed structure through reduced competition [195]. Plotkowski et al. from the same group, then takes this further by designing a method to produce a

stochastic scan strategy based on these two concepts. The scan strategy sub divides the domain into voxels, and assigns a grain type based on these two different concepts. However, this time, instead of a raster scan pattern, a neighbourhood melt difference (difference in temperature from cells closest to the spot size) (Δt_i) was calculated. A neural network would then generate scan strategies that either had a close melt neighbourhood difference, or a high one. Low values of Δt_i have a low solidification cooling rate (low G and low R) with a high Δt_i having higher cooling rates. Figure 2-36 shows the results. A clear distinction can be made between the two concepts, a low cooling rate gives equiaxed grains, and a high cooling rate gives columnar grains. However, it must be noted that this would not be possible without the extreme pre-heating temperatures from the electron beam source, heating the layer to 1000 °C before the main strategy.

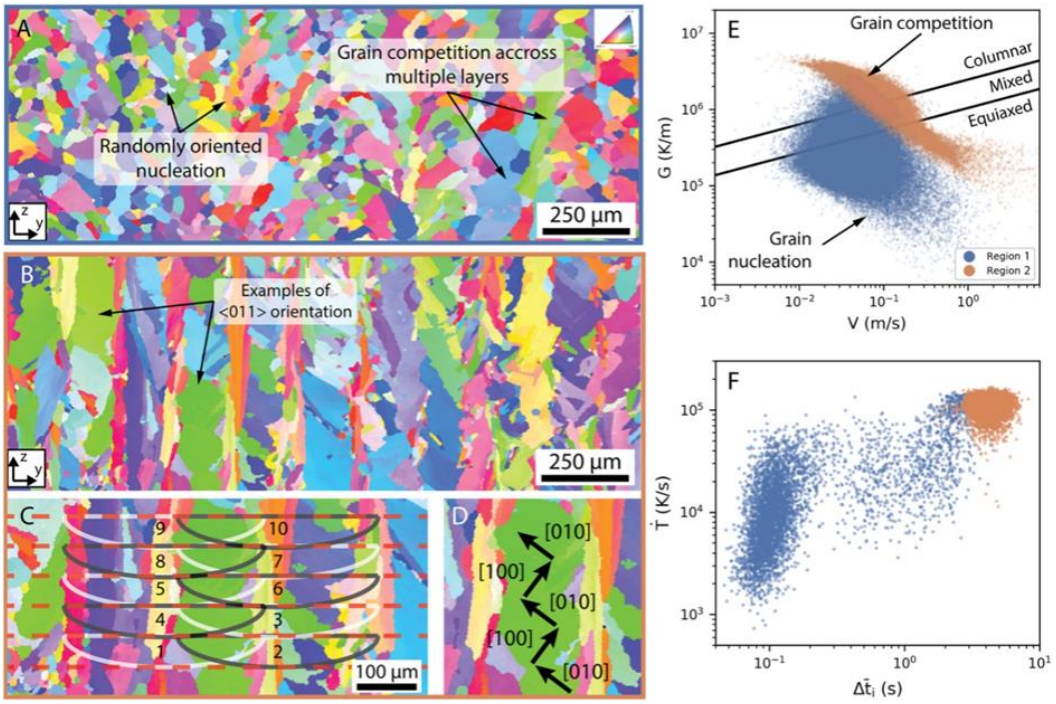

Figure 2-36a and b show the grain structure from a low Δt_i and a high Δt_i . E shows the G and R values for the different regions, showing a low GR for region 1 and a high GR for region 2. F shows how the distribution of Δt_i splits the two microstructures [196]

Large area heating has been demonstrated in LPBF, via large area diode heating. Matthews et al. used an optically addressable light valve (OALV), to mask certain areas of a laser diode, to print a whole layer at once. While no microstructure results were provided, this has the potential to reduce cooling rates in LPBF to levels where equiaxed dendritic events can occur in LPBF through lower thermal gradients[198]. Roehling et al. also used laser diode heating for an in-situ residual stress treatment. An entire layer of 316L stainless steel, was heated to 1000 °C, post scanning to reduce residual stresses

by 90 % [199]. While these results did not change the microstructure, this technique could be used as method to decrease cooling rates through ramp down heating.

2.6 Process parameter optimisation and defect elimination strategies

2.6.1 Traditional process parameter optimisation

2.6.1.1 Overview

Producing a component in LPBF to specification can be difficult, especially with a new material, component design, or LPBF machine. Extensive trial and error testing must be conducted to produce a part within specification (density, mechanical properties). Process parameter optimisation therefore, is a costly and time consuming process that is in-efficient [200], [201]. As explained in section 2.5.1, two processing windows can be explored for parameter optimisation, a consolidation and microstructural processing space. Historically, only the first window of consolidation has been studied extensively in literature [10], [147]. A multitude of literature exists on the journey for optimal process parameters for every material used in LPBF [23], [186].

Most optimisation starts with the reduction of key processing parameters to a single variable. This can help reduce the complexity of the problem, as well as compare processing parameters to each other. A common variable used to try and define a set of process parameters is the volumetric energy density (J per m^3). This is given by;

$$volumetric\ energy\ density = \frac{\alpha P}{VhL} \qquad \textit{Equation 2-17}$$

Where α is the average absorptivity, P is the laser power [W], V is the laser velocity [m/s], h is the hatch distance [m] and L is the layer thickness [m]. This is an oversimplification of the energy delivery in LPBF, due to the highly localised heat source in addition to variable absorptivity. In addition, equivalent energy densities can be calculated based on parameters that give vary different processing characteristics [202]. An alternative to this, are process parameter maps, predominantly made of laser power vs scan speed [203]. Different regions of the map are associated with either being in conduction or keyhole mode. As discussed in Section 2.3.5.4, the transition period shows the best comprise between lack of fusion defects and keyhole porosity [6]. One effective method used in multiple studies is the normalised enthalpy [98], [204]–[207]. The formula for the normalised enthalpy is shown below;

$$\overline{\Delta H} = \frac{\alpha P}{\rho(C_p \Delta T + L_m)\sqrt{\pi \omega^3 V D}} \qquad \textit{Equation 2-18}$$

Where α is the absorptivity, P is the laser power [W], ρ is the density [kg/m^3], C_p is the heat capacity [J/Kg.K], ΔT is the difference between the melting and initial temperature [K], L_m is the latent heat of melting [kJ/kgJ], ω is the laser spot radius [m], V is the laser velocity [m/s] and D is the thermal diffusivity [m^2/s].

Normalised melt pool depth ($\bar{d}$) is used in conjunction with the normalised enthalpy and is given by;

$$\bar{d} = \frac{d}{\omega} \qquad \textit{Equation 2-19}$$

Where d is the melt pool depth. King et al. studied plots of normalised depth vs normalised enthalpy for 316L stainless steel [6] (Figure 2-37). They found that this metric was a reasonable indicator for different process parameters to be analysed in the same context. It was also able to distinguish the conduction to keyhole transition zone. However, above the initial keyhole regime, the normalised enthalpy does not take into account physics due to vaporisation, and the dependence of melt pool depth based on beam size. Developing the approach used by Ion et al. [208] for laser welding, Thomas et al. used additional dimensionless parameters added to the normalised enthalpy for predicting the microstructure of parts [209]. Zhou et al. proposed a similar formula for predicting the process parameters based on material properties shown below [35];

$$Q_a \geq Q_{melting} + Q_{vaporisation} + Q_{heatloss} \qquad \textit{Equation 2-20}$$

Where Q_a is the energy absorption and $Q_{melting} + Q_{vaporisation} + Q_{heatloss}$ is the energy consumption. This formula however, neglects temperature dependant parameters, heat loss parameters through vaporisation and material loss, surface tension, recoil pressure and Marangoni convection. While these models can provide a rough indication of the region in which dense material can be fabricated, they neglect a lot of physics and still need a high number of experiments to find an optimal process parameter set.

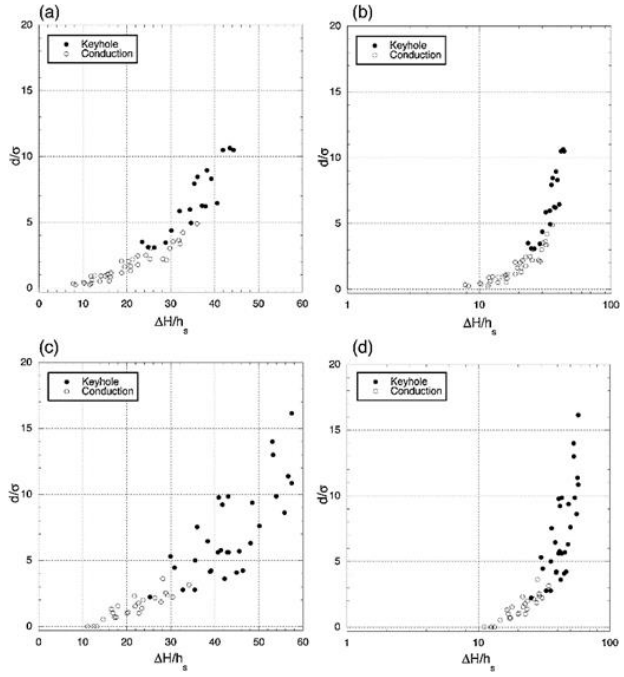

Figure 2-37 shows normalised melt pool depth vs normalised enthalpy for 316L stainless steel. Conduction mode and keyhole modes can be seen from gradient changes [6]

2.6.2 Feed forward control in laser powder bed fusion

Process parameter selection however, has progressed in recent years. Static process parameters are becoming outdated, and dynamic feed forward control in LPBF is the future of process parameter control [10], [210]–[212]. This area can be split into two areas, in-situ sensor feedback control and model based feed forward control. In situ methods use sensors in an experimental environment. Feedback signals from a sensor is used as a critical factor to make adjustments to a process parameter in-situ. Model based feed forward control, uses computational methods to make an optimised strategy in a digital environment before the part is built. Of course, these two areas can be combined, so that a strategy can be optimised beforehand, and then tailored in-situ to achieve absolute control over the LPBF process.

2.6.2.1 In-situ sensor data feedback control

In-situ sensor driven feed forward control or feedback control, uses the output of a sensor in the LPBF process, and uses this to modify an input into the LPBF parameters. Early systems used optical sensors to examine the powder bed and check for irregularities. The concept behind them is to monitor the powder bed and melt pool optically, and any discontinuities would be rescanned to improve consolidation, or to increase laser power for an increased layer thickness [213]–[215]. Hooper demonstrates a system that can be used to measure temperature fields in LPBF spatially and temporally [13]. Using two high speed imaging cameras, both fitted with a bandpass

filter (700 nm and 950 nm respectively) temperatures with a range of 1000 – 4000 K can be imaged at a 100 kHz sampling rate with a resolution of 20 µm. This accurate temperature information can be used to feedback high resolution temperature information to in-situ variable power controllers. This work by Hooper also experimentally confirms that temperatures on the melt pool surface can rise much higher than the atmospheric boiling temperature values. Previous to this Kie et al. [216], Semak et al.[217], and Khairallah et al. [86] all predict temperatures 500 – 900 K above the boiling temperature, but this was yet to be proved experimentally.

Other variations use temperature measurements to adjust laser power on the fly to reduce peak temperatures in the melt pool[218]–[220]. One major limitation to this technique however is the speed in which sensors can analyse the process, feedback the information to a controller and the controller change a process parameter. Acoustic signals can also be used to provide information on the quality of parts for LPBF. Shevchik et al. showed how acoustic signals monitored by neural networks could be used to detect porosity in-situ, although development for feed forward control using this method has not been reported [221]. The information required to assert precise control on the melt pool in real time, is still limited by hardware speed. Modern systems can provide effective closed loop control, but this is still in its infancy to provide the exact control needed for real time process changes.

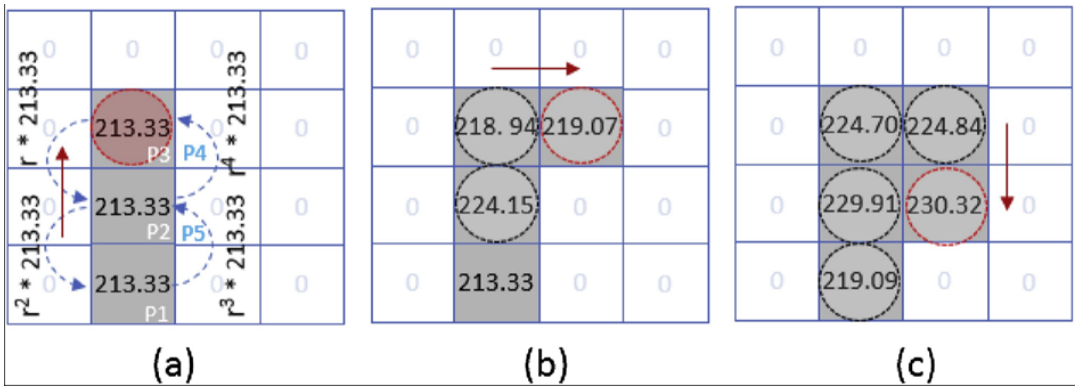

Figure 2-38 shows how a camera voxelises the powder bed into individual areas. Each individual area is given a GCF value and then a subsequent scan matches the GCF constant to the previous one. GCF values vary dynamically as the print progresses, due to the GCF constant changes due to residual heat [222]

Common process parameters are static, with machine inputs designed to use a parameter set for large areas of the build (Bulk, down skin, borders etc.). Philips et al. showed that the hardware for variable power exists and can be used in metal AM. A position based laser power controller can modify the laser power signal generated by a commercial laser. Combined with a feed forward control system, this resulted in a reduction of temperature fluctuations by 33% [223], [224]. Yeung et al. also

demonstrated how variable process parameters can be advantageous in the production of parts made by LPBF [222]. Typical laser scan strategies as shown previously, use constant process parameters throughout the scan, leading to variations in the melt pool size and shape, particularly near geometric features such as overhangs, or large spatter particles. The difference in melt pool sizes can come from thermal conductivity and absorptivity differences between an area with powder on top of consolidated metal, vs powder on top of powder, as would be the case in an overhanging region. The authors use a critical factor called GCF (geometric conductance factor) as a constant to which laser power is changed, so that GCF is kept constant throughout the process. High speed cameras measure and split the powder bed into voxels. These voxels then have a GCF value associated with them (Figure 2-38). This GCF value is then kept constant as to the previous scan voxel by the variable laser power. GCF values can also change dynamically due to residual heat in the layer scan. Due to the sequential nature of this process however, complex scan strategies encompassing a large number of voxels over a large number of layers is a limiting factor. As this technique uses in-situ methods to control the GCF factor, no pre-build optimisation is done – meaning that computational power is a limiting factor of this technique. Results from this work also showed that parts produced with variable process parameters, were overall higher quality than those produced with static parameters.

Williams et al. shows how temperature is crucial in determining optimal processing parameters[225]. They show that research into variable process parameters that take into account variations in part geometry, number of parts and interlayer cooling times can result in changes in porosity, local microstructure and mechanical properties. They show that even from changing fundamental process parameters like the interlayer cooling time, can affect surface temperatures up to 200 °C. Higher surface temperatures are attributed to spatter formation, and is inversely proportional to porosity, in addition to changing the melt pool geometry leading to lack of fusion defects.

2.6.2.2 Model based feed forward control

Model based feed forward control often uses the solution to the 'inverse problem' to optimise process parameters [226]. The inverse problem uses models of the physical system to find the parameters that can achieve a level of desired consolidation/microstructural control. So far in the literature, only models that solve the inverse solution to reduce defects are considered. Druzgalski et al. observe that for feed forward models, F, can map parameters, p, to observable data. So that;

$$d = F(p) \qquad \textit{Equation 2-21}$$

They comment that this is dependent on two factors. The first is that the model can accurately represent the physical system. The second is that the solution must minimise the function;

$$\phi(p) = \|F(p) - d_{obs}\|^2 \qquad \textit{Equation 2-22}$$

This introduces a dilemma, for simple models where F is linear and the inverse solution is inexpensive to compute, normally do not represent the system well enough. However, highly non-linear models are costly and time consuming. Therefore the crucial factor with inverse systems is to accurately model the physical system of interest [10].

2.6.2.2.1 Inverse solution

These inverse solutions are either data driven, or are from first principles. Data driven models use sensor data and information that is gathered ex-situ. Calculations from first principles use physics simulations that solve governing partial differential equations.

Lee and Prabhu designed regression metamodels for heat transfer from the laser beam. They use the outputs from a computational model as the temperature inputs for a metamodel prediction of future scans. This data is then fed to an optimal controller, that can take either modelling or experimental temperature data and be used to adjust scan speed to keep a constant peak temperature throughout the melt pool [12]. The model-free optimal controller improved the scan path to reduce the temperature fluctuations in the model, through change of scan speed, in addition to reducing the time taken to get to a target temperature. This model however did not take into account temperature dependant properties or phase changes from melting and re-solidification. This would reduce the accuracy of the computational model, shown to be a critical factor by Druzgalski. Papacharalampopoulos et al. uses melt pool depth as a critical factor in determining optimal conditions for laser welding and LPBF [227]. Through the use of a low-fidelity model they controlled the cooling rates of the process, through change of laser power. However, they make use of a low fidelity model that does not consider variable absorptivity, phase changes and temperature dependant properties, which have shown to be crucial. As shown in section 2.3.5.1, these factors play a large role in melt pool depths, so it is unclear how this was used as a critical factor. Nevertheless, this shows how critical factors in LPBF can be used to control factors such as the cooling rate. The authors only mentioned this in regard to residual stress reduction, and no comment on microstructural design was made. Wang et al. uses a feed forward model through melt pool width to depth ratios using an analytical model [228]. Changes to the laser power were made to keep melt pool sizes constant. This was done to try and keep the laser in the transitional zone from conduction to keyhole mode. This was largely achieved by the

feed forward control. However the model did overestimate the laser power at track turns, and constant power values were used for the experiments. The analytical model neglected the advanced physics of the process and only considered the first layer, that included multiple laser passes. Stathatos and Vosniakos provide a method of using variable power to keep a constant peak melt pool temperature. During their review, they comment that peak temperature of the melt pool is the key 'proxy' parameter for overall build quality [210], [229]. An extremely fast finite element analysis model (FEA) was developed to give training data to an artificial neural network (ANN). The ANN could then predict a variable power output to keep a melt pool at a constant peak temperature. This work compromises of an extremely complicated modelling setup to achieve the desired outcome, but once setup, provides fast results for layer scans. This work has only been tested for 'digital' experiments and does not consider variability in powder layers, difficult to print materials or offer any explanation as to how the peak temperature can be modified to produce optimal results. This work provides a framework for peak temperature optimisation for LPBF but does not experimentally validate their conclusions, or provide answers on what the optimal surface temperature should be.

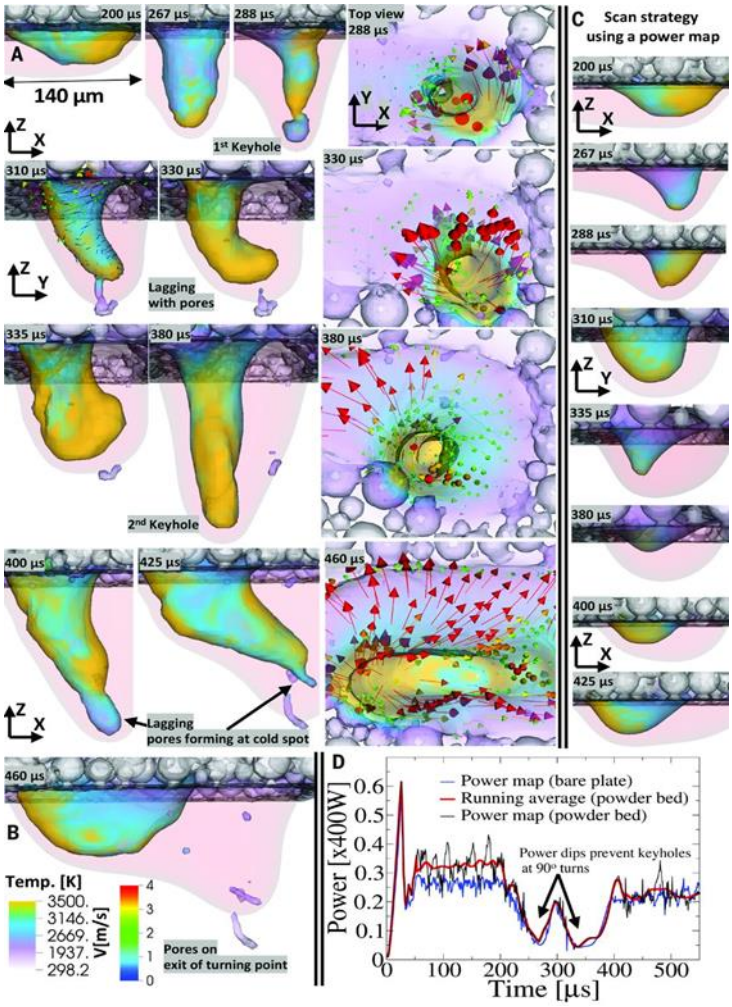

Figure 2-39a) shows a melt pool during a turn in LPBF. Overheating during the turn creates two keyholes, creating porosity. B) shows the pore after the laser has passed the turn. C) Shows how the stability criterion can generate a stable keyhole and eliminate porosity in the turn. D) shows the power modulation that was generated through the stability criterion [78]

Khairallah et al. uses a high fidelity FEA simulation that accounts for most of the advanced physics in LPBF that have been shown to affect the process considerably [78]. Ray tracing analysis provides an accurate account for the variable absorptivity during the process, and temperature dependant material properties are used. The only major factor they do not represent is the free movement of powder particles during the process. This is one of the only studies that uses feed forward control with a high fidelity model. Their study uses a criterion based on the Weber number (ratio of inertial pressure to the surface tension) to prevent spatter forming in the melt pool, in addition to creating a constant melt pool depth based on this ratio. The dimensionless Weber number can be represented as;

$$Weber\ number = \frac{pV^2r}{4\gamma} \qquad \textit{Equation 2-23}$$

Where p is the melt density, V is the melt velocity, r is the beam radius and γ is the surface energy. They defined a critical flow velocity as;

$$V_{critical} = 2\sqrt{\gamma/pr} \qquad \textit{Equation 2-24}$$

Where if the Weber number is > 1 then the melt will produce surface turbulence and liquid droplets, causing spatter. This was developed so that a critical ratio of equation 6.24 gives a criterion for the amount of backscatter produced;

$$\frac{dz}{dt} < \frac{r^2}{w^2 V_{critical}} \qquad \textit{Equation 2-25}$$

Where dz is the melt pool depth and w is the weber number. They then digitally and experimentally verified this by using it to reduce back spatter and also eliminate porosity during a turn (Figure 2-39). Therefore, Khairallah at al. showed that using a stability criterion to set a limit on the laser power can reduce back spatter and stabilise melt pool dynamics.

2.7 Representing LPBF through Computational modelling

The processing of metals in LPBF is a highly complex process, that happens over a wide range of timescales and length scales. As shown in section 2.6.2.2, modelling and simulation will play a critical role in the process optimisation of LPBF, in addition to improving our fundamental knowledge on the process. LPBF is a difficult process to simulate, due to the massive length scale differences (1 µm – 10km) that are found over the course of a single build.

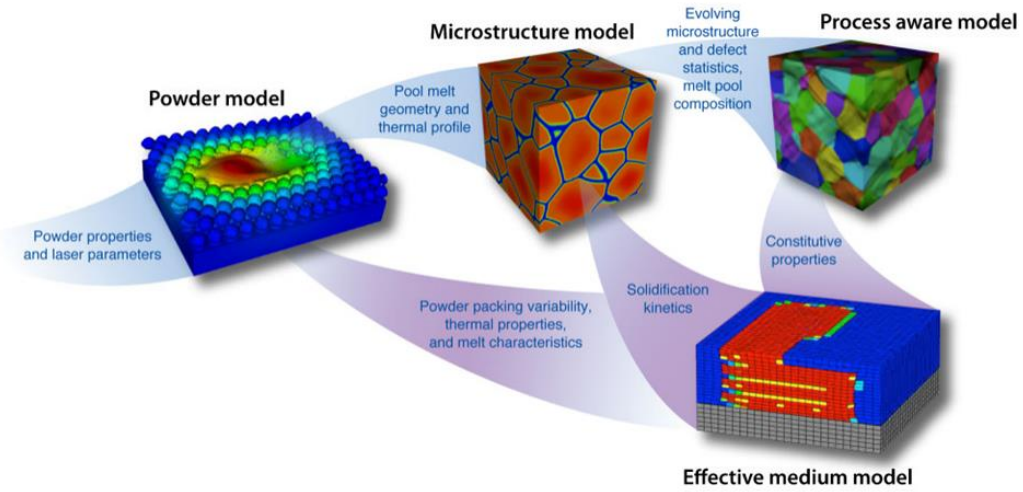

Figure 2-40 shows the multiscale modelling strategy from LLNL for LPBF [43]

Due to computational limitations, current models are split into two categories; meso-scale and macro scale modelling. Meso-scale multi-physics modelling are typically high-fidelity models that encompass most of the physics in the LPBF process. Factors such as; a stochastic powder bed geometry, melting and solidification, buoyancy effects, surface

tension, temperature dependant surface tension (Marangoni flow), vaporisation phenomena including recoil pressure, evaporation flux, melt pool flow, variable absorptivity from the Fresnel equations and the motion of the powder dynamics can all be included in meso-scale modelling. Due to the high velocity flows from both liquid and gas phases, a high resolution mesh is needed, typically in the region of 1 – 4 μm^3 , modelled with very small time steps (1 ns – 0.5 μs). Due to these factors, even running on high performance supercomputers in parallel, simulations can only run over a few mm at most before computational times exceed weeks. For a large number of simulations, running at length scales longer than this is inefficient. However, these models are not designed to model entire layer scans at super high resolution. Figure 2-40 shows how meso scale models can be connected with other types of simulations, so that the entire build process can be captured. Macro scale models in an ideal setting, will use properties such as absorptivity, and scaling factors calculated in high fidelity simulations. This allows the macro scale simulation to simulate entire single layer scans, and even complete components with properties validated from high fidelity meso scale models.

2.7.1 Meso-scale modelling

2.7.1.1 Stochastic powder bed

The initial powder bed configuration has been shown to have a substantial effect on the produced component, in terms of absorptivity, but also melt pool dimensions and defects [52], [163], [164], [230]. Therefore, the geometry of a typical powder bed has to be included in a high-fidelity model. Discrete element method (DEM) simulations can be used to model the powder feedstock [231]–[233]. Open source software such as LIGGGHTS and LAMMPS, and GEODYN-L are DEM models that can be used to model this process [234]. These models can simulate the cohesion, friction, deformation, rolling resistance which are calculated from inter-particle contact interactions. Particles are dropped in a 'rain drop' style, above a bounding box to capture realistic powder bed configuration. Particles can then be spread over a substrate, to approximate the recoating process[233].

He et al. shows how particles can also be simulated by a spreading method [235]. The authors investigate how particle cohesiveness affects particle packing and the variability of the powder bed. Strongly adhesive powders form chain like structures and weakly cohesive powders bind together in large agglomerates. This active area of research faces many challenges, owing to complex spreading behaviours of different powder types. Xiang et al. considers the effect of substrate surface roughness for LPBF, finding powder

layer roughness increasing with increasing surface roughness [236]. They also found correlations with increasing packing density and decreasing recoater speeds.

2.7.1.2 Single track simulations

Due to the computational limitations as explained previously, meso-scale models can only simulate a laser pass for 1 – 2 mm. This limits the modelling efforts to generally 1 – 3 single tracks, but is enough for the laser to enter a steady state mode, where the melt pool dynamics can be studied. LPBF can be described as a laser induced, heat driven fluid flow problem. For this reason, computational fluid dynamics (CFD) is often used to model this process. For this highly non-linear problem, the Navier-Stokes equations for momentum, mass conservation and energy can be solved to represent the physics of the process.

$$\frac{\partial p}{\partial t} + U \cdot \nabla p + p \nabla \cdot U = 0 \qquad \textit{Equation 2-26}$$

$$\frac{\partial (pU)}{\partial t} + \nabla \cdot (pUU) = \nabla \cdot (\mu \nabla U) - \nabla p + S_m \qquad \textit{Equation 2-27}$$

$$\frac{\partial (pT)}{\partial t} + \nabla \cdot (pUT) = \nabla \cdot \left(\frac{k}{C_p} \nabla T \right) + S_T \qquad \textit{Equation 2-28}$$

Where equations 6.26 – 6.28 represent the mass, momentum and energy equations for CFD for LPBF. These equations will be discussed further in chapter 3. Including the specific LPBF physics is done through the source terms S_m and S_T representing the momentum and energy source terms. The momentum source term will include the forces due to melting and solidification, surface tension, Marangoni flow, buoyancy and recoil pressure. The energy source term will include the heat sources from the laser, and negative heat fluxes from evaporation and radiative cooling. To represent the free surface of the melt pool, CFD LPBF models have two phases, metal and argon (from the protective atmosphere in LPBF). This is so that the free surface of the melt pool can be modelled, to give single track morphology. The reconstruction of the interface is commonly achieved by a volume of fluid (VOF) method, where the volume fraction of each phase is tracked inside the computational cell. For a cell containing 100% metal phase, the VOF value would equal 1, and for a cell containing 100% argon, the VOF value would be 0. Then, the interface of the two phases will be between 0 and 1. This is tracked with the continuity equation of volume fraction. Geometry in CFD can either be tracked via Eulerian or Lagrangian particle tracking techniques. Purely Eulerian tracking means that geometry in the CFD will only move, if the temperature is above the melting point, restricted by a Darcy condition in the momentum source term. This doesn't allow particle movement (unless above the melting temperature), or entrainment into the laser beam. Lagrangian tracking however, allows geometry to move at any condition.

This means models that include Lagrangian tracking can model powder entrainment and spatter accurately.

Different research groups use different software and methodologies for meso scale models in LPBF. Zhang and Zhang use commercial AM Eulerian software, Flow3D to model the LPBF process using CFD methods [233]. Tang et al., Yuan et al., Gu and Li and Hozoorbakhsh et al. use ANSYS Fluent Eulerian software with heavily customised user defined functions to model the LPBF process [233], [237]–[239].

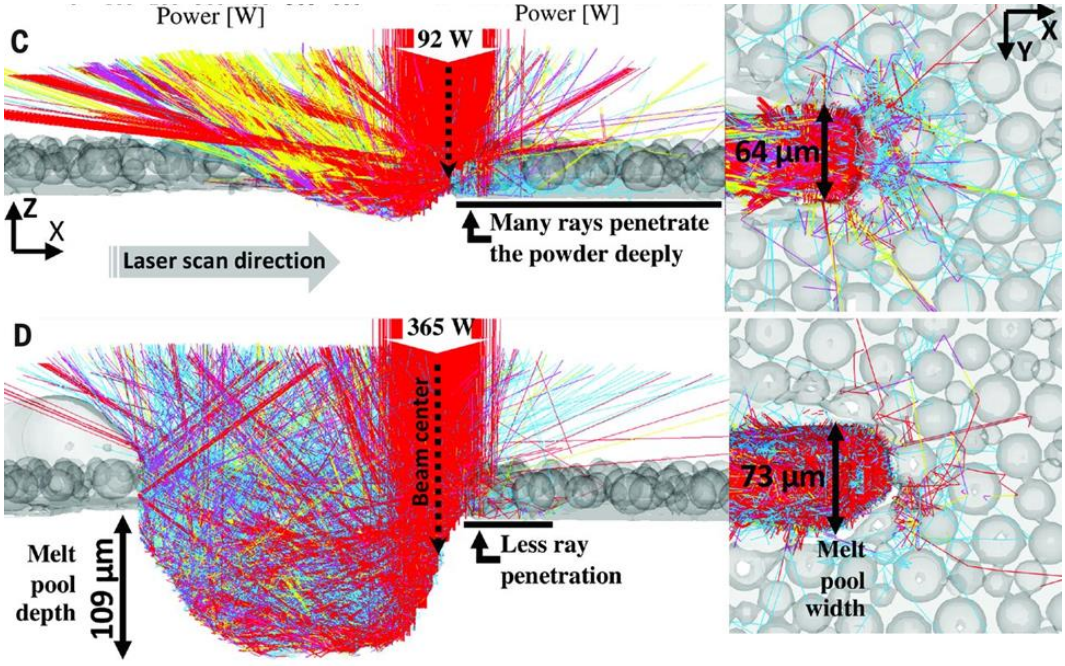

Figure 2-41 shows full laser ray tracing. C) shows laser ray tracing in conduction mode, with the colours representing how many reflections the ray has undergone . D) shows laser ray tracing for a keyhole mode track. This clearly shows the multiple reflections inside the keyhole formed in the cavity [78]

The research from LLNL uses ALE3D software which is a hybrid finite element and finite volume method model, using an arbitrary Lagrangian-Euler methodology. This method uses a uniform cartesian grid as the background mesh, which the geometry of the model is superimposed upon. This method uses operator splitting to model the hydrodynamics and thermal parts separately. The code uses a mixture of Lagrangian motion phase, to model the geometry. In between each timestep this geometry is then passed to a thermal analysis module, where the thermal analysis is calculated. Then the model is transferred back on to the original mesh [78], [86].

The University of Utah uses CFD to resolve melt pool dynamics, but tracks powder particles with a Lagrangian particle tracking technique. This means that unlike CFD LPBF simulations that happen exclusively on a cartesian Eulerian mesh, particles are tracked

throughout the domain much more realistically, without the use of a Darcy condition to restrict movement below a certain temperature[164], [240], [241].

Zakirov et al. uses the lattice Boltzmann method (LBM) to model the electron beam melting process [242]. This method can approximate the Navier-Stokes equations, and can be used for weakly compressible fluid flow problems, such as LPBF/EBPBF. The advantage of this method is that LBM's are fast and can be easily scaled in parallel to run on graphical processing units (GPGPUs). This allows for an order of magnitude faster results compared to CFD processing, with approximately 1 ms of simulation time taken 1 hour. This allows for entire layer processing at extremely high resolution. The downside is that models of this type are extremely complex, and so far, require custom built code to run.

In meso-scale models, the heat source term is crucial in determining the correct melt pool dimensions to correctly represent the fluid flow and thermal conditions. Early and lower computational cost approaches model the heat input as a volumetric heat source[243]. However, this approach has to be tailored for either conduction or keyhole mode against experimental validations, and assumes a constant absorptivity. Khairallah et al. proposed a new surface ray tracing approach, that only considered the rays impact on the melt pool surface without further reflections. This technique is beneficial as it allows for shadowing effects to be modelled, and captures melt pool dynamics with good agreement to experimental validations[86], [233], [238], [244]. However, this method still requires an approximation of a constant absorptivity found from experimental data or theory[39]. Full ray tracing requires more computational power, but allows for the absorptivity to be fully calculated. Full ray tracing gives the most accurate method of providing a heat source to LPBF simulation and modelling[52], [78], [164], [240], [241]. Figure 2-41 shows full laser ray tracing for conduction vs keyhole mode[78].

Table 2-1 Table showing an example of software and numerical methods used in the literature.

Author/Institution	Software	Modelling method	Tracking method
Zhang & Zhang	Flow3D	CFD	Eulerian
Tang et al.	ANSYS Fluent	CFD	Eulerian
LLNL	ALED3D	FEA/Multiphysics	Eulerian
University of Utah	In House	CFD	Lagrangian
Zakirov et al.	In House (FastLab)	LBM	Eulerian

2.7.1.3 Solidification simulation

Meso-scale models are often used for solidification models, for their high representation of the fluid flow and thermal analysis inside a melt pool. Data from these models or experimental data can be exported to cellular automata (CA) or phase field (PF) models[245], like the G and R plots discussed in section 2.5.3. These models can be used to model the grain growth during a LPBF single track. Integration between FEA and CFD models with CA/PF models can give insight into the grain formation strategy in LPBF [185], [233]. Yang et al. published work of the PF modelling integrated into Flow3D AM LPBF software. They were able to track the grain evolution over multiple layers [185].

2.7.2 Macro-scale modelling

Macro scale modelling can be modelled on length scales from single layer scans up to full components builds. Macro scale models tend to model the powder bed and substrate as a continuum, which allows for a much coarser mesh to be used, decreasing the computational workload required. Thermo-mechanical models are often modelled in this space, and are used to calculate residual stress build up within LPBF components. Thermo-mechanical modelling uses a coupling of a transient heat analysis, of which every timestep is interfaced with a mechanical modelling step[169], [246]. Parry et al. used this model to investigate scan strategies for the reduction of residual stress. The transient heat analysis uses the well-known Rosenthal equation, which forms the foundation for most transient heat analysis in LPBF [43], [247], [248].

$$T(x,R) = T_0 + \frac{\lambda P}{2\pi kr} exp\left\{-\frac{v}{2a}(R + (x - Vt))\right\} \qquad \textit{Equation 2-29}$$

Where T_0 is the temperature at a location far from the immediate location, λ is the absorptivity, P is the laser power, k is the thermal conductivity, r is the distance from the heat source, v is the laser velocity, a is the thermal diffusivity, and t is time.

Stump and Plotkowski adapted this equation for extremely fast transient thermal analysis for LPBF. Adapting the integration scheme for the solution in addition to optimising the code for parallel use. Using this adaptive integration technique, the model had a 50x speedup compared to normal analytical methods. In comparison, to simulate a entire layer scan with CFD would take a high performance supercomputer weeks of simulation time, a non-adaptive integration scheme analytical model 23.5 hours, and the adaptive integration scheme just 32.9 minutes on a 4-core laptop. This 50x speed up allows models like this one to be used to simulate entire components with a reasonable amount of detail. Additionally, these models can now feasibly be used as a mid-tier fidelity model for neural network optimisation.

2.8 Shortfalls in the literature

Process parameter optimisation is limited by the intuitive nature of the link between process parameters, the thermal environment and the solidification dynamics. There is a need to connect process parameters directly to the events that happen within the melt pool. Due to the large number of process parameters available, a linking variable needs to found that can help with this disconnect.

LPBF shows itself as a complex thermally driven process, with highly non-linear behaviour that develops transiently as a function of process parameters. It is clear that the physical phenomena happening at a melt pool scale, affects the part consolidation and mechanical properties considerably. The predominant driving force for these defect mechanisms, is the dynamic transfer of energy from the laser beam to the materials surface. Optimising this energy delivery is key to a stable and consistent process, free from defects.

Peak temperature and temperature distribution have been shown to have the largest effect on the melt pool properties. Control of the peak temperature governs the processing mode of LPBF, with the critical tipping point occurring above the boiling temperature of the material. The recoil pressure formed on the surface of the material is essential in creating a stable single track at high speeds, whilst allowing bonding to the previous layer. Control of the surface temperature here is critical, as excessive energy leads to spatter, the formation of keyhole porosity and interactions with the vapour plume.

Traditional parameter optimisation, as shown in section 2.6.1, is material specific, slow and can only optimise a limited number of infinite parameter combinations. Section 2.6.2 shows how the use of computational modelling can simplify this process by adjusting processing parameters based upon sensor inputs, such as temperature. Druzgalski et al. show us that the more physics that are represented in this model, the more accurate the model and therefore the prediction becomes [10]. However, research in this area is limited. Stathatos and Vosniakos show that variable power can be used to keep a constant surface temperature during the process, and Vasileska show that monitoring temperature fields in-situ can provide data to correct laser power based on previous layers [229].

A review of the literature to date shows no work focussed on providing the overall package of temperature optimisation for LPBF. Parts of the puzzle are solved, but lack in some areas. Temperature optimisation is achieved through the modulation of either

laser power or laser speed, but the combination of both is not studied. The temperature optimisation is generated through complicated and difficult to use methods, that do not scale to other forms of computational modelling, or have to be used in partnership with physical sensors during processing. Most of all however, is that none of these studies show a method to calculate what is the optimal surface temperature of LPBF, with a method that can be applied to any material.

Following this review of current literature, the key opportunities are outlined below.

- Models that are created to modify laser process parameters are complicated, difficult to use, and can only be used with that certain model.
- Models still need input from empirical experiments to inform optimal process conditions.
- Whilst methods have been presented in literature that can modify a single laser process parameter (laser power or laser speed), these methods do not inform the community on what the optimal temperature of LPBF should be, to produce defect free components.
- These frameworks do not include work on difficult to use materials, that suffer from not only porosity based defects, but also cracking.

The work of this thesis aims to address these opportunities by building a high fidelity model to simulate the LPBF process. This approach to modelling LPBF has been previously explained in literature. This work will be the combination of state of the art CFD modelling features found in such literature, such as ray tracing and stochastic powder bed modelling. In addition, the model will be used to create a novel temperature controlled inverse solution for parameter optimisation. The model will therefore be highly customisable and not bound by commercial LPBF software limits. The resultant model will showcase the frameworks potential, provide optimal surface temperatures for optimisation and demonstrate this experimentally, with a case study using a high strength aluminium alloy. This work has not been found in literature.

Chapter 3

3 Combined discrete element model with computational fluid dynamics for simulating laser powder bed fusion

3.1 Overview

This chapter will cover the methods used to produce the high fidelity LPBF simulations, in addition to an experimental setup to measure the absorptivity, a critical input value for the model in-situ. This will be used to validate the ray tracing model that will be used in the LPBF simulations. Section 3.2 shows the method for producing the stochastic powder bed geometry used in this study. The stochastic powder bed used in this study is generated once for the particle size distribution used in the experimental validation results, and is only used to provide a starting geometry for the main model. This allows the model to simulate initial conditions, as shown in Figure 2-7. The theory and implementation of the CFD model is then presented in section 3.3. This covers the governing equations and numerical methods used to solve the partial differential equations to simulate fluid flow and thermal transport in the melt pool. Section 3.4 shows how the high performance computing facility (HPC) is used to improve the speed of the LPBF simulation. Section 3.5 covers the thermophysical properties used for the materials in the model. The validation of the model will then be shown in Chapter 4 for 316L stainless steel and AA2024.

This chapter also describes the implementation of a ray tracing heat source, with the absorptivity calculated through the refractive index of the metal. Using the refractive index of the material for the calculation of absorptivity, allows investigation of the development of porosity etc, in addition to measuring absorptivity throughout the single track. This data is crucial in supplying information that is required for the inverse solution for different materials. This also gives a much more realistic representation of absorptivity for difficult materials, such as aluminium.

3.2 Discrete element modelling for a stochastic powder bed

The discrete element method (DEM) was used to model the powder bed particle arrangement stochastically. This was achieved with LIGGGHTS open source software. LIGGGHTS stands for “LAMMPS improved for general granular and granular heat

transfer simulations", where LAMMPS stands for "large scale atomic/molecular massively parallel simulator". Due to its physical and algorithmic basis, LIGGHTS is widely used in molecular dynamics, and is an ideal platform for DEM simulations. The package can account for a large number of particles, and the handling of moving geometries. This makes it ideal for modelling the powder deposition process. In this work, the 'rain drop' method will be used to distribute the particles randomly. To generate the initial powder bed configuration, the particles are dropped form a height into an open topped box. The box has dimensions of 800 x 300 x 100 μm^3 , with the top facing surface removed. The particles are generated from a circular aperture with a diameter of 1000 μm above this box. Particles then fall into the enclosure, and any that fall outside of the box are deleted. Once the powder particles have settled, any particles that have a centre height greater than the layer thickness + its radius, are deleted. This process mimics the recoating process to achieve a specific layer height. The particle dynamics during recoating are not considered in this study. Once the powder layer has been finalised, the coordinates of the particle centres are logged and stored in an array for use in the CFD code. This method has been chosen as it gives a good approximation of the powder bed, and has been used in literature for similar models [1], [244], [249]. Most powder layers used in this study only use powder layers one powder particle thick, simulating low layer thicknesses. For example, using a PSD of 15-45 μm, and a layer thickness of 50 μm, gives a good approximation of the layer thickness.

The particles follow a normal distribution from 15 – 45 μm, which is taken after the particle size distribution (PSD) in Figure 3-1. The script used for the generation of the powder bed in LIGGGHTS is included in Appendix 10.1. This study does not investigate the effects of different powder beds, and therefore this powder model is used for all simulations in this study. All experimental validations use this PSD.

Particles translation and rotations are defined by Newton's second law of motion for translation (Equation 7.1) and rotation (Equation 7.2)[250];

$$m_i \ddot{x}_i = m_i g + \sum_j F_{ij} \qquad \textit{Equation 3-1}$$

$$I_i \ddot{\theta} = \sum_i (r_{ij} \times F_{ij}) \qquad \textit{Equation 3-2}$$

Where m_i is the mass of the particle i, $\ddot{x}_i$ is the acceleration of the particle i, g is the force due to gravity, F_{ij} is the force acting on the particle i, from particle j. I_i is the moment of inertia of particle i, due to the angular acceleration $\ddot{\theta}$. $\sum_i (r_{ij} \times F_{ij})$ is the total rotational force acting on particle i. For the inter-particle interactions a Hertzian contact force model is used[251];

$$F_{hz} = \sqrt{\delta}\sqrt{\frac{R_i R_j}{R_i + R_j}}\left[\left(k_n \delta n_{ij} - m_{eff}\gamma_n v_n\right) - \left(k_t \Delta s_t + m_{eff}\gamma_t v_t\right)\right] \qquad \textit{Equation 3-3}$$

Where R_i and R_j are the radii of the particles i and j, δ is the distance of the overlap between the two particles, k is the elastic constant, γ is the viscoelastic damping constant, n_{ij} is the unit vector along the line connecting the centres of the two particles, where indices n and t refer to the normal and tangential components and m_{eff} is the effective mass of the two particles.

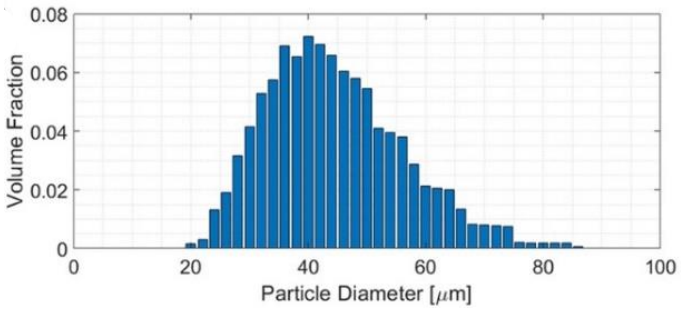

Figure 3-1 shows the particle size distribution which was adopted into the DEM model. Here, a PSD of 15 – 45 μm is adopted for the PSD of the model, after the measured distribution of powder from the experimental study.

3.3 Computational fluid dynamics for a high fidelity meso-scale model of LPBF

Computational fluid dynamics (CFD) are used to model the LPBF process. As shown in section 2.7.1.2, CFD is an ideal method for representing the fluid flow and heat transfer in the melt pool[43]. The model processes complex physical phenomena such as: melting and solidification, buoyancy effects, surface tension, temperature dependant surface tension (Marangoni flow), vaporisation phenomena including recoil pressure and evaporation flux, melt pool flow and variable absorptivity from the Fresnel equations. This section will cover the numerical methods needed to model the LPBF process through CFD in ANSYS Fluent 2021 R1.

The model works off the following assumptions concerning the fluid flow and heat transfer inside the melt pool:

- The fluid in the melt pool is Newtonian and laminar.
- The thermophysical properties of the materials used in this work are a function of temperature only.
- The plasma effect (attenuation and particle formation) is ignored.

- Powder particles below the melting temperature cannot move, due to an imposed Darcy condition, therefore powder entrainment is not captured within the model.

These assumptions are based from literature that have defined this process of modelling LPBF [233], [244]. The methodology of using these assumptions have not been altered during this work.

3.3.1 Basic fluid flow

To solve the liquid metal hydrodynamics inside the melt pool, three phases are needed; solid, liquid and gas. This allows the modelling of the free surface of the melt pool. The gas phase allows for the liquid-gas interface to deform, instead of being fixed at the computational domain boundaries. The basic governing equations of this process are defined by the following continuum equations of the conservation of mass, momentum and energy [252]:

$$\frac{\partial p}{\partial} + U \cdot \nabla p + p\nabla \cdot U = 0 \qquad \textit{Equation 3-4}$$

$$\frac{\partial (pU)}{\partial t} + \nabla \cdot (pUU) = \nabla \cdot (\mu \nabla U) - \nabla p + S_m \qquad \textit{Equation 3-5}$$

$$\frac{\partial (pT)}{\partial t} + \nabla \cdot (pUT) = \nabla \cdot \left(\frac{k}{C_p} \nabla T\right) + S_T \qquad \textit{Equation 3-6}$$

Where p is the fluid density, U is the velocity vector, t is time, p is the pressure, μ is the dynamic viscosity, C_p is the specific heat capacity, T is temperature and k is the thermal conductivity. S_m and S_T are source term equations for the momentum and energy equations. These will be discussed in sections 3.3.1.1 and 3.3.4.

3.3.1.1 Momentum equation

The S_m source term includes additional formula such as the effects from buoyancy, melting and solidification, surface tension and the recoil pressure from vaporisation.

$$S_m = S_b + S_d U + S_{sf} + S_{rp} \qquad \textit{Equation 3-7}$$

Where S_b is the source term due to the buoyancy effect of temperature dependant density:

$$S_b = pg\hat{e}_y \beta (T - T_{ref}) \qquad \textit{Equation 3-8}$$

Where g is the force due to gravity, $\hat{e}_y$ is a unit vector, and β is the thermal expansion coefficient. S_d represents the term for melting and solidification. This condition allows for one fluid phase to represent both solid and liquid metal. The term S_d acts as a momentum sink, so that the velocity field is forced to zero if the temperature is less than

the solidus temperature. This stops the solid phase from moving, to represent solidification and melting in the CFD code [252].

$$S_d = \frac{C(1-f_l)}{f_l^3 + e_0} \quad \textit{Equation 3-9}$$

Where C is a constant (with a value of 1e6), f_l is the fraction of liquid in a cell, and e_0 is a constant (1e-9) to stop division by zero when the liquid fraction is zero and the material is solid. S_{sf} and S_{rp} terms for the surface tension and recoil pressure will be discussed further in section 3.3.1.1.1.

3.3.1.1.1 Surface forces

The momentum source terms S_{sf} and S_{rp} represent the surface tension and the recoil pressure. Both of these forces are the main driving force for the melt pool flow in LPBF. Surface tension forces are temperature dependant, and are further sub divided into tangential and normal components. These forces are represented as smeared volume forces, that act on the interface cells between the gas and metal phase[253]. These cells have a volume fraction between 0 and 1.

Surface forces (f) need to be transformed into volumetric surface forces (F_s) for the momentum source term. They are transformed by the normalised volume fraction gradient ($|\nabla\alpha_1|$). Where α_1 is the volume fraction of the metal phase[233].

$$F_s = f_s|\nabla\alpha_1| \quad \textit{Equation 3-10}$$

The surface tension can be divided into a normal and tangential component. The normal component is a function of the surface tension and the curvature of the surface. The tangential component is formed by the surface tension gradient otherwise known as the Marangoni flow.

$$f_s = f_{sf,n} + f_{sf,t} = \sigma\kappa\vec{n} + \nabla_t\sigma \quad \textit{Equation 3-11}$$

Where κ is the curvature, $\vec{n}$ is the surface normal vector, and ∇_t is the tangential gradient operator. The curvature κ and $\vec{n}$ are defined as:

$$\kappa = -(\nabla\cdot\vec{n}) \quad \textit{Equation 3-12}$$

Where $\vec{n}$ is defined as:

$$\vec{n} = \frac{\alpha_1}{|\alpha_1|} \quad \textit{Equation 3-13}$$

The tangential ($\nabla_t\sigma$) component of the surface tension can be expressed as:

$$\nabla_t\sigma = \frac{d\sigma}{dT}[\nabla T - \vec{n}(\vec{n}\cdot\nabla T)] \quad \textit{Equation 3-14}$$

Where $\frac{d\sigma}{dT}$ is the surface tension gradient and ∇T is the temperature gradient.

Due to the density difference between the two phases, (8000:1, steel:argon) problematic shear forces develop in the flow, causing spurious currents (high velocities) a common problem in volume of fluid (VOF) modelling. Due to the CFL (Courant-Friedrich-Levy) stability criterion, this forces very small timesteps for the simulation, significantly slowing down the calculation. Brackbill et al. introduces a multiplier term that redistributes the smeared forces towards the heavy phase. This method has been shown to reduce the spurious current build up for VOF models[90], [253]. Therefore the surface tension force source term S_{sf}, can be written as:

$$S_{sf} = \left[\sigma\kappa\vec{n} + \frac{d\sigma}{dT}[\nabla T - \vec{n}(\vec{n}\cdot\nabla T)]\right]|\nabla\alpha_1|\frac{2\rho}{(\rho_1+\rho_2)} \qquad \textit{Equation 3-15}$$

The source term due to the recoil pressure S_{rp} can be defined as:

$$S_{rp} = 0.54 p_0 exp\left[\frac{L_{vap}M(T-T_b)}{RTT_b}\right]\vec{n}|\nabla\alpha_1|\frac{2\rho}{(\rho_1+\rho_2)} \qquad \textit{Equation 3-16}$$

Where 0.54 represents the pressure which is taken away due to the vapour leaving the surface, p_0 is the atmospheric pressure, L_{vap} is the latent heat due to vaporisation, M is the molar mass, T is the temperature, T_b is the boiling temperature and R is the universal gas constant. This formula uses this simplified formula from Anisimov, which is used in other LPBF models [244], [254].

3.3.2 Multiphase flows

As mentioned in section 3.3.1, to model the free surface of the melt pool, a second gas phase has to be modelled in addition to the metal phase. The main challenge associated with this, is the modelling of the interface between the two phases. There are three types of approaches to predict the interface between the phases: interface tracking, interface fitting and interface capturing. In this work, the method of interface capturing will be used, achieved with the volume of fluid (VOF) method. The VOF method solves the continuity equation for volume fraction. For this, a volume fraction variable is introduced, where the volume fraction is 1 in the metal phase (the primary phase) and the volume fraction is 0 in the gas phase (the secondary phase). At the interface between the two, shown in Figure 3-2, the volume fraction is between 0 and 1. The fields for all the variables are shared between the phases. Thus the variables are either representative of either pure metal, pure gas, or a mixture of the two. The volume fraction of the metal phase satisfies the volume fraction equation[252]:

$$\frac{\partial(\bar{\rho}\alpha_1)}{\partial t} + \nabla\cdot(\bar{\rho}\vec{u}\alpha_1) = 0 \qquad \textit{Equation 3-17}$$

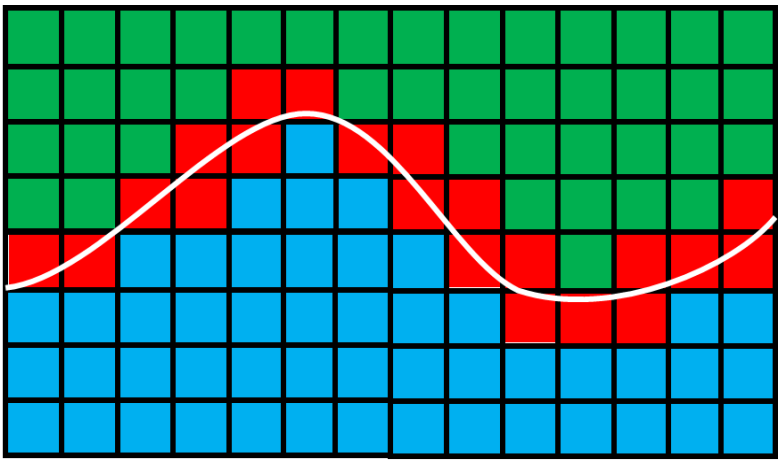

Figure 3-2 shows the interface capturing method used in the VOF scheme, to model the free surface. Blue cells show the metal volume fraction of 1, the green cells show a volume fraction for the gas phase which equals 0, and then red cells are the interface cells, which are between 0 and 1.

Where $\vec{u}$ is the flow velocity, t is time, $\bar{\rho}$ is the volume averaged density and α_1 is the volume fraction of the metal phase. Any material property of the mixture (Φ) can be computed through the calculation of the volume fraction equation. For example, the density is calculated by;

$$\overline{\Phi} = \alpha_1 \Phi_1 + (1 - \alpha_1)\Phi_2 \qquad \textit{Equation 3-18}$$

The geometric reconstruction scheme is the numerical method used to model the interface. This approach uses a piecewise-linear approach, as used by Liu et al. [1]. This scheme is the most accurate representation of the fluids surface. It assumes that the interface between each fluid has a linear slope within each cell representing the free surface. Due to the reconstruction scheme being used to represent the interface, the volume fraction equation is solved explicitly, while the mass, momentum and energy equations are solved implicitly.

3.3.3 Solidification and melting model

The movement of the metal phase when it is solid, is stopped through the Darcy condition, which creates a momentum sink in the momentum source term (Section 3.3.1.1). In addition to this, the enthalpy and porosity model is used to simulate melting and solidification. The melting and solidification model also includes the ability to model alloys. An additional liquid fraction (f_l) variable is applied which has a value of either 0 (for solid) or 1 (for liquid) or between 0 and 1 for when the material is between its solidus and liquidus temperatures. This model can be described as:

$$H = h_{ref} \int_{T_{ref}}^{T} C_p dT + f_l L \qquad \textit{Equation 3-19}$$

Where h_{ref} is the reference enthalpy, T_{ref} is the reference temperature, C_p is the heat capacity and L is the latent heat of melting. The reference temper is set to 300 K. The liquid fraction (f_l) is defined as:

$$f_l = \begin{cases} 0 & if\ T \leq T_{solidus} \\ \frac{T - T_{solidus}}{T_{liquidus} - T_{solidus}} & if\ T_{solidus} < T < T_{liquidus} \\ 1 & if\ T \geq T_{liquidus} \end{cases}$$ *Equation 3-20*

By this method the solidification and melting is included in the model[252].

3.3.3.1 Boundary conditions

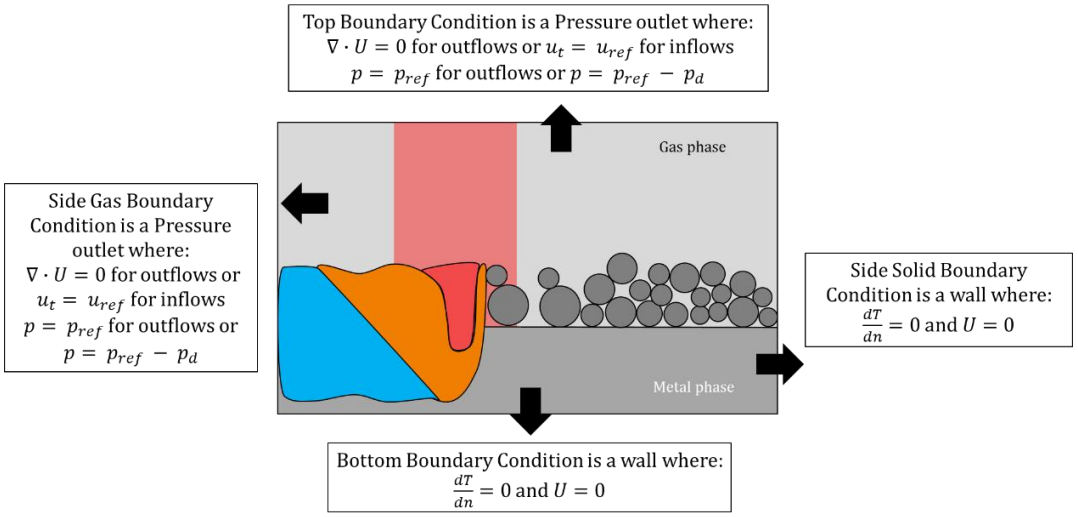

Figure 3-3 shows the boundary conditions for LPBF model. The model has two boundary conditions. One is the metal boundary condition (side solid boundary and bottom boundary condition). These are modelled as 'Wall' boundary conditions within fluent where the zero normal derivative is used. The other is the pressure outlet boundary condition, which is applied to any boundary that is argon. These are the top boundary condition and the side gas boundary condition.

Figure 3-3 shows the boundary conditions for the LPBF model. The solid boundaries of the model are the zero normal derivative, and are considered as continuative. These are given as the boundary condition 'Wall' type in ANSYS Fluent. The gas phase top and four sides, fixes the pressure and sets the gradient of velocity to zero. These are modelled as 'Pressure Outlets' in ANSYS Fluent.

3.3.3.2 Meshing

For the LPBF simulation, a 3D domain is used, as seen in Figure 3-4. The mesh used in this work is a structured cartesian grid of hexahedral cells, all with a cell length of 3 µm. Sensitivity studies have been performed in literature show that a cell size from 2.5 µm^3 to 4 µm^3 is acceptable for a sufficient resolution of the melt pool simulation[86], [233], [239], [244]. A value of 3 µm x 3 µm x 3 µm was chosen for a blend of accuracy and speed after Tang et al [244]. Each cell is the same size in the domain. The dimensions of each domain will vary slightly in each chapter, but will based on a nominal size of 1000 x 340

x 300 μm^3, with 2 – 4 million cells in the domain. The mesh was generated in ANSYS Meshing, through ANSYS Workbench on version 2020R2.

The mesh was produced with a Cartesian grid, as cells need to have maximum quality (A skewness of 0) for the best representation of the free surface. The melt pool geometry during the domain will also be highly changeable from the initial powder bed configuration. For these two reasons, the initial powder geometry is patched into the cartesian grid, rather than a conformal mesh being generated around the particles. In order to represent a smooth surface for the powder particles, the patching process also splits up the cartesian cell, into smaller cells. The patching user defined function first splits the 3 µm x 3 µm x 3 µm cell into 125 smaller cells. Then, the code checks to see whether each point is inside the radius of a powder particle. By splitting the cell, the cell can be given a volume fraction between 0.008 and 1, increasing the resolution of the curvature further than using the whole cell. This approach is used from literature works by Tang et al. [244]. The complete patching code is shown in Appendix 10.2.

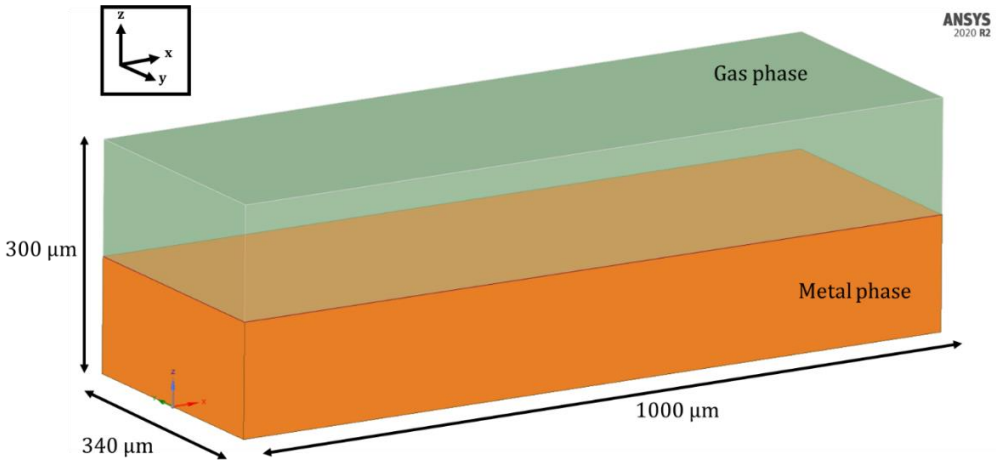

Figure 3-4 showing a typical domain for the LPBF model. The metal phase is highlighted in orange, whilst the gas phase is highlighted in green. The convention used throughout this thesis is shown in the top left.

3.3.4 Modelling of the heat source

Section 2.3.5 highlights the importance of being able to properly model the heat source. As the literature shows, the absorptivity is a crucial factor to determining the processing mode the laser will operate in, detecting the different defect generation modes, in addition to affecting the power input from the laser by as much as 50%. Additionally, use of high thermal conductivity materials such as aluminium, show a high sensitivity to laser power, and therefore absorptivity. This sensitivity must be captured if the LPBF process is to be correctly simulated, and worthwhile conclusions made with a high fidelity feed forward model. Literature also shows that this accuracy comes down to the method in which the heat source is modelled[86].

In this work, the absorptivity will be calculated through the Fresnel equations, and therefore the heat source will be modelled with full ray tracing. This will allow the most accurate representation of the heat source, able to distinguish between conduction and keyhole mode. Not having to assume the absorptivity also means that the modelling of variable power can be done accurately. This is also especially relevant for the high sensitivity materials such as aluminium. Experimental validation will be used to compare the ray tracing model to experimentally generated values, with the fabrication of a laser micro calorimetry (LMC) system. The primary function of the LMC in this work is to provide a platform to deposit single tracks onto a small removable substrate that can be easily sectioned to measure melt pool dimensions. Conflicting information from the refractive index of aluminium and the measured absorptivity puts a question as to the actual absorptivity of aluminium. In this work the refractive index will be tailored to melt pool dimensions only. The secondary function of the LMC is to measure experimentally what the absorptivity of the aluminium powder is. The experimental setup for the LMC, will be explained in section 3.6.

The ray tracing in the LPBF model takes advantage of ANSYS Fluent's discrete particle method (DPM), to simulate the ray tracing. The DPM model within ANSYS Fluent uses a Euler-Lagrange approach to track the DPM particle through the domain. The Lagrangian method of particle tracking uses a Lagrange frame of motion rather than a Eulerian one. A Lagrangian method tracks the individual particle through space and time, rather than in a Eulerian approach, where the field is represented as a function of position and time. A popular analogy to describe these two methods, uses the example of a car passing by a tree on the side of the road. For a Eulerian approach, the observer would be standing by the tree, watching the car go by. For this observer, the car is considered in a static frame of reference, where the origin is the tree, and the car is travelling along the x axis (the road) with a certain velocity in the positive direction. For a Lagrangian frame of reference however, the observer is in the car driving. Her origin is the car itself, and the world around her is moving. When she drives past the tree, the tree is the object moving in a negative direction in the x axis along the road. This is the frame of reference of the DPM particle. This allows a particle to be tracked through the domain in between each timestep, the location calculated quickly and simply, without being referenced by the static mesh. ANSYS Fluent tracks this particle from the following formula[252]:

$$m_p \frac{d\vec{u}_p}{dt} = m_p \frac{\vec{u} - \vec{u}_p}{\tau_r} + m_p \frac{\vec{g}(\rho_p - \rho)}{\rho_p} + \vec{F} \qquad \textit{Equation 3-21}$$

Where m_p is the particle mass, $\vec{u}$ is the fluid phase velocity, $\vec{u}_p$ is the particle velocity, ρ is the fluid density, ρ_p is the density of the particle, $\vec{F}$ is an addition force and $m_p \frac{\vec{u}-\vec{u}_p}{\tau_r}$ is the drag force.

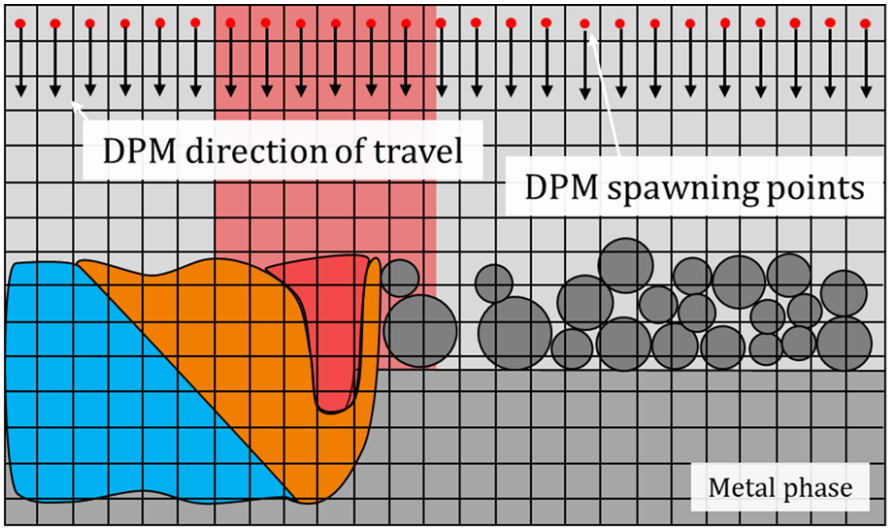

Figure 3-5 shows a schematic of the spawning locations and direction of travel of the initial DPM step. Grey regions in the image represent powder at ambient temperature, blue regions represent previously melted powder, orange shows melted powder, and the red region represents the keyhole cavity. .

The DPM particles for the ray tracing will not interact with the fluid, their only job is to deliver an energy to the surface of the powder particles, reflect off that surface, and repeat, until the particle exits the domain, or the energy falls to below 1% of its original value. Therefore the DPM body and drag forces are made equal to zero, and just the particle motion is tracked. The DPM particles start in an initial position at the top of the domain, where they are spawned in the centre of each cell. Between each timestep, the DPM particles are fired in a negative z direction towards the meltpool, with a portion of the overall laser energy. The DPM particles movement and delivery of energy to the melt pool, is carried out in a pre-timestep action that does not happen during melt pool movement. The DPM particles are fired, energy positions and values stored, before the solution continues to calculate fluid motion. The motion of the DPM particles is carried out in discrete time steps which are separate to the main flow in the model. This energy is a function of the X and Y position in the beam. This is shown in Figure 3-5. Note here the discretisation of the domain into cells is not to scale. After the initial ejection of the particles, only the particles inside the laser beam area are allowed to continue travelling. This reduces the computational burden of tracking particles unnecessarily, as only particles inside the beam diameter will transfer energy. A custom UDF (DPM_SCALAR_UPDATE) is executed at every DPM particle timestep to check whether the particle has come into contact with a cell with a solid volume fraction > 0 (or argon

volume < 1). The full custom code for this is attached in section 10.2.1. Once a DPM particle comes into contact with a metal cell, it will impart a portion of its energy to the cell, and have a new velocity calculated, based upon its incident direction. The initial energy (Q_{init}) of the DPM particle is first calculated in W/m^2 from the following equation:

$$Q_{init} = \frac{2P}{\pi r^2}\exp\left(-2\frac{(x-vt-x_0)^2+(y-y_0)^2}{r^2}\right) \quad \textit{Equation 3-22}$$

Where P is the laser power, r is the beam radius, v is the laser speed, x and y are the coordinates, and x_0 and y_0 are the initial positions of the laser centre. Once this DPM particle reaches a cell that has a metal volume fraction, a portion of energy is transferred (Ab), with the absorptivity based upon the materials refractive index, and the incident angle[29]:

$$Ab_s = 1 - \left|\frac{cos\,\theta - (n^2 - sin^2\theta)^{1/2}}{cos\,\theta + (n^2 - sin^2\theta)^{1/2}}\right|^2 \quad \textit{Equation 3-23}$$

$$Ab_p = 1 - \left|\frac{n^2 cos\,\theta - (n^2 - sin^2\theta)^{1/2}}{n^2\,cos\,\theta + (n^2 - sin^2\theta)^{1/2}}\right|^2 \quad \textit{Equation 3-24}$$

$$Ab = 0.5Ab_s + 0.5Ab_p \quad \textit{Equation 3-25}$$

Where Ab_s and Ab_p are the absorptivity of the S and P polarisations of the electromagnetic wave respectively, and Ab is the absorptivity calculated from the average of the S and P polarisations. n is the complex refractive index and θ is the incident particle's angle to the surface normal. Once the absorptivity has been calculated, the initial DPM particle's energy is multiplied by the absorptivity and stored in a user defined memory location. This value is then subtracted off the DPM particles total energy. The particle is then given a new velocity from:

$$\vec{R} = \vec{I} + 2(-\vec{I}\cdot\vec{N})\vec{N} \quad \textit{Equation 3-26}$$

Where $\vec{R}$ is the unit vector of the reflected DPM particle, $\vec{I}$ is the unit vector of the incident DPM particle, and $\vec{N}$ is the unit normal vector of the surface. At each reflection event, the amount of energy given to the cell is accumulated, so that once all reflections have finished, the total energy in each cell is given by:

$$Q_{end} = \sum Q_{init}\,Ab \quad \textit{Equation 3-27}$$

Q_{end} gives the irradiance at each cell location that has been designated by the ray tracing program. This information is then passed to a DEFINE_SOURCE function, that adds this information to the energy source term. Before this step however, the irradiance in W/m^2 needs to be converted to W/m^3. This is done by:

$$Q_{laser} = \frac{Q_{end}A}{V} \quad \textit{Equation 3-28}$$

Where A is the area of the surface in the cell, and V is the volume of the cell. By this means the heat source is calculated.

3.3.4.1 Energy equation

The energy equation, similar to the momentum equations, requires a source term to represent the energy from the laser, and the energy lost through radiative and evaporative cooling. The energy equation as described in section 3.3.1, is shown again for convenience:

$$\frac{\partial(pT)}{\partial t} + \nabla \cdot (pUT) = \nabla \cdot \left(\frac{k}{C_p}\nabla T\right) + S_T \quad \textit{Equation 3-29}$$

Where S_T can be further defined as:

$$S_T = Q_{laser} + |\nabla\alpha_1|\frac{2\overline{\rho C_p}}{\rho_1 C_{p1} + \rho_2 C_{p2}}(Q_{rad} + Q_{evap} + Q_{melt}) \quad \textit{Equation 3-30}$$

Where Q_{rad} is the heat loss due to radiative cooling and can be defined as:

$$Q_{rad} = -\sigma\varepsilon(T^4 - T^4) \quad \textit{Equation 3-31}$$

Where σ is the Stefan-Boltzmann constant and ε is the emissivity of the metal. Q_{evap} is the heat loss due to evaporation, and is defined as:

$$Q_{evap} = -0.82\frac{L_{vap}M}{\sqrt{2\pi MRT}}P_0 exp\left(\frac{L_{vap}M(T - T_b)}{RTT_b}\right) \quad \textit{Equation 3-32}$$

Where L_{vap} is the latent heat of vaporisation, M is the molar mass, R is the universal gas constant and T_b is the boiling temperature. Q_{melt} is the enthalpy change due to melting, and is given by:

$$Q_{melt} = -\alpha_1\rho_1 L_{melt}\left(\frac{\partial\gamma}{\partial T} + \vec{u}\cdot\nabla\gamma\right) + \nabla\cdot(\bar{k}\nabla T) \quad \textit{Equation 3-33}$$

Where L_{melt} is the latent heat of melting. Q_{rad} , Q_{evap} and Q_{melt} are then multiplied by $|\nabla\alpha_1|\frac{2\overline{\rho C_p}}{\rho_1 C_{p1} + \rho_2 C_{p2}}$ in equation 7.30 to transform the heat loss from W/m^2 into W/m^3, in addition to redistributing the heat source towards the metal phase.

The thermal gradients (G) and solidification speeds (R) were calculated from,

$$G = |\nabla T| \quad \textit{Equation 3-34}$$

and,

$$R = v\frac{|\nabla T_x|}{G} \qquad \textit{Equation 3-35}$$

respectively. Where v is the laser velocity, and $|\nabla T_x|$ is the normalised x component of the temperature gradient.

3.3.5 Solver theory

ANSYS Fluent solves the equations using the PISO (pressure-implicit with splitting of operators) pressure-velocity coupling method. The energy and velocity fields are discretised with a second order upwind scheme, and the pressure field was discretised with the 'PRESTO!' (Pressure-staggering option) scheme. The transient calculation was solved with a first order implicit computation. The under relaxation factors for the solution were 0.5 for pressure, 1 for density, 1 for body forces, 0.4 for momentum, 0.9 for liquid fraction, 1 for the energy, and 0.5 for the DPM sources.

The timestep was set to variable time stepping, so that the solutions satisfy the CFL (Courant- Friedrichs-Levy) condition < 1. The CFL condition (C) is expressed as:

$$C = \frac{u\Delta t}{\Delta x} \qquad \textit{Equation 3-36}$$

Where t is the timestep and u is the velocity. This ensures that scalar quantities do not pass through more than one cell volume in one timestep, enhancing the stability of the solution. The timestep range is from 9 ns to 0.5 μs, and changes so that C < 1 is satisfied.

3.3.6 Implementation within ANSYS Fluent 2021R1

In order to implement the complex physics and source terms described in the previous sections, custom user defined functions (UDFs) are written, to integrate with the ANSYS Fluent CFD code. Each UDF is a function that ANSYS Fluent calls at a predetermined time in the solution. In this work, DEFINE macros are used to implement the ray tracing, momentum and energy source terms, allocation of volume fraction and temperature gradients and the patching of the powder bed. Figure 3-6 shows the order of operations for the pressure-based solver, including the order of execution of the UDFs. First, the solution is initialised, with the DEFINE_INIT called to patch the domain with the powder particle initial locations. Next the solution is started, with the DEFINE_ADJUST called, that allocates variables such as the volume and temperature gradients to user defined memory (UDM). Next the mass and momentum equations are solved, in addition to the source terms that are included in a DEFINE_SOURCE. The energy equation is solved next, with the energy source terms also included in a DEFINE_SOURCE. The loop then checks convergence and then closes, moving onto the next timestep if the solution has

converged. Between each loop, the DPM particles are called. Here, a DPM_SCALAR_UPDATE is called every DPM time step. It is here that the ray tracing calculations are performed. An example of each UDF is included in section 10.2.

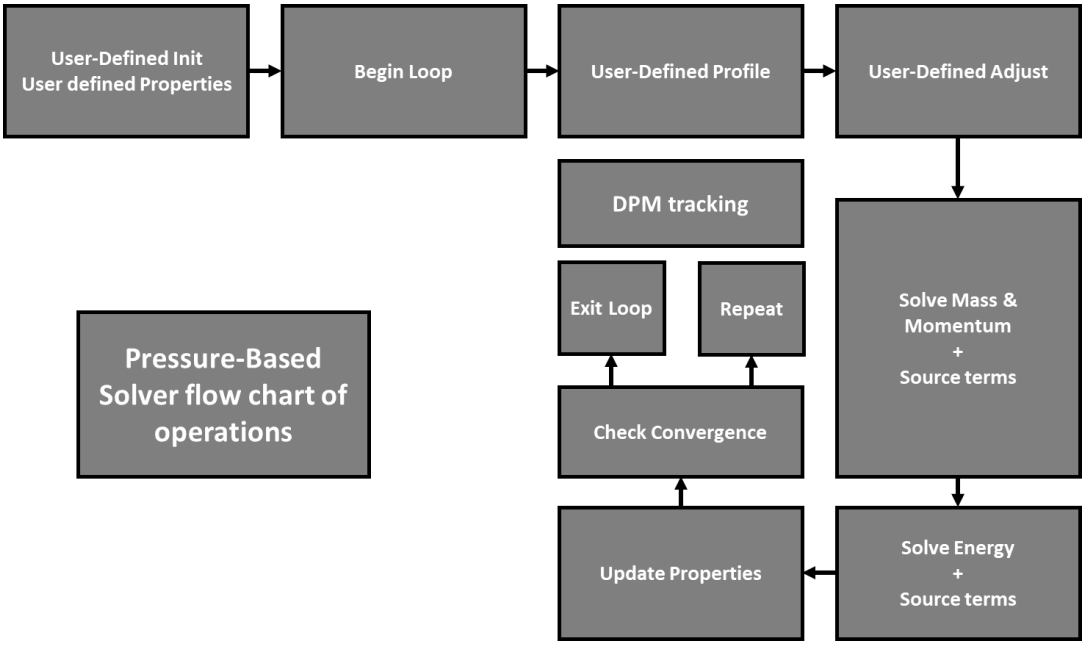

Figure 3-6 shows a flowchart of the pressure-based solver order of operations

3.4 High performance computing (HPC)

The typical timestep used for the calculation of the solution is 3e-8 s. With a typical high performance laptop with four processing cores, one timestep would take approximately 5 mins. Simulating a 500 μm long single track at 0.5 m/s would take 1 ms of flow time, equating to 33,333 timesteps. On a high performance laptop with 4 cores, this would take 2,777 hours or 115 days to complete. Due to this fact, the high performance computing (HPC) (Augusta) at Nottingham was used to reduce the calculation time. The HPC facility at the University of Nottingham (UoN) has 4,720 cores, 31 TB of RAM, 6 GPGPUs and 750 TB of storage. The facility has 100 standard nodes each with 2 x 20 Intel Xeon Gold 6138 20C 2.0GHz processors and 192 Gb of RAM each.

ANSYS recommends for maximum performance in parallel, using 10 – 15k cells per core for maximum efficiency. To run at near maximum efficiency (2 -3 seconds per timestep) for the largest domain size (4 million cells), will use 280 cores, or 7 nodes. Using a larger amount than this reduces the codes performance, as the transfer of information from one node (a cluster of cores) to another negatively impacts the performance. Running the code in parallel on 10 – 15k cells per core, can reduce the 5 mins per timestep to 2 seconds. For the same use case, this would reduce the time taken to run the model to 18.5 hours for an equivalent of 1 ms of real time. These prohibitive timescales make

simulating entire layers impractical. However, the wealth of information captured during a run cannot be replicated by experimental means, and can be done without incurring expensive equipment costs.

To run the code in parallel, the UDFs had to be customised to allow for information to be shared across all nodes. When running in serial mode, the core executing the simulation has access to every single cell and variable in the domain. When running in parallel, the domain is split into partitions, each partition given a computer core that calculates the values in this partition. However, this means that certain cores cannot access information from another partition without explicit permission. These permissions have to be written into the UDF code, to ensure that the code works as intended, and runs quickly. Any maximums, minimums, summations in the code have to collect information from every partition, not just the information from the current partition. These additions are shown in the code in Appendix 10.2.

3.5 Thermophysical material properties

In order to represent the LPBF process accurately, the materials properties must be as close to reality as possible. All material parameters are a function of temperature. Temperature dependant properties for every material are difficult to acquire, and the methods used to obtain some properties can be affected by elements such as oxygen significantly. This paper predominantly focuses on the modelling of AA2024, a 2000 series aluminium alloy. Properties for AA2024 have been adapted slightly from the temperature dependant properties of pure aluminium [43], [86], [244]. Limited information exists for the temperature dependant properties of AA2024. Therefore the properties of pure aluminium will be used with two modifications. The liquidus and solidus temperatures for AA2024 will be used for the temperature dependence across the mushy zone. This is shown in Figure 3-7. Pure aluminium, while theoretically melting instantaneously at a single temperature, is modelled with a small mushy zone (solidus and liquid over 10 K), so that a sharp change in properties from liquid to solid does not make the model unstable. The second change is the absorptivity, which will be discussed more in section 4. The properties for 316L stainless steel are taken from Tang et al. [244] and the properties for aluminium are taken from Gheribi and Chartrand, and Leitner et al. [255], [256] respectively. These are shown in Table 3-1.

Table 3-1 showing the thermophysical properties for the 316L stainless steel, AA2024 and aluminium.

Property	Unit	Symbol	316L stainless steel	AA2024	Aluminium
Solidus temperature	K	T_s	1658	775	923
Liquidus temperature	K	T_l	1723	911	933
Boiling temperature	K	T_b	3086	2743	2743
Latent heat of melting	$m^2\ s^{-2}$	L_{melt}	270000	399925	399925
Latent heat of vaporisation	$m^2\ s^{-2}$	L_{vap}	7.45e6	9.46e6	9.46e6
Viscosity	$Kg\ m^{-1}\ s^{-1}$	μ	1.3e-3	1.3e-3	1.3e-3
Surface tension	$kg\ s^{-2}$	σ	1.6	0.84	0.84
Temperature coefficient of surface tension	$Kg\ s^{-2}K^{-1}$	$\frac{d\sigma}{dT}$	8e-4	0.35e-3	0.35e-3
Molar mass	$Kg\ mol^{-1}$	M	55.93	26.98	26.98
Refractive index	n/a	n	3.02 + 5.05I	2.8 + 7.8I	2.8 + 7.8I
Universal gas constant	$Kg\ m^2\ s^{-2}\ K^{-1}\ mol^{-1}$	R	8.314		
Stefan-Boltzmann constant	$Kg\ s^{-3}\ k^{-4}$	σ_s	5.67e-8		
Emissivity	n/a	ε	0.26		

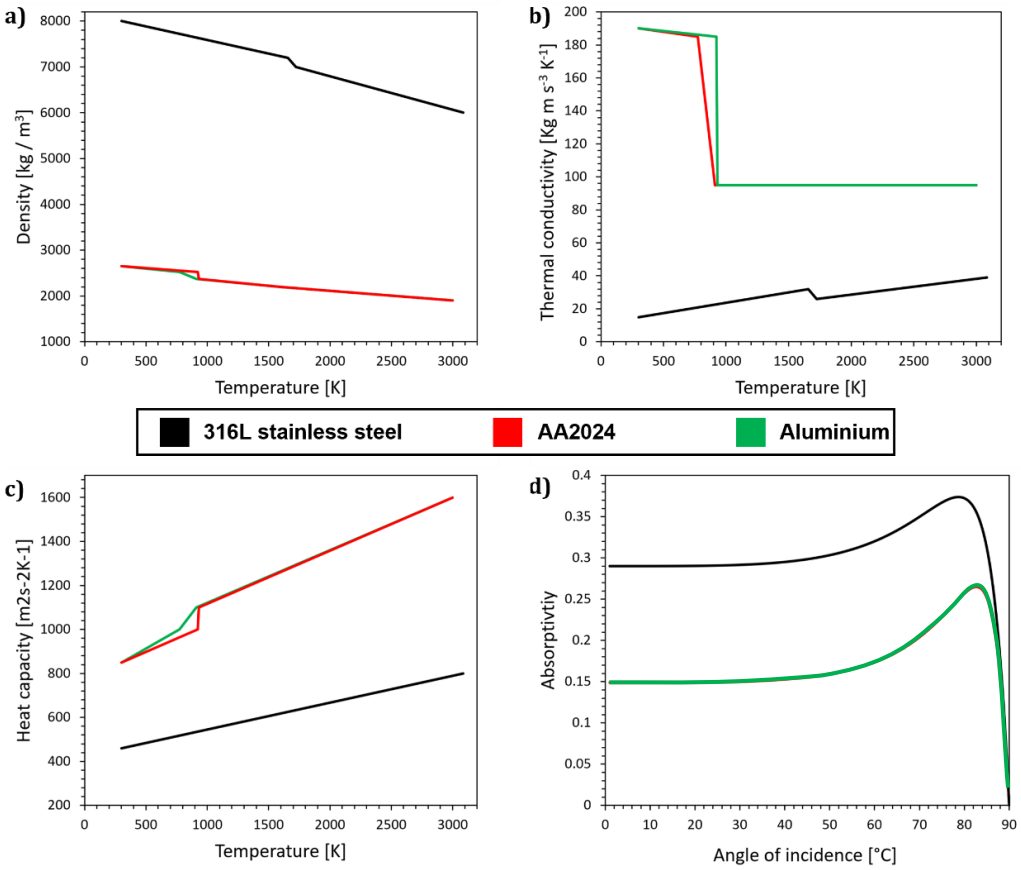

Figure 3-7 shows the temperature dependant properties for density (a), thermal conductivity (b), Heat capacity (c), and the dependence on the angle of incidence for the absorptivity from the refractive index (d). Properties taken from [244], [255], [256]

3.6 Laser micro calorimetry (LMC)

3.6.1 Overview

For the experimental validation studies, single tracks will be deposited onto small discs mounted onto a laser micro calorimetry system (LMC). This system allows for single tracks to be deposited onto a replaceable substrate that can be easily sectioned for analysis of melt pool dimensions.

The LMC can also be used to measure absorptivity. Trapp et al. showed how a calorimetry system can be used to calculate the absorptivity for LPBF in-situ [39]. In this work, an adapted version of this method can be used to calculate absorptivity, with some improvements made to the systems ergonomics. To measure the absorptivity in process, the method uses a disc of material, fabricated from the same material as the metal powder to be tested. The test relies on a temperature measurement from underneath the disc, with a high time resolution to capture the heating and cooling of the disc. The original method uses two spot welded thermocouples attached to the underside of the disc for the temperature measurement. The main difference in the experimental setup

introduced here, is that a pyrometer is used instead of the thermocouples. This allows for a non-contact method of temperature measurement, reducing the thermal losses from the disc, in addition to reducing the time taken to test each disc.

The method uses a low conductivity polymer (Formlabs clear resin, RS-F2-GPCL-04) for the disc holder, which has been designed to minimise the thermal losses from the disc. The fixture was designed so that it secures the disc with a very small contact area, (1 mm^2) and allows for the pyrometer to be kept at a 50 mm working distance from the disc (Figure 3-8). The fixture was 3D printed with a Formlabs stereolithography (SLA) printer, with a layer thickness of 50 µm. The fixture is bolted to a steel baseplate, manufactured with a 250 x 250 mm area, so it fits inside the Renishaw AM400 and AM250 machines. The baseplate was initially laser scanned with the Renishaw AM250 to show the centre position, so that the fixture could be aligned perfectly with the centre of the baseplate. When installing the baseplate into the machine, there are also additional spacers, so that the centre of the disc aligns with 0,0 in the machine software. This is crucial so that the single tracks can be placed precisely on the disc. A small piece of foil is placed on the back of the LMC so that excess powder from the hopper does not blow onto the lens of the pyrometer during use.

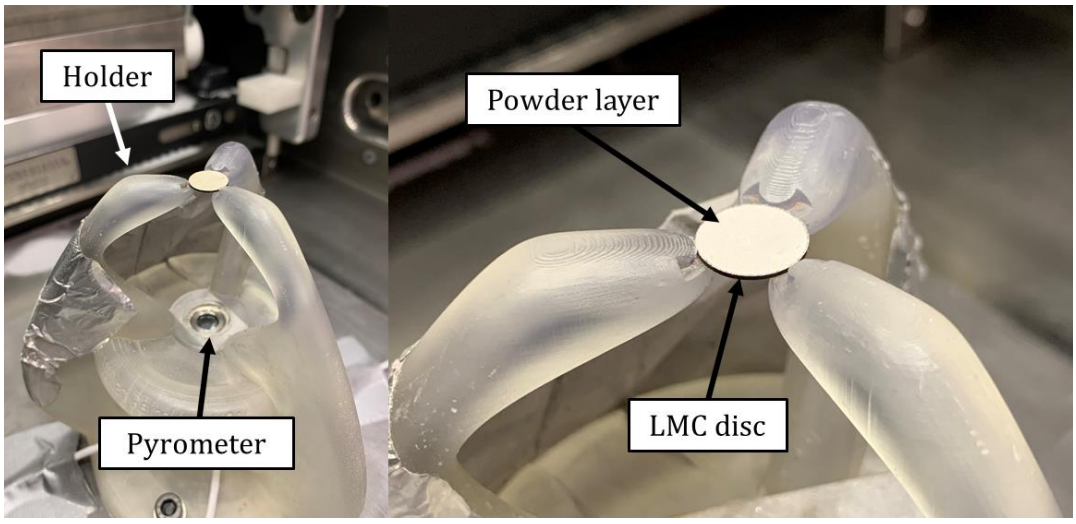

Figure 3-8 shows the LMC setup, inside the Renishaw AM400 machine with the key constituents labelled. The design is easily adapted for other systems and can be integrated with other instruments as necessary.

The disc has dimensions of 10 mm across the diameter, 0.5 mm thick, that has a recess machined with a radius of 9.6 mm into the top surface. This is machined on a milling machine, with the depth of the recess equalling the layer thickness, which was 50 or 100 µm in this work. The disc is ideally made from the same material as the powder, so that the post-processing software only needs to use the same material parameters for both powder and disc.

The pyrometer is a Micro-Epsilon CT-CF22 with a working distance of 50 mm, correlating to its minimum spot size of 2.3 mm. The temperature is measured as an average over this spot. The pyrometer measures at a sampling rate of 50 ms, and is directed at the middle of the underside of the disc. The pyrometer works most accurately when the emissivity of the material is closest to 1 (black body radiation). Due to the fact most materials measured on the LMC are metallic, they have a low emissivity (0.2 for aluminium). Therefore the underside of the disc is spray painted in a high temperature spray paint, so that the emissivity of the disc is increased to 1. A calibration of the pyrometer at this emissivity was conducted by putting the entire system in a furnace, and setting the temperature to 50 °C. This was sufficient in determining the correct emissivity allocation for the setup, by checking the temperature reading of the pyrometer was also 50 °C.

The LPBF machines used in this study were a Renishaw AM400 and AM250. Both these machines use a pulsed Yb-fibre laser with a wavelength of 1070 nm. The Renishaw AM400 has a spot size of 70 µm while the AM250 has a spot size of 75 µm. The maximum laser power for the AM400 is 400 W and 200 W for the AM250. Each machine has an identical build platform in X and Y, with dimensions of 250 x 250 mm.

3.6.2 LMC working calculations

The complete method to calculating the absorptivity from the calorimeter is described below. Using the setup as described previously, a 6 mm long single track is deposited onto the powder layer as shown in Figure 3-8. The temperature of the disc is recorded throughout this deposition, with a typical result displayed by the black line in Figure 3-9a. A post-processing script executed in MATLAB, then takes the data, and fits a curve to the temperature profile from 5 s, to 120 s after the laser has fired. This fitted line represents a least-squares fit to the function:

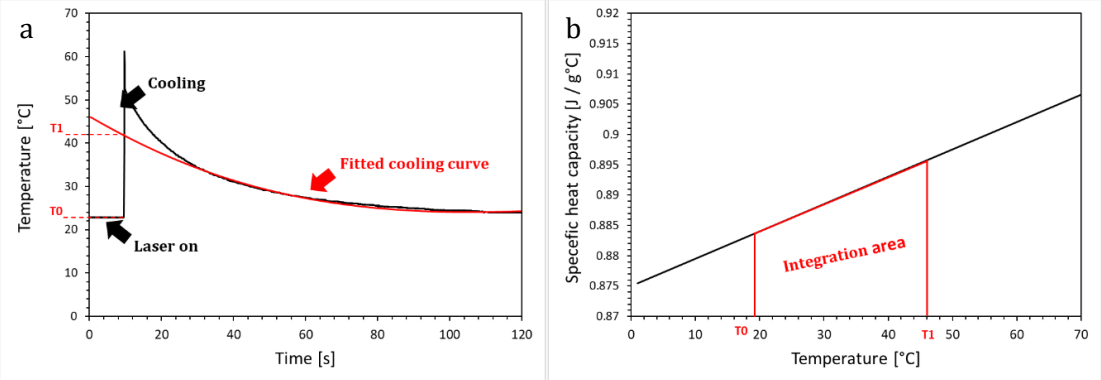

Figure 3-9a shows the temperature trace captured by the pyrometer, with the fitted cooling curve. b) shows the temperature dependant heat capacity, with the integration area shown for the points T0 and T1.

$$T(t) = T_1 exp\left(\frac{-t}{t_{\frac{1}{2}}}\right) + T_0$$ *Equation 3-37*

The script then takes two points from this data, T_0 and T_1, (also shown in Figure 3-9) where T_1 is the point where the fitted cooling curve crosses the initial temperature increase from the laser. T_0 is the initial temperature before the laser is fired. The absorptivity is then calculated from:

$$Ab = \frac{E_m}{E_{in}} = \frac{\int_{T_0}^{T_1} mC_p(T)dT}{l/vP}$$ *Equation 3-38*

Where E_m / E_{in} is the is the energy measured divided by the energy supplied by the laser. m is the mass of the disc, l is the scan track length, v is the laser velocity, and P is the laser power. The integral term, is the integration of the temperature dependant heat capacity (C_p) from T_1 to T_0. The temperature dependence of the heat capacity is given by:

$$C_p(T) = C_{p0}(1 + \alpha T)$$ *Equation 3-39*

Where C_{p0} is the heat capacity at 0 °C, and α is the temperature coefficient of the heat capacity. The MATLAB script used to calculate these formulas is shown in Appendix 10.3.

Chapter 4

4 Evaluation of Model Performance

4.1 Introduction

The high fidelity model to reproduce LPBF has been shown in Chapter 3. This chapter focuses on the validation of this model to experimental results. This is to ensure that the results from the model can be used with confidence in Chapter 5 and 6. The validation chapter will contain validation results for two types of materials, aluminium alloy 2024 which will be used within Chapter 6 and 316L stainless steel which will be used in Chapter 5. This chapter will be split into two main sections, split into material types.

1. The first section uses a generic continuous wave laser validation to experimental results. This is to demonstrate that the model is capable of representing the LPBF process with a 'typical' laser system used in LPBF. The simulation results will be compared using measured single track melt pool depths and widths. This is an accepted form of validation as outlined in previous literature works [1], [43], [244]. 316L stainless steel will be used as the powder and substrate material, due to the abundance of temperature dependant material properties available. These properties are critical in representing LPBF. Additionally, this section will look at validating this process under non typical conditions, using a variable laser power. This section is important, as Chapter 5 will cover the inverse solution, which uses variable laser power to moderate surface temperature.
2. The second section looks at the model validation of aluminium in LPBF. Aluminium is a difficult material to simulate through computational modelling, as its absorption properties measured empirically do not match with the theoretical values. Section 2.3.5.5 discusses the reasons for this in more detail. Past literature shows that this can be overcome by using a constant value for absorptivity based upon trial and error varying of the absorptivity compared to empirical results. However, this approach, as discussed in Section 2.6.2.2.1 and Section 2.7.1.2, does not provide accurate simulation results, and does not result in a high fidelity model. A different approach must be used to calibrate the absorptivity to empirical values. Simulation literature shows that the primary method for calibration a model to simulate LPBF, is to adjust the absorptivity value so that the melt pool dimensions for both simulation and experiment match. In this work, a different approach is used, that rather than adjusting absorptivity to be used with a volumetric or ray tracing

without reflections heat source, the refractive index is adjusted instead. This gives significant advantages over adjusting the bulk absorptivity value. The main advantage this is the accurate representation of keyhole dynamics inside the keyhole. Ray tracing without reflections, or volumetric heat sources do not capture keyhole dynamics, as most of these dynamics are driven from secondary reflections from the keyhole wall [154]. This enables models with full ray tracing to capture the mechanisms of keyhole porosity. Ray tracing also allows for the live measurement of absorptivity throughout a single track deposition.

This section encompasses two novel sets of results. The first is using a high fidelity model to simulate non typical laser conditions such as a Ramp Up laser profile. Literature does not show simulation results that are verified to variable laser power conditions. The second is the modification of the refractive index of aluminium to increase the absorptivity, and the benefits of changing the refractive index, rather than the absorptivity directly. This also has not been shown in literature to date.

4.2 Methodology

4.2.1 Continuous and variable pulsed 316L stainless steel validation

The experimental validation for the continuous wave and variable laser power was performed at Politecnico di Milano in Italy under the instruction of the author. This facility was used as they have access to a LPBF machine that is custom built and adaptable to different laser sources and optical chains, that can produce variable laser pulses at high frequencies. The laser source is manufactured by nLight, with a 1 kW maximum power at 1080 nm. The $1/e^2$ diameter of the laser beam is 78 μm, with a modulation frequency of ≤ 100 kHz with a response time of 5 μs (rise and fall times). The system uses a Smart Move SH30G-XY2 scanner, and a Powderful powder bed. This machine always operates in 'continuous' mode, i.e. the spot size of the laser always traverses the powder bed surface at a constant speed, even though the power is modulated. This in comparison to the Renishaw machines at the University of Nottingham, where the laser is stationary at each pulse. Modulation is achieved through adjusting the laser power value from the source. The distance between modulation events is given by the peak distance.

The single tracks were deposited onto a 316L stainless steel build plate. To show the variable nature of the ramp up profile, XZ longitudinal cross sections are taken of the empirical single tracks. To ensure that the tracks were polished to the middle of the track, two holes were drilled 50 μm off centre of the middle of the track at the start and

finish positions. The wire from precision wire electrical discharge machining (EDM), is then threaded through the two holes, ensuring the track is cut down the middle. Then, the final 50 μm is polished back to reveal the middle of the track. This prevents the microstructure being affected by the cutting process. The section is then imaged with a Hitachi TM3030 SEM, in addition to electron backscatter detection (EBSD) to reveal the grain orientations and structure.

The model validation uses the same laser parameters as the experimental version. The methodology for the model is explained in depth in Section 3.3. The domain size for the simulation is 520 x 260 x 500 μm, with a 3 μm^3 cell size. The simulated track length is 300 μm. The layer thickness for both experiment and simulation are 50 μm, with a PSD of 15 – 45 μm. The initial temperature in the domain is set to 300 K.

Three experimental studies are used to validate the model for 316L stainless steel. High energy density single tracks are achieved with the single track depositions at POLIMI, with an additional lower energy density single track operating exclusively in conduction mode. This was chosen as chapter 5 uses some laser powers that are between 20 and 65 W. The conduction mode track will be validated against results from Yadroitsev et al. [257]. Yadroitsev et al. uses a single mode continuous wave Ytterbium fibre laser operating at 1075 nm, with a 35 μm radius spot size. The single track used was deposited at 50 W with a laser velocity of 0.28 m/s. For the conduction mode validation, the models parameters mirror those by Yadroitsev et al.. The modelling for the high energy density single tracks, have parameters that mirror the conditions of POLIMI.

4.2.1.1 Laser parameters for continuous and variable laser power

Table 4-1 shows the laser parameters for both the experiment and model.

*Table 4-1 shows the laser parameters for both continuous and variable (Ramp up) laser profiles. * Average laser power is the average laser profile over the length of the track.*

Type	Av laser power * [W]	Peak laser power [W]	Base laser power [W]	Peak distance [μm]	Laser velocity [m / s]	Beam diameter [μm]	Wave frequency [kHz]
Continuous	200	200	200	0	0.3	78	n.a.
Ramp Up	200	300	100	150	0.3	78	2
Yadroitsev et al.	50	50	50	0	0.28	70	n.a.

Figure 4-1 shows the laser profiles graphically.

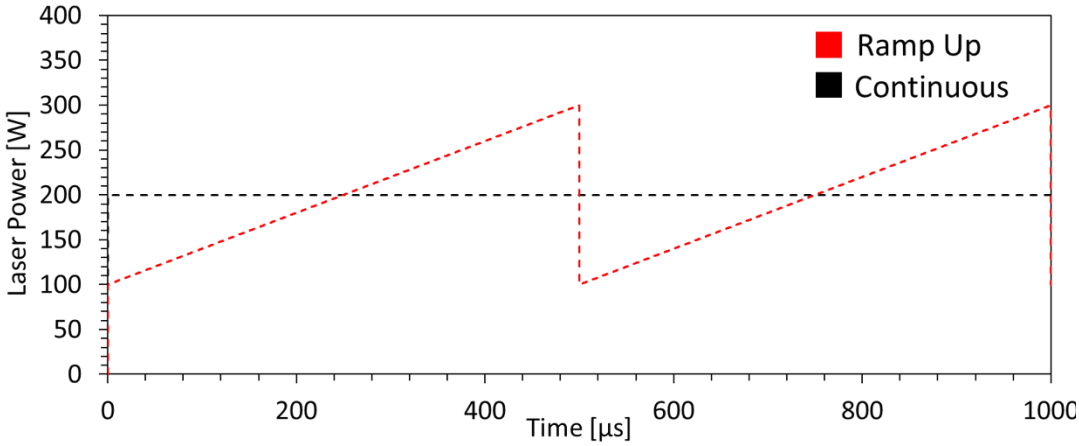

Figure 4-1 shows the laser profile for the continuous and variable (Ramp up) profiles.

4.2.2 Aluminium validation

The experimental validation for the aluminium was completed at the University of Nottingham. The LPBF machine used a Renishaw AM400 for the experimental work, the details of which are covered in Section 3.6. This machine operates in 'pulsed' mode, whereby the spot size of the laser always traverses the powder bed at discrete points. The laser delivers energy for a duration of time equalling to the exposure time at a fixed location. Upon completion of this exposure, a delay time of 20 µs (minimum 20 µs) separates the next exposure time. This distance separating subsequent exposures is given by the point distance. This difference is explained graphically in Figure 4-2. For the aluminium validation results, two parameter sets, PD15 and PD60 are used. These two parameters sets are used in chapter 6, and so serve as a direct validation. The reasons for the these two parameter sets are also detailed in chapter 6.2.

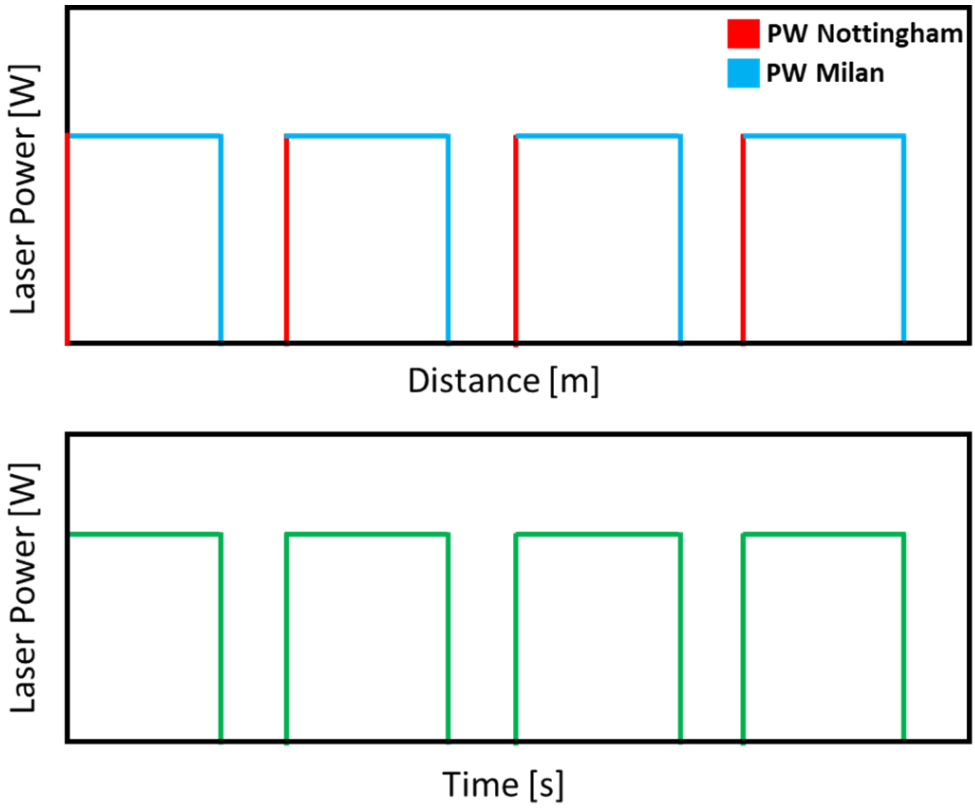

Figure 4-2 shows the difference between the two different representation of a pulsed laser. The first image shows laser power vs distance for both the PW laser in Milan (Blue) and the PW laser in Nottingham (Red). The second image shows laser power vs time for both PW lasers. With respect to time, both lasers have exactly the same laser on and off times throughout the track length (Green). However, with respect to distance, they both differ. The PW laser in Nottingham, acts in stationary spots during its laser pulse, whereas the PW in Milan constantly moves, applying its power over its point distance.

The LMC methodology is explained in Section 3.6. In the validation experiments for aluminium, AA2024 aluminium alloy is used for the disc material. A total of 6 single tracks are deposited onto the 10 mm diameter, 0.5 mm thick disc. The scan tracks are 6 mm in length and 0.4 mm apart, with each disc weighing approximately 0.1 g. The powder used for the experiments is pure AA2024 from TLS Technik GmbH & Co, and the layer thickness is 50 µm to match the model. The validation was repeated three times on separate discs made from wrought AA2024. The error bars are representative of the standard deviation between each repeat.

The disc was then sectioned, mounted and polished to examine the YZ cross section of the disc. The Z direction is in the positive build direction, and the tracks are deposited in a single line in the X direction. The polished sample was then imaged with a Hitachi TM3030 SEM.

4.2.2.1 Laser parameters for the aluminium validation

Table 4-2 shows the laser parameters for both the experiment and the model. The following parameters were chosen to provide a direct validation of the experimental results in Chapter 6. The justification for these parameters are also provided in Chapter 6.

The parameter sets for both PD15 and PD60 are outlined in Table 4-2. The relative velocity of PD15 is 0.107 m/s and 0.423 m/s for PD60. The effective speed for the pulsed laser is calculated through Equation 4-1.

$$\frac{point\ distance}{exposure\ time + delay\ time} \qquad \textit{Equation 4-1}$$

Table 4-2 shows the laser input parameters for the aluminium validation.

Type	Laser Power [W]	Point distance [μm]	Exposure time [μs]	Delay time [μs]	Effective velocity [m / s]	Beam diameter [μm]
PD15	200	15	120	20	0.107	75
PD60	200	60	120	20	0.428	75

The model validation uses the same laser parameters as the experimental version. The methodology for the model is explained in depth in Section 3.3. The domain size for the simulation is 800 x 340 x 300 μm, with a 3 μm^3 cell size. The simulated track length is 600 μm. The layer thickness for both experiment and simulation are 50 μm, with a PSD of 15 – 45 μm. The initial temperature in the domain is set to 300 K.

4.2.2.2 Modification of the refractive index

The literature refractive index of aluminium is 1.36 + 10.43i, giving an absorptivity of 4.76 % at 1080 nm at an incident angle of 0 ° [258]. The use of this refractive index in the high fidelity model, for PD60, produces a melt pool depth of 3 μm. This is compared to an experimental melt pool depth measurement of 40.47 μm. This discrepancy has been reported in literature and is detailed in Section 2.3.5.5. In this work, for the first time, the refractive index is artificially increased to 2.8 + 7.8i, giving an absorptivity of 15 % at 1080 nm at an incident angle of 0 °. The increase to 15 % from 4.76 % is calculated from the experimental absorptivity of a flat plate of aluminium from Bergstrom et al. [28]. The increase is due to aluminium oxide on the surface of the metal, and the rough surface, increasing the effective absorptivity. Figure 4-3 shows both of the refractive index's, with absorptivity plotted as a function of incident angle.

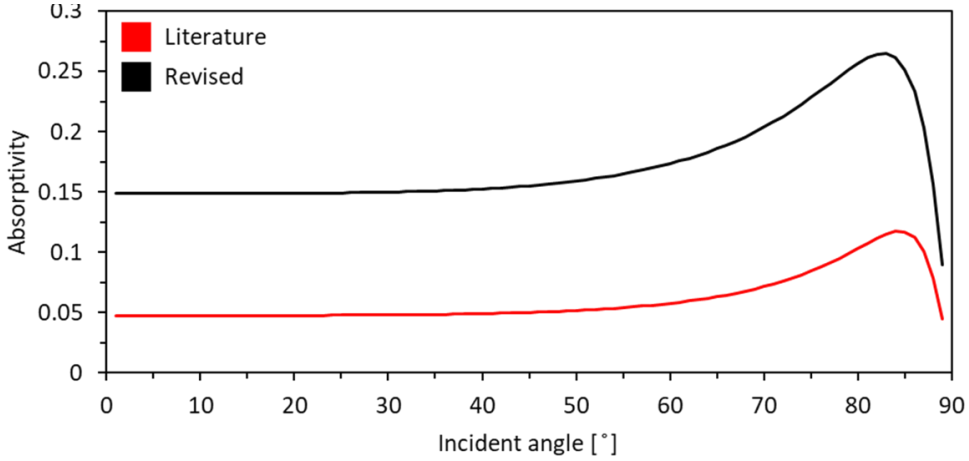

Figure 4-3 shows the literature value and the revised value of the refractive index. The plot shows how the absorptivity changes depending on the angle of incidence of the incoming photon.

4.3 Results

4.3.1 316L Stainless Steel validation results

Table 4-3 shows the overview of the validation results for 316L stainless steel. The validation results focus on the melt pool width and melt pool depth, and the associated error between the experimental and simulation results. Figure 4-4 shows both experimental and simulation results for the 200 W CW validation study. The image shows a 15 µm difference between the melt pool depth, with an 8.1 % error for the simulation result. The melt pool width however, has only a 7 µm difference, resulting in a 3.8 % error. The two images are aligned so that the top of the substrate is the same height on both images. This is true for all the validation comparison images.

Table 4-3 shows the validation results for 316L stainless steel. Shown is the three validation cases, along with the respective melt pool widths and depths for both the model and the experimental single track. Errors presented are the percentage error between measured experimental measurements (of which 3 different measurements were taken in 3 different locations) and measurements from the model results. The melt pool depth and width value for the Ramp Up single track, are taken from the second peak.

Type	Model melt pool width [µm]	Experimental melt pool width [µm]	Error [%]	Model melt pool depth [µm]	Experimental melt pool depth [µm]	Error [%]
Continuous	191	184	3.8	170	185	8.1
Ramp Up	171	178	3.9	241	243	0.8
Yadroitsev et al.	95	91 ± 6	4.3	20 ± 2	22	9

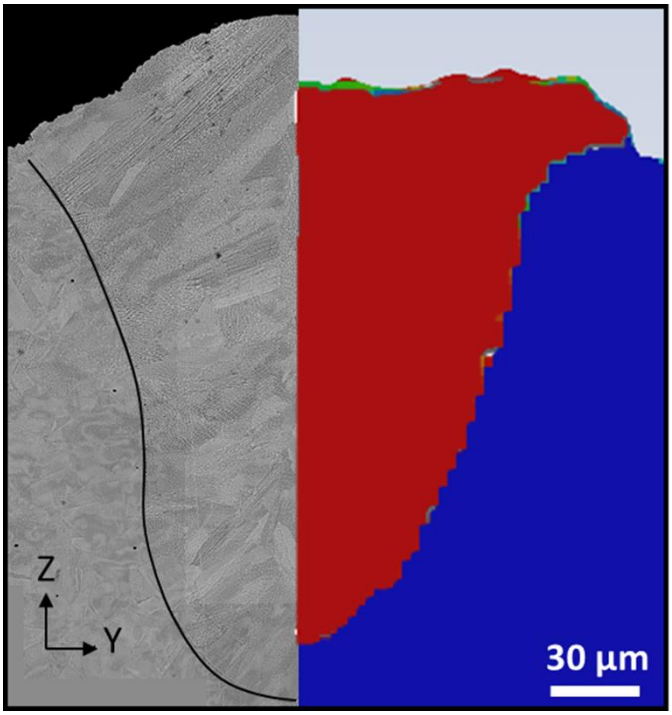

Figure 4-4 shows the validation for the 316L stainless steel 200 W CW single track with a laser velocity of 0.3 m/s. The left portion of the image, is an SEM image of the YZ cross section of the experimental track. The black line denotes the melt pool boundary. The right portion of the image represents the simulation result. Here, the red region represents the material that has melted during the process, mimicking the melt pool. The images are aligned so the substrate is the same height in both images at the same scale.

Figure 4-6 shows the XZ cross section comparison of the experiment and simulation. In this image, the solid black line denotes the melt pool boundary. Figure 4-5 shows the melt pool boundary, which has been enhanced with a black outline in subsequent images.

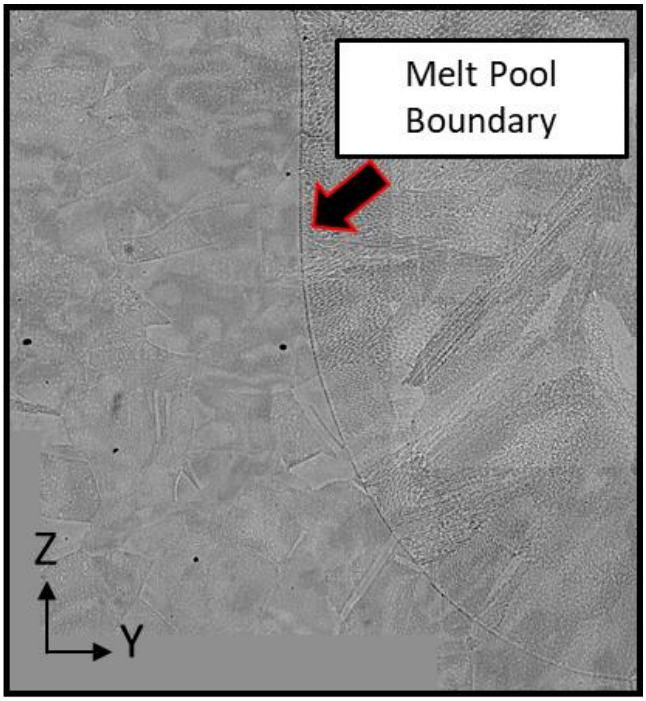

Figure 4-5 shows the melt pool boundary line

The image also compares the melt pool depth of the YZ cross section, to that of the XZ cross section for the experimental and simulation cases respectively. It can be seen that the black dotted line representing the YZ melt pool depth is between 10 – 15 μm deeper than the XZ cross section suggests for the beginning of the CW single track deposition. The red dotted line represents the deepest YZ melt pool depth for the simulation, which is within ± 5 μm of the deepest sections of the longitudinal XZ cross section of the experiment single track deposition. The potential reasons for this will be discussed in Section 4.4.1.

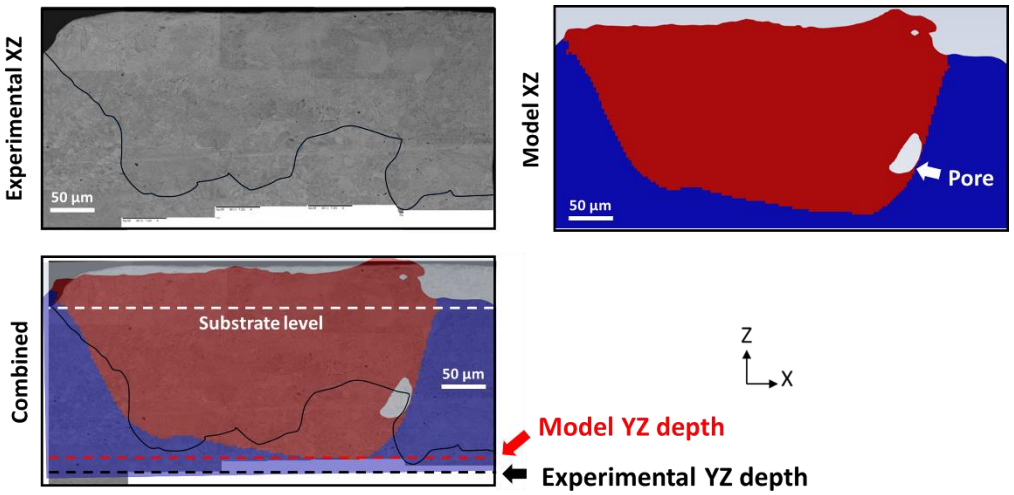

Figure 4-6 shows the longitudinal XZ cross section of both the experiment and the model for 316L stainless steel. Both XZ cross sections are cut in the middle of the track. Top left of the image shows the longitudinal XZ cross section of the experimental single track. Here, the undulating black line represents the melt pool boundary. The top right image shows the simulation melt pool boundary, with the red region representing the amount of material that has been melted during the simulation. Marked at the end of the CW track is a pore. The bottom image shows the experimental XZ cross section with the simulation result overlayed. The white dotted line represents the substrate level, with the red line denoting the model XY depth, as shown in Figure 4-4, and the black line showing where the XY melt pool depth for the experimental track lies. The images are aligned so the substrate is the same height in all three images at the same scale.

Figure 4-7 shows the YZ cross section of the Ramp Up single tracks. A very good agreement between simulation and experiment is observed in both the YZ and XZ (Figure 4-8) cross sectional images. Figure 4-7 shows the melt pool depth for the YZ cross section to be within 3 µm between simulation and experiment, a 0.8 % error. The width comparison is also calculated in this image, with a 3.9 % error between the two, the simulation slightly underpredicting the melt pool width by 7 µm. The measurement for all melt pool widths is taken from the width of the track at the substrate level. A similar profile of melt pool shape is also observed in the YZ image, with the bottom half of the melt pool tapering slightly in width halfway down the melt pool depth. Here it can be seen the track height compares better to the experimental measurement, than the CW simulation.

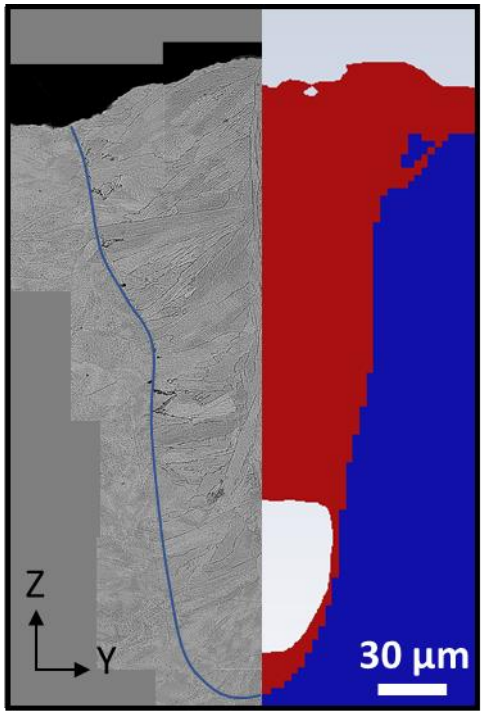

Figure 4-7 shows the YZ cross sections of the Ramp Up experimental and simulation single track results for 316L stainless steel. The left image shows the XZ cross section of the experimental track, viewed in a SEM. The blue line represents the melt pool boundary for the experimental XZ cross section. The right image shows the XZ cross section of the simulation single track. Here, the red region is the region that has gone above the melt pool temperature during the simulation. The white space represents Argon that has been trapped in the melted region during the single track deposition. The images are aligned so the substrate is the same height in both images at the same scale.

Figure 4-8 shows the longitudinal sectioning of both experiment and model. It can be clearly seen from these images that the simulation accurately predicts the experimental results. The melt pool depth measurement is taken from the second Ramp Up pulse. The combined image in Figure 4-8 shows how the model is able to accurately predict even the slope of the melt pool boundary from the first pulse into the transition between the first and second pulses. The simulation also shows remarkable representation of the porosity that is formed between the Ramp Up pulses. Porosity is shown by the black regions in the experimental SEM images, and by white regions in the modelling images. It is clear that at the end of the Ramp Up pulse, porosity is formed. The pore formed by the model at the end of the second pulse is considerably larger than the pore at in the experimental image. This will be discussed further in Section 4.4.1.

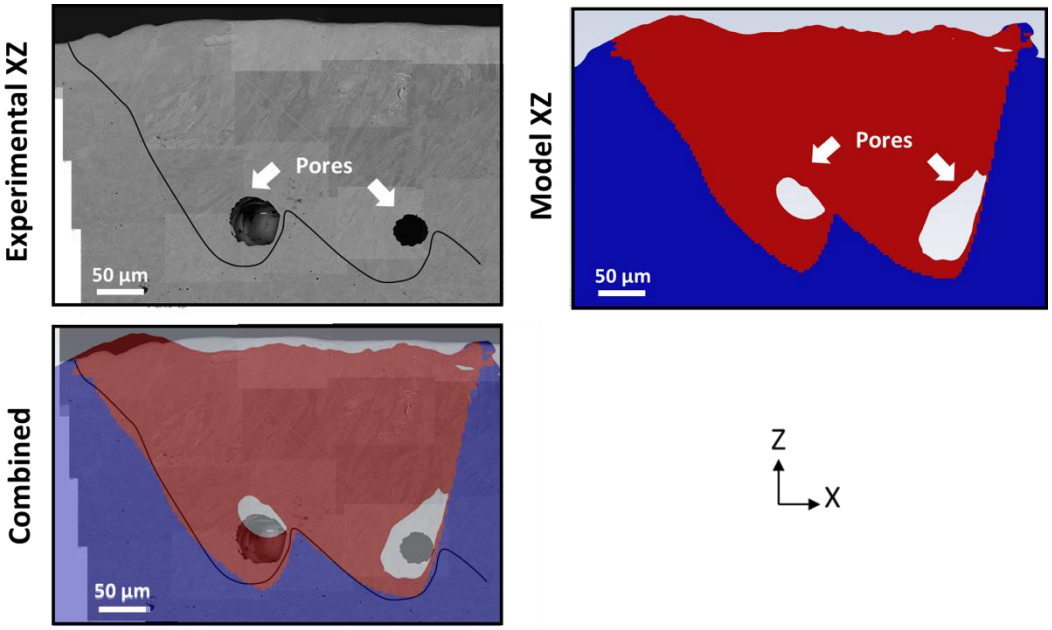

Figure 4-8 shows the XZ cross section for the Ramp Up experimental and simulation single track depositions for 316L stainless steel. Both XZ cross sections are cut in the middle of the track. The top left image shows the XZ cross section of the experimental single track, viewed on an SEM. The black line denotes the melt pool boundary. The black regions at the bottom of each melt pool peak are porosity. The top right image shows the simulation XZ cross section of the deposited single track. The simulation result shows the regions in red that have been above the melting temperature during the deposition. Again, the white regions labelled in the image, is porosity. These appear in the same region as the porosity in the experimental sample. The bottom images are both experimental and simulation overlayed atop one another. This image shows how well these two single track measurements match. Porosity is also shown to be produced in the same location for both model and experiment. The images are aligned so the substrate is the same height in all three images at the same scale. The jagged edges of the SEM images are from multiple SEM images stitched together.

Figure 4-9 shows the experimental validation of a conduction mode single track deposition. No image was available for a visual comparison of the two melt pools, one from Yadroitsev et al. [257]. However, Table 4-3 shows the differences between the experimental and simulation melt pool measurements. Here the results are within 9 % for the melt pool depth, and 4.3 % for the melt pool width. These error results are to the nominal values of the experimental measurements by Yadroitsev et al. Changing these measurements to the maximum measured value of 22 µm (20 µm + 2 µm) for the melt pool depth, gives a 0 % error for the simulation. Similarly, changing to the maximum measured melt pool width of 97 µm (91 + 6 µm) gives an error of 1 %.

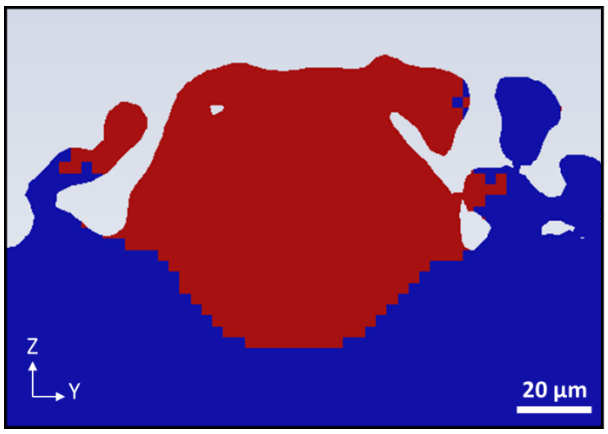

Figure 4-9 shows the validation to Yadroitsev et al for 316L stainless steel. No comparison image was produced in the extant paper by Yadroitsev et al, so the simulation image is presented here only. The red region in the image shows cells that have gone above the melt pool temperature during the single track deposition.

Figure 4-10 shows the benefit of using a ray tracing method as the heat source for the high fidelity model. Figure 4-10 shows absorptivity of both the Ramp Up and CW laser profiles as a function of time, in addition to the power profile of both the CW and Ramp Up single track. The track length for both laser profiles is 300 µm, lasting 1000 µs at 0.3 m/s. The Ramp Up profile is split into its two Ramp Up profiles, with the peak of the first Ramp Up occurring at 500 µs. Here, between 0 – 500 µs both laser profiles ramp up in absorptivity, with the CW laser profile reaching its average absorptivity of 0.64 within 150 µs from 0.46. The Ramp Up profile in comparison, increases in absorptivity from approximately 0.46 to a peak of 0.7 within its first Ramp Up. Between 0 – 150 µs, the Ramp Up profile lags behind the CW profile, until the Ramp Up hits 180 W. The profiles have a similar absorptivity between 175 µs and 275 µs, and then the Ramp Up profile increases to 0.7. Immediately after 500 µs the absorptivity drops drastically to 0.43. This is due to the collapse of the keyhole cavity, decreasing the amount of reflections in the melt pool. The Ramp up profile then increases to 180 W at 700 µs, whereby it levels off to an absorptivity of 0.63, 0.07 lower than its first peak. Interestingly, within the first 200 µs, both profiles follow the same peaks and troughs of absorptivity, most noticeably at 80 µs and 160 µs.

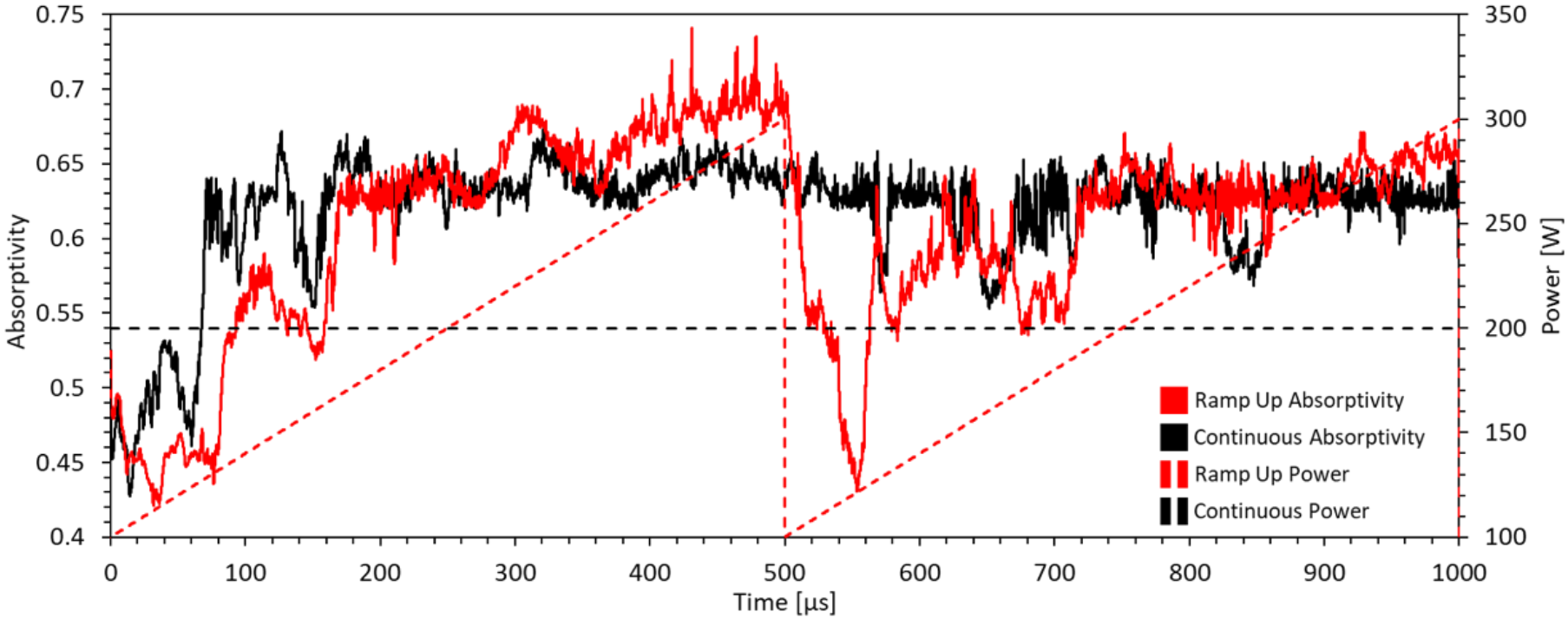

Figure 4-10 shows absorptivity as a function of time for the 316L stainless steel validations on the primary axis, and Laser Power as a function of time on the secondary axis. The Red traces are for the Ramp Up, and the black traces for the Continuous laser power. The Ramp Up profile consists of two peaks, one at 500 µs and one at 1000 µs. The total track length for both profiles is 300 µm.

Figure 4-11 shows three sequential images of the Ramp Up profile, covering the 1st peak of laser power. This time period has been captured, as it directly shows the event of the argon capture, and pore inclusion for the Ramp Up profile. The time stamps cover 50 μs before the peak at a power of 260 W, immediately just after the peak at a power of 100 W, and 50 μs after the peak at a power of 120 W. The image is presented as a XZ cross section of the melt pool, with the metal geometry shown as a function of temperature, in addition to the DPM particles (rays) being shown as a function of particle power in W/m^2. At the 450 μs time stamp, the keyhole is nearly fully developed, with the majority of high energy rays (5e10 W/m^2) travelling into the keyhole cavity. Most impact the front wall of the keyhole cavity, and a large majority reflect and hit the back wall of the keyhole. Due to the high intensity of the rays and already high temperature of the keyhole wall, temperatures rise well in excess of the boiling temperature, creating a strong recoil pressure at the back wall. This pushes the backwall out. This often occurs cyclically, and due to the depth of the keyhole, is the main cause of keyhole porosity [154]. At 500 μs, the laser power has been decreased sharply from 300 W to 100 W. This reduction in power can be seen on the particle tracking legend at the bottom of the image. Now, the maximum power has reduced from 1.17e11 to 4.19e10 W/m^2. These lower energy incoming rays now have a much reduced energy, (<2.5e10) after the first reflection off the front keyhole wall. The temperature can no longer be sustained at the level it was 1 μs ago, when these rays has energies of (approx. 5e10 W/m^2). This causes a sudden drop in recoil pressure, rapidly collapsing the bottom and back keyhole wall. Most notably, the labelled unstable region at the top of the backwall, no longer has a recoil pressure to support itself. The aftermath of this event is shown in the last image of Figure 4-11, at 550 μs as a pore.

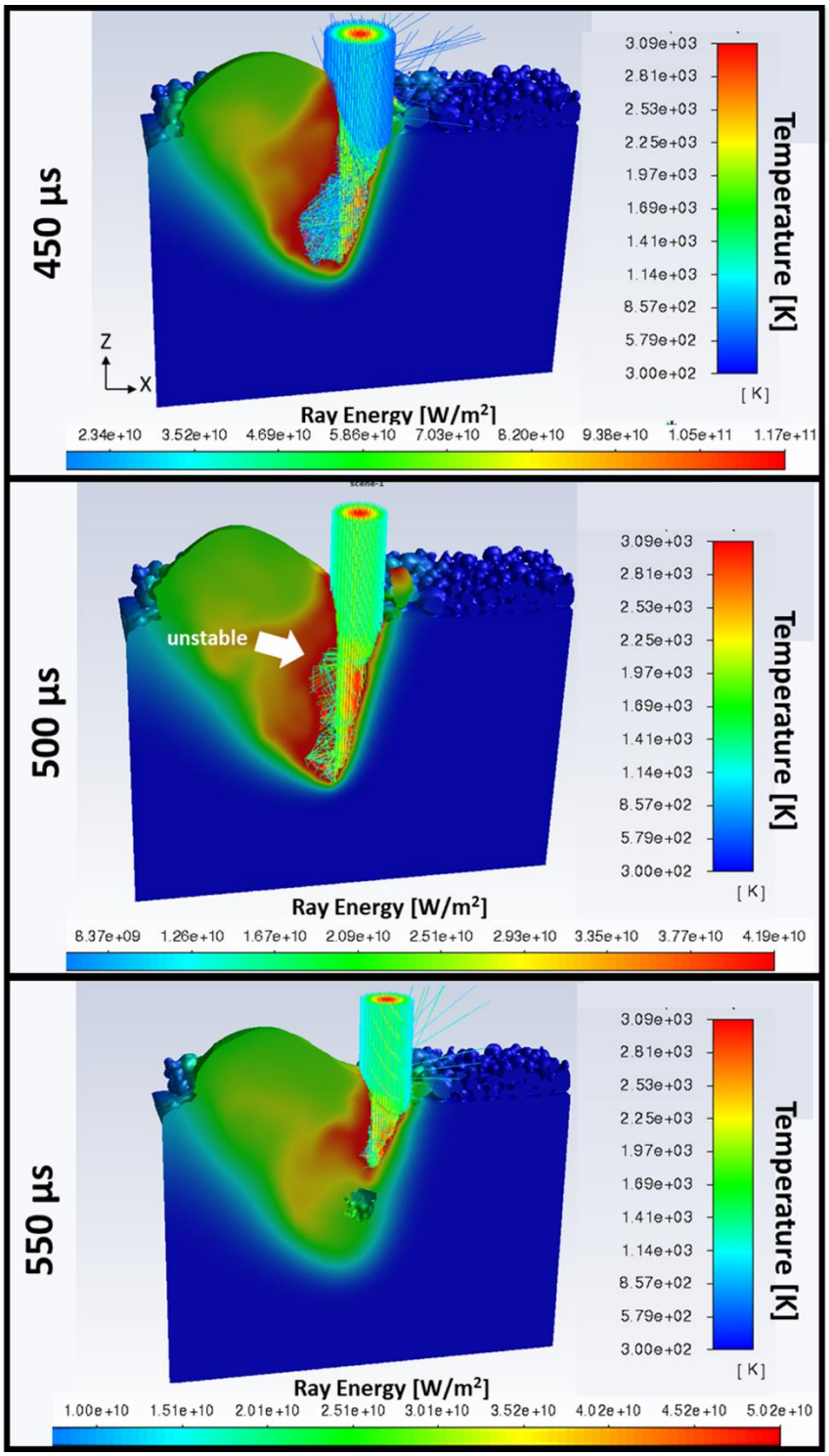

Figure 4-11 shows 3 sequential images during a crucial phase of the Ramp Up power profile for 316L stainless steel. The peak distance for the Ramp Up profile is 500 µs. Therefore these three images show the Ramp Up profile from the peak power, to the lowest power, and shows how the porosity is formed during this change. The first image at 450 µs, shows a near maximum laser power of 260 W, the second image a laser power of 100 W, and the third a laser power od 120 W. The colours shown on the simulation represent temperature, the amounts given by the scale bar on the left side of the images. The column of rays show each individual ray tracing DPM particle and their trajectories. The colours of the DPM particles are the power (W/m^2) carried by each particle. The scale bar on the bottom of the image shows the values for the DPM particle power values.

In this image, the fall of the top region of the keyhole cavity, as impacted the front wall, trapping argon inside the metal liquid volume. This causes the porosity inclusion. This porosity inclusion is then pushed downwards through a combination of Marangoni flow and convection, to its resting place at the bottom of the melt pool, as it is seen in Figure 4-8.

4.3.2 Aluminium 2024 validation results

Figure 4-12 shows the YZ cross section of the melt pool, after the simulation has cooled to room temperature for the parameters of PD60. The red in the image denotes cells that have risen above the solidus temperature of the metal during the simulation. This simulates the melt pool weld lines, allowing for calculation of the melt pool dimensions post track deposition. Figure 4-12 shows the comparison between using the literature value for the refractive index, vs using the revised version. In the image the melt pool dimensions are 3 µm for the literature value, 40.47 +/- 1.03 µm for the model, and 46.9 +/- 17.14 µm for the experiment. Here using the literature value for the model has an error 93.8 %.

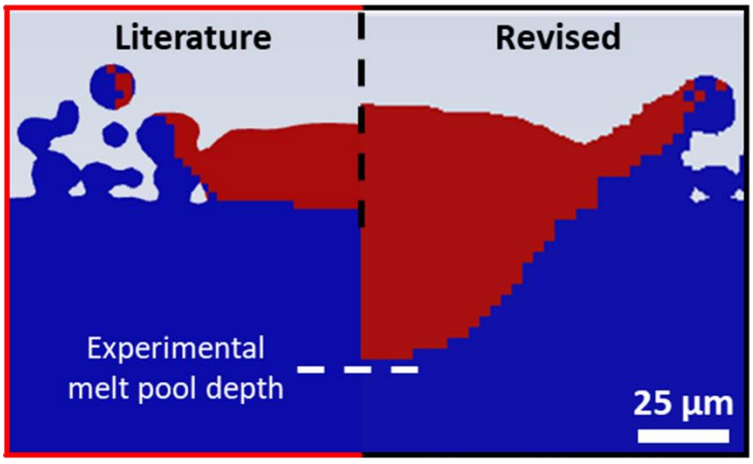

Figure 4-12 Left: shows the YZ cross section of the melt pool produced with the parameters for PD60 for AA2024. The literature value shows a melt pool depth of 3 µm, against the dotted white line, which is the melt pool depth for the average experiment, at 46.9 µm. Right: The revised version of the refractive index is shown, with an average melt pool depth of 40.47 µm.

Table 4-4 shows the tabulated validation results for PD15 and PD60, for the LMC experimental melt pool dimensions and the model melt pool dimensions using the revised refractive index. These results are plotted in Figure 4-13. Figure 4-13 shows the average value for melt pool width and melt pool depth for both PD15 and PD60, along with error bars showing the +/- standard deviation for each dimension, to show the variability in each experiment.

Table 4-4 Table shows the individual validation results from the AA2024 validation study. Here the PD15 parameter represents a laser power of 200 W with a 15 µm point distance, a exposure time of 120 µs and a delay time of 20 µs. The PD60 parameters are a mirror of AA2024, the only difference being the point distance is increased to 60 µm. Therefore the effective speed of PD15 is 0.107 m/s, and PD60 is 0.429 m/s.

Sample	**PD15**				**PD60**			
	Model		Experiment		Model		Experiment	
	Depth [µm]	Width [µm]	Depth [µm]	Width [µm]	Depth [µm]	Width [µm]	Depth [µm]	Width [µm]
1	40.98	164.00	66.19	245.39	41.62	187.00	53.39	186.24
2	40.88	167.25	33.97	179.80	38.84	170.91	63.88	195.62
3	40.89	169.60	33.97	164.00	40.42	167.6	23.43	135.30
Average	40.92	166.95	44.71	196.40	40.47	174.66	46.90	172.39
StDev	0.06	2.81	15.19	35.24	1.03	11.45	17.14	26.50

The variability in experimental melt pool depths is 15.19 µm for PD15 depth, and 17.14 µm for PD60. The variability in experimental melt pool width is 35.24 µm for PD15 and 26.5 µm for PD60. The model has much lower average variability, with 0.06 µm and 1.03 µm standard deviations for PD15 and PD60 melt pool depth, and 2.81 µm and 11.45 µm for the melt pool width. The reasons for more variability within experimental samples is discussed in section 4.4.2. The model shows excellent agreement with all experimental data, including the variability, and sit within the experimental spread of the LMC 50 µm layer thickness samples. The melt pool width for PD15 remains on the lower end of the experimental validation variation. The possible reasons for this are discussed in section 4.4.2.

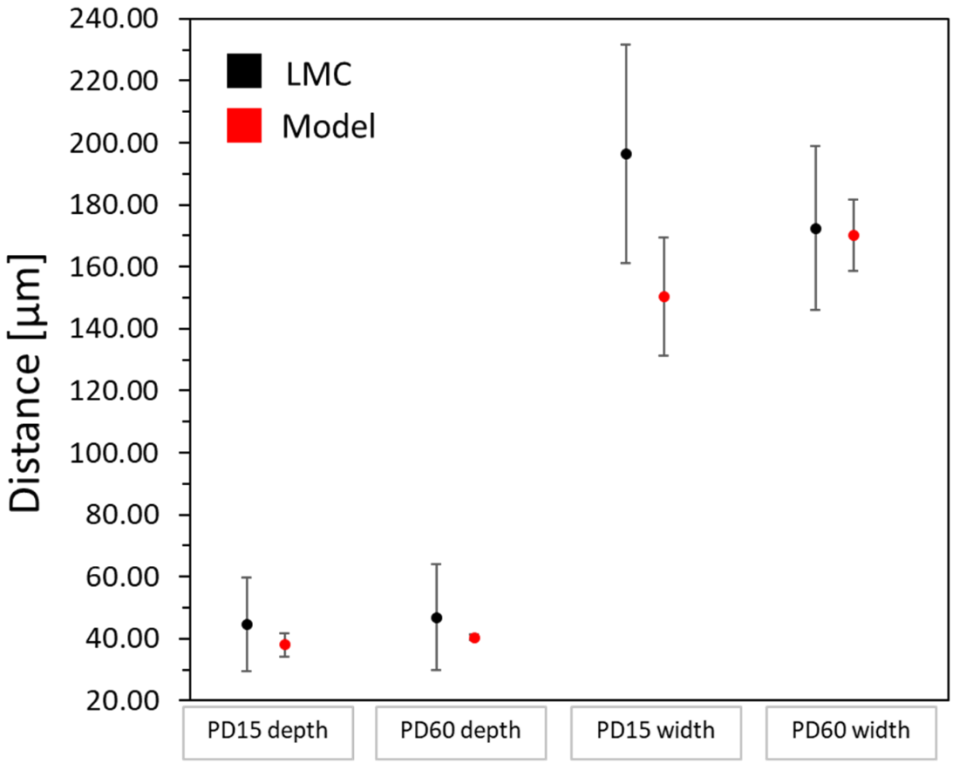

Figure 4-13 shows a plot of the validation study for AA2024. Melt pool dimensions from the LMC are compared with that of the model, both using 50 µm layer thickness with no preheat at the same laser conditions. Two laser parameter cases are used for the validation, PD15 and PD60. The results for the LMC are shown in black, and the model results shown in red. Error bars represent the +/- standard deviation for the results, measured at 3 different locations along the track length for the model, and across 3 different tracks for the LMC. Melt pool depth and width values are shown here.

Figure 4-14 and Figure 4-15 show the physical YZ cross sections of the experimental melt pools (viewed on a SEM), and the cross sections from the model. Figure 4-14 shows the XZ cross sections for PD15. The images are paired so that they show the smallest to biggest melt pool widths from left to right, and so that the middle of the melt pool is aligned to the one below. This shows the variability in the experimental measured values. Only one modelling single track was simulated, as the powder bed remains the same for each model. Additionally, the PD15 model takes approximately 240 hours to run, and PD60 96 hours for a 600 µm long single track. To mimic the semi-random nature of the experimental process, three sections of the model are taken along the track. The powder bed is stochastic, and therefore introduces some randomness into the simulation. The three different slices and their relative position along the track are shown in Figure 4-14 and Figure 4-15. The heights of the tracks are not compared.

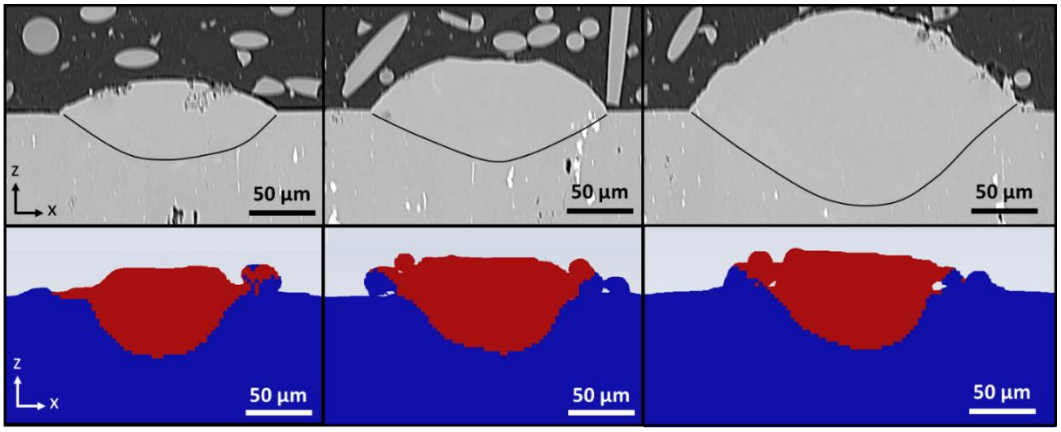

Figure 4-14 shows XZ SEM cross sections from the LMC experiment (top row) and the XZ cross sections of the model (bottom row) for PD15 for AA2024. The bottom row shows the XZ cross sections from the model. Here, the red region shows cells that have been melted during the single track deposition. Blue shows cells that have not melted. Multiple images are shown for the LMC experiment to showcase the variation in measured melt pool dimensions. To mimic the semi-random sectioning of the LMC tracks over several mm, the model has been sectioned at 3 different points along the track length.

Figure 4-15 shows the experimental melt pool YZ cross section for PD60. The bottom row shows the modelling results for PD60, showing similar sized melt pools throughout the single track. The SEM YZ cross sections show more variability. The attention of the reader can also be pointed at the difference in cracking between the two experimental SEM samples. PD15 shows a crack free YZ face, whereas PD60 shows multiple fracture lines in the YZ face of the single track.

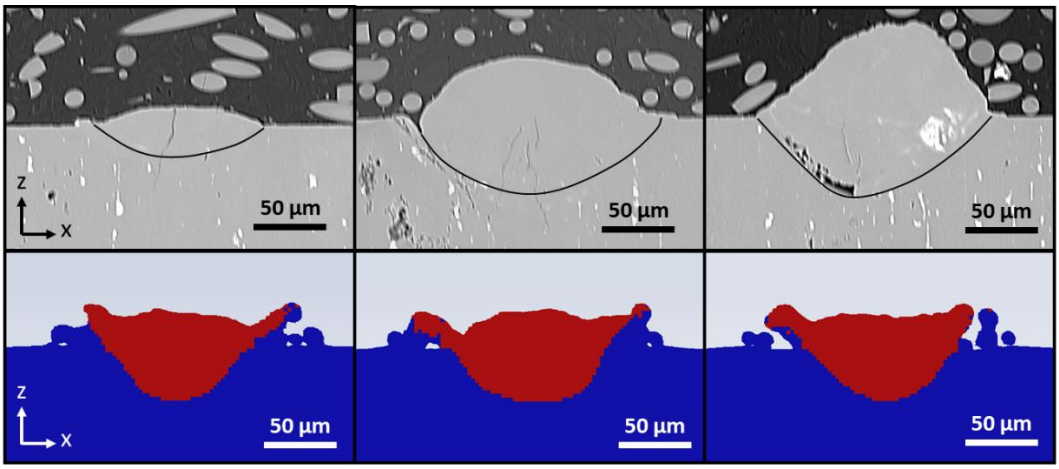

Figure 4-15 shows XZ SEM cross sections from the LMC experiment (top row) and the XZ cross sections of the model (bottom row) for PD60 for AA2024. The bottom row shows the XZ cross sections from the model. Here, the red region shows cells that have been melted during the single track deposition. Blue shows cells that have not melted. Multiple images are shown for the LMC experiment to showcase the variation in measured melt pool dimensions. To mimic the semi-random sectioning of the LMC tracks over several mm, the model has been sectioned at 3 different points along the track length.

Figure 4-16 and Figure 4-17 show the XY top view of the track and the XZ longitudinal cross section of both PD15 and PD60. Figure 4-16 and Figure 4-17 also show the locations of the slices taken in the model. PD60 has slices at positions 160 µm, 368 µm and 533 µm and PD15 at 160 µm, 368 µm and 533 µm. The top view for PD60 shows

small overspills at locations matching the point distance of the laser. Additionally ripples in the track surface can be seen, caused by melt pool flow solidifying from each exposure point.

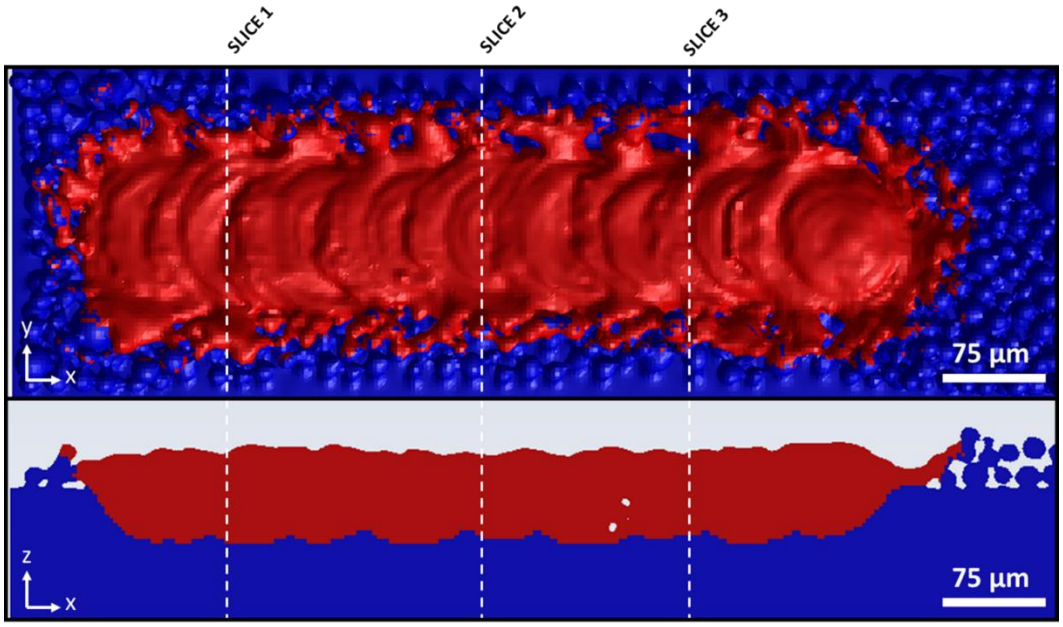

Figure 4-16 shows the top view in the YX plane, and also the longitudinal view of the track in the XZ plane for PD60 for AA2024. The top view shows the track width variation along the single track length. Overspills at periods of 60 µm match to the point distance. The locations of the validation XZ slices are shown at arbitrarily chosen positions of 160 µm, 368 µm and 533 µm. The bottom image shows the XZ cross section of the track, also showing where slice locations are taken from.

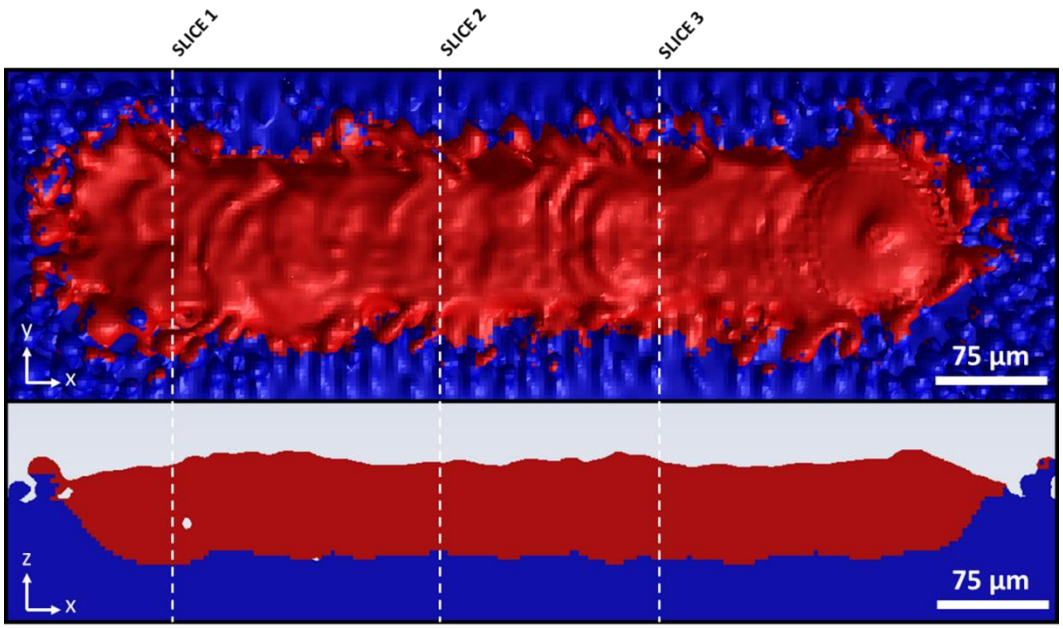

Figure 4-17 shows the top view in the YX plane, and also the longitudinal view of the track in the XZ plane for PD15 for AA2024. The top view shows the track width variation along the single track length. The locations of the validation XZ slices are shown at arbitrarily chosen positions of 134 µm, 335 µm and 488 µm. The bottom image shows the XZ cross section of the track, also showing where slice locations are taken from.

Figure 4-18 shows the corresponding backscattered SEM XY top view of PD15 and PD60 experimental single tracks. Cracking on the PD60 track is seen clearly, whereas no cracking is observed for PD15. Large satellites adhering to the track edges can be observed in both samples. A dust particle can be seen as the white ball shown on PD60 and can be ignored. The melt pool stability is much worse on the PD15 sample as opposed to the PD60 sample. This is shown with a much more varied width on the PD15 sample. The model shows good agreement with the nominal widths measured from the PD15 track, however the large amount of variation is not seen in the model. The potential reasons for this are discussed in section 4.4.2.

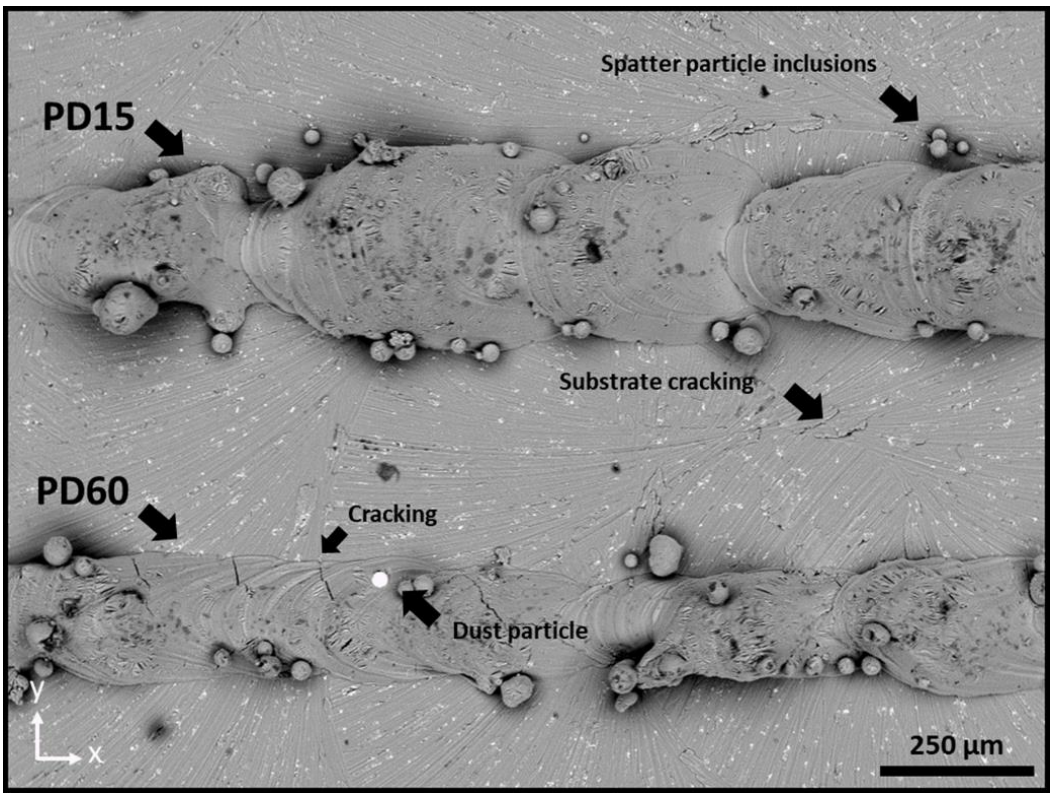

Figure 4-18 show a top SEM view of the PD15 (top) and PD60 (bottom) tracks for AA2024. Much more variability can be observed in the PD15 track. PD60 shows cracking at the left side of the track. Tracks were deposited in the LMC using a Renishaw AM400.

Figure 4-19 shows the live absorptivity trace for a period of 1250 µs for both PD15 (black top) and PD60 (red bottom). The black and red dotted line in both images shows the average absorptivity of the single track deposited in the model. Due to the absorptivity dropping to zero in each pulse, the average is taken without the zero absorptivity value in each delay section of the track. These results show the variability in the measured live absorptivity across the track length for both samples. The average absorptivity for PD15 is 0.19 and 0.21 for PD60. The plot measures absorptivity at very small timescales. Any

oscillation in the surface of the melt pool surface corresponds to peak and troughs in absorptivity.

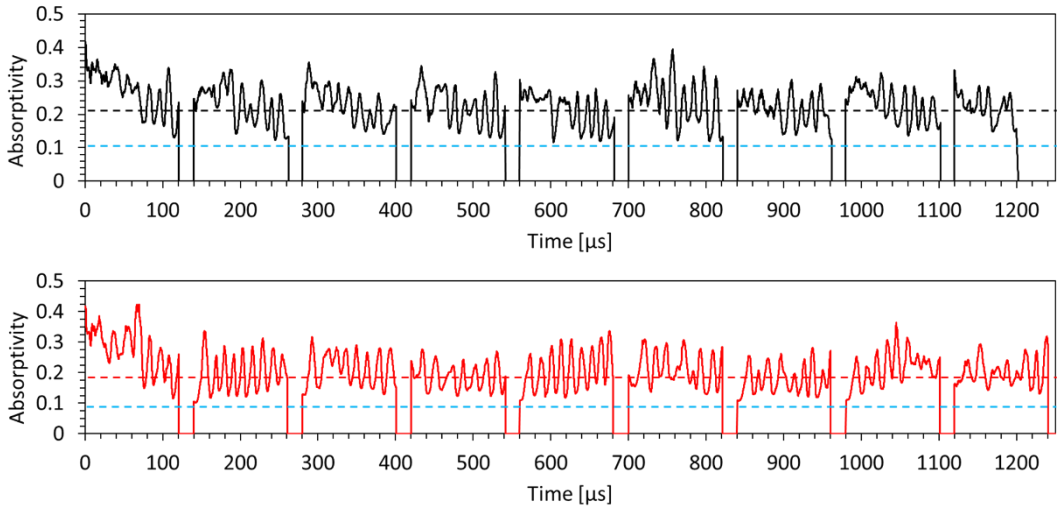

Figure 4-19 shows the absorptivity as a function of distance for PD15 and PD60. Here, the top plot shows the absorptivity vs distance of PD15, the black solid line representing the average absorptivity from the track length. The bottom plot shows absorptivity vs distance for PD60, with the red solid line showing the average absorptivity across the track length. This plot only shows the first 1250 µs, in addition to being smoothed, taking an average of 1 µs to aid in readability. The blue dotted line represents the absorptivity measured from the LMC.

Figure 4-20 shows a plot of absorptivity values comparing the model to experiment. The error bars for the model represent the fluctuations in absorptivity as seen in Figure 4-19. In this plot it must be noted that the absorptivity value for the LMC is calculated as an average for the entire track length (blue dotted line), measured as a function of the temperature at the bottom of the disc (500 µm away from the substrate surface). The differences in this plot are discussed in section 4.4.2.

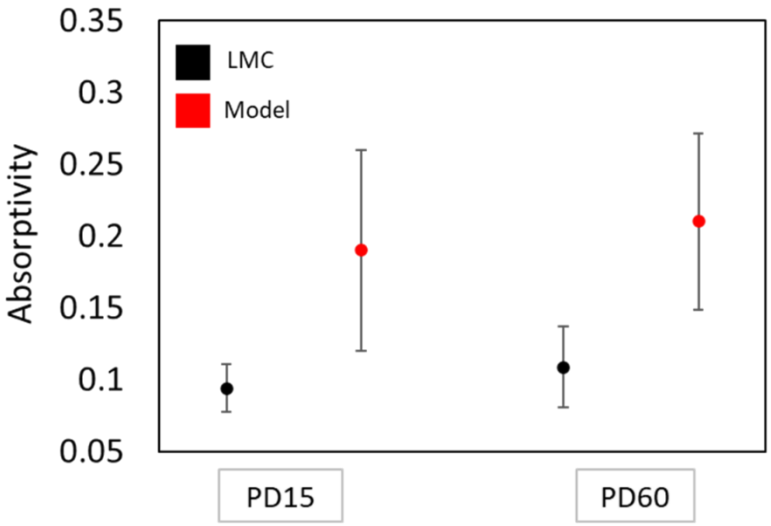

Figure 4-20 shows a plot of the absorptivity results for both the LMC and the model. The results for the LMC show the average absorptivity value that the experiment generates as the average absorptivity for the entire track length. In contrast, the model generates a 'live' absorptivity value that varies throughout the entire track length. Therefore, the absorptivity results for the model have been plotted with error bars showing the standard deviation throughout the live absorptivity trace.

4.4 Discussion

4.4.1 316L stainless steel validation

Three validation studies were performed with 316L stainless steel to verify the models ability to replicate the process of LPBF. These three studies included two cases using a continuous wave laser beam and one study using a variable power laser. The two continuous wave case studies have one parameter operating in conduction mode, and the other in keyhole mode. These are the typical validation cases that literature presents to verify LPBF models[1], [86], [242]. The variable power case was used to ensure the model can also be validated to simulate laser beams not operating in typical conditions. Additionally, there is no literature that empirically compares variable laser power conditions to simulation results. These will be used so that the model can been verified to run under variable laser power conditions, which is an integral part to the inverse solution, presented in Chapter 5.

Figure 4-4 shows the YZ cross section of the 200 W CW single track, at a laser velocity of 0.3 m/s. The error in this result is 8.1 % for the simulation when directly compared to the experimental melt pool depth. Agreement within 10 % of the experimental values has been shown to be acceptable for LPBF modelling [163]. This agreement is also confirmed by the longitudinal cross section in the XZ plane in Figure 4-6. Figure 4-6 shows that the simulation actually shows a much closer agreement to experimental results than Figure 4-4 originally suggests. It is unknown exactly where in the single track Figure 4-4 was sectioned at, and therefore Figure 4-6 shows a much more accurate

depiction of the experimental conditions at the start of the laser track. Here, the red dotted line on Figure 4-6 is within ± 5 μm (2.8 %) of the nominal melt pool boundary for the CW experimental XZ cross section. It is unclear on the exact reason why the experimental melt pool boundary fluctuates so much during the first portion of the track. This could be due to local powder bed height discontinuities, spatter interference, or an artifact of the polishing method. The artifact could have occurred due to a local region being over polished, resulting in the black line not following the middle line of the melt pool, but slightly erring to one side. Care was taken to ensure that the track was sectioned in the middle. The distance of the track was assessed by viewing the track in a plan view, and polishing until half of the track had been removed. This process however is very skill dependant, and has the potential to influence the results. However, ignoring the large fluctuation in the experimental melt pool boundary, the experimental YZ measurement of the melt pool depth indicates that the track melt pool depth increases later on in the single track deposition. Therefore, the model shows very good agreement with experimental results for the 200 W 0.3 m/s CW single track in keyhole mode.

The second validation case for the model uses a low laser power, where the melt pool depth is mainly affected by heat conduction through the liquid metal. This low power run is necessary as the inverse solution predicted power outputs in Chapter 5 have laser powers that range from 20 – 250 W. Simulation results were compared with literature from Yadroitsev et al., with a laser power of 50 W, at a laser velocity of 0.28 m/s, the closest literature result concerning laser spot size and laser velocity that matches with the experimental setup from POLIMI [257]. Here, the simulation matches with a 9 % error for the melt pool depth, and 4.3 % for the melt pool width. Yadroitsev et al. provides error bars for the melt pool depth and melt pool width values that come from variation in the experimentally measured melt pool sizes [257]. If the maximum values for the melt pool width and melt pool depth are used, then the errors decrease to 0 % for the melt pool depth, and to 1 % for the melt pool width. These errors would be from local discontinuities in powder spreading and size variations. Due to the low power of the laser, rouge spatter particles and local powder bed changes could result in these small fluctuations. Therefore, the model shows good agreement with the experimental 50 W, 0.28 m/s single track deposition from Yadroitsev et al. in conduction mode.

The third validation case is for the Ramp Up variable laser profile. Chapter 5 demonstrates the inverse solution, which will constantly vary laser power to keep a constant surface temperature. An empirical validation of variable laser power has not been found in the literature review. Khairallah et al. uses variable laser power in their

study to reduce porosity at corners in an LPBF scan strategy, but do not show a direct comparison from empirical to simulation results [78]. Similarly, Stathatos and Vosniakos present work that uses an extremely fast FEA model as training data for an ANN [229]. Both of these studies only validate their models to static results. Here, for the first time a high fidelity model will be compared to empirical results for a Ramp Up in laser power for LPBF. Ordinarily, simulation results are compared to the YZ through plane of the single track. This provides a snapshot of the melt pool depth and width, that is adequate for constant laser profiles. However, with a variable laser power applied over a 150 μm peak distance, this random snapshot is no longer suitable, as the YZ cross section could intersect at any point over the 150 μm peak distance. Therefore a new method of cross sectioning the single track was developed at the University of Nottingham and the Politecnico di Milano which was used for this study.

Figure 4-8 shows the XZ cross section of the experimental single track deposition. Two and half peaks are seen in the image, where the power is ramped up from 100 W to 300 W over 150 μm. Figure 4-8 also shows the overlay of the simulation result over the experimental measurement. It can be seen clearly from this image that the simulation has an excellent agreement with the experimental result. The first validation of the validity of the model to the experiment, is the melt pool depth and width, which is taken at the highest melt pool depth in the second peak. The simulation error to experiment here is 0.8 %. The second validation comes from the melt pool width, which was measured from the YZ cross section in Figure 4-7. The exact location along the single track is unknown, however the melt pool width has a 3.9 % error from simulation to empirical. It is has not been determined how the melt pool width fluctuates during this study.

The third validation of the models accuracy is the simulation of the pore formation at the end of each Ramp Up cycle. Figure 4-8 shows that both the simulation and the experimental single tracks both show porosity at the end of each cycle. Figure 4-11 shows how the first pore is generated. This type of analysis can only be measured using a ray tracing approach to the heat source. High energy rays impact and then reflect off the front keyhole wall at 450 μs, ballooning out the back wall of the keyhole cavity due to high recoil pressure forces. As the power transitions rapidly from 300 W to 100 W, the previously supported back wall of the keyhole starts to collapse as there is insufficient recoil pressure from the lower energy rays. This keyhole cavity collapse causes the unstable region (labelled in Figure 4-11) to fall, and capture argon in its decent. This causes the inclusion of the first pore as seen in Figure 4-8. This method of

keyhole pore formation is also captured in X-Ray synchrotron experiments, as shown by Zhao et al. [58]. Therefore the Ramp Up laser profile simulation shows excellent agreement with the experimental results.

The keyhole collapse can also be shown in Figure 4-10. This figure shows the total absorptivity of the laser beam for each timestep in the simulation. It can be seen clearly that the absorptivity of the Ramp Up increases in-line with the power ramp up from an initial value of 0.46, to 0.7 within its first ramp up duration. After the first 300 W peak laser power, the absorptivity rapidly declines. This is due to the collapse of the keyhole. Less reflections occur inside the keyhole cavity, drastically reducing the absorptivity.

4.4.2 Aluminium Alloy 2024 validation

The simulation of aluminium for LPBF is complex, due to the varying measured absorptivity values of the metal when compared to its refractive index. The literature value for the refractive index of pure aluminium is 1.36 + 10.43i. At an incident angle of 0 °, this gives an absorptivity of 4.76 %. If this refractive index is applied for a 200 W 60 µm point distance, 120 µs exposure time, 20 µs pulsed laser single track deposition, it gives a melt pool depth of 3 µm (Figure 4-3). This is contrast to the measured melt pool depth at the same parameters of 46.9 µm. This large difference is arguably mostly attributed to the energy input into the structure. The largest driver for the amount of energy delivered to the melt pool is the proportion of energy that is reflected and absorbed by the metal surface. Therefore, the literature value of the refractive index is not representative of the genuine conditions in LPBF. This is supported by literature. Bergström et al. experimentally measured the absorptivity of rough aluminium surfaces, and for pure aluminium (with a surface roughness (Sa) of 0.25 µm) measured a value of 15.7 % with a wavelength of 1053 nm [259]. Rubenchik et al. compares the absorptivity of aluminium alloy 6061 (AA6061), when measuring aluminium powder calorimetrically [56]. They find the absorptivity to be approximately 20 % for a wavelength of 1000 nm. Additionally, Trapp et al. found that the nominal value for the absorptivity of AA6061, to be 15 % in the conduction mode regime during laser calorimetry testing at 1070 nm [39]. The disparity comes from the aluminium oxide on the surface of the aluminium, and scattering effects from surface roughness. This is in comparison to the experimental test for the literature refractive index, that evaporates aluminium at ultra-high vacuums to avoid any oxides, onto a atomically flat surface, before measurement of its absorptivity [258], [260]. This clearly is not representative of the conditions in LPBF.

This inconsistency in experimental and theoretical calculations of the absorptivity of aluminium presents a problem to the LPBF community. Direct calorimetric measurements of the absorptivity of LPBF in situ gives an absorptivity value for a specific set of parameters. But, this still requires the calorimetry to be run for each parameter set, which is time consuming. In addition to this, only having the bulk absorptivity information negates the benefits of using a ray tracing in the model. These benefits include information such as Figure 4-11, which gives an accurate keyhole representation, allowing insight into porosity formation. Many literature models such as works from Tang et al. and Zhang et al., approximate absorptivity, getting good agreement to experimental data, but have to adjust absorptivity in order to match with the experimental melt pool dimensions [233], [244].

This work for the first time, demonstrates the advantages of using a revised refractive index, instead of using a revised absorptivity value. Modifying the refractive index of the material instead of the bulk absorptivity, allows for high fidelity modelling of the development of porosity etc, in addition to supplying a live trace of the absorptivity throughout the single track. Also, it shows that this value of a revised refractive index can be used under different processing conditions. Additional work is needed to confirm this is true for all speeds in the LPBF of AA2024, and to compare this to experimental data. This data is crucial in supplying information that is required for the inverse solution for different materials. An accurate absorptivity value is crucial in the calculation of the inverse solution, as the solution initially assumes an absorptivity of 1, and then scales the predicted power based on the actual absorptivity value. This would give inaccurate values from using a bulk absorptivity alone. Using a revised refractive index allows for the 'live' absorptivity value in the inverse solution, giving a geometry dependant absorptivity value for more precise calculations of an optimal laser power. Once set for the base absorptivity of the metal, the absorptivity can then be calculated on an individual basis accounting for local geometry by using the revised refractive index value. This gives a much more realistic representation of absorptivity for difficult materials, such as aluminium.

Modifying the refractive index to 2.8 + 7.8i, increases the absorptivity at an incident angle of 0 ° to 15 % from 4.76 %. Figure 4-12 shows how the melt pool depth is now within the experimental value ranges, as also shown in Figure 4-13. This is the primary validation method used in literature, the modification of the absorptivity value to match with melt pool dimensions. In this work however, advantages have been demonstrated that show the refractive index should be modified instead. Therefore, the model shows

a good agreement with experimental data for the 200 W 60 μm and 15 μm point distance, 120 μs exposure time, 20 μs pulsed laser single track depositions.

As mentioned previously, a revised refractive index to calculate absorptivity is beneficial to the inverse solution framework. This absorptivity value is calculated during the inverse solution run, and directly affects the predicted value. However, a direct comparison between experimental and simulation shows a disparity between LMC and model absorptivity values. Figure 4-20 shows the values of absorptivity measured by the LMC and the model respectively. It can be clearly seen that the values of absorptivity measured are lower when measured on the LMC, rather than from the model. The relative difference between the LMC and the model is 0.099 and 0.1 for both PD15 and PD60 respectively. The increase from PD15 and PD60 for the LMC is 13.4 %, and the increase from PD15 to PD60 for the model is 9.5 %. Whilst currently it is difficult to tell which value is correct, it suggests that the absorptivity values can be compared relative to one another when comparing samples measured by the same method (either LMC or model). In addition, the percentage increases show a similar relative position between PD15 and PD60 from both methods. However, the model gives an accurate account of the melt pool depths when compared to melt pool dimensions with the revised refractive index. The model also shows substantially less variation in both melt pool depth and width. Figure 4-13 shows this to be true, with a standard deviation difference increase of 1111 % and 231 % for melt pool depth and width when comparing model results to the experiments.

The differences in absorptivity measurement appear to be relative. That is that comparisons can be made between samples measured on the same method. However, the correct absolute value of absorptivity is more difficult to discern. Due to complex optical and heat transfer phenomena occurring at the surface of the metal powder, direct measurement/simulation of this process is extremely difficult. What is clear however, is that using a revised value of refractive index with a base absorptivity of 15 %, gives melt pool dimensions that have excellent agreement with experimental data. This, also agrees well with experimental observations by Bergstrom et al., that aluminium has a base absorptivity of approximately 15 %, an increase due to oxides on the aluminium surface. The LMC is an attractive piece of technology, not only for its ability to generate values of absorptivity, but also as a compact device that can output high throughput material validation/testing, that can be adapted to any LPBF machine. However, the results from the LMC do not correlate with expected values. This main source of variation in the LMC is the powder bed height differences, stemming from manual spreading of the powder

across the disc. Whilst every care is taken to ensure a minimum deviation across the disc, variations can still occur. Small differences in layer thickness can have large effects on measured absorptivity, as demonstrated by Boley et al. [52]. In addition, effects of the substrate strongly influence the LMC, as back reflection from the substrate decreases the measured absorptivity. These local discontinuities in the powder bed height will also reduce the absorptivity. In comparison, within 'steady state' LPBF processing, layer thicknesses can be very reproducible, with less height variation [25]. Additionally, the layer below the powder would either be comprised of powder, or previously melted powder. This suggests that during steady state processing, the absorptivity of the layer below could be higher than what is measured in the LMC. In comparison to the model, the simulated powder bed has been designed to be a consistent 50 μm layer height. Further research is needed to compare these two tests to discern these differences in absolute absorptivity.

It can be seen in the melt pool widths, experimental values vary between 164 μm and 245 μm across the different sections measured. This can also be observed in the top view of Figure 4-18. A potential reason for the disparity in modelling and experimental results for this specific PD15 and PD60 absorptivity values, are powder denudation and entrainment. As detailed in section 2.4.4, powder is sucked in from either side of a melt pool during deposition. High velocity argon gas and metal vapour are ejected from the melt pool centre, forming a vapour jet. This high velocity jet forms the reactionary force that generates a recoil pressure on the liquid surface of the melt pool. The flow of gas/vapour, pulls in surrounding argon gas either side of the melt pool, also pulls with it powder particles, as shown in work from Li et al. [164]. Also shown in Li et al.'s work, is that large particles pulled in from the sides create a shadowing effect on the melt pool, temporarily decreasing power to the melt pool and increasing melt pool instability. The slow speed of PD15 (0.107 m/s) and PD60 (0.43 m/s), could cause large amounts of powder entrainment, shadowing and melt pool instability [38]. Melt pool instability can be seen in the top view SEM image (Figure 4-18), as well as the measured melt pool widths. The shadowing effect, coupled with large amount of material being added to the melt pool, can cause large temperature drops during the instability [164]. These temperature drops could be associated with the decrease in absorptivity, as the LMC calculates the absorptivity by measuring the temperature at the bottom of the disc. To verify these results would need further investigation to compare the absorptivity results from LMC experiments with simulation absorptivity values. Differences in denudation, layer thickness and substrate reflectivity could explain differences seen in absorptivity

measurements calculated on the LMC. This is further compounded by a complicated absorption process on the aluminium surface through multiple oxides from metals in the alloy.

However, results from the simulations revised refractive index, increased to the base absorptivity of experimentally verified values, gives excellent agreement to experimental melt pool measurements, the primary validation technique for LPBF modelling in literature. Therefore, in this work, absolute absorptivity values from the simulation will be used. Further comparisons and sensitivities studies are recommended to be completed to increase the confidence of absolute aluminium absorptivity measurements on the LMC.

4.5 Summary

This chapter presents the necessary foundational work to validate the model to experimental results. Validation is achieved with two different materials, 316L stainless steel and AA2024, under four different types of laser operation, continuous, stationary pulsed, and moving pulsed with a ramp up profile.

This novel work shows that the simulation can be validated for variable laser powers. This condition is important to the work in this thesis, as chapters 5 and 6 discusses the use of using variable laser conditions within the inverse solution framework.

The model is validated for use with ray tracing on AA2024. Due to the complex relationship of absorptivity with aluminium alloys, using the literature value of the refractive index is not possible. In this work for the first time, the use of a modified refractive index is considered, and found to work well at representing the absorptivity of AA2024. Additionally, this work considers the validation with a pulsed laser beam setup, to predict process parameters with a pulsed laser for AA2024 in chapter 6.

Chapter 5

5 Model Informed Temperature regulation in laser powder bed fusion

5.1 Introduction

Reducing the amount of defects in components made through LPBF is still the largest barrier for entry in high strength mechanical applications. Optimising laser power and speed are considered two of the most influential factors in LPBF which drive track consolidation, reducing porosity. These parameters though, are difficult to link to desirable melt pool properties, without extensive experimental testing. Controlling the process via melt pool surface temperature has been shown to substantially improve processing, as well as provide a more direct link with the process. However, no literature examines which melt pool temperatures are optimal in producing highly dense components. This chapter aims to provide a foundational framework to allow process parameters to be optimised via surface temperature, and the benefits of doing so. Understanding optimal melt pool peak temperatures is a valuable approach since increasingly machine tools are able to monitor surface temperature and, in the future, attenuate energy density accordingly. A means to define this temperature is required and is demonstrated in this chapter.

The ideal processing space exists in the region between conduction (below the materials boiling point) and keyhole (well exceeding the boiling point) modes. This has been widely explored by multiple authors including Martin et al. who show that porosity is largely eliminated in this zone, in addition to Zhao et al. who, through X-Ray synchrotron experiments, elucidated the physical mechanism of the transition to keyhole mode [58], [158]. Literature has shown that the presence of a transition zone, exists within a variety of materials. Trapp et al. designed an experimental process to measure this zone by directly measuring the material's absorptivity in-situ [39]. Clare et al. developed this work, and showed that this region of transition is heavily affected by material composition, and powder morphology[99]. Boley et al. also shows that the absorptivity can heavily depend on the size distribution of the powder bed layer[52]. Xie and Kar, showed that surface oxides also play a large role in influencing the absorptivity of metals. This shows that while absorptivity can be used as a metric to determine the mode of processing, it is a sensitive parameter, material dependant, and difficult to measure in a

conventional build environment and practically impossible to assess with current technology in the production setting.

Surface temperature has been previously shown to provide a stable measure with which to control the process of LPBF [25]. Using surface temperature as a melt pool stability reference value, feed forward models have been shown to provide a dynamic control over the LPBF process, without extensive parametric testing. These can be either used in-situ to vary power or scan speed based upon a target temperature or melt pool size, or before the build, using model based approaches[11]. Surface temperature has also been shown to correlate with porosity and spatter formation. Through control of the inter-layer cooling time, measured by in-situ temperature monitoring Williams et al. showed that spatter formation is increased with high surface temperatures, and is inversely related to porosity[225].

As previously discussed, the stability of melt pool temperature in LPBF is of extreme importance for maintaining a stable melt pool that decreases both lack of fusion and keyhole porosity. Therefore, this chapter discuss a methodology to optimise LPBF by stabilising temperature fluctuations over a single track length, by calculating and constantly modulating the amount of power into the melt pool.

5.2 Methodology

This chapter uses the core of the model that is outlined in Section 3.3. In addition to this, extra functionality has been added through the use of additional UDFs, to control the melt pool temperature by laser power modulation.

5.2.1 Inverse solution for melt pool temperature control

Control of the melt pool peak temperature via the inverse solution can be achieved via the following. The inverse solution represents the method of temperature control via power modulation in LPBF. In order to achieve a specific temperature in the melt pool, one has to calculate the energy needed to raise the temperature from an initial value, to a target value in a given period of time. This transient calculation is performed during a single pass of a simulated laser beam over a metallic powder bed. The variable energy input that is calculated across a single pass represents the ideal amount of energy that the laser beam needs to supply the powder bed to keep the melt pool temperature at a constant value. Energy input will initially be high to raise the material from the ambient temperature to the target temperature, above the materials melting point. The energy input will then gradually decrease as the temperature approaches the target, falling into

a steady state region, whereby, the energy supplied is sufficient to match energy being lost through heat transfer into the surrounding material.

Calculation of the ideal energy input in the example presented here, replaces P in Q_{init} (Equation 3-22) with P_c (Equation 5-2). Instead of delivering the energy that would be given by a specific laser power, the model calculates how much energy is needed to keep the melt pool temperature at its target value and converts this into a laser power at each timestep. Equation 5-1 shows how the energy needed for this change is calculated. First, the maximum temperature in the melt pool is found, and the difference between this and the target temperature is taken (dT). This location limits the melt pool temperature, and is typically at the centre of the beam. This cell is further defined as having the maximum temperature in the domain, where the metal volume fraction is higher than 0.5, and is attached to the main melt pool, shown in Figure 3b. Equation 5-2 then converts this value into a laser power in W.

$$E_c = \frac{\rho C_p dT}{t_s} \qquad \textit{Equation 5-1}$$

$$P_c = \frac{E_c V \pi r^2}{2A} \qquad \textit{Equation 5-2}$$

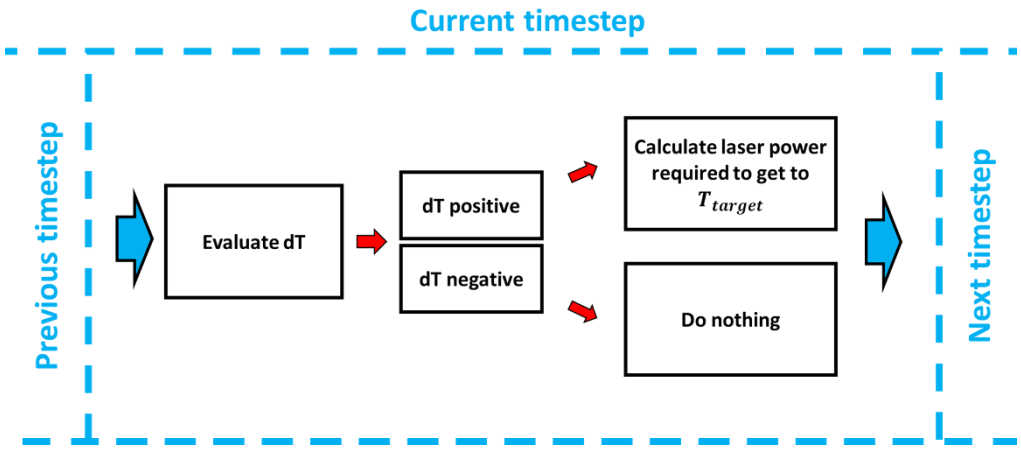

Figure 5-1 shows an example of the methodology behind the inverse solution process. Each timestep evaluates dT, and if the temperature is below T_{target} (dT is positive) then the solution calculates the power required to raise the temperature to the target. If dT is negative, where the temperature is above T_{target}, no power is inputted.

The calculated energy (E_c) where ρ is the density of the cell, C_p is the specific heat capacity, dT is (T_{target} - T) and t_s is the timestep value. For the calculated power (P_c), V is the volume of the cell, r^2 is the square of the laser beam radius, and A is the area of the metal surface in the chosen computational cell. Figure 5-1 shows a snapshot of the inverse solution logic. Each timestep evaluates dT, and if the temperature is below

T_{target} (dT is positive) then the solution calculates the power required to raise the temperature to the target. If dT is negative, where the temperature is above T_{target}, no power is inputted. This target temperature is arbitrarily defined at the start of this chapter, and then refined via the recoil pressure in section 5.4.2 and section 5.4.3. To account for the material absorptivity, the ray tracing sub routine runs at the same timestep as the inverse solution. This calculates an average global absorptivity (A_G) for that timestep. Therefore, the power for that timestep is given as:

$$Q_{inv} = \frac{P_c}{A_G} \qquad \textit{Equation 5-3}$$

Consequently, Q_{inv} is substituted for Q_{end} in Equation 3-27 for the inverse solution. This means that the absorptivity will scale the power at a given timestep. For example, a high absorptivity will decrease the demanded power, and a low absorptivity will increase the demanded power. At the next timestep, a new power is calculated as the difference to the target temperature will have changed. By recording this calculated power at each timestep across the whole laser pass, an ideal power input can be found based upon the set (desirable) target temperature. By monitoring these two variables, idealised parameters can be gained from the power curves generated from the inverse solution.

The material used in this chapter is 316L stainless steel.

5.3 Results

5.3.1 Demonstration of inverse solution

A demonstration of the inverse solution is presented in Figure 5-2. Figure 5-2a shows that by using the inverse solution, laser power can be adjusted automatically, so that the peak melt pool temperature is kept at a specified target of 3700 K (approx. 20% over the normal boiling temperature). The 20 % was an arbitrary value that was chosen to see if the inverse solution could sustain an average peak melt pool temperature above the boiling point. Calculating the optimum temperature will be calculated and discussed in Section 5.4.2. An average power output of 106 W is used across the length of the track to maintain this temperature. Figure 5-2b shows the XZ cross section of the melt pool, taken at 150 μs, 225 μm after the start of the track. Fluctuations in the laser power required, match the powder morphology before melting. Dense regions of the powder bed, with larger single particles are shown to match with peaks in the applied laser power. Figure 5-2e validates the process, showing that the average power given by the inverse solution, results in the same average peak temperature. Taking the average power value of 106 W, the temperature is kept at an average of 3716 K during the length of the track. This compares well with empirical results from Trapp et al. that show the onset of the transition region at 80 W [39].

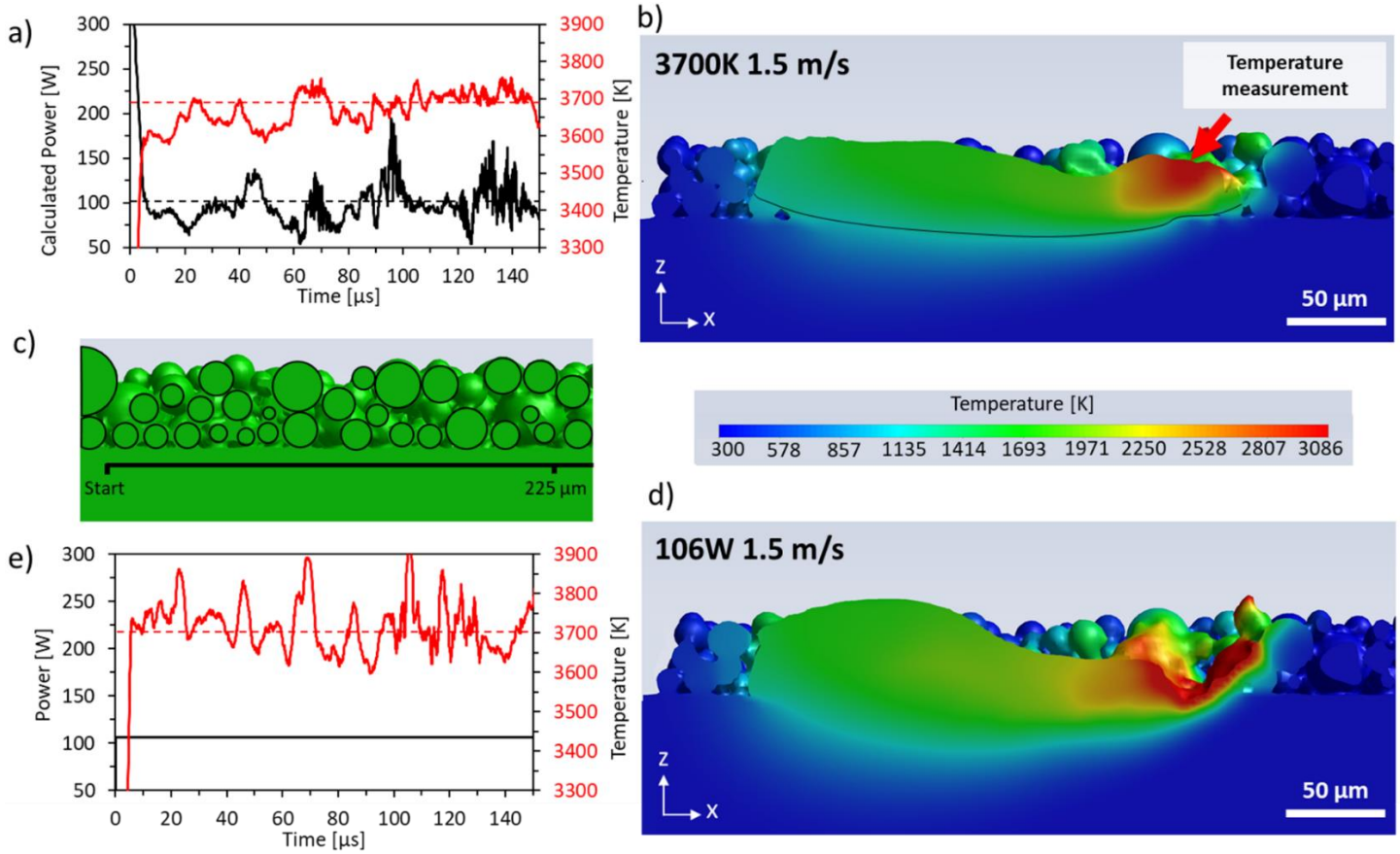

Figure 5-2 shows how the power is changed to keep the peak temperature of the melt pool at the target temperature of 3700 K, while maintaining a constant traverse speed of 1.5 m/s. b) shows an image of the melt pool track at 150 µs. The black line denotes the melt pool boundary (cells which exceeded the melt temperature of SS 316L). The temperature measurement point corresponds to the power calculation cell. c) shows a cross section of the powder before the laser is turned on. The image is aligned so that each power fluctuation can be matched with a powder level change. An identical powder bed is used in each simulation e) The inverse solution process is validated, by taking the average of the power from a). Using this constant predicted power of 106W, the melt pool temperature is shown to average out to an average temperature of 3716 K. d) shows the cross section of the melt pool from 106W, showing a similar profile to b).

Figure 5-3 shows how this also applies for temperatures below the materials boiling temperature, operating in conduction mode only. Figure 5-3a and c show how the power profile changes to maintain the melt pool temperature at 2200 K and 2500 K respectively. The average temperature for the 2200 K target was 2199 K, and 2496 K for the target of 2500 K. The average value is within 4 K for the temperatures below the boiling point, while 60 K within the target for the 3700 K track above the boiling temperature. Figure 5-3b and c show how a 300 K peak temperature difference can mean the difference between balling and a consolidated track at 0.3 m/s. A 2200 K surface temperature does not provide a large enough melt pool to melt the substrate. The 2500 K however provides enough energy to melt the substrate and does not show any balling effect. To achieve a 2200 K surface temperature, the average power is 22.5 W, while 26 W is needed to achieve a surface temperature of 2500 K at 0.3 m/

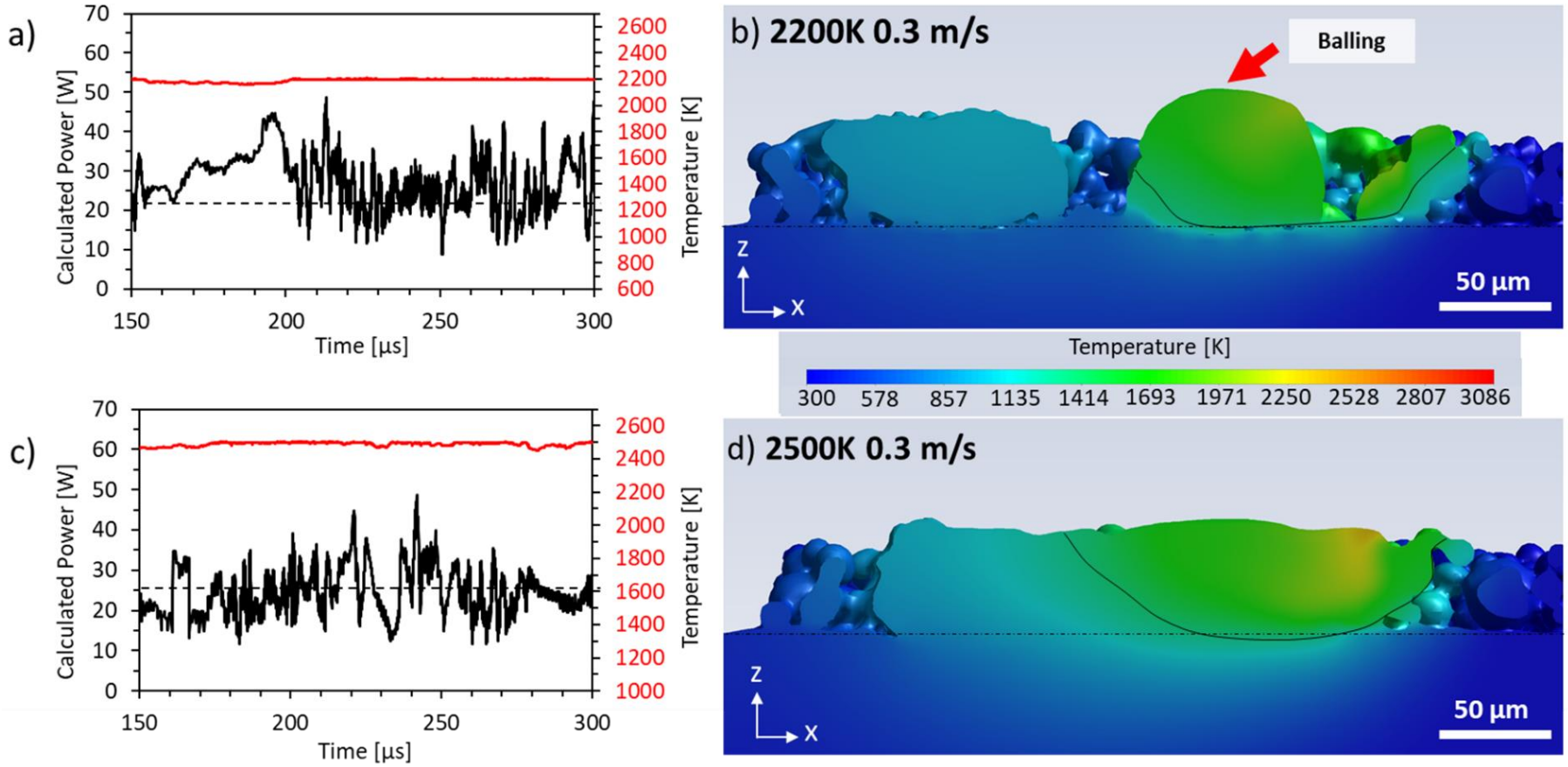

Figure 5-3 a) and c) show how the power is changed to keep a constant temperature of 2200 K and 2500 K, below the boiling point of the metal, at 0.3 m/s. b) shows how a constant peak surface temperature of 2200 K is insufficient at creating a large enough melt pool to produce a consolidated track. d) shows how a 300 K higher surface temperature is sufficient to create a melt pool large enough to prevent balling.

Figure 5-4 shows the three modes of processing in LPBF at 1.5 m/s, demonstrated by different peak surface temperatures. A peak surface temperature of 3300 K is insufficient to melt the substrate surface and create a track (Figure 5-4a). Figure 5-4b shows a YZ cross section of the track. Here, the small volume of the melt pool can be seen clearly. Also shown is the recoil pressure at the track surface, with the arrow pointing in the direction of the force generated from that pressure. The average power needed to achieve the surface temperature of 3300 K is 27 W (shown in Figure 5-4g). However, this does not result in a consolidated track. Figure 5-4b and e, show how a surface temperature of 3700 K puts the track into the conduction to keyhole transition zone. Figure 5-4e shows how the recoil force generated is sufficient to overcome the surface tension and push the melt pool downwards, towards the substrate. The melt pool is much larger, and in this image (taken from directly underneath the centre of the laser beam), the melt pool is just touching the substrate level. Figure 5-4b shows how heat conduction moves the melt pool boundary below the substrate line. The average power needed to achieve this surface temperature of 3700 K is 65 W. Figure 5-4c and f show the peak surface temperature of 4100 K. Here, the recoil pressure has created a large cavity into the substrate. Increased absorptivity through multiple reflections, increases the temperature of the surface of the cavity, so that a force is exerted on all sides of the cavity, not just at the bottom. In this instance, the more desirable melt pool depth would be between Figure 5-e and f.

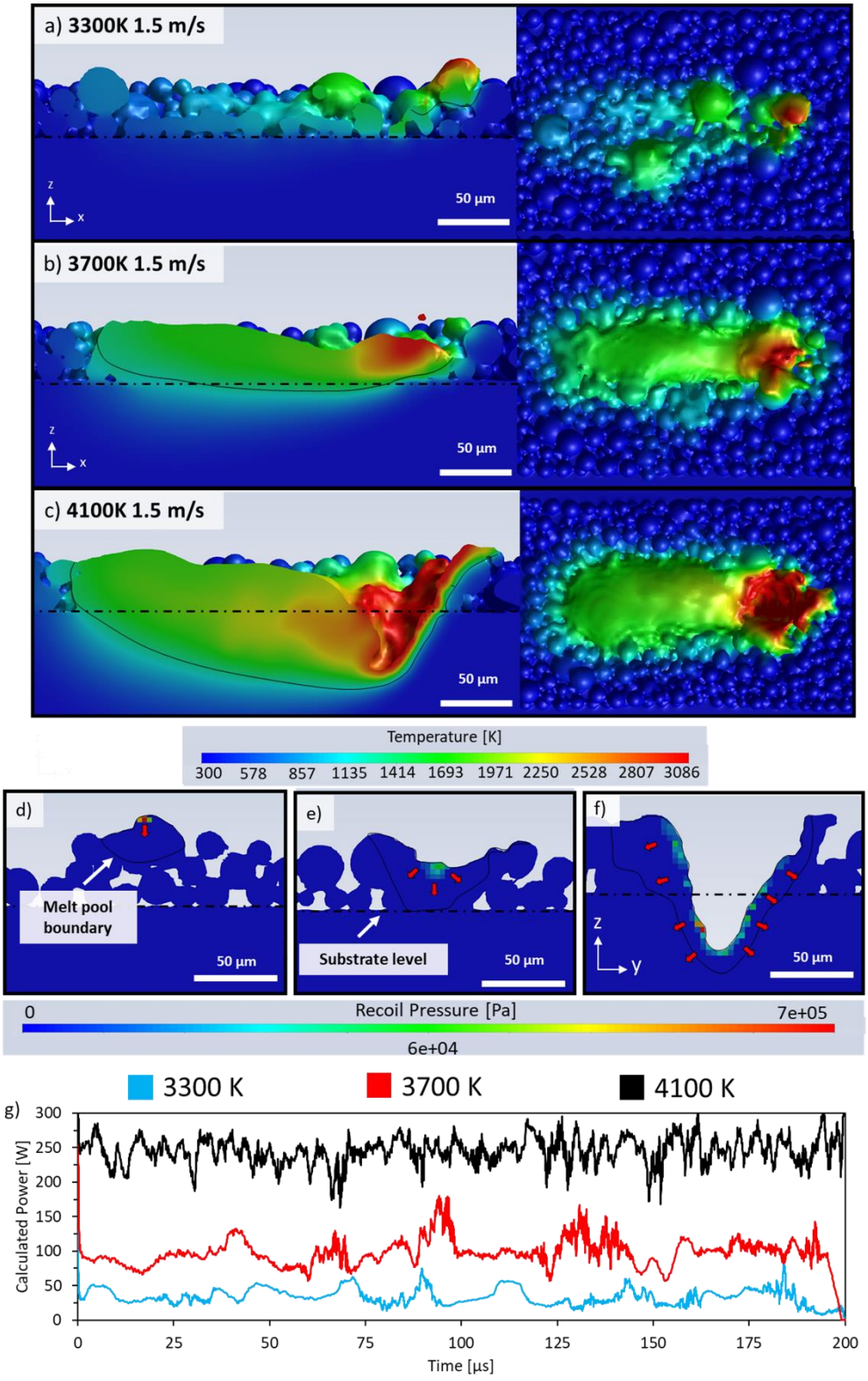

Figure 5-4 a), b) and c) Side, and top view of the melt pools created with a constant peak surface temperature of 3300 K, 3700 K and 4100 K, at 1.5 m/s. a) Underpowered melt pool, with an insufficient peak temperature to achieve consolidation at 1.5 m/s. b) Consolidated track, on the edge of the keyhole transition, with a peak surface temperature of 3700 K. c) Overpowered melt pool, with a peak surface temperature of 4100 K, which has created a keyhole cavity. d), e) and f) show the YZ plane through the centre of the laser spot. The arrows indicate the direction of the force generated by the recoil pressure. g) Power given over the length of the track for the 3300 K, 3700 K and 4100 K targets.

The average power to achieve the target temperature of 4100 K is 249 W. The results from Figure 5-2, Figure 5-3, and Figure 5-4 are summarised in Table 5-1.

Table 5-1 shows the properties of the tracks produced at different surface temperatures. The average peak temperature is the average peak melt pool temperature measured across the track length, whilst trying to stay at the target peak temperature. The average power to achieve target is the average power value across the length of the track, to achieve the average peak temperature.

Target peak temperature [K]	Scan speed [m/s]	Average peak temperature [K]	Average power to achieve target [W]	Melt pool depth below substrate [μm]
2200	0.3	2199	22.5	0
2500	0.3	2496	26.2	2.5
3300	1.5	3272	27.6	0
3700	1.5	3640	65.3	9.2
4100	1.5	3954	249.8	54.1

5.4 Discussion

5.4.1 The Inverse Solution

Literature has already proven the link between melt pool temperatures and process stability [164], [257]. Substituting laser power for peak melt pool temperature, presents a direct link to the energy transfer from the laser beam to the melt pool. The inverse solution to this problem, offers a new method of model-based feed forward modelling to control laser power based upon the peak melt pool temperature. The simplicity of this method can not only be applied to CFD, but other numerical modelling methods, such as lower fidelity analytical models, where a constant melt pool temperature is required. Additionally, by monitoring the laser power during the laser track deposition, average power values can be found that give the same average target temperature. This allows users that do not have a temperature measuring capable machine, to use these parameters which some insight to powder bed morphology has been acquired.

The inverse solution is shown in Figure 5-2a and b allowing for the appropriate energy distribution to achieve a target temperature to be reached. By varying the amount of energy supplied to the melt pool via a variable laser power, the temperature is kept to an average of 3640 K throughout the track length, with a 3700 K target temperature. The peak temperature fluctuates around this average value within 100 K of the target temperature. These fluctuations are caused by the evaporative cooling on the melt pools surface, and from changes in absorptivity, that affect the over/under shoot of the temperature calculation. However, below the boiling temperature, the inverse solution

can keep the peak melt pool temperature to within 15 K of the target temperature, as shown in Figure 5-3a and c. In this case evaporation and drastic absorption changes are not observed. To maintain a constant pool temperature, the laser power is adjusted, so that the dependency of laser power and absorptivity is no longer a significant factor. Large changes in absorptivity will only affect the peak melt pool temperature, which is modulated through this approach. This results in a much more stable melt pool. Using an average power of 106 W obtained from the inverse solution, the melt pool average peak temperature is kept to an average of 3716 K. However, the fluctuations in the temperature vary to within 250 K of the 3700 K target temperature. This is thought to be due to the constant energy input supplied by a constant laser power, not equating to constant energy absorption from the melt pool. Variations in absorptivity translate to greater fluctuations in peak melt pool temperature, as opposed to a constant melt pool temperature. Despite this, the inverse solution ensured the average temperature throughout the track length was kept within 16 K of the original target temperature. It must be noted that the laser power values for the 3700 K target temperature show a very small melt pool depth. This may be affected by spatter particles landing in the powder bed. In this instance it would perhaps be better to use the direct temperature modulation based upon particle size, so that any large spatter particles present in the powder bed, would have correspondingly larger laser powers applied to them.

A distinct advantage of using peak melt pool temperature instead of laser power, is the ability to lower thermal gradients in the melt pool, through the reduction of the peak melt pool temperature. Figure 5-3b and d show a peak temperature of 2200 K and 2500 K respectively at a speed of 0.3 m/s. However, there is a limit to how low the peak temperature can be dropped, that also results in a consolidated single track. Figure 5-3b shows how a peak temperature of 2200 K is insufficient to create a continuous laser track at 0.3 m/s. As shown by Yadroitsava et al., the laser power and speed must be tailored so that balling does not occur, critically showing that the substrate surface must be melted for a continuous track [5]. Here, the track does not melt the substrate surface. This results in surface tension forces pulling the melt pool into distinct and separate balls to reduce the surface energy. For the 2500 K track, the melt pool is sufficiently large enough to melt the substrate. This causes good metallurgical mixing at the substrate and provides incentive to form a continuous melt pool.

5.4.2 Melt Pool Manipulation via Tailored Recoil Pressure

However, whilst reducing the peak melt pool temperature is a positive step forward, relying on heat conduction alone to produce a consolidated track will result in a low laser

speed. To increase the speed of the process, an additional factor is needed to provide remelting of the substrate layer, without relying on heat conduction alone. Pushing the peak melt pool temperature to above the boiling point can provide that factor. The process of LPBF has been shown to operate much better in the transition from conduction to keyhole mode, where there is a recoil pressure acting on the surface of the melt pool [39], [147], [261], [262]. This recoil pressure aids in remelting the substrate layer, reducing lack of fusion defects and allowing higher laser scan speeds to be used.

Figure 5-4a, b, and c, show how the recoil pressure can be used to alter the track morphology, via the application of different peak melt pool temperatures. Figure 5-4d, e, and f, show a slice through the XY plane at the centre of the laser spot. Here, it can be clearly seen that a certain value of recoil pressure is needed to assert the level of melt pool movement needed to remelt to the substrate level. A peak surface temperature of 3300 K (20% over the boiling point) does not generate enough force to overcome the internal pressure of the melt pool. Therefore, the track cannot be pushed towards the substrate for remelting. At the opposite end of the scale, a peak surface temperature of 4100 K (32% over the boiling point) generates a large recoil pressure, that is sufficient in pushing the melt pool down to create a notable cavity . This relationship is shown in Figure 5-5. This presents an opportunity for keyhole porosity to develop and should be avoided. The peak surface temperature of 3700 K however, provides the ideal amount of force needed for the transitional mode, using the recoil pressure in a minimum amount to sufficiently remelt the substrate surface without forming defects.

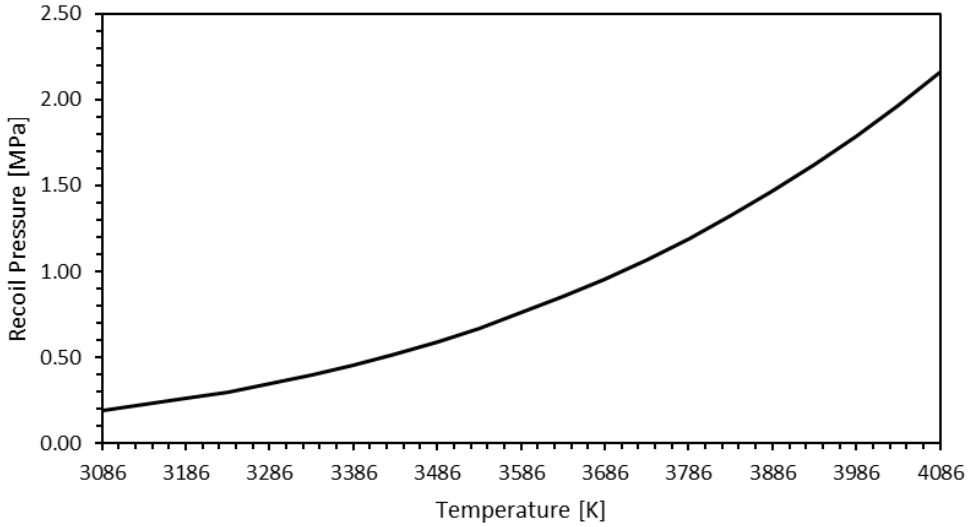

Figure 5-5 shows a plot of temperature vs recoil pressure for 316L stainless steel

Substitution of laser power with peak melt pool temperature as the principle control consideration, provides a unique opportunity to optimise this process, as this optimum

amount of recoil pressure can be calculated, and maintained by the inverse solution, through peak temperature. Figure 5-4 shows that the optimum recoil pressure must be greater than the internal pressures of the melt pool, but less than the amount needed to create a large keyhole. The internal pressure of a liquid droplet can be calculated from [42]:

$$P_i = \frac{2\sigma}{R_d} \qquad \textit{Equation 5-4}$$

Where σ represents the surface tension, R_d represents the radius of the droplet. To overcome the pressure of the droplet, P_i must be summed with P_0 the ambient pressure. To use this expression, the melt pool is simplified to a 2D droplet, sitting on a flat surface. To overcome the internal fluid pressure, the recoil pressure must exceed this, to cause a keyhole to form:

$$P_{ratio} = \frac{P_r}{P_i + P_0} \qquad \textit{Equation 5-5}$$

Where P_r equals the recoil pressure, as defined in Equation 17 [31]:

$$P_r = 0.54 p_0 exp\left[\frac{L_{vap} M(T - T_b)}{RTT_b}\right] \qquad \textit{Equation 5-6}$$

P-ratio must be larger than 1, for the internal pressure to be overcome, and for the melt pool surface to be pushed downwards. Figure 5-6a, c, and e, show the assumptions and working practice of this calculation. Figure 5-6a shows this with an example of when the ratio P-ratio is below 1. This ratio assumes that the melt pool is one surface, sitting halfway on the substrate, with the radius of the circle, equalling half the melt pool width. Applying this ratio to the peak surface temperatures of 3300 K, 3700 K and 4100 K, we can study the competing effect of recoil pressure and surface tension.

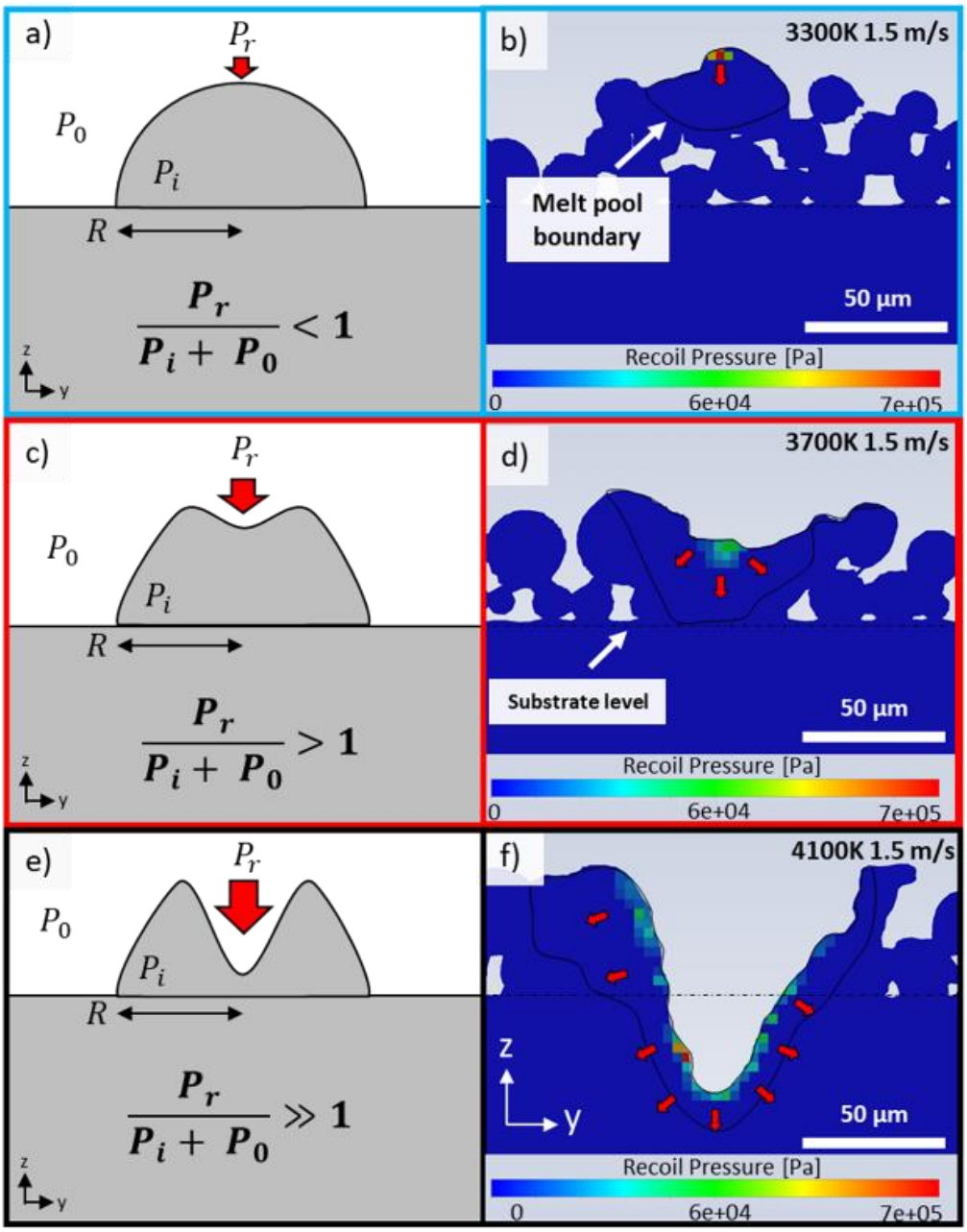

Figure 5-6 a) shows a schematic of the melt pool, with the surface temperature above the boiling point, but with the ratio Pr/Pi + Po below 1. The recoil pressure is insufficient to overcome the internal pressure. b) shows this with a peak surface temperature of 3300 K. c) shows how a surface temperature of 3700 K, has enough force to overcome the internal pressure, creating a depression in the melt pool. Here Pr / Pi + Po is greater than 1, and so a depression is created. This is demonstrated in d), where the recoil pressure is strong enough to start pushing the melt pool surface downwards. e) shows how if Pr / Pi + Po is large enough, the melt pool surface can be pushed substantially downwards. f) shows this with a surface temperature of 4100 K, where the whole surface of the newly created cavity has a force acting on the surface.

Trapp et al. assume that the normalised boiling temperature (T/T_b) should be 1.05 with R equalling the beam radius, to overcome the internal pressure. However, it can be seen that R cannot be assumed to be equal to the beam radius in all processes. At a peak melt pool temperature of 3300 K, a ratio of T/T_b is 1.06, but the P-ratio (calculated with the melt pool width) is 0.82. The internal pressure has not been overcome, due to a larger internal pressure from the smaller melt pool radius (Figure 5-6b). Figure 5-6c, and d,

shows how using a peak melt pool temperature of 3700 K, increases the value of P-ratio to 4.26. Figure 5-6d shows how this value of P-ratio has pushed the melt pool surface down 20μm, creating a consolidated track. A peak surface temperature of 4100 K shows a P-ratio value of 17.1, the large over pressure creating the keyhole cavity shown in Figure 5-6f.

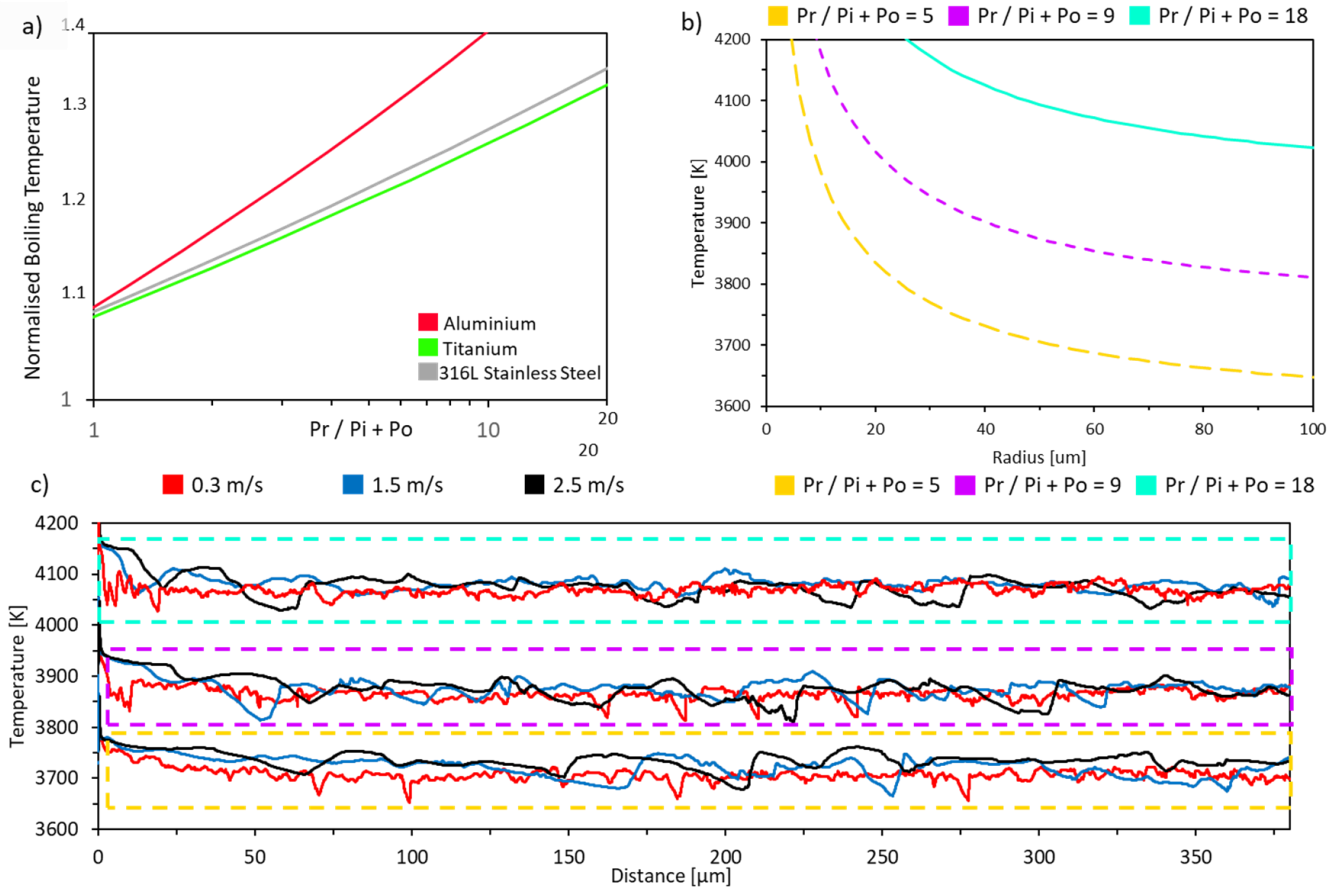

Figure 5-7 a) shows how the normalised boiling temperature (T/Tb) varies with Pr / Pi + Po for the 3 popular LPBF metals/alloys, aluminium, titanium and 316L stainless steel. Note, the logarithm of both axis is taken here. b) shows how the calculated peak temperature, tends towards the same value, regardless of R or speed. Each bounding box represents a Pr / Pi + Po value of 5, 9 and 18 respectively. c) shows us that the calculated temperature T_cpk is not dependant on speed, as each speed tends to the same temperature value. T_cpk only depends on the value of Pr / Pi + Po. (i) shows the dependence of the calculated temperature on the radius of the melt pool.

Figure 5-7a shows how the normalised boiling temperature varies P-ratio , for aluminium, titanium and 316L stainless steel, three main base metals/alloys that are commonly used in LPBF. This plot gives an indication of the sensitivity of each metal to temperature with respect to P-ratio. Aluminium has a larger gradient, indicating that it requires more energy to reach higher values of P-ratio, than either titanium or stainless steel. It is speculated that this could be partly due to the large latent heat of evaporation for aluminium. This will cause a reactionary opposite heat flux to temperatures over the boiling point. Therefore, to achieve large P-ratio values, the temperature must be increased when compared to titanium or 316L stainless steel. However, the temperature and alloying element dependency on the properties of the metal could affect the surface tension, thus affecting the internal pressure, increasing this sensitivity. Dependencies of the melt pool width from different thermal conductivities on the internal pressure would also affect these plots. But, this ratio, as it considers material specific properties related to its own surface tension, should be material agnostic.

5.4.3 Melt pool manipulation via a constant P_{ratio}

Therefore, to study the relationship of how P-ratio varies with melt pool width with respect to temperature, P-ratio will be kept constant in the numerical model. Rearranging Equation 5-5 with respect to temperature, allows the peak melt pool temperature (T_{cpk}) to be calculated based upon a constant P-ratio value. The inverse solution will then be used to regulate the melt pool peak temperature to T_{cpk}.

$$T_{cpk} = L_{vap}MT_b\left[L_{vap}M - RT_b ln\left(\frac{P_{ratio}\left(\frac{2\gamma}{R}+P_0\right)}{0.54P_0}\right)\right]^{-1} \qquad \textit{Equation 5-7}$$

Where L_{vap} is the latent heat of evaporation, M is the molar mass of the metal, and T_b is the boiling temperature. Using this equation for T_{cpk}, P-ratio is kept constant at 5, 9, and 18, for three different laser speeds, 0.3 m/s, 1.5 m/s and 2.5 m/s. This calculation uses the 'live' melt pool radius, so that T_{cpk} changes dynamically. This is done so that P-ratio represents the internal pressure of different sized melt pools. At any speed, the ratio of recoil pressure to the internal pressure should be constant, regardless of melt pool size. The independence from speed is important, as the recoil pressure should can compensate for the lack of heat conduction at high speeds. Figure 5-7b shows how at small melt pool radius's, the T_{cpk} is much higher. Figure 5-7c shows the T_{cpk} values for 0.3 m/s, 1.5 m/s and 2.5 m/s, at P-ratio values of 5, 9 and 18. The results show that the calculation of T_{cpk} is within ~20 K for the P-ratio value of 18, suggesting that the melt pool radius (R) is stable throughout the track length for all speeds tested. The P value of 9 shows a stable T_{cpk} for the track length for the 0.3 m/s, with more variation in the 1.5

m/s and 2.5 m/s values. The most variation for 1.5 m/s and 2.5 m/s speeds comes from a lower P-ratio value of 5. Here, both tracks fluctuate in T_{cpk} by ~80 K, whilst the 0.3 m/s speed is constant. A stable T_{cpk} could predict a stable track length through only small variations in the melt pool width. Figure 5-7c demonstrates this by illustrating that the calculated temperature T_{cpk} , tends to the same value at each P-ratio. This shows that laser velocity is independent of P-ratio. Furthermore, it shows that by having a stable T_{cpk}, indicates a stable melt pool radius, that indicates a stable melt pool. This can be used a metric to describe the stability of a single track in LPBF. Figure 5-7c demonstrates that P-ratio can be used as the sole factor to tailor the LPBF process.

Figure 5-8a - i show a cross section through the XZ plane to view the melt pool depth and morphology. Here we can see the visual representation of Figure 5-8h. Each P-ratio value should give an equal recoil pressure, due to a constant P-ratio value, that is maintained through the inverse solution. Figure 5-8j -l shows this through the applied force on the melt pool during the track length. Each P-ratio value inputs the approximately the same recoil force on the melt pool surface. At a P-ratio value of 5, melting occurs primarily in conduction. The track produced with a laser speed of 2.5 m/s shows balling. Here, the high speed of 2.5 m/s severely reduces the heat transfer through conduction into the substrate, causing the balling effect. This may suggest that the assumptions for Pi breakdown at very high speeds. This could be combated by increasing the value of P-ratio. These results are confirmed by experimental work from Cullom et al., that shows to be in the transitional zone, the recoil force has to be between 0.5 mN and 10 mN, and keyhole mode occurs beyond 10 mN [85]. Figure 7j and k, show an average recoil force of ~5 mN when a P-ratio value of 5 is considered. Similar behaviour are observed for P-ratio value of 9, where an average recoil force of ~10 mN is estimated. When the P_{ratio} is increased to 18 a significant increase in the average recoil force (~25 mN) is observed., It is obvious that a P_{ratio} value of 18 gives keyhole mode melting for laser scan speeds of 0.3 m/s and 1.5 m/s. An interesting transitional behaviour is instead observed in the track produced with a scan speed of 2.5 m/s (Figure 5-8i).

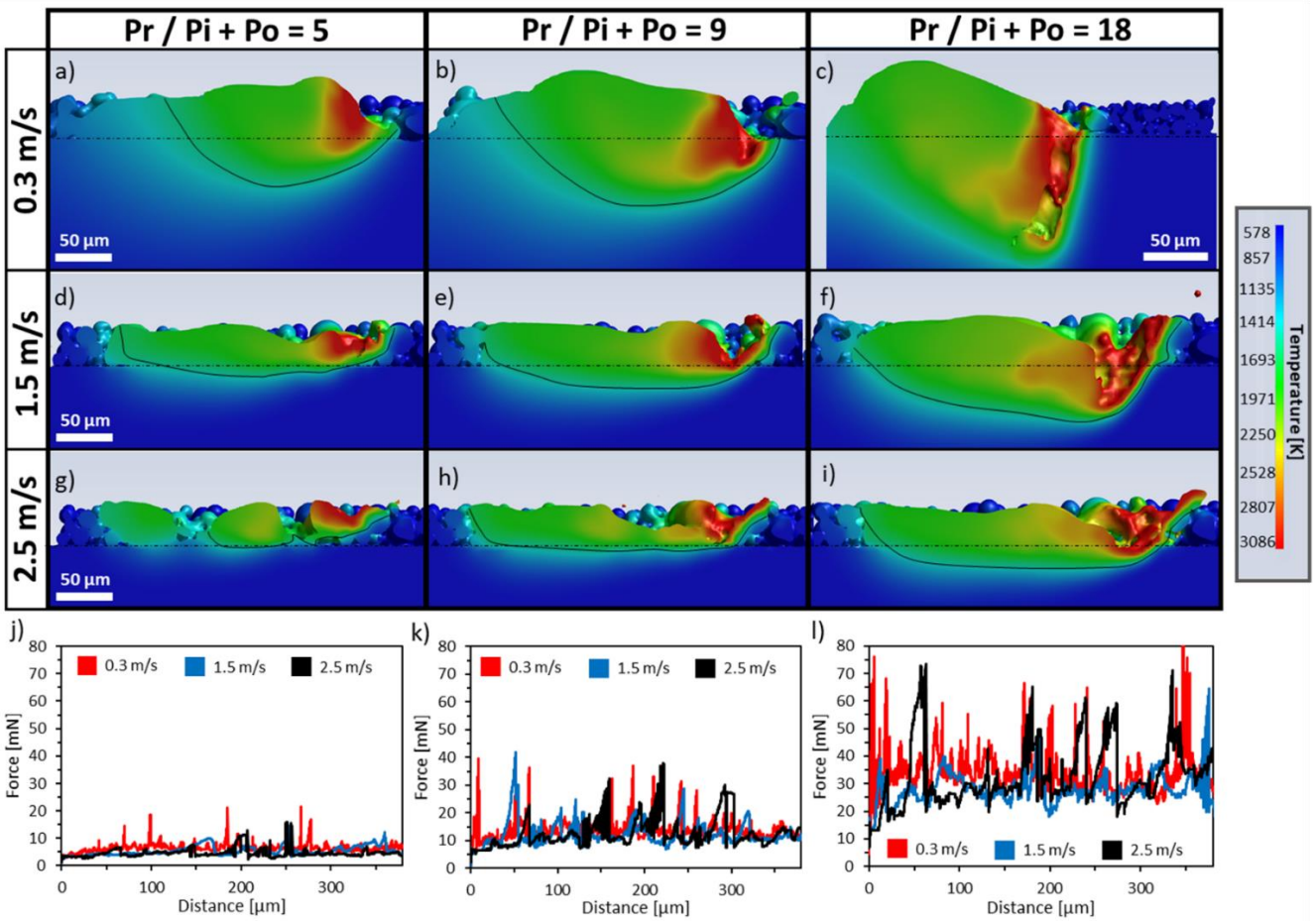

Figure 5-8 a-i show an XZ cross section through the domain. a), b) and c) show a Pr / Pi + Po of 5, 9 and 18, at the speed of 0.3 m/s. d), e) and f) show a Pr / Pi + Po of 5, 9 and 18 with a speed of 1.5 m/s. g), h) and i) shows the 3 different Pr / Pi + Po 5, 9 and 18 with a speed of 2.5 m/s. j), k) and i) show the maximum force generated by the recoil pressure over the melt pool area in mN for Pr / Pi + Po = 5, 9 and 18 at 1.5 m/s respectively.

Figure 5-9 shows how if desired, a deeper melt pool can be obtained without developing into keyhole mode via a reduction in speed. Fixing P_{ratio} at 9 and lowering the speed will ensure the same amount of recoil pressure to stay in the transition zone, but with additional melt pool depth from heat conduction.

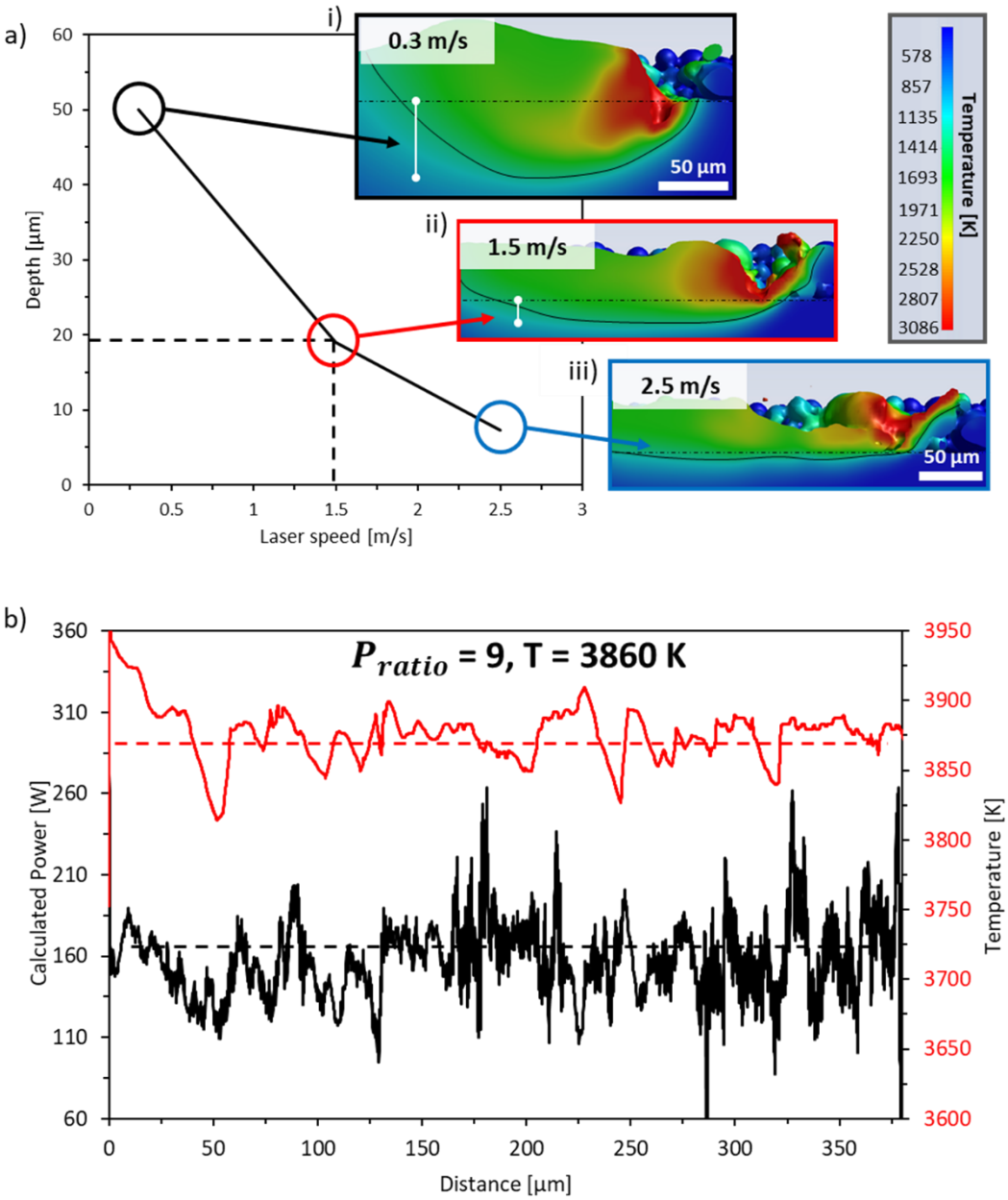

Figure 5-9 a depth vs laser scan speed for a P value of 9. This plot shows how different melt pool depths can be obtained through different laser scan speeds. For a speed of 2.5 m/s heat conduction is very limited, resulting in the lowest melt pool depth. 1.5 m/s and 0.3 m/s show how through a reduction in speed, larger melt pool depths can be obtained, without entering into keyhole mode. b) shows how using a P value of 9, results in a temperature target of 3860 K. The inverse solution is then used to keep the melt pool surface at this target while varying the laser power. An average of 161 W gives this surface temperature.

Nevertheless, the results show that, P_{ratio}, can be used as a controlling factor for track consolidation independently of speed, at least when a relative compact range of laser speeds are considered.

5.4.4 Practical Implications

Monitoring the surface temperatures of the melt pool instead of laser power, opens the door for optimisation directly based upon desirable melt pool characteristics. The calculation of T_{cpk} based upon the value of P_{ratio} provides only one variable to optimise. Furthermore, the inverse solution provides a robust platform for this model-based feed forward system, to provide not only an optimised peak temperature for the transition region, but also the accompanying laser power. Figure 5-9 gives an indication of the optimisation process. First, a laser speed is chosen so that the desired melt pool depth can be obtained, whilst still operating in the transition zone. Figure 5-9b shows the temperature target needed to operate exclusively in the transition zone, in addition to the constant laser power required for the same. This allows feed forward optimisation from three types of user. The first, is a user with an advanced variable power/ closed loop LPBF machine, with real time temperature and melt pool size monitoring. In this case, Equation 5-7 can be directly used to calculate T_{cpk} using the actual melt pool radius. This system now has an optimal peak melt pool temperature to achieve by adjusting laser power to hit the target. The simple structure of Equation 5-7 allows for T_{cpk} to be calculated quickly and on the fly. User two, has the same capability of users 1, minus the melt pool size monitoring equipment. This user would use the inverse solution with constant P_{ratio}= 9, to find T_{cpk} based upon the simulations melt pool radius. This would not be able to be calculated on the fly, and would require the inverse solution to be run pre-build. User three, has a standard LPBF machine and only can input a constant laser power. Here, the user would use the average value of the calculated power, predicted by the inverse solution. In the future, the scaling of computational power could realise the development of a fourth user. This user would be able to calculate the inverse solution in-situ, based on measured temperature fields from the build. The inverse solution framework could then be used to calculate the next power delivery based upon highly accurate temperature information. Currently due to computational restrictions, this could not be implemented with existing hardware. However, the framework presented would be valid until such time. Future applications of this work could also include substrate/part surface temperature optimisation, covering a wider area than peak surface temperature. This however is outside the scope of this work.

To validate this current framework, a P_{ratio} value of 9 is selected at 1.5 m/s, and using the inverse solution, a peak melt pool temperature of 3860 K is selected, equalling a laser power of 161 W (Figure 5-9). This should give a power value which results in a track in the transition region. Trapp et al. show us that for a laser speed of 1.5 m/s, the transitional mode for 316L stainless steel is between 120 W and 190 W [39]. The predicted value of 161 W sits in the middle of this range.

5.5 Summary

This chapter demonstrates the benefits of optimising parameters for LPBF, based upon the surface temperature of the melt pool. Manipulating laser power to control surface temperature allows compensation for large absorptivity changes during the process resulting from local variations in the powder bed. The liberation of this dependency also allows for a more direct relationship with process parameters and melt pool characteristics. The inverse solution provides a new method for keeping the surface temperature of the melt pool constant, while varying the laser power accordingly. This has allowed the process to be varied based upon an optimal recoil pressure, needed to consolidate the track at high speeds, through the manipulation of the melt pool surface. This chapter has shown that if a constant recoil pressure is applied throughout a single track, by calculating the necessary peak temperature, a consolidated track can be realised, independent of laser speed. This work allows users of feed forward models, to calculate a peak temperature value that will ensure the laser is kept in an optimal processing mode to reduce the amount of porosity. In addition to this, the inverse solution can also produce a laser power needed to keep the melt pool temperature at that optimal constant peak melt pool temperature value. This is so that systems without a temperature monitoring facility can also be optimised through a similar methodology.

The methodology is demonstrated here with 316L stainless steel, but this methodology can be applied to all material systems in LPBF. Limiting peak temperature below the boiling point could be used for challenging materials such as magnesium and zinc alloys, that are prone to boiling as a result of excessively energetic melt pools. Additionally, the inverse solution is not limited to high fidelity models, its simplicity ensures it can be used in other numerical modelling techniques.

Chapter 6

6 Model informed strategy for the processing of a high strength aluminium alloy

6.1 Introduction

This chapter focuses on the calculation of process parameters for AA2024 for a pulsed laser system, that will predict parameters needed for a consolidated track, without cracks. As outlined in the summary of chapter 5, the inverse solution can be applied to any material system for a rapid evaluation of optimal processing conditions for LPBF.

Unlike 316L stainless steel, AA2024 can exhibit solidification cracking during processing. To gain more insight into this cracking mechanism, section 1 of this chapter will use the model to measure and visualise reasons for cracking, comparing two different process parameter sets, one that cracks, and one that doesn't. Section 2 will use the inverse solution, with the effective laser speed found in section 1, to optimise the laser power for AA2024.

Many materials undergo cracking during processing, and need to be optimised for both cracking and consolidation. Cracking must also be considered for calculating the optimal properties needed for consolidation. An ideal test bed material system is high strength aluminium alloys. The selection of aluminium alloys in LPBF are limited to readily castable alloys, such as the Al-Si alloys. High strength aluminium alloys are limited in their use by cracking, caused by large solidification ranges, and unsuitable microstructures, leading to solidification cracking (hot tearing) during processing [183]. High strength aluminium alloys are a highly sought after material to use in LPBF, due to its low weight and high strength. One area in which processing of high strength aluminium alloys has improved, is in grain refinement. The addition of grain refiners promotes an equiaxed grain structure, which is able to resist solidification cracking [263]. However, this method increases raw feedstock material costs, and cannot be implemented easily in an industrial setting [264].

This work focuses on the use of a high strength aluminium alloy, AA2024. This alloy has been chosen as it can exhibit cracking but also crack free behaviour modes, influenced by changes in process parameters [8], [264]. Therefore, AA2024 presents itself as an ideal testbench to understand cracking mechanisms with the high fidelity model. The

physical process of cracking is not explicitly simulated in the model, but the predominant forces that drive crack growth can be shown in great detail. The work presented here is part of a larger project encompassing the processing of high strength aluminium alloys for LPBF at the University of Nottingham. The work presented in this chapter comprises of the effort to combat cracking. The scope of this chapter shows how a high fidelity model can be used to visualise and evaluate crack mechanisms in materials for LPBF, generating data that cannot be obtained through experimental measurements. The next stage of this project goes into the prediction and process of the elimination of cracks in high strength aluminium alloys. This work will only show results from the initial effort to combat cracking, but uses experimental data for AA2024 porosity and a post processing script to plot results that have been developed for use in the second part of the project.

Section 2 of this chapter showcases how the inverse solution can be applied to a different material system. This section will provide further validation on the use of surface melt pool temperature as the primary processing condition for optimisation. This chapter will capitalise on using the calculated peak temperature needed for track consolidation by using a P-ratio suitable for pulsed mode processing of AA2024. The results of the laser power prediction will be compared to an experimental parametric study done at the University of Nottingham to achieve optimal densification.

6.2 Methodology

6.2.1 AA2024 cracking analysis method

As outlined in the introductory section, the cracking analysis framework presented in this work will include initial work combating cracking. Namely, how the model generates the values, and initial results generated by the model and the post processing script.

The model exports a .txt file every 14 μs for every cell in the XZ plane, where y = 0. The file contains cell coordinates, temperature, cell liquid fraction, metal volume fraction, tags for the melt pool boundary and x, y and z components of velocity and temperature gradient. In addition to this, the model measures and exports, absorptivity, mushy zone volume and maximum temperature for the entire domain at each timestep. All this information is collated in the post processing script which can be used to plot this data as a function of distance and time.

The temperature gradient is calculated directly from ANSYS Fluent by [252]:

$$\Delta T(x,y,z) = \nabla \cdot \nabla f = \frac{\partial^2 T}{\partial x^2} + \frac{\partial^2 T}{\partial y^2} + \frac{\partial^2 T}{\partial z^2} \qquad \textit{Equation 6-1}$$

Where T is the temperature.

The solidification speed (R) is calculated from ANSYS Fluent during the calculation by [133]:

$$R\left(\frac{\Delta T_x}{\Delta T}\right) \qquad \textit{Equation 6-2}$$

Where T_x is the x component of the temperature gradient T. The cooling rate is calculated by:

$$\dot{T} = \frac{\partial T}{\partial t} \qquad \textit{Equation 6-3}$$

Where $\dot{T}$ is the cooling rate and t is time. The strain rate is calculated by [265]:

$$\dot{\varepsilon} = \dot{T}\alpha \qquad \textit{Equation 6-4}$$

Where α is the coefficient of thermal expansion of the metal.

6.2.2 Cracking model parameters

Two processing parameters are used in this section, PD15 and PD60. The parameters of PD15 are based on work by Zhang et al. and experimental studies performed at the University of Nottingham [8]. The effective laser speed of 0.107 m/s is used in this study as it elicits a crack free structure, whilst moving to a higher effective speed of 0.43 m/s produces cracks. The comparison of these two parameters aims to visualise the driving crack mechanisms in this alloy. The parameters for PD15 and PD60 are stated again below for reference.

Table 6-1 shows the laser input parameters for the aluminium validation.

Type	Laser Power [W]	Point distance [µm]	Exposure time [µs]	Delay time [µs]	Effective velocity [m / s]	Beam diameter [µm]
PD15	200	15	120	20	0.107	75
PD60	200	60	120	20	0.428	75

The domain size is 800 x 340 x 300 µm, with a substrate height of 150 µm, powder layer of 50 µm, spot radius of 35 µm, with the same PSD used in the validation study. To mimic the pre-heat inside the Renishaw AM400 build chamber during process of the cube samples, the domain walls and initial modelling conditions are set at a temperature of 443 K. The track length is 600 µm, with a total of 9.5 pulses for PD60 and 39.5 pulses for PD15.

6.2.3 AA2024 process prediction framework

6.2.3.1 Overview

This chapter focuses on the prediction of process parameters for AA2024 using a pulsed laser system identical to the one used in a Renishaw AM400 LPBF machine. The prediction of the laser power needed for a consolidated track at a relative laser speed of 0.107 m/s is achieved with a revised version of the inverse solution, to work with a pulsed laser.

Control of the melt pool peak temperatures is achieved with the inverse solution, as outlined in section 5.2.1. This regulates the maximum temperature of the metal domain, through the control of laser power inputted into the melt pool. The revised refractive index will be used for AA2024, to get an absorptivity value at each timestep, the value of which is driven by the local geometry within the laser beams spot size.

The domain size for the inverse solution is 500 x 260 x 400 μm, with a substrate height of 250 μm, powder layer of 50 μm, spot radius of 35 μm, with the same PSD used in the validation study. To mimic the pre-heat inside the Renishaw AM400 build chamber during process of the cube samples, the domain walls and initial modelling conditions are set at a temperature of 443 K.

6.2.3.2 Inverse solution parameters

The inverse solution will be used to predict process parameters for a pulsed laser system. Therefore the inverse solution has a modifier to reduce the calculated temperature (T_{cpk}) to zero when there would be no power supplied during the delay section of the pulse.

As derived and described in section 0 and 5.4.3, a constant P ratio of 5 and 3 will be used in the prediction of the AA2024 parameters. A P-ratio of 5 was the starting value for this optimisation, but showed porosity during the single track deposition. This porosity can be seen in Figure 6-10. Therefore, the optimisation was restarted with a lower P-ratio of 3.

6.2.3.3 Experimental cube parameters

Cubes are printed for the verification of predicted process parameters, to see if the inverse solution has correctly outputted a laser power that will give a consolidated track at the speed of 0.107 m/s. The cubes are printed on a Renishaw AM400 LPBF machine with AA2024 powder procured from TLS Technik GmbH & Co. Details on the Renishaw AM400 are provided in section 3.63.6. The chamber is preheated to 443 K during the building process. An experimental window of between 200 – 220 W has been empirically

formed through extensive process optimisation. Therefore, the laser powers chosen for the empirical study are 180 W, 200 W, 220 W and 240 W to cover the laser power range that the model should predict. The 10 x 10 x 10 mm cubes were printed with a meander scan strategy with a 67 ° rotation at each 30 µm layer thickness, with 120 µm hatch distance. The cubes are sectioned, ground, polished and viewed under a Nikon Eclipse LV100 ND optical microscope to view porosity. Porosity calculations were made with ImageJ.

6.3 Results

Figure 6-1 shows the plot labelling conventions that are to be used in this chapter. Variables presented in these images are only for the metal portion of the image, the argon portion of the image is coloured only to provide contrast to the melt pool edge. Contour gradients have been capped in images to clearly show the gradient in the mushy zone of the melt pool rather than in the bulk melt pool liquid. Pulse time duration is a number that represents how far through one lase pulse the image that is displayed was captured. For example; if the pulse time duration is between 3 and 4, then this is displaying the 3rd pulse along the single track. For instance Figure 6-1 shows the 3rd pulse in the cycle, and the 0.4 represents that this is 40% of the way through the 3rd pulse. This number gives clarity on which pulse is being displayed, for images comparing different effective laser speeds, would be on a different pulse for the same timestamp.

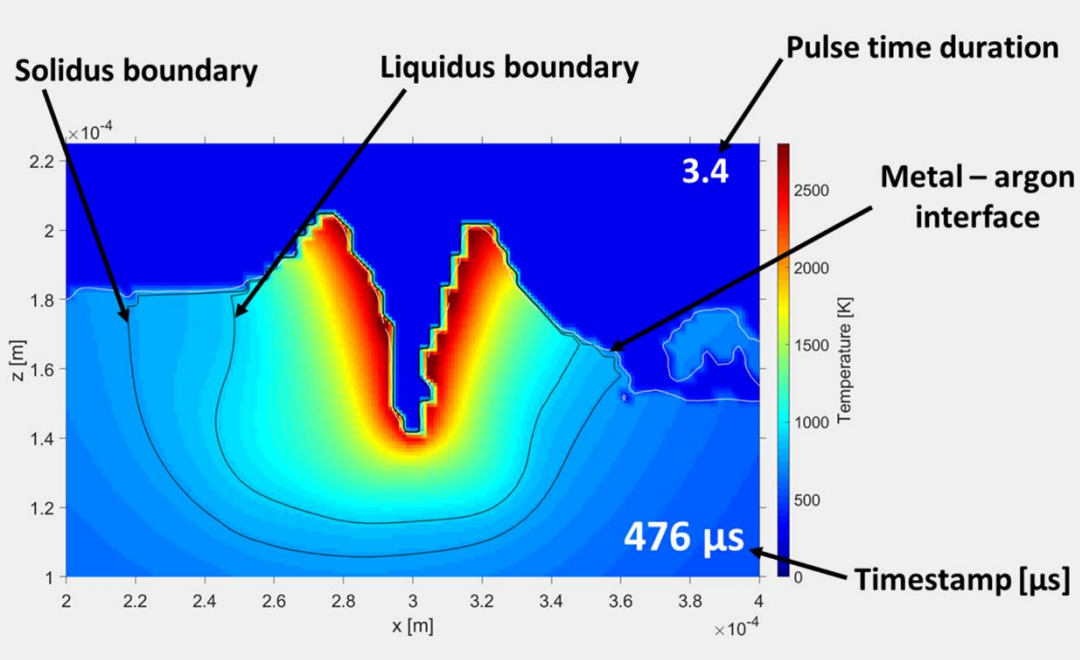

Figure 6-1 shows an explanatory figure showing the different aspects of each figure presented in this results chapter.

6.3.1 AA2024 cracking analysis framework

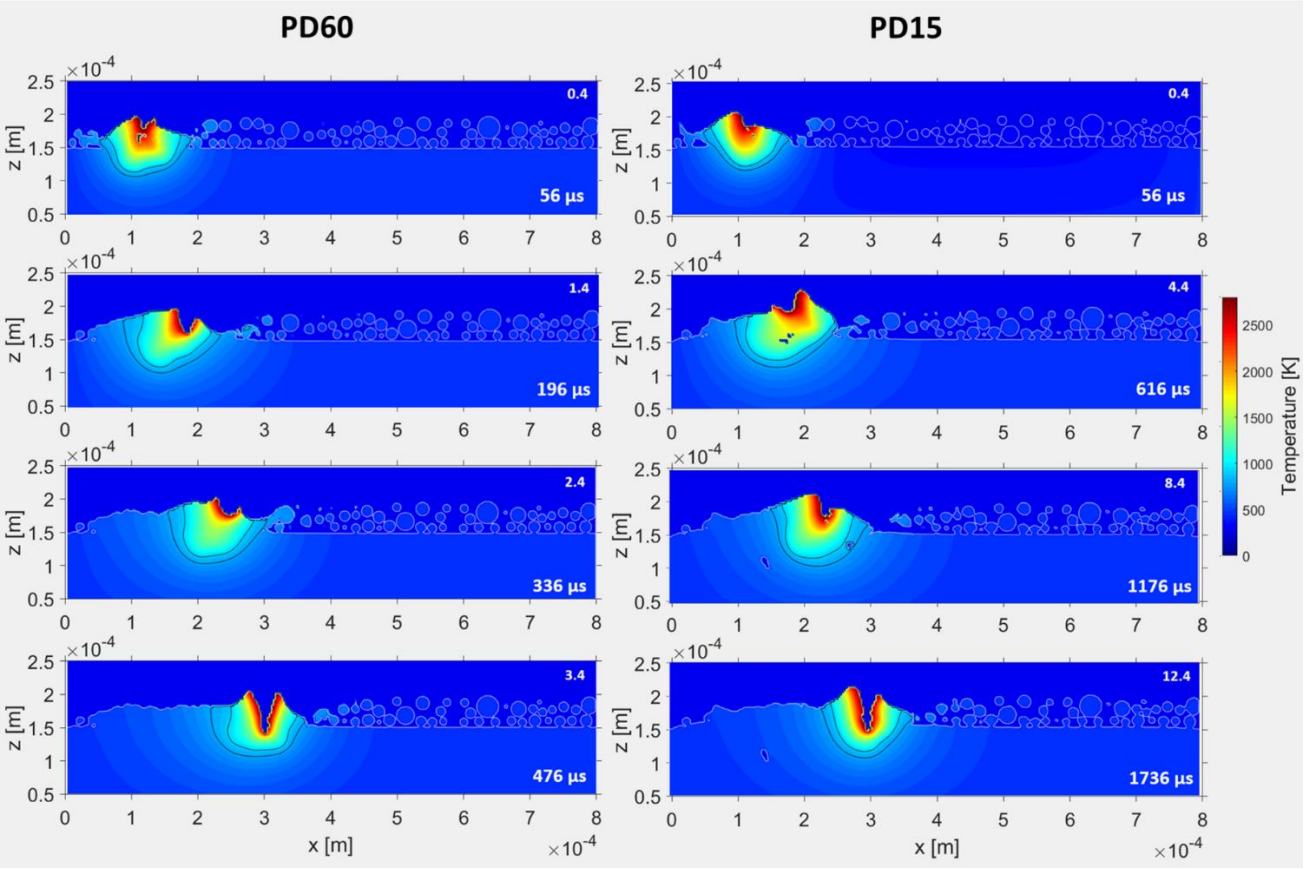

Figure 6-2 shows XZ cross sections of PD60 and PD15, showing the temperature field in the XZ plane. The contour bars show temperature, with the top limit set to the boiling temperature of AA2024 (2743 K). The left column shows PD60, and the right column shows PD15. Rows represent different time series of both PD60 and PD15. Each row is matched so that the corresponding PD15 pulse impacts in the same location. The upper right corner of each plot shows the pulse at each snapshot. 1.0 represents the end of the first pulse, so therefore 0.4 represents the snapshot at 48 µs through the pulse duration.

The results presented in this section show the power of high resolution, high fidelity modelling. Figure 6-2 shows a sequence of images showing how the temperature field in the XZ plane changes through time. Due to different effective speeds of PD60 and PD15, the images are taken at different timepoints, but at the same geometric location on the x axis. The images are taken at 0.4 of the way through the duration of the laser exposure, at 48 μs through the pulse duration. Black lines encompass the mushy zone boundary within the melt pool, with the white lines denoting the interface between metal and argon cells. These sequence of images show initial similarities between each of the temperature fields, with both displaying similar melt pool sizes and temperature distribution. However, large differences occur in the size of the mushy zone at the back end of the melt pool.

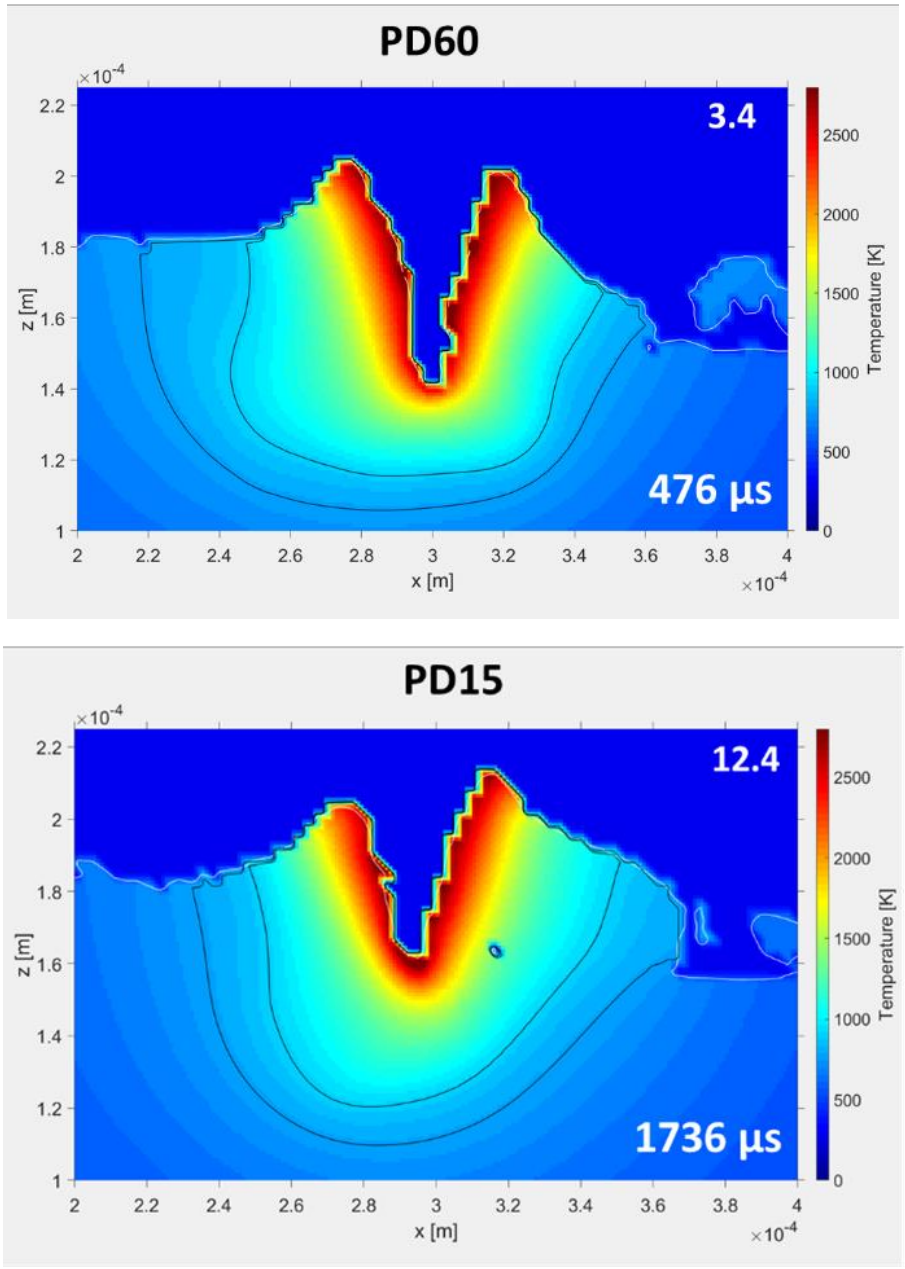

Figure 6-3 shows a magnified image of the last row in figure 6-1, for both PD60 and PD15. The contour bars show the temperature field in the window between x position 200 µm and 400 µm. The contour bars show temperature, with the top limit set to the boiling temperature of AA2024 (2743 K). Here, the white line represents the interface between argon and metal cells. The outside black line shows the solidus temperature boundary, whilst the inner black line denotes the liquidus temperature boundary.

Figure 6-4 shows these differences in a magnified image of the 3rd and 12th pulse of PD60 and PD15 respectively. Both melt pools show a distinct, small keyhole cavity, with both sets of parameters using the same laser power of 200 W. Differences occur however, in the location of the cavity relative to the melt pool width in the x direction. PD60 displays a slightly more forward cavity relative to the front of the melt pool. PD15 shows a higher and wider front section of the melt pool, between 320 and 365 µm. The largest difference is the width of the mushy zone at the back of the melt pool. This zone is more critical, as

it will not see complete remelting in subsequent pulses, and so microstructure/phases formed here could stay throughout the build process.

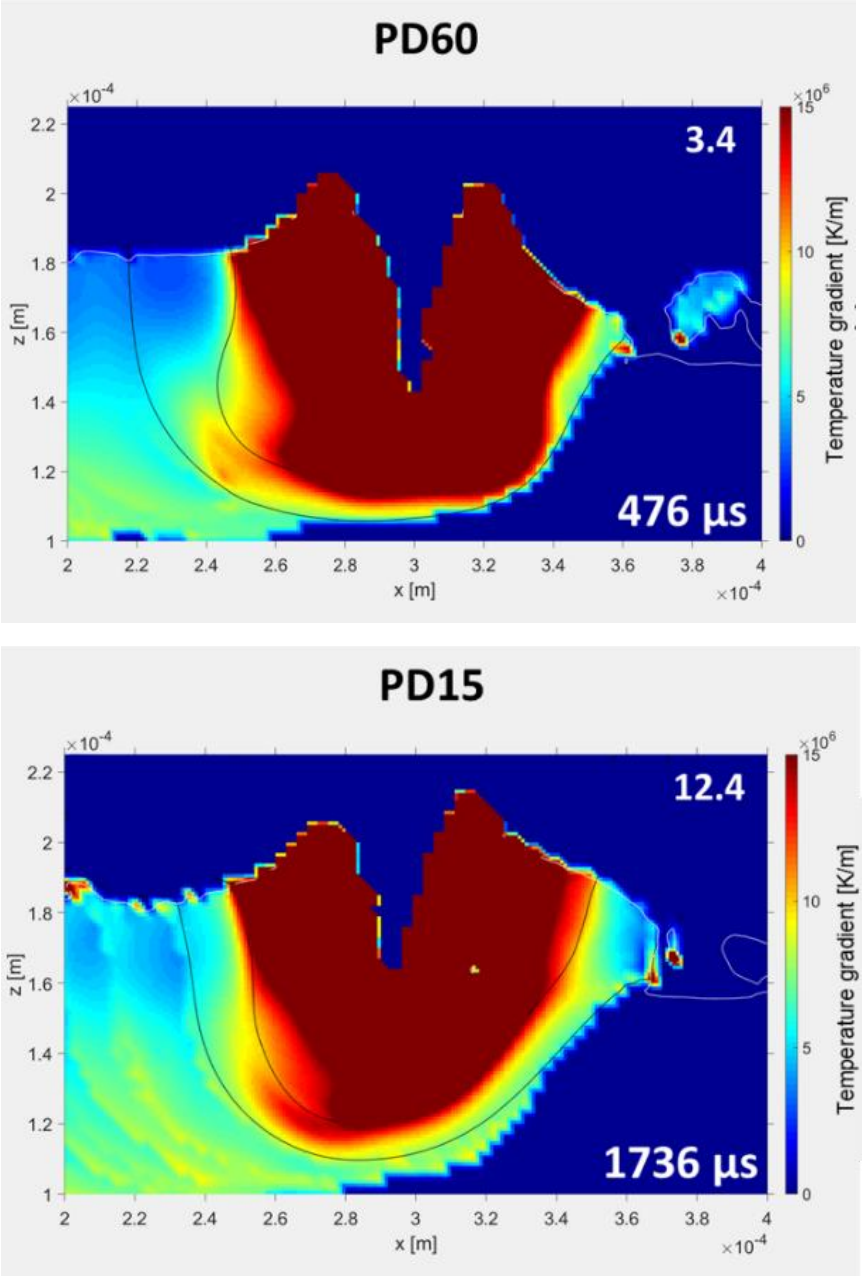

Figure 6-4 shows a magnified image of the last row in Figure 6-1, for both PD60 and PD15. The contour bars show the temperature gradient field in the window between x position 200 µm and 400 µm with the top limit set to 1.5e7 K/m. Here, the white line represents the interface between argon and metal cells. The outside black line shows the solidus temperature boundary, whilst the inner black line denotes the liquidus temperature boundary.

This difference can also be seen in the temperature gradient and solidification speed shown in Figure 6-4 and Figure 6-5. This critical size difference between the two mushy zones in PD60 and PD15, can be seen by focussing again on the back portion of the melt pools. PD60 shows a large gradient of the temperature gradient near the surface of the melt pool at XZ position 240, 180 µm. This gradient of the temperature gradient is not

observed in the PD15 sample across the mushy zone width. An overall higher G is overserved in the mushy zone for PD15.

The attention of the reader is directed towards the rear of the melt pool in Figure 6-4 and Figure 6-5. Values of G are frozen in time if the cell is no longer liquid. Hence values of G and R remain at the values they were at the moment the cell changes to a liquid fraction of 0. Values of G behind the mushy zone at XZ position 220, 120 µm in Figure 6-4 show distinct streaks behind the melt pool of PD15, whereas this is more continuous in PD60. These streaks represent microstructure conditions which would be solidified at this particular instance in time.

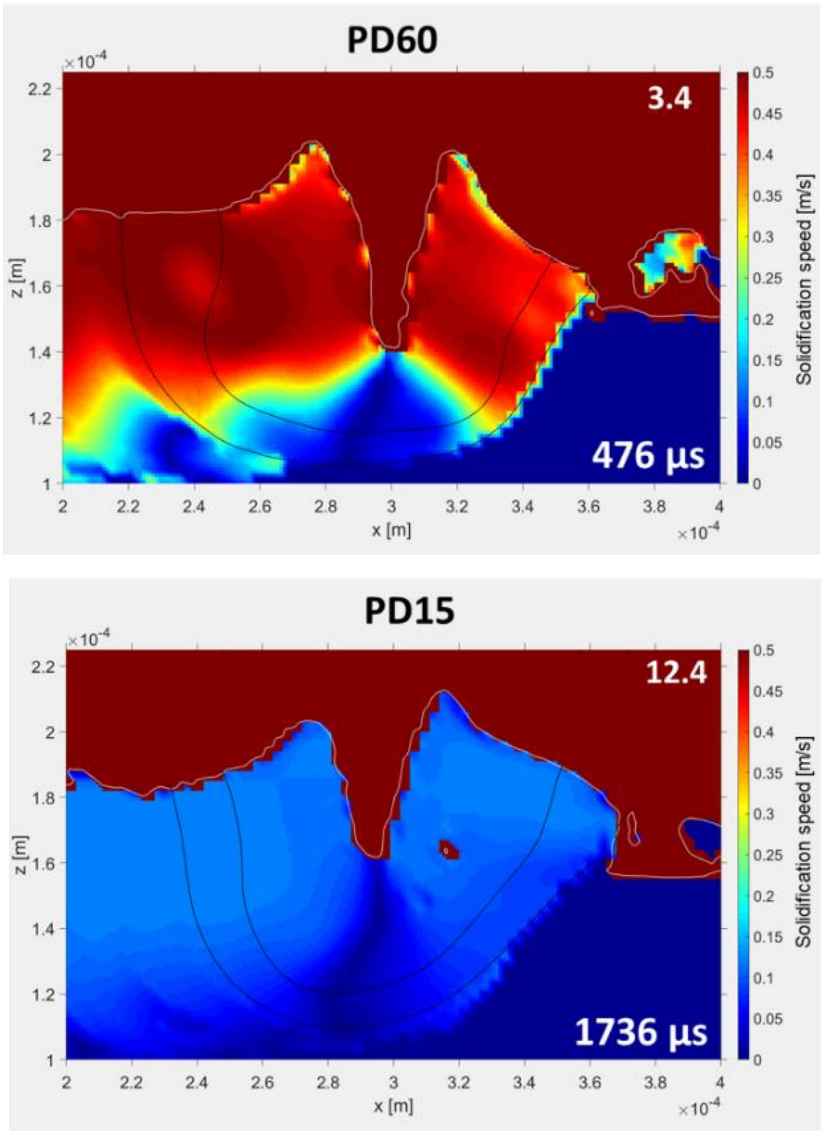

Figure 6-5 shows a magnified image of the last row in Figure 6-1, for both PD60 and PD15. The contour bars show the solidification speed in the window between x position 200 µm and 400 µm with the top limit set to 0.5 m/s, close to the maximum speed for PD60. Here, the white line represents the interface between argon and metal cells. The outside black line shows the solidus temperature boundary, whilst the inner black line denotes the liquidus temperature boundary.

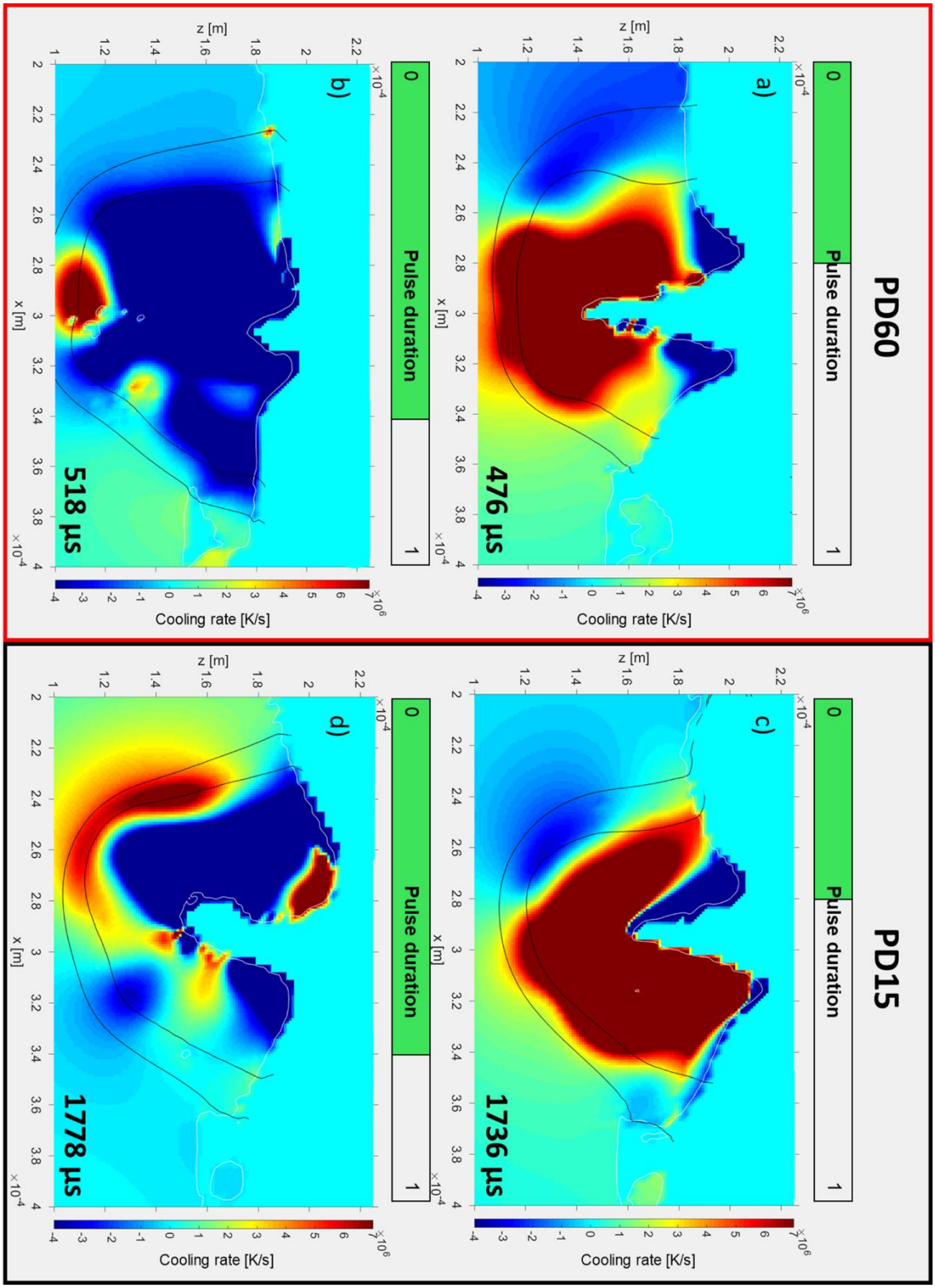

Figure 6-6 shows a magnified image of the last row in Figure 6-1, for both PD60 and PD15, but showing sequential images showing the transition from 0.4 of a pulse, though 0.7, 0.8 and 0.9. Images a – b show PD60 and images c – d show PD15. The images show that when the laser is turned off at 0.85 of a laser pulse, how the melt pool cools. The contour bars show the cooling rate in the window between x position 200 µm and 400 µm with the limit between 7e6and -4e6 K/s. A negative cooling rate shows cooling, whilst a positive cooling rate shows heating. Here, the white line represents the interface between argon and metal cells. The outside black line shows the solidus temperature boundary, whilst the inner black line denotes the liquidus temperature boundary.

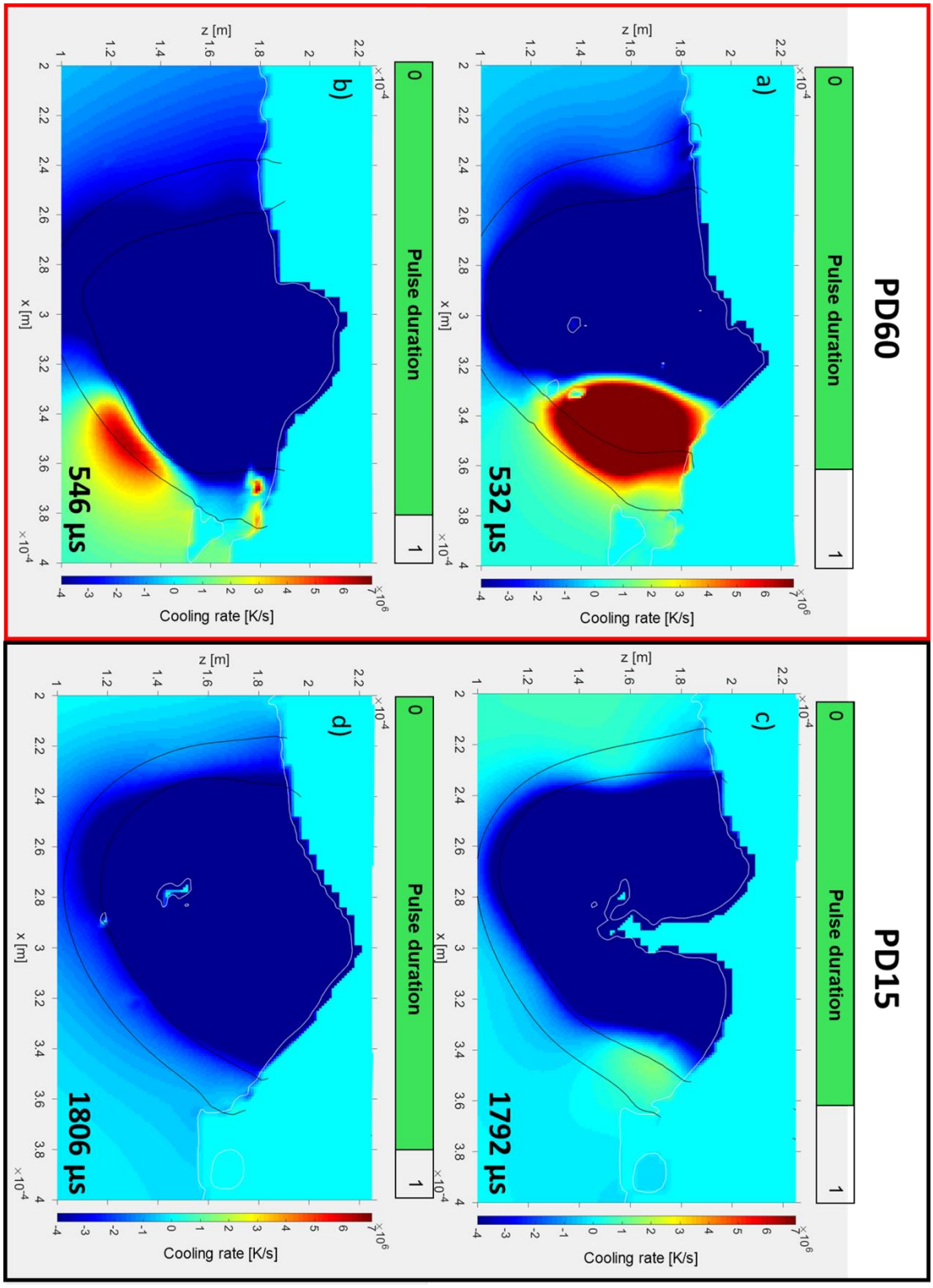

Figure 6-7 shows a magnified image of the last row in Figure 6-1, for both PD60 and PD15, but showing sequential images showing the transition from 0.4 of a pulse, though 0.7, 0.8 and 0.9. Images a – d show PD60 and images e – h show PD15. The images show that when the laser is turned off at 0.85 of a laser pulse, how the melt pool cools. The contour bars show the cooling rate in the window between x position 200 µm and 400 µm with the limit between 7e6and -4e6 K/s. A negative cooling rate shows cooling, whilst a positive cooling rate shows heating. Here, the white line represents the interface between argon and metal cells. The outside black line shows the solidus temperature boundary, whilst the inner black line denotes the liquidus temperature boundary.

Figure 6-5 shows this same timestamped image for solidification speed for PD60 and PD15. The scale for both images is capped at 0.5 m/s, the max value of R seen in PD60. The max values of R are valued at close to their respective effective laser speeds. R shows the solidification speed of the melt pool, a value which influences the critical cooling rate.

Figure 6-6/7 shows the cooling rate for both PD60 and PD15 throughout a laser pulse. Both Figure 6-6 and Figure 6-8 use Equation 6-1 and Equation 6-2 for the calculation of G and R. Ordinarily literature uses G*R as the value for cooling rate. However, the use of a pulsed laser questions the validity of that calculation of R, as a pulsed laser is stationary when it delivers its power to the melt pool. Hence, the cooling rate in this instance is calculated by Equation 6-3, which calculates the cooling rate based upon the results from the next timestep file. Additionally, these values are not frozen when the cell has a liquid fraction of 0, they are 'live' throughout the XZ plane. Figure 6-6/7 shows the differences in cooling rate for both samples in the magnified XZ plane. Here, a positive value of cooling rate shows heating, and a negative value shows cooling. Care must be taken when observing the trends in cooling rate, as the cooling rate is calculated by measuring the cooling rate from the current time file to the subsequent file. Hence, the cooling rate is between the two pulse time durations. For example, at a pulse time indicator of 0.7, this shows the heating/cooling from pulse 0.7 to 0.8. Higher resolution time frames will provide more detail in this analysis. Over the course of a 5 ms long however, the amount of data files becomes time consuming to process through the post processing script. However, definite trends can still be observed in this data.

The heat transfer in Figure 6-6/7 throughout the melt pool is shown to be very different for PD60 and PD15. Due to close successive pulses with a low point distance, resulting in a low effective speed, PD15 shows a cooling rate of close to zero for the majority of material at the back of the melt pool at 0.4 pulse time duration. In contrast, PD60 shows a much higher negative cooling rate of 2.5e6 K/m at the back of its melt pool. Throughout the mushy zone, PD15 shows a majority of positive cooling rate (heating), whilst PD60 shows negative cooling rate. Large variations in the negative and positive cooling rates occur up to the time when the laser is switched off at 0.85 pulse time duration. Consistent trends are observed in this critical transition period at the end of the laser exposure. PD60 shows a severe negative cooling rate compared to PD15 within the mushy zone at the back of the melt pool. High negative cooling rates are present all the way through the cooling of the melt pool. Conversely, PD15 shows much a much higher positive cooling rate when compared to PD60 in its mushy zone over the same time period.

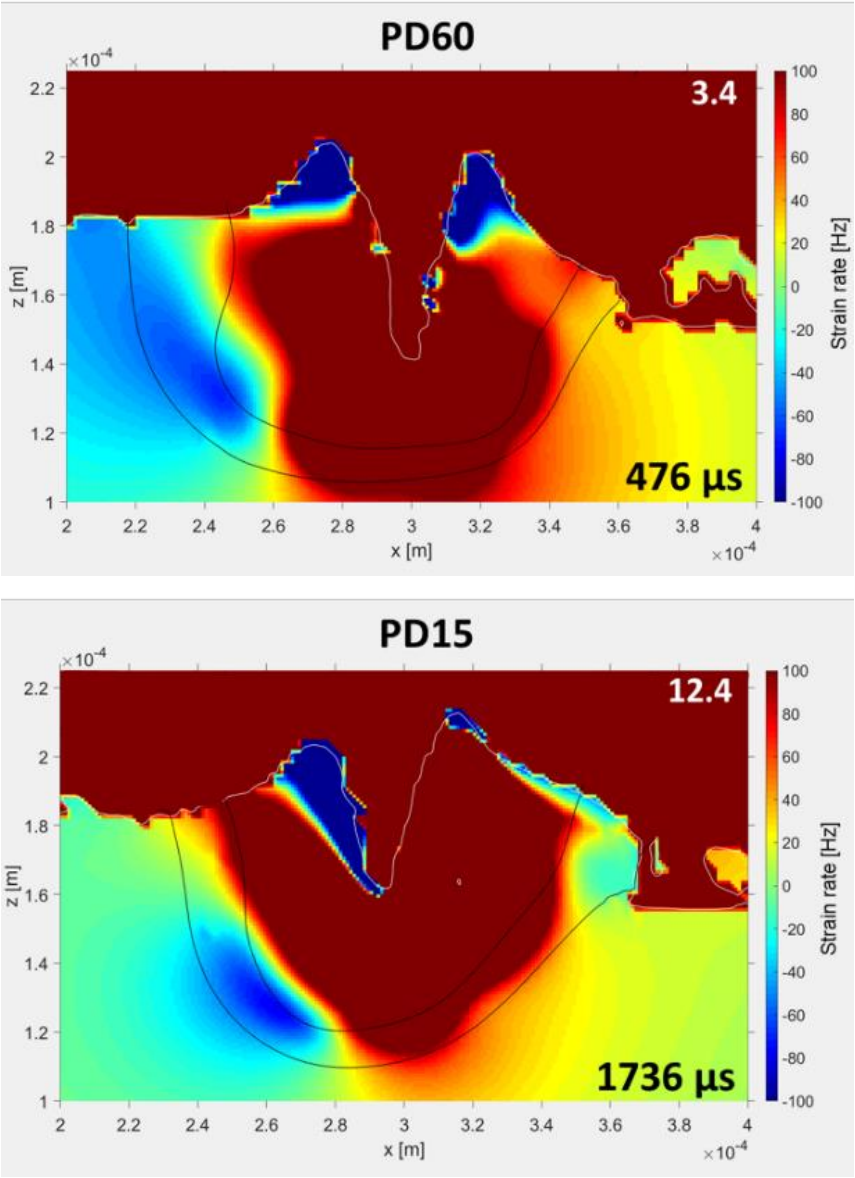

Figure 6-8 shows a magnified image of the last row in Figure 6-1, for both PD60 and PD15. The contour bars show the strain rate in the window between x position 200 µm and 400 µm with the top limit set to 100 Hz and the bottom limit set to -100 Hz. Here, the white line represents the interface between argon and metal cells. The outside black line shows the solidus temperature boundary, whilst the inner black line denotes the liquidus temperature boundary.

Figure 6-8 shows the cooling rate multiplied by the coefficient of thermal expansion of AA2204, to give the strain rate values given by the cooling rate in the melt pools.

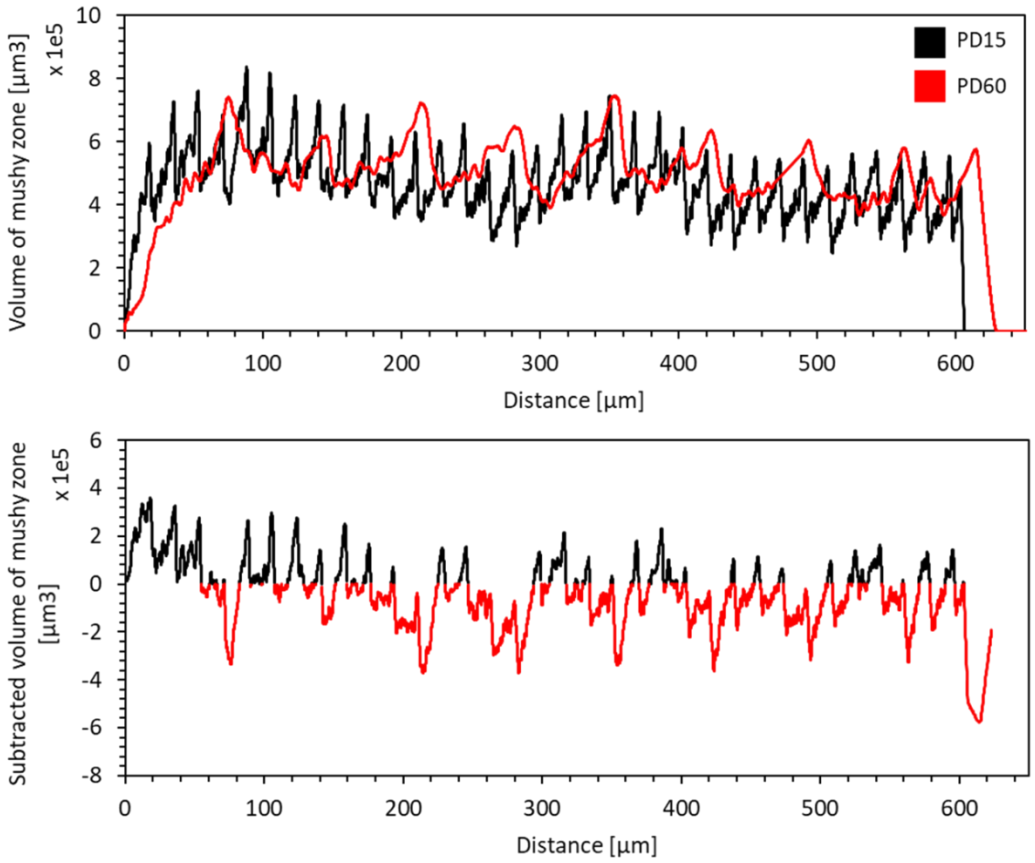

Figure 6-9 shows the volume of the mushy zone, for PD15 (in black) and PD60 (in red). As the two different parameter sets use different point distances (and therefore different effective speeds), this plot depicts the volume of the mushy zone as a function of distance and not time. The top plot shows the volume of the mushy zone as a function of the entire track length. The lower plot shows the plot PD15 subtracted by PD60, showing the amount that PD15 is under/over PD60.

Figure 6-9 shows a plot of the mushy zone volume as a function of distance. The top plot shows the comparison of mushy zone volume for PD60 vs PD15. Due to the differences in effective speed, this plot drawn as a function of distance and not time. It can be seen that the volume of the mushy zone for PD60 is higher than PD15 for the majority of the track length. This is shown in the amount of red in the bottom image of Figure 6-9. The bottom plot of Figure 6-9 shows the subtraction of PD15 against PD60, to clearly show when the mushy zone size of PD15 is below PD60. When the volume of the mushy zone for PD15 falls below PD60, this is shown as red trace in the plot, whilst black shows when the mushy zone volume is larger for PD15. This critical parameter shows that PD15 has a predominantly lower mushy zone volume than PD60. It must be noted that PD15 has 4x as many pulses than PD60 for the same track length. During each pulse duration, the melt pool volume gets progressively larger as more material melts during the laser exposure. These peaks after the first pulse are larger for PD60 than PD15.

6.3.2 AA2024 behaviour prediction

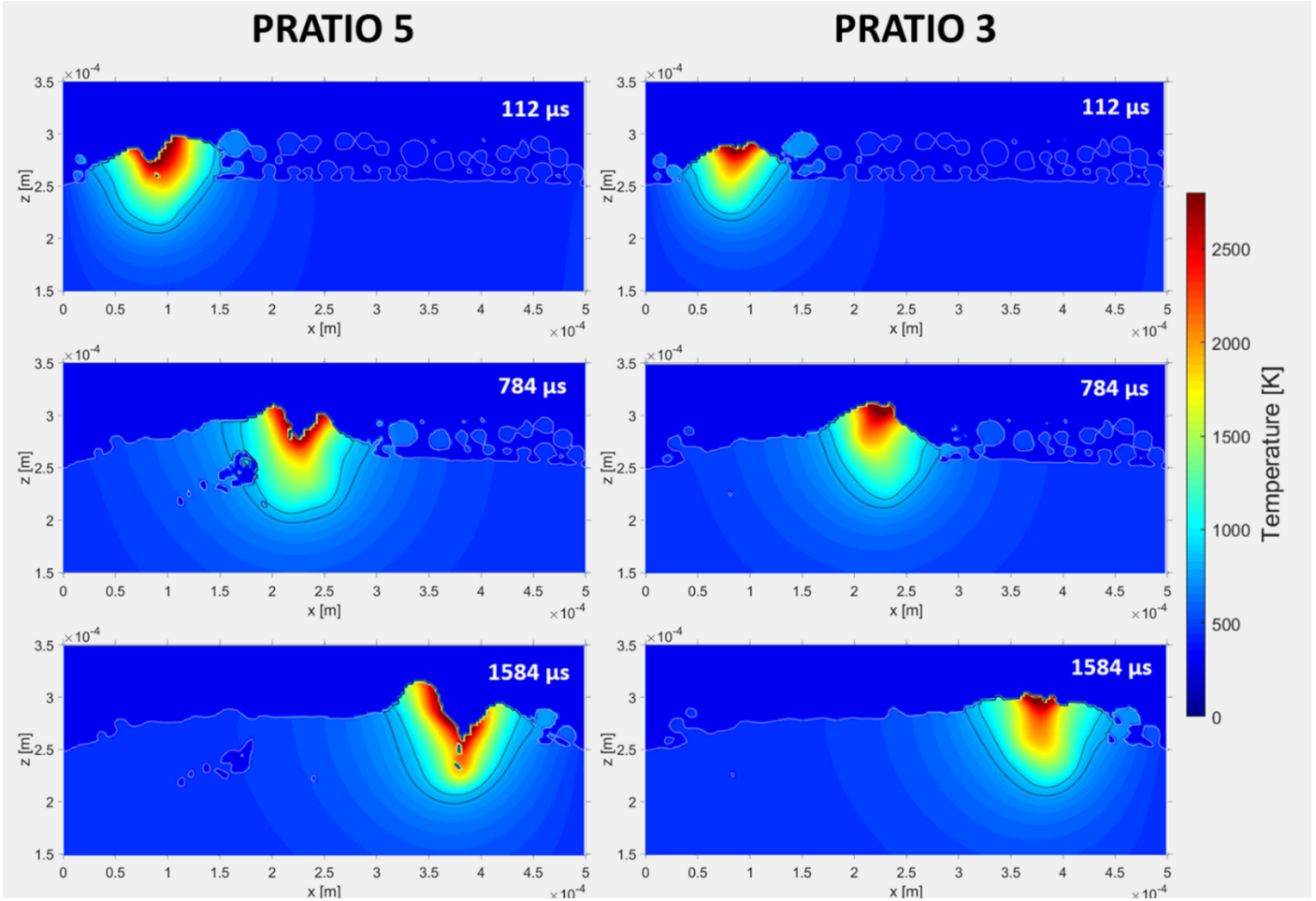

Figure 6-10 shows the XZ cross section of P-ratio 5 and P-ratio 3. The left column shows P-ratio 5 and the right column shows P-ratio 3, with the rows increasing sequentially from 112 µs, 784 µs, 1584 µs. The contour bars show temperature, with the top limit set to the boiling temperature of AA2024 (2743 K). The images show the effect of different power inputs on the temperature fields experienced at different sections of the track.

Figure 6-10 shows how the temperature field in the XZ plane develops over time, during three successive intervals for a P-ratio of 5 and a P-ratio of 3. It can be clearly seen that a P-ratio of 5 provides excessive energy into the melt pool. Porosity is generated close to 784 μs , and then is fully captured by solidified material at 1584 μs. P-ratio 5 was initially chosen as the P-ratio value from the study with 316L stainless steel. This value was decreased to 3, with the discovery of porosity in the single track of a P-ratio of 5, due to excessive energy input. In contrast, a P-ratio value of 3 gives a consolidated track without the presence of porosity. Figure 6-10 shows the melt pool cavity size differences between P-ratio 5 and P-ratio 3. P-ratio 5 progressively develops a deep keyhole cavity, increasing to a height of approximately 100 μm at 1584 μs. In contrast, a lower P-ratio of 3 gives a more stable melt pool. Melt pool fluctuations do not give rise to porosity.

Table 6-2 shows the melt pool dimensions of P-ratio 5 and P-ratio 3.

Type	Model melt pool width [μm]	Model melt pool depth [μm]
P-ratio 5	164.7	74.35
P-ratio 3	147.6	35.6

The melt pool dimensions of both P-ratio 5 and P-ratio 3 are given in Table 6-2.

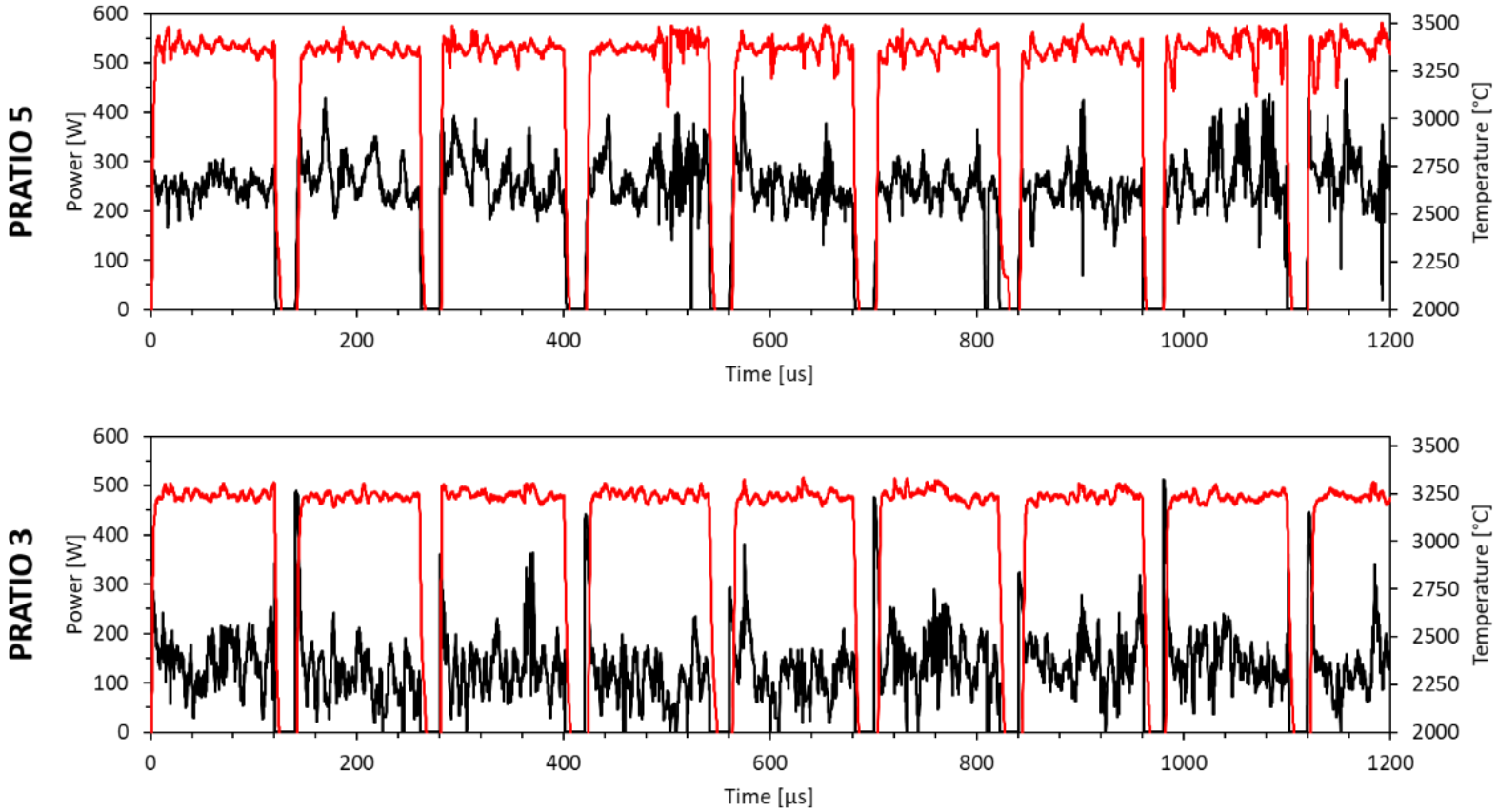

Figure 6-11 shows calculated power and the peak temperature as a function of time for P-ratio 5 and P-ratio 3. The red line denotes temperature and is measured off the secondary axis (right). The black line is the calculated power and is measured off the primary axis (left). Average values of power for P-ratio 5 are 268 W and 216 W for P-ratio 3.

Figure 6-11 shows the plot of calculated power and peak melt pool temperature of both P-ratio 5 and P-ratio 3. The average calculated power for P-ratio 5 is 268 W, and 216 W for P-ratio 3. The power and temperature decrease within the laser delay period between each pulse.

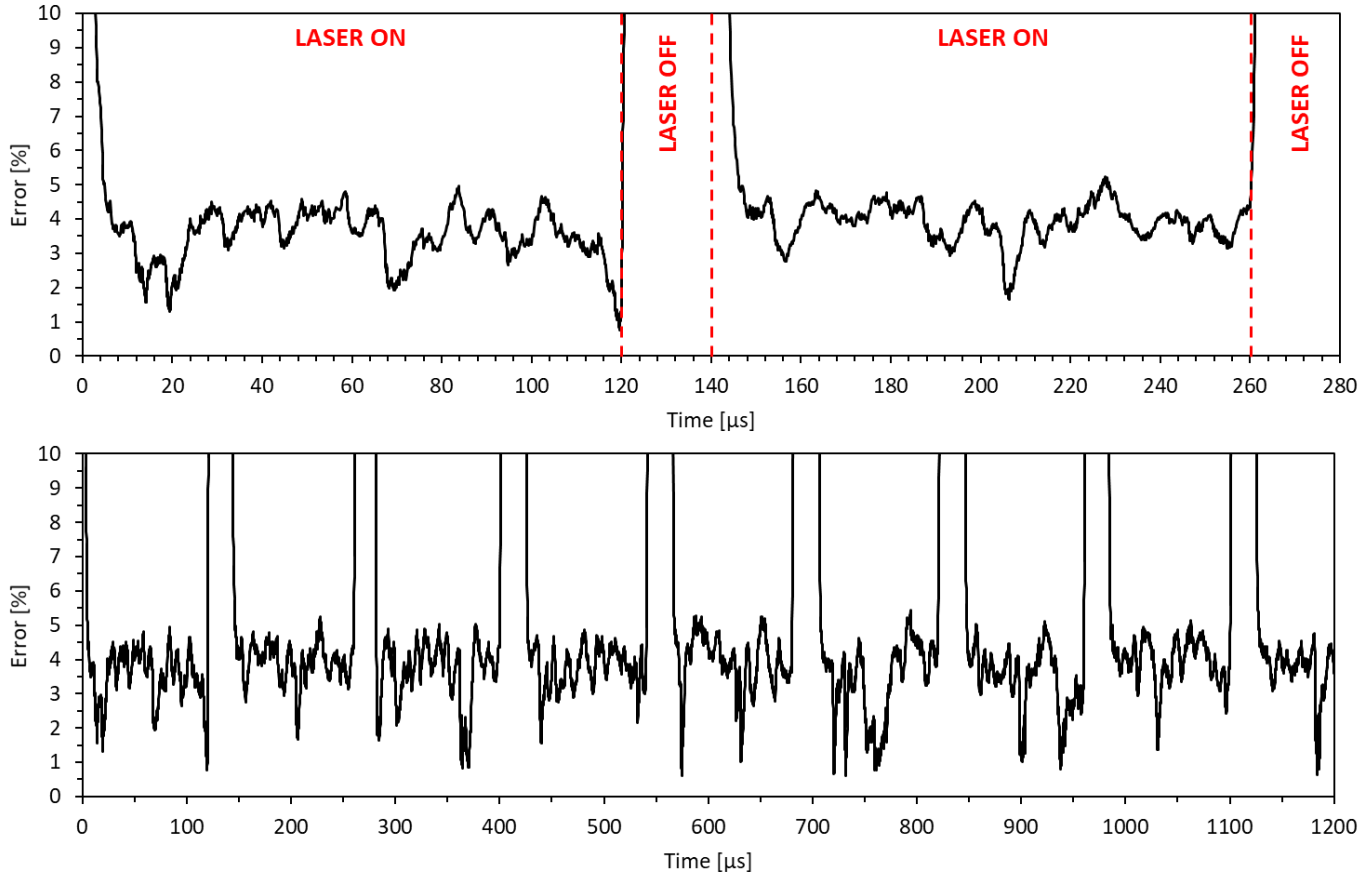

Figure 6-12 shows plots of the error throughout the inverse solution for P-ratio 3, of the peak melt pool temperature and the calculated temperature by Tpk. The bottom plot shows this percentage error over a period of 1200 µs, whilst the top plot shows a magnified view between 0 and 280 µs (the duration of 2 pulses). The image is overlayed with labels displaying periods where the is laser on and laser off.

Figure 6-12 shows the percentage error between the calculated value from *Tpk* (Equation 5-7) and the peak melt pool temperature of the metal in the domain for P-ratio 3. Error rises to a maximum value between each pulse when the laser is off, shown in Figure 6-12 as 'laser off'. The absolute average error for the inverse solution for AA2024 is 3.5 %, and fluctuates between 1 % and 4.8 % over the duration of a single laser exposure.

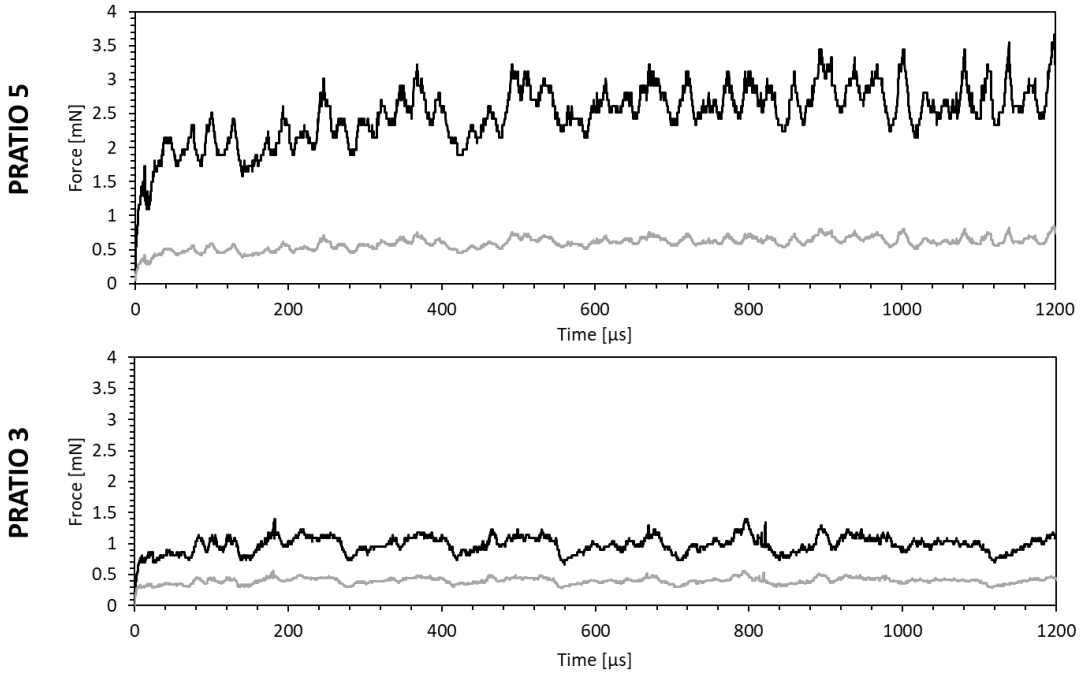

Figure 6-13 shows the maximum force (in mN) generated by the recoil pressure over the melt pool area for P-ratio 5 and P-ratio 3, shown with the force needed to be equal to the internal pressure of the melt pool. The black line represents the maximum force, and the grey line shows the force needed to match the internal pressure of the melt pool.

Figure 6-13 shows the force generated by the recoil pressure during the track deposition for P-ratio 5 and P-ratio 3. The grey line fluctuates from the melt pool width varying considerably during track deposition. It can be seen that the force generated by P-ratio 5 has a higher and more erratic trace than P-ratio 3. The highly variable force on the melt pool surface could be generated from higher melt pool fluctuations seen in P-ratio 5 as opposed to P-ratio 3. The different ratios of P-ratio can also been seen visually, through the ratio of internal force and external force of the melt pool. It can also be seen that the recoil force for P-ratio 5, fluctuates at a higher amplitude and frequency when compared with P-ratio 3.

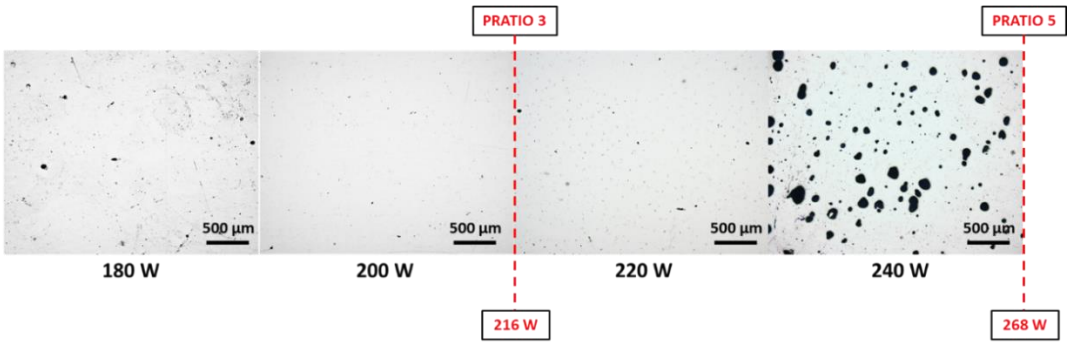

Figure 6-14 shows XZ cross sections of 10 x 10 x 10 mm cubes printed on the Renishaw AM400 for the inverse solution validation study. Cubes progress from low density to high density (at a peak between 200 – 220 W), and then back down to low density. The red text and dotted lines denote at which point in the scale (from 180 W to 240 W) the inverse solution has predicted the laser power. P-ratio 5 shows porosity in its single track, and predicts a power of 268 W. P-ratio 3 shows a consolidated track with a predicted power of 216 W, which falls in the middle of the highest density region between 200 – 220 W.

Figure 6-14 shows the experimental validation for the inverse solution. Four laser powers are shown from 180 W to 240 W, from left to right in the image. This range has been determined by experiment parametric testing carried out at the University of Nottingham. The range shows the ideal power range for AA2024, enclosed by insufficient (< 180 W) and excessive laser powers (> 240 W). For a laser power of 180 W, lack of fusion defects occur, whilst at 240 W, large keyhole porosity is observed. Superimposed onto the porosity images are the predicted powers for a P-ratio of 5 and a P-ratio of 3. Using a P-ratio of 5 results in porosity in the experimental samples, as is observed in the modelling. The predicted power of P-ratio 3 however, predicts a laser power of 216 W. This power falls inside the region of the two highest density cubes, at 200 and 220 W. Solidification cracks are not observed in this image, as the primary driver for solidification is laser speed, and this variable has been fixed due to results from experimental results from Zhang et al [8].

6.4 Discussion

6.4.1 AA2024 cracking analysis framework

High strength aluminium alloys suffer from solidification cracking that severely impacts their use in structural applications when produced by LPBF. Alloys such as AA2024 can provide vital information on how cracking behaviour can be influenced by processing parameters alone, as under certain processing conditions it does not crack. A critical laser speed was found experimentally by Zhang et al. and shows that using slow scan speeds can change the solidification conditions enough, so that cracking does not occur [8]. In this section, two sets of parameters have been modelled, PD15, that uses a speed of 0.107 m/s and PD60, that uses a speed of 0.43 m/s. Both parameter sets have single

tracks deposited with the same exposure, delay and pre heat conditions, the only parameter that changes is the point distance between successive pulses. The aim of this section is to showcase how the model can be used to visualise the main driving forces of cracking by comparing cracked to crack free AA2024. Ultimately these visualisations can be used as rules once fully verified, and could be integrated into the inverse solution. Cracking could then be regulated by modulating surface temperature values and rates of heating/cooling.

The critical zone for cracking occurs in the mushy zone, and specifically at the last stages of solidification higher than 0.85 of solid material within the mushy zone, after Eskin and Katgerman [266]. High thermal strains pull apart narrow channels of inter-dendritic fluid, causing cracks at the last stages of solidification [174]. Different LPBF processing parameters cause differences in the cooling rates, solidification speeds, temperature gradients and strain rates experienced in the melt pool. These conditions affect material specific solidification events, such as dendrite arm spacings, mushy zone volume, and dendritic growth rates and strain rates.

Solidification cracking is driven through dendrite geometries, spacings and growth rates. While not simulated explicitly in the model, precise information can be obtained which can be used to predict dendrite behaviour and hence the cracking propensity of the alloy. The thermal characteristics of the LPBF process lend itself to mainly dendritic growth for high strength aluminium alloys without grain refiners. Hence, a large factor for preventing solidification cracking, is the backfill or healing between inter-dendritic regions with liquid metal. The model supplies this information with cooling rates. A slower cooling rate from the same reference temperature takes longer than one with a higher cooling rate. A longer time at temperature allows for more time for this backfilling process to occur [121]. In addition to this, microsegregation at dendrite roots, can provide low melting point eutectic liquid to flow into the spacings between dendrites [267]. This liquid has a smaller melting range, that reduces strain in the dendrite spacings, reducing cracking. Figure 6-6 shows clearly the differences in the cracked sample (PD60) and the crack free sample (PD15). Throughout the sequence of images, PD60 has a much higher negative cooling rate than PD15. In addition to this, the mushy zone of PD60 is wider, resulting in a larger negative cooling rate at the roots of the dendrites at the outermost mushy zone boundary (solidus line). In contrast PD15 shows a lower negative cooling rate at the solidus boundary. The lower cooling rate for PD15 could potentially allow more time for liquid to backflow along inter-dendritic channels, preventing more solidification cracks.

$$\lambda_1 = C(G^2R)^{-\frac{1}{4}}$$ *Equation 6-5*

Equation 6-5 shows the formula for primary dendrite arm spacing proposed by Hunt [268]. Where C is a material constant, G is the temperature gradient, and R is the solidification speed. Figure 6-4 and Figure 6-5 show that on the left side of the melt pool, PD15 has a lower R values, in addition to higher G values than PD60. Equation 6-5 shows that higher values of G and R increase the dendritic arm spacing of growing dendrites. This has been shown to increase the proportion of liquid that can backfill the between dendrites, reducing solidification cracking. This is shown in Figure 6-15. In addition to this, higher temperature gradients (G) within the mushy zone, also contribute to a shorter dendrite length. Equation 6-6 shows this by calculating the cellular dendritic length (I_c) [269].

$$I_c = \frac{\Delta T'}{G} = \frac{(T^* - T_s')}{G}$$ *Equation 6-6*

Where $\Delta T'$ is the difference between the cell tip temperature T^* and the dendrite root temperature T_s'. This fact, coupled with the shorter distance across the mushy zone, decreases PD15's chances of solidification cracking due to liquid having to travel less distance to backfill dendrites. A larger mushy zone increases the distance between solidus and liquidus boundaries, in addition to a smaller G in the mushy zone (Figure 6-4) for PD60, increases the probability of cracking. These differences are schematically explained in Figure 6-15.

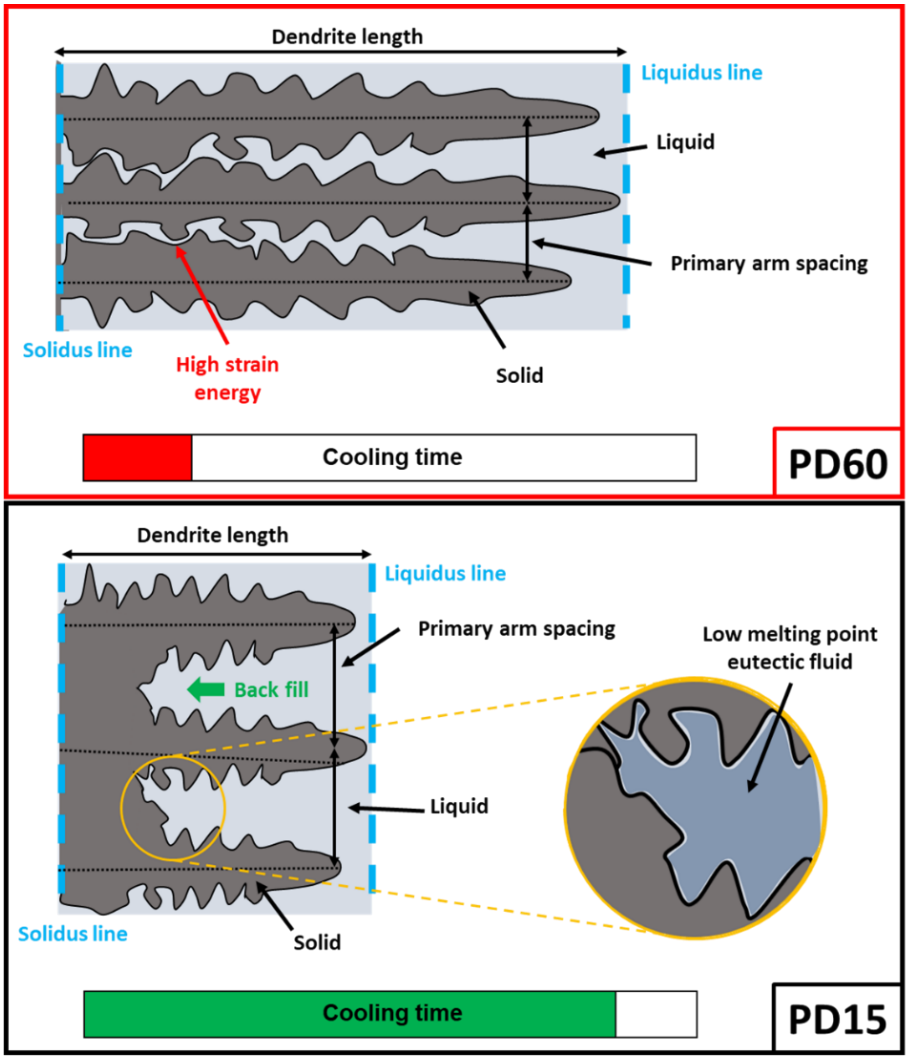

Figure 6-15 shows the main differences in PD60 compared to PD15 through the dendrite growth. PD60 shows long, closely spaced dendrites, that cannot back fill easily, causing high strain rate areas. PD15 shows shorter dendrites spaced further away, with a larger tendency to back fill. Additionally PD15 shows low melting point eutectic fluid from microsegregation at the dendrite roots.

This section shows that the model can be used to successfully discern and quantify differences in samples that do and do not suffer from solidification cracking. High fidelity modelling of LPBF provides precise data sets that can be used to gather information on cracking behaviour in LPBF materials. This work shows that the model can be used as a powerful tool in the analysis of cracking in high strength aluminium alloys.

6.4.2 AA2024 process prediction framework

The objective of Section 2 is to validate the inverse solution with a different material system, using cube density experiments by way of experimental validation. This chapter also provides users with a methodology of optimising a difficult material system for LPBF.

Some aluminium alloys are difficult to process materials owing to their low absorptivity, high thermal conductivity, high heat capacity and low surface tension. Low absorptivity means much higher laser powers have to be used to melt the powder. The heat transfer is high due to a high thermal conductivity, with the material requiring a high energy input for it to melt due to its large heat capacity. As shown previously, absorptivity values also change drastically depending on the geometry of the melt pool. Large power inputs can cause harsh changes in absorptivity, and often lead to a narrow processing window. In sufficient energy input (as shown in Figure 6-14) causes lack of fusion defects, whereas higher powers cause boiling, leading to keyhole cavities. This is made increasingly difficult as aluminium has a low surface tension, as melt pools are naturally more viscous. Furthermore, the oxygen content of the metal can also alter these properties. Cavities caused by excessive energy input increase the absorptivity and can significantly increase the energy absorbed by the melt pool. Over boiling the melt pool, creates large melt pool fluctuations that cause keyhole porosity (as seen in Figure 6-14). A fine window exists to achieve good densification for aluminium alloy processing.

The inverse solution has demonstrated that stable melt pools can be created through adjustment of laser power based upon a constant peak melt pool temperature. Furthermore, using a constant P-ratio value with the optimal peak melt pool temperature (through *Tpk*) can provide a near constant ratio of pressure to the melt pool, to ensure that keyhole fluctuations are kept to a minimum, reducing keyhole porosity. Chapter 5 shows us that a P-ratio of 5 is suitable from speeds between 0.3 and 1.5 m/s for 316L stainless steel. Figure 6-10 shows the initial inverse solution optimisation single track for AA2024, at a P-ratio value of 5. It can be clearly seen from the sequential images of temperature in the XZ plane, that the melt pool is more volatile than for the same P-ratio value of 5 for 316L stainless steel. From these images it can be seen that a P-ratio value of 5 leads to porosity generated by a unstable melt pool. However, a P-ratio is merely the ratio between the recoil pressure and the internal pressure on the melt pool. As stated in chapter 5, P-ratio should be material agnostic, as the formulas for recoil pressure and internal pressure include material specific properties. A lower P-ratio value of 3 is modelled instead, and implemented for the same single track length. Figure 6-10 shows that a P-ratio of 3 calculates a more optimal peak surface temperature than a P-ratio of 5. No porosity is observed in the deposited single track, and the melt pool does not fluctuate wildly during the deposition. The melt pool depth for P-ratio 5 is 2.08x bigger than the melt pool depth for P-ratio 3.

A constant P-ratio should theoretically provide consistent results across different material types. However, the difference in volatility in this case is more likely due to the condition of the melt pool during deposition. A comparison between Figure 6-13 and Figure 5-8 shows that for a P-ratio of 5, approximately the same recoil pressure is generated for a P-ratio of different material. Taking a 100 μm wide melt pool, with a temperature of 3600 K, equates to a recoil force of 4.2 mN for 316L stainless steel and 6.16 mN for AA2024. This small difference in recoil pressure does not explain the difference in melt pool cavity depths or porosity difference in the two materials. However, a more significant factor could come from the volume of liquid metal beneath the liquid surface (Figure 6-16). The optimisation for AA2024 has been achieved with a pulsed laser system. The exposure time governs the period of time the laser is on during a pulse, and is stationary until moved to the next point distance. This is in contrast to a continuous laser system, where the melt pool is constantly moving forward. Therefore, melt pool geometries for the pulsed and continuous laser system are very different. Pulsed laser systems change their 'effective' laser speed by changing either point distance or the exposure time. A simple formula of distance divided by time (plus the delay time) gives the effective speed. However, regardless of the point distance and exposure time combination, the melt pool is still stationary for a fixed period of time. Short pulse times coupled with short delay times might join successive pulses together, but Figure 6-10 shows in this instance discrete melt pools that shift along the positive x axis with each pulse. This is in contrast to the relatively long melt pools seen in Figure 5-8. Thermal conductivity plays a role here by allowing faster heat conduction through the AA2024, transferring heat rapidly away from the melt pool, keeping the melt pool smaller. 316L stainless steel retains most of its heat in its melt pool, with higher temperature gradients over shorter distances, creating larger melt pools. The discrete pulses from the pulsed laser in AA2024, provide a much larger volume of material directly beneath the melt pool surface, vs a much short distance in the 316L stainless steel. This is captured with a direct comparison in Figure 6-16. Figure 6-16 shows the geometrically differences in the distances between the melt pool centre and the melt pool boundary. Even though the recoil pressure values for a P-ratio of 5 are similar, the melt pool in Figure 6-16 cannot be pushed further than there is liquid metal. Figure 6-10 for a pulsed laser system shows the consequence of having a large volume of melted material below a melt pool surface. A large cavity is more easily created, causing melt pool fluctuations at the bottom of the melt pool, capturing argon gas as porosity during the track deposition. These fluctuations can also be seen graphically in Figure 6-13. P-ratio 5 shows a higher frequency and amplitude to recoil pressure fluctuations than P-

ratio 3, potentially marking these melt pool oscillations. It must be noted that the effective speeds of the comparison made in Figure 6-16 are different (0.3 m/s for the continuous SS316L and 0.107 m/s for AA2024), but due to the drastic melt pool shape differences, this is thought to be the main contributing factor to this effect. However, as mentioned in Chapter 5, a more detailed calculation of the internal pressure could alleviate the differences seen here. Note that this does not diminish the effectiveness of the P-ratio solution to calculating process parameters. This method is not intended to also optimise P-ratio, but rather provides the user with one parameter in which to control both laser power and laser speed. Optimisation of P-ratio can be done quickly as there is only variable to change. In addition, this work provides results of values of P-ration which can be suitable for both continuous and pulsed laser systems.

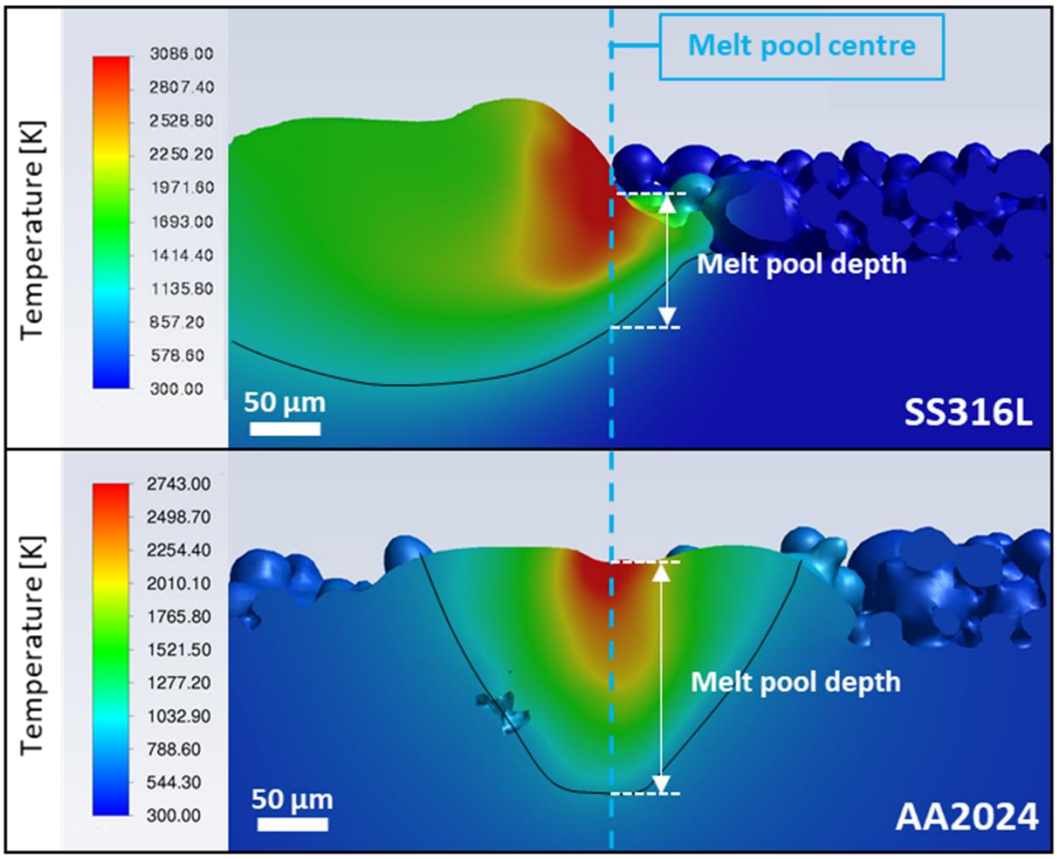

Figure 6-16 shows the XZ cross section of the optimisation run for 316L stainless steel and AA2024 with a P-ratio of 5. Both images are aligned to the melt pool centres, and show an image halfway along the single track. The images show the difference between a continuous optimisation (top) and a pulsed optimisation (below), with respect to the melt pool depths. The cooling time for the speed of the pulse needed for AA2024 resulted in identical small melt pools of this size, that are not affected by track length. These melt pools were captured half way along its length.

Reducing the calculated peak melt pool temperature, and subsequently reducing the recoil pressure, stops the formation of large cavities and prevents porosity formation in P-ratio 3. This result shows that different values of P-ratio need to be considered for

pulsed laser systems as opposed to continuous ones. Regardless of this fact, only two P-ratio single track deposition simulations had to be modelled to predict an optimal laser power for AA2024. Figure 6-14 shows optical microscopy images from an experimental parametric study done for AA2024. The results show the results of extensive parametric testing for different combinations of point distance, exposure time, delay time and laser power. This snapshot of results show that for a point distance of 15 μm and exposure time of 120 μs the ideal laser power is between 200 and 220 W. Using a P-ratio of 3 with these conditions gives a predicted laser power of 216 W. For users with a feed forward capable machine, this equates to a target temperature of 3323 K.

6.5 Summary

The aim of this chapter is to provide a case study on how a high fidelity model can be used to evaluate and visualise precise time and space dependant information for LPBF, in addition to using this information to predict process parameters based upon a surface temperature.

Section one of this chapter shows the initial stage of the project at the University of Nottingham to measure, evaluate, predict and then eliminate cracking in high strength aluminium alloys. This chapter presents evidence that the high fidelity model presented in this thesis can measure and evaluate cracking conditions seen in AA2024. The amount of precise data that is generated has been shown to produce information to discern clear differences between a cracked and crack free AA2024 sample. Specifically for AA2024, PD15 shows a reduced negative cooling rate and higher thermal gradients throughout a predominantly smaller mushy zone volume than PD60. These factors provide evidence that these conditions produce significantly different results that can explain the difference in cracking seen in experimental results. Subsequent work of this project work can then evaluate this data to produce rules to predict and eliminate cracking in high strength aluminium alloys. In the future, these results could be integrated within the inverse solution, to provide limits on positive and negative cooling rates. The model could actively adjust power to consider these limits when calculating surface temperature.

Section two of this chapter demonstrates that the inverse solution can be used on a pulsed laser system with a different, difficult to use material system. The inverse solution was able to correctly predict a laser power for a consolidated single track, which was validated by experimental testing. This adds confidence to this method of optimisation framework to be used in LPBF that is material agnostic.

Chapter 7

7 Conclusions

In this study a high fidelity model has been created, to provide a platform for a novel optimisation method for LPBF. This novel optimisation is based upon providing the melt pool with a calculated amount of energy, to reduce temperature fluctuations and therefore reduce both lack of fusion and keyhole porosity. The optimisation process framework, via an inverse solution method, has been demonstrated with 316L stainless steel, and experimentally validated with AA2024, a high strength aluminium alloy.

Experimental validation was achieved by comparison to experimental melt pool dimensions for both 316L stainless steel and AA2024. Experimental validation was attained through four different types of laser operation; continuous, stationary pulsed, and continuous/pulsed with a ramp up profile. For the first time this work shows that the simulation can be validated for variable laser powers. This work also highlights how using a revised refractive index instead of changing the bulk absorptivity value benefits modelling of LPBF. Due to the complex relationship of absorptivity with aluminium alloys, using the literature value of the refractive index was not possible. The primary advantages of this approach is that the melt pool is modelled much closer to reality. The development of porosity can be investigated in high detail as keyhole fluctuations are caused by the reflecting energy source. This gives much more confidence in predicting laser parameter conditions that do not result in porosity. Additionally a live trace of absorptivity throughout the single track can be used in the optimisation framework.

A predictive framework for LPBF parameter optimisation has been proven for two different material systems, 316L stainless steel and AA2024. Using the inverse solution, a major link is created between laser power and melt pool temperature, allowing for stable melt pools to be established and maintained throughout a single track deposition. Manipulating laser power to control surface temperature allows compensation for large absorptivity changes that can occur during the process, resulting from local variations in the powder bed and melt pool geometry. Optimising the laser power to surface temperature allows for much greater stability, reducing porosity. This work also shows the necessity of a high fidelity model to accurately capture melt pool dynamics with a stochastic powder bed. Links have also been established with surface temperature and common LPBF defects, such as a lack of fusion defects and keyhole porosity. Recoil pressure has been exploited as a control mechanism to maintain stable single track

deposition in the transition mode of laser processing. To maintain this stability, a new parameter, P-ratio, has been derived and validated as the single processing variable that LPBF can be optimised too. P-ratio has proven to be independent of laser speed, and provides a constant recoil pressure to the surface of a melt pool to ensure track consolidation. This constant pressure acting on the surface of the melt pool through the fast modulation of laser power, acts as a stabiliser to combat melt pool fluctuations.

The analysis of state of the art literature in Chapter 3 show methods to modulate laser power based upon a surface temperature. However, these methods do not demonstrate or evaluate what are the optimal surface temperatures for LPBF. This work ultimately provides a framework to calculate these temperatures, under conditions that result in a consolidated single track with low porosity. This work also takes this a step further, and provides P-ratio, a parameter that can stabilise melt pools through the constant application of a recoil pressure achieved with a near constant surface temperature. In addition, for users without feed forward capabilities (such as high speed cameras, temperature monitoring equipment etc.), this framework can also produce a laser power needed to keep the melt pool temperature at a constant value. This is so that systems without a temperature monitoring facility can also be optimised through a similar methodology.

This work provides a demonstration that this optimisation framework can be material agnostic. Chapter 5 demonstrates the methodology for 316L stainless steel, but this methodology can be applied to all material systems in LPBF. Chapter 6 demonstrates the optimisation framework for a difficult to use material, AA2024, a high strength aluminium alloy. Section two of this chapter demonstrates that the inverse solution can be used on a pulsed laser system with a different, difficult to use material system. The inverse solution was able to correctly predict a laser power for a consolidated single track, which was validated by experimental testing. This adds confidence to this method of optimisation framework to be used in LPBF that is material agnostic. Currently the inverse solution works only in a single track mode. While this work has proven single tracks make a good proxy for component builds, a highly accurate prediction system has to account for variable geometry and multiple layers. This work also raises important differences in modelling pulsed and continuous laser systems. The results show that whilst the P-ratio parameter could be considered as material agnostic, lower P-ratio values must be used in pulsed laser systems as opposed to continuous wave systems. Limiting peak temperature below the boiling point could also be used for challenging materials such as magnesium and zinc alloys, that are prone to boiling as a result of

excessively energetic melt pools. Additionally, the inverse solution is not only limited to high fidelity models, its simplicity ensures it can be used in other numerical modelling techniques.

Section one of chapter 6 displays the initial stage of the project at the University of Nottingham to measure, evaluate, predict and then eliminate cracking in high strength aluminium alloys. This chapter presents evidence that the high fidelity model presented in this thesis can measure and evaluate cracking conditions seen in AA2024. The amount of detailed data that is generated has been shown to produce information to discern clear differences between a cracked and crack free AA2024 sample. Specifically for AA2024, PD15 shows a reduced negative cooling rate and higher thermal gradients throughout a predominantly smaller mushy zone volume than PD60. These factors provide evidence that these conditions produce significantly different results that can explain the difference in cracking seen in experimental results. The second stage of this project can then evaluate this data to produce rules to predict and eliminate cracking in high strength aluminium alloys. In the future, the results of the work could be integrated within the inverse solution, to provide limits on positive and negative cooling rates. The model could actively adjust power to consider these limits when calculating the optimal surface temperature. The model has successfully shown it can be used to measure and evaluate cracking for high strength aluminium alloy, AA2024. Data generated by the model clearly shows differences between cracked and crack free parameter sets. Large differences in cooling rates and temperature gradients show that the main drivers for cracking in LPBF can be evaluated with the high fidelity model. Results from this work will be used to predict and eliminate cracking in high strength aluminium alloys, allowing more aluminium alloys to be used in LPBF.

This work shows the power of using a high fidelity model for the evaluation and prediction of single track parameters for LPBF. Reducing porosity and mitigating defects are still the largest barrier to entry for LPBF in high strength mechanical applications. This work provides a framework in which the probability of porosity and cracking defects can be markedly reduced through optimal process parameter calculation.

Chapter 8

8 Recommendations for future work

The present research discusses the use of a high fidelity model to calculate optimal processing conditions for LPBF. Due to the complex nature of this work and the limited time frame to achieve it, not all aspects of this research could be feasibly addressed. This chapter will discuss the recommendations for future work.

This research has highlighted the complex nature of absorptivity for aluminium alloys. In this work, comparisons have been made from experimentally and numerically measured values of absorptivity for aluminium. The LMC is a compact piece of equipment, with significant advantages for high throughput testing, combined with the measurement of absorptivity in-situ. But, further work is needed to correlate the differences between the LMC and the model. For example, the LMC could be calibrated to the model, by conducting a single track simulation on a disc with the same thickness. Both experiments could use the same absorptivity calculation technique to calibrate the LMC. This information could be used to compare the two absolute values.

The main future recommendations for this work concern the calculation of optimal processing conditions through the inverse solution. This work has demonstrated using two materials, that optimisation via surface temperature shows serious potential as an optimisation technique that can be adapted for use across a wide range of powder bed fusion techniques. The advent of high fidelity models, feed forward modelling and the calculation of optimal parameters coupled with high performance computing, is a glimpse to the future of additive manufacturing.

The inverse solution control mechanism over the peak surface temperature by modulating laser power has potential to heavily impact processing of temperature sensitive materials such as magnesium and zinc alloys. By regulating peak temperature, excessive evaporation of low boiling point alloys could be avoided by optimising the amount of energy delivered to the melt pool. This could increase safety in processing highly oxidising materials such as magnesium, and other high volatility elements/alloys. Another research area this could help in, is the reduction of preferential evaporation in aluminium and titanium alloys.

With the increasing power of computational equipment, the potential for the inverse solution framework also increases. Future work could be directed to incorporating LPBF machines more with simulations. Feedback from the model could be used as a direct

input to LPBF machines, that use high frequency pulsed lasers to more closely match the output of the inverse solution. In the period between this ramp up in computational power, the inverse solution simple optimisation formulas could be integrated to a faster analytical model. This lower fidelity model could be used to generate calculated laser powers for larger scans of the LPBF laser strategy, in addition to being directly included in LPBF machines for real time power modulation calculation. These lower fidelity models would be calibrated to a higher fidelity model, to ensure correct calculation of the laser power.

This work also briefly discusses the matching of powder bed height variation to laser power. Future research could examine the behaviour of ideal laser powers for different powder bed heights. This work could be useful in determining better scan strategies to cope with large spatter particles in the powder bed. Standard constant processing parameters struggle in melting larger particles, and lack of fusion defects would be incorporated into the component. Knowledge of ideal laser powers, that ramp up when a large particle is detected, could be valuable in reducing lack of fusion defects in LPBF.

Lastly, at present, the inverse solution only considers the optimisation of single tracks for LPBF. However, the process of LPBF is inherently more complicated than this simplification. Multiple layers, advanced scan strategies and component geometry all significantly affect the ideal parameters for LPBF. Whilst it has been experimentally proven that the inverse solution can provide optimal processing conditions based upon single track studies, the next step in this frameworks development could be to move to multi-layer structures.

****

9 References

[1] B. Liu, G. Fang, L. Lei, and W. Liu, “A new ray tracing heat source model for mesoscale CFD simulation of selective laser melting (SLM),” *Applied Mathematical Modelling*, vol. 79, pp. 506–520, Mar. 2020, doi: 10.1016/j.apm.2019.10.049.

[2] W. E. Frazier, “Metal additive manufacturing: A review,” *Journal of Materials Engineering and Performance*, vol. 23, no. 6, pp. 1917–1928, 2014, doi: 10.1007/s11665-014-0958-z.

[3] H. Gong, K. Rafi, H. Gu, T. Starr, and B. Stucker, “Analysis of defect generation in Ti–6Al–4V parts made using powder bed fusion additive manufacturing processes,” *Additive Manufacturing*, vol. 1–4, pp. 87–98, Oct. 2014, doi: 10.1016/j.addma.2014.08.002.

[4] R. W. Cunningham, “Defect Formation Mechanisms in Powder-Bed Metal Additive Manufacturing,” thesis, Carnegie Mellon University, 2018. doi: 10.1184/R1/6715691.v1.

[5] I. Yadroitsev, A. Gusarov, I. Yadroitsava, and I. Smurov, “Single track formation in selective laser melting of metal powders,” *Journal of Materials Processing Technology*, vol. 210, no. 12, pp. 1624–1631, Sep. 2010, doi: 10.1016/j.jmatprotec.2010.05.010.

[6] W. E. King *et al.*, “Observation of keyhole-mode laser melting in laser powder-bed fusion additive manufacturing,” *Journal of Materials Processing Technology*, vol. 214, no. 12, pp. 2915–2925, Dec. 2014, doi: 10.1016/j.jmatprotec.2014.06.005.

[7] X. Nie, H. Zhang, H. Zhu, Z. Hu, L. Ke, and X. Zeng, “Analysis of processing parameters and characteristics of selective laser melted high strength Al-Cu-Mg alloys: From single tracks to cubic samples,” *Journal of Materials Processing Technology*, vol. 256, pp. 69–77, Jun. 2018, doi: 10.1016/j.jmatprotec.2018.01.030.

[8] H. Zhang, H. Zhu, T. Qi, Z. Hu, and X. Zeng, “Selective laser melting of high strength Al–Cu–Mg alloys: Processing, microstructure and mechanical properties,” *Materials Science and Engineering: A*, vol. 656, pp. 47–54, Feb. 2016, doi: 10.1016/j.msea.2015.12.101.

[9] A. B. Spierings, T. L. Starr, and K. Wegener, “Fatigue performance of additive manufactured metallic parts,” *Rapid Prototyping Journal*, vol. 19, no. 2, pp. 88–94, Jan. 2013, doi: 10.1108/13552541311302932.

[10] C. L. Druzgalski, A. Ashby, G. Guss, W. E. King, T. T. Roehling, and M. J. Matthews, “Process optimization of complex geometries using feed forward control for laser powder bed fusion additive manufacturing,” *Additive Manufacturing*, vol. 34, p. 101169, Aug. 2020, doi: 10.1016/j.addma.2020.101169.

[11] E. Vasileska, A. G. Demir, B. M. Colosimo, and B. Previtali, “Layer-wise control of selective laser melting by means of inline melt pool area measurements,” *Journal of Laser Applications*, vol. 32, no. 2, p. 022057, May 2020, doi: 10.2351/7.0000108.

[12] J. Lee and V. Prabhu, “Simulation modeling for optimal control of additive manufacturing processes,” *Additive Manufacturing*, vol. 12, pp. 197–203, Oct. 2016, doi: 10.1016/j.addma.2016.05.002.

[13] P. A. Hooper, “Melt pool temperature and cooling rates in laser powder bed fusion,” *Additive Manufacturing*, vol. 22, pp. 548–559, Aug. 2018, doi: 10.1016/j.addma.2018.05.032.

[14] L. Cherdo, “Best metal 3D printers in 2021: comprehensive overview,” *Aniwaa*. https://www.aniwaa.com/buyers-guide/3d-printers/best-metal-3d-printer/ (accessed Jul. 14, 2021).

[15] W. Associates, “Wohlers Report 2021.” 2021.

[16] T. DebRoy *et al.*, “Additive manufacturing of metallic components – Process, structure and properties,” *Progress in Materials Science*, vol. 92, pp. 112–224, 2018, doi: 10.1016/j.pmatsci.2017.10.001.

[17] L. E. Murr *et al.*, “Metal Fabrication by Additive Manufacturing Using Laser and Electron Beam Melting Technologies,” *Journal of Materials Science & Technology*, vol. 28, no. 1, pp. 1–14, Jan. 2012, doi: 10.1016/S1005-0302(12)60016-4.

[18] I. Gibson, D. Rosen, and B. Stucker, *Additive Manufacturing Technologies: 3D Printing, Rapid Prototyping, and Direct Digital Manufacturing*, 2nd ed. New York: Springer-Verlag, 2015. doi: 10.1007/978-1-4939-2113-3.

[19] H. Galarraga, D. A. Lados, R. R. Dehoff, M. M. Kirka, and P. Nandwana, “Effects of the microstructure and porosity on properties of Ti-6Al-4V ELI alloy fabricated by electron beam melting (EBM),” *Additive Manufacturing*, vol. 10, pp. 47–57, Apr. 2016, doi: 10.1016/j.addma.2016.02.003.

[20] W. J. Sames, F. A. List, S. Pannala, R. R. Dehoff, and S. S. Babu, “The metallurgy and processing science of metal additive manufacturing,” *International Materials Reviews*, vol. 61, no. 5, pp. 315–360, Jul. 2016, doi: 10.1080/09506608.2015.1116649.

[21] “Peak Productivity: SLM Solutions launches 12-Laser Machine,” *SLM Solutions*. https://www.slm-solutions.com/company/news/detail/peak-productivity-slm-solutions-launches-12-laser-machine/ (accessed Jul. 14, 2021).

[22] J. A. Manriquez-Frayre and D. L. Bourell, “Selective Laser Sintering of Binary Metallic Powder,” p. 8.

[23] C. Y. Yap *et al.*, “Review of selective laser melting: Materials and applications,” *Applied Physics Reviews*, vol. 2, no. 4, p. 041101, Dec. 2015, doi: 10.1063/1.4935926.

[24] A. G. Demir, P. Colombo, and B. Previtali, “From pulsed to continuous wave emission in SLM with contemporary fiber laser sources: effect of temporal and spatial pulse overlap in part quality,” *Int J Adv Manuf Technol*, vol. 91, no. 5–8, pp. 2701–2714, Jul. 2017, doi: 10.1007/s00170-016-9948-7.

[25] S. K. Everton, M. Hirsch, P. Stravroulakis, R. K. Leach, and A. T. Clare, “Review of in-situ process monitoring and in-situ metrology for metal additive manufacturing,” *Materials & Design*, vol. 95, pp. 431–445, Apr. 2016, doi: 10.1016/j.matdes.2016.01.099.

[26] M. Simonelli *et al.*, “Materials Characterization A comparison of Ti-6Al-4V in-situ alloying in Selective Laser Melting using simply-mixed and satellited powder blend feedstocks,” *Materials Characterization*, no. November 2017, pp. 0–1, 2018, doi: 10.1016/j.matchar.2018.05.039.

[27] I. Yadroitsava, J. Els, G. Booysen, and I. Yadroitsev, “Peculiarities of single track formation from Ti6Al4V alloy at different laser power densities by selective laser melting,” *SAJIE*, vol. 26, no. 3, Nov. 2015, doi: 10.7166/26-3-1185.

[28] D. Bergström, “The Absorption of Laser Light by Rough Metal Surfaces,” p. 226.

[29] Fresnel, “Ueber das Licht,” *Annalen der Physik*, vol. 81, no. 10, pp. 223–256, 1825, doi: 10.1002/andp.18250811009.

[30] H. R. Abedi and M. Hoseinpour Gollo, “An experimental study of the effects of surface roughness and coating of Cr2O3 layer on the laser-forming process,” *Optics & Laser Technology*, vol. 109, pp. 336–347, Jan. 2019, doi: 10.1016/j.optlastec.2018.07.064.

[31] A. F. H. Kaplan, “Absorptivity modulation on wavy molten steel surfaces: The influence of laser wavelength and angle of incidence,” *Appl. Phys. Lett.*, vol. 101, no. 15, p. 151605, Oct. 2012, doi: 10.1063/1.4759126.

[32] J.-T. Wang, C.-I. Weng, J.-G. Chang, and C.-C. Hwang, “The influence of temperature and surface conditions on surface absorptivity in laser surface treatment,” *Journal of Applied Physics*, vol. 87, no. 7, pp. 3245–3253, Apr. 2000, doi: 10.1063/1.372331.

[33] S. Y. Bang, S. Roy, and M. F. Modest, “CW laser machining of hard ceramics—II. Effects of multiple reflections,” *International Journal of Heat and Mass Transfer*, vol. 36, no. 14, pp. 3529–3540, Sep. 1993, doi: 10.1016/0017-9310(93)90170-B.

[34] J. Xie and A. Kar, “Laser Welding of Thin Sheet Steel with Surface Oxidation,” p. 7.

[35] Y. H. Zhou *et al.*, “Selective laser melting of typical metallic materials: An effective process prediction model developed by energy absorption and consumption analysis,” *Additive Manufacturing*, vol. 25, pp. 204–217, Jan. 2019, doi: 10.1016/j.addma.2018.10.046.

[36] S. D. Jadhav, J. Vleugels, J.-P. Kruth, J. V. Humbeeck, and K. Vanmeensel, “Mechanical and electrical properties of selective laser-melted parts produced from surface-oxidized copper powder,” *Material Design & Processing Communications*, vol. 2, no. 2, p. e94, 2020, doi: 10.1002/mdp2.94.

[37] P. Lassègue *et al.*, “Laser powder bed fusion (L-PBF) of Cu and CuCrZr parts: Influence of an absorptive physical vapor deposition (PVD) coating on the printing process,” *Additive Manufacturing*, vol. 39, p. 101888, Mar. 2021, doi: 10.1016/j.addma.2021.101888.

[38] A. Speidel *et al.*, “The interaction of volatile metal coatings during the laser powder bed fusion of copper,” *Journal of Materials Processing Technology*, vol. 299, p. 117332, Jan. 2022, doi: 10.1016/j.jmatprotec.2021.117332.

[39] J. Trapp, A. M. Rubenchik, G. Guss, and M. J. Matthews, “In situ absorptivity measurements of metallic powders during laser powder-bed fusion additive manufacturing,” *Applied Materials Today*, vol. 9, pp. 341–349, Dec. 2017, doi: 10.1016/j.apmt.2017.08.006.

[40] D. Herzog, V. Seyda, E. Wycisk, and C. Emmelmann, “Additive manufacturing of metals,” *Acta Materialia*, vol. 117, pp. 371–392, Sep. 2016, doi: 10.1016/j.actamat.2016.07.019.

[41] T. D. Ngo, A. Kashani, G. Imbalzano, K. T. Q. Nguyen, and D. Hui, “Additive manufacturing (3D printing): A review of materials, methods, applications and challenges,” *Composites Part B: Engineering*, vol. 143, pp. 172–196, Jun. 2018, doi: 10.1016/j.compositesb.2018.02.012.

[42] G. N. Levy, R. Schindel, and J. P. Kruth, “RAPID MANUFACTURING AND RAPID TOOLING WITH LAYER MANUFACTURING (LM) TECHNOLOGIES, STATE OF THE ART AND FUTURE PERSPECTIVES,” *CIRP Annals*, vol. 52, no. 2, pp. 589–609, 2003, doi: 10.1016/S0007-8506(07)60206-6.

[43] W. King, A. T. Anderson, R. M. Ferencz, N. E. Hodge, C. Kamath, and S. A. Khairallah, “Overview of modelling and simulation of metal powder bed fusion process at Lawrence Livermore National Laboratory,” *Materials Science and Technology*, vol. 31, no. 8, pp. 957–968, Jun. 2015, doi: 10.1179/1743284714Y.0000000728.

[44] D. Bourell, H. Marcus, J. W. Barlow, and J. Beaman, “Selective laser sintering of metals and ceramics,” 1992, doi: 10.1016/0026-0657(93)90473-6.

[45] N. K. Tolochko, S. E. Mozzharov, N. V. Sobolenko, I. A. Yadrojtsev, V. I. Goryushkin, and V. S. Dubovets, “Laser selective layer-by-layer sintering of powders: problems and vistas,” *Poroshkovaya Metallurgiya*, no. 3–4, pp. 32–37, 1995.

[46] J.-P. Kruth, P. Peeters, T. Smolderen, J. Bonse, T. Laoui, and L. Froyen, “Comparison between CO2 and ND:YAG lasers for use with selective laser sintering of steel-copper powders,” *Revue International de CFAO et d’informatique graphique*, vol. 13, no. 4, pp. 95–112, 19990130.

[47] N. K. Tolochko, Y. V. Khlopkov, S. E. Mozzharov, M. B. Ignatiev, T. Laoui, and V. I. Titov, “Absorptance of powder materials suitable for laser sintering,” *Rapid Prototyping Journal*, vol. 6, no. 3, pp. 155–161, Sep. 2000, doi: 10.1108/13552540010337029.

[48] Van Der Schueren B., “Basic contributions to the development of the selective metal powder sintering process.,” p. 1, 1998.

[49] A. V. Gusarov and J.-P. Kruth, “Modelling of radiation transfer in metallic powders at laser treatment,” *International Journal of Heat and Mass Transfer*, vol. 48, no. 16, pp. 3423–3434, Jul. 2005, doi: 10.1016/j.ijheatmasstransfer.2005.01.044.

[50] R. W. McVey, R. M. Melnychuk, J. A. Todd, and R. P. Martukanitz, “Absorption of laser irradiation in a porous powder layer,” *Journal of Laser Applications*, vol. 19, no. 4, pp. 214–224, Nov. 2007, doi: 10.2351/1.2756854.

[51] X. C. Wang and J.-P. Kruth, “A simulation model for direct selective laser sintering of metal powders,” in *Proceedings of the 5th International Conference on Computational Structures Technology*, 20000901, pp. 57–71. Accessed: Jul. 14, 2021. [Online]. Available: https://lirias.kuleuven.be/retrieve/124339

[52] C. D. Boley, S. A. Khairallah, and A. M. Rubenchik, “Calculation of laser absorption by metal powders in additive manufacturing,” *Appl. Opt.*, vol. 54, no. 9, p. 2477, Mar. 2015, doi: 10.1364/AO.54.002477.

[53] M. S. Knieps, W. J. Reynolds, J. Dejaune, A. T. Clare, and A. Evirgen, “In-situ alloying in powder bed fusion: The role of powder morphology,” *Materials Science and Engineering: A*, vol. 807, p. 140849, Mar. 2021, doi: 10.1016/j.msea.2021.140849.

[54] J. H. Tan, W. L. E. Wong, and K. W. Dalgarno, “An overview of powder granulometry on feedstock and part performance in the selective laser melting process,” *Additive Manufacturing*, vol. 18, pp. 228–255, Dec. 2017, doi: 10.1016/j.addma.2017.10.011.

[55] H. Lim and N. A. Khan, “EFFECTS OF PARTICLE SIZE DISTRIBUTION ON SURFACE FINISH OF SELECTIVE LASER MELTING PARTS,” p. 14.

[56] A. Rubenchik, S. Wu, S. Mitchell, I. Golosker, M. LeBlanc, and N. Peterson, “Direct measurements of temperature-dependent laser absorptivity of metal powders,” *Appl. Opt.*, vol. 54, no. 24, p. 7230, Aug. 2015, doi: 10.1364/AO.54.007230.

[57] D. Bäuerle, *Laser Processing and Chemistry*. Springer Science & Business Media, 2013.

[58] C. Zhao *et al.*, “Critical instability at moving keyhole tip generates porosity in laser melting,” *Science*, vol. 370, no. 6520, pp. 1080–1086, Nov. 2020, doi: 10.1126/science.abd1587.

[59] S. Patel and M. Vlasea, “Melting modes in laser powder bed fusion,” *Materialia*, vol. 9, p. 100591, Mar. 2020, doi: 10.1016/j.mtla.2020.100591.

[60] K. H. J. Buschow, *Encyclopedia of Materials: Science and Technology*. Elsevier, 2001.

[61] D. T. Swift-Hook and A. E. F. Gick, "PENETRATION WELDING WITH LASERS.," *Welding Journal (Miami, Fla)*, vol. 52, no. 11, pp. 492s–499s, 1973.

[62] J. Mazumder and W. M. Steen, "LASER WELDING OF TITANIUM 6A1-4V.," pp. 307–315, 1977.

[63] J. Dowden, M. Davis, and P. Kapadia, "Some aspects of the fluid dynamics of laser welding," *Journal of Fluid Mechanics*, vol. 126, no. 3, pp. 123–146, 1983, doi: 10.1017/S0022112083000075.

[64] J. Dowden, M. Davis, and P. Kapadia, "The flow of heat and the motion of the weld pool in penetration welding with a laser," *Journal of Applied Physics*, vol. 57, no. 9, pp. 4474–4479, 1985, doi: 10.1063/1.334571.

[65] M. Davis, P. Kapadia, and J. Dowden, "MODELLING THE FLUID FLOW IN LASER BEAM WELDING.," *Welding Journal (Miami, Fla)*, vol. 65, no. 7, pp. 167s–174s, 1986.

[66] R. Rai and T. Debroy, "Tailoring weld geometry during keyhole mode laser welding using a genetic algorithm and a heat transfer model," *Journal of Physics D: Applied Physics*, vol. 39, no. 6, pp. 1257–1266, 2006, doi: 10.1088/0022-3727/39/6/037.

[67] R. Rai, J. W. Elmer, T. A. Palmer, and T. DebRoy, "Heat transfer and fluid flow during keyhole mode laser welding of tantalum, Ti–6Al–4V, 304L stainless steel and vanadium," *J. Phys. D: Appl. Phys.*, vol. 40, no. 18, pp. 5753–5766, Aug. 2007, doi: 10.1088/0022-3727/40/18/037.

[68] I. Langmuir, "The Vapor Pressure of Metallic Tungsten," *Phys. Rev.*, vol. 2, no. 5, pp. 329–342, Nov. 1913, doi: 10.1103/PhysRev.2.329.

[69] V. Juechter, T. Scharowsky, R. F. Singer, and C. Körner, "Processing window and evaporation phenomena for Ti-6Al-4V produced by selective electron beam melting," *Acta Materialia*, vol. 76, pp. 252–258, 2014, doi: 10.1016/j.actamat.2014.05.037.

[70] R. T. C. Choo, J. Szekely, and R. C. Westhoff, "On the calculation of the free surface temperature of gas-tungsten-arc weld pools from first principles: Part I. modeling the welding arc," *Metallurgical Transactions B*, vol. 23, no. 3, pp. 357–369, 1992, doi: 10.1007/BF02656291.

[71] R. T. C. Choo and J. Szekely, "Vaporization Kinetics and Surface Temperature in a Mutually Coupled Spot Gas Tungsten Arc Weld and Weld Pool," p. 17.

[72] F. Verhaeghe, T. Craeghs, J. Heulens, and L. Pandelaers, "A pragmatic model for selective laser melting with evaporation," *Acta Materialia*, vol. 57, no. 20, pp. 6006–6012, Dec. 2009, doi: 10.1016/j.actamat.2009.08.027.

[73] A. Block-bolten and T. Eagar, "Metal vaporization from weld pools," 1984, doi: 10.1007/BF02657376.

[74] J. Lucas, "Laser Powder Bed Fusion of Magnesium Alloys," Aachen University.

[75] J. Blackburn, C. Allen, P. Hilton, and L. Li, "Nd:YAG Laser welding of titanium alloys using a directed gas jet," *Journal of Laser Applications - J LASER APPL*, vol. 22, May 2010, doi: 10.2351/1.3455825.

[76] J. Greses, P. A. Hilton, C. Y. Barlow, and W. M. Steen, "Plume attenuation under high power Nd:yttritium–aluminum–garnet laser welding," *Journal of Laser Applications*, vol. 16, no. 1, pp. 9–15, Feb. 2004, doi: 10.2351/1.1642636.

[77] Z. Szymanski, J. Kurzyna, and W. Kalita, “The spectroscopy of the plasma plume induced during laser welding of stainless steel and titanium,” *J. Phys. D: Appl. Phys.*, vol. 30, no. 22, pp. 3153–3162, Nov. 1997, doi: 10.1088/0022-3727/30/22/014.

[78] S. A. Khairallah *et al.*, “Controlling interdependent meso-nanosecond dynamics and defect generation in metal 3D printing,” p. 7, 2020.

[79] A. B. Anwar and Q.-C. Pham, “Study of the spatter distribution on the powder bed during selective laser melting,” *Additive Manufacturing*, vol. 22, pp. 86–97, Aug. 2018, doi: 10.1016/j.addma.2018.04.036.

[80] M. M. Avedesian and H. Baker, *ASM Specialty Handbook: Magnesium and Magnesium Alloys*. ASM International, 1999.

[81] C. C. Ng, M. M. Savalani, H. C. Man, and I. Gibson, “Layer manufacturing of magnesium and its alloy structures for future applications,” *Virtual and Physical Prototyping*, vol. 5, no. 1, pp. 13–19, Mar. 2010, doi: 10.1080/17452751003718629.

[82] N. A. Zumdick, L. Jauer, L. C. Kersting, T. N. Kutz, J. H. Schleifenbaum, and D. Zander, “Additive manufactured WE43 magnesium: A comparative study of the microstructure and mechanical properties with those of powder extruded and as-cast WE43,” *Materials Characterization*, vol. 147, no. August 2018, pp. 384–397, 2019, doi: 10.1016/j.matchar.2018.11.011.

[83] R. Cunningham *et al.*, “Keyhole threshold and morphology in laser melting revealed by ultrahigh-speed x-ray imaging,” *Science*, vol. 363, no. 6429, pp. 849–852, Feb. 2019, doi: 10.1126/science.aav4687.

[84] S. Shevchik *et al.*, “Supervised deep learning for real-time quality monitoring of laser welding with X-ray radiographic guidance,” *Sci Rep*, vol. 10, no. 1, p. 3389, Dec. 2020, doi: 10.1038/s41598-020-60294-x.

[85] T. Cullom *et al.*, “Frequency domain measurements of melt pool recoil force using modal analysis,” *Sci Rep*, vol. 11, no. 1, p. 10959, May 2021, doi: 10.1038/s41598-021-90423-z.

[86] S. A. Khairallah, A. T. Anderson, A. Rubenchik, and W. E. King, “Laser powder-bed fusion additive manufacturing: Physics of complex melt flow and formation mechanisms of pores, spatter, and denudation zones,” *Acta Materialia*, vol. 108, pp. 36–45, Apr. 2016, doi: 10.1016/j.actamat.2016.02.014.

[87] M. Rombouts, J. P. Kruth, L. Froyen, and P. Mercelis, “Fundamentals of Selective Laser Melting of alloyed steel powders,” *CIRP Annals*, vol. 55, no. 1, pp. 187–192, Jan. 2006, doi: 10.1016/S0007-8506(07)60395-3.

[88] Tolochko Nikolay *et al.*, “Balling processes during selective laser treatment of powders,” *Rapid Prototyping Journal*, vol. 10, pp. 78–87, Apr. 2004, doi: 10.1108/13552540410526953.

[89] C. X. Zhao *et al.*, “The effect of oxygen on transitional Marangoni flow in laser spot welding,” *Acta Materialia*, vol. 58, no. 19, pp. 6345–6357, Nov. 2010, doi: 10.1016/j.actamat.2010.07.056.

[90] Z. S. Saldi, “Marangoni driven free surface flows in liquid weld pools.,” [s.n.], S.l., 2012.

[91] T.-N. Le and Y.-L. Lo, “Effects of sulfur concentration and Marangoni convection on melt-pool formation in transition mode of selective laser melting process,” *Materials & Design*, vol. 179, p. 107866, Oct. 2019, doi: 10.1016/j.matdes.2019.107866.

[92] D. K. Aidun and S. A. Martin, “Effect of sulfur and oxygen on weld penetration of high-purity austenitic stainless steels,” *J. of Materi Eng and Perform*, vol. 6, no. 4, pp. 496–502, Aug. 1997, doi: 10.1007/s11665-997-0121-1.

[93] C. Zhao and I. Richardson, “Complex Flow Motions During Laser Welding,” in *40th AIAA Plasmadynamics and Lasers Conference*, American Institute of Aeronautics and Astronautics, 2009. doi: 10.2514/6.2009-3739.

[94] R. Fabbro, “Melt pool and keyhole behaviour analysis for deep penetration laser welding,” *J. Phys. D: Appl. Phys.*, vol. 43, no. 44, p. 445501, Oct. 2010, doi: 10.1088/0022-3727/43/44/445501.

[95] P. Solana and G. Negro, “A study of the effect of multiple reflections on the shape of the keyhole in the laser processing of materials,” *J. Phys. D: Appl. Phys.*, vol. 30, no. 23, pp. 3216–3222, Dec. 1997, doi: 10.1088/0022-3727/30/23/006.

[96] S. Ly, A. M. Rubenchik, S. A. Khairallah, G. Guss, and M. J. Matthews, “Metal vapor micro-jet controls material redistribution in laser powder bed fusion additive manufacturing,” *Sci Rep*, vol. 7, no. 1, p. 4085, Jun. 2017, doi: 10.1038/s41598-017-04237-z.

[97] K. C. Mills, *Recommended Values of Thermophysical Properties for Selected Commercial Alloys*. Woodhead Publishing, 2002.

[98] A. M. Rubenchik, W. E. King, and S. S. Wu, “Scaling laws for the additive manufacturing,” *Journal of Materials Processing Technology*, vol. 257, pp. 234–243, Jul. 2018, doi: 10.1016/j.jmatprotec.2018.02.034.

[99] L. Gargalis *et al.*, “Determining processing behaviour of pure Cu in laser powder bed fusion using direct micro-calorimetry,” *Journal of Materials Processing Technology*, vol. 294, p. 117130, Aug. 2021, doi: 10.1016/j.jmatprotec.2021.117130.

[100] A. M. Rubenchik *et al.*, “Temperature-dependent 780-nm laser absorption by engineering grade aluminum, titanium, and steel alloy surfaces,” *OE*, vol. 53, no. 12, p. 122506, Jul. 2014, doi: 10.1117/1.OE.53.12.122506.

[101] E. D. Palik, *Handbook of Optical Constants of Solids: Volume 1*. Elsevier, 2012.

[102] S. Krishnan and P. C. Nordine, “Analysis of the optical properties of liquid aluminum,” *Phys. Rev. B*, vol. 48, no. 6, pp. 4130–4131, Aug. 1993, doi: 10.1103/PhysRevB.48.4130.

[103] “Laser Heating of Metals,” *Routledge & CRC Press*. https://www.routledge.com/Laser-Heating-of-Metals/Prokhorov/p/book/9781315894843 (accessed Jul. 18, 2021).

[104] N. R. Comins, “The optical properties of liquid metals,” *Philosophical Magazine*, vol. 25, no. 4, pp. 817–831, Apr. 1972, doi: 10.1080/14786437208229306.

[105] T.-Y. Kuo and Y.-D. Lin, “Effects of Different Shielding Gases and Power Waveforms on Penetration Characteristics and Porosity Formation in Laser Welding of Inconel 690 Alloy,” *Materials Transactions*, vol. 48, no. 2, pp. 219–226, 2007, doi: 10.2320/matertrans.48.219.

[106] R. plc, “Renishaw: RenAM 500Q,” *Renishaw*. http://www.renishaw.com/en/renam-500q--42781 (accessed Jul. 19, 2021).

[107] A. G. Demir and B. Previtali, “Additive manufacturing of cardiovascular CoCr stents by selective laser melting,” *Materials & Design*, vol. 119, pp. 338–350, Apr. 2017, doi: 10.1016/j.matdes.2017.01.091.

[108] K. Mumtaz and N. Hopkinson, "Top surface and side roughness of Inconel 625 parts processed using selective laser melting," *Rapid Prototyping Journal*, vol. 15, no. 2, pp. 96–103, Jan. 2009, doi: 10.1108/13552540910943397.

[109] K. A. Mumtaz and N. Hopkinson, "Selective Laser Melting of thin wall parts using pulse shaping," *Journal of Materials Processing Technology*, vol. 210, no. 2, pp. 279–287, Jan. 2010, doi: 10.1016/j.jmatprotec.2009.09.011.

[110] L. Caprio, A. G. Demir, and B. Previtali, "Comparative study between CW and PW emissions in selective laser melting," *Journal of Laser Applications*, vol. 30, no. 3, p. 032305, Aug. 2018, doi: 10.2351/1.5040631.

[111] L. Caprio, A. G. Demir, and B. Previtali, "Influence of pulsed and continuous wave emission on melting efficiency in selective laser melting," *Journal of Materials Processing Technology*, vol. 266, pp. 429–441, Apr. 2019, doi: 10.1016/j.jmatprotec.2018.11.019.

[112] T. Sparks, J. Ruan, Z. Fan, Y. Bao, and F. Liou, "Effect of structured laser pulses on grain growth in H13 tool steel," *17th Solid Freeform Fabrication Symposium, SFF 2006*, pp. 261–267, Jan. 2006.

[113] T. M. W. WEEDON, "Nd-YAG Lasers with Controlled Pulse Shape," *Proc.of LAMP '87*, pp. 75–80, 1987.

[114] "Effects of the spacial and temporal pulse energy-distribution of a laser-beam on welding." http://leadserv.u-bourgogne.fr/fr/publications/000218-effects-of-the-spacial-and-temporal-pulse-energy-distribution-of-a-laser-beam-on-welding?print=1 (accessed Jul. 19, 2021).

[115] "Petrov: New advances in industry application of YAG... - Google Scholar." https://scholar.google.com/scholar_lookup?title=New%20advances%20in%20industry%20applications%20of%20YAG%20pulse%20lasers&publication_year=1992&author=A.L.%20Petrov&author=A.A.%20Gusev&author=K.S.%20V (accessed Jul. 19, 2021).

[116] S. Katayama, S. Kohsaka, M. Mizutani, K. Nishizawa, and A. Matsunawa, "Pulse shape optimization for defect prevention in pulsed laser welding of stainless steels," *ICALEO*, vol. 1993, no. 1, pp. 487–497, Oct. 1993, doi: 10.2351/1.5058609.

[117] J. Zhang, D. C. Weckman, and Y. Zhou, "Effects of Temporal Pulse Shaping on Cracking Susceptibility of 6061-T6 Aluminum Nd:YAG Laser Welds," p. 13.

[118] E. J. Michaud, D. C. Weckman, and H. W. Kerr, "Effects of pulse shape on predicted thermomechanical strains in Nd:YAG laser welded aluminum," in *International Congress on Applications of Lasers & Electro-Optics*, Orlando, Florida, USA, 1994, pp. 461–470. doi: 10.2351/1.5058824.

[119] A. Matsunawa, M. Mizutani, and S. Katayama, "Mathematical Modeling of Fusion and Solidification in Laser Welding and Evaluation of Hot Cracking Susceptibility," *undefined*, 1996, Accessed: Jul. 19, 2021. [Online]. Available: https://www.semanticscholar.org/paper/Mathematical-Modeling-of-Fusion-and-Solidification-Matsunawa-Mizutani/a27f096b64eb975a7c43b4d8ee2eccbcfd4b0eef

[120] S. Katayama, M. Mizutani, and A. Matsunawa, "Modelling of melting and solidification behaviour during laser spot welding," *Science and Technology of Welding and Joining*, vol. 2, no. 1, pp. 1–9, Feb. 1997, doi: 10.1179/stw.1997.2.1.1.

[121] E. J. Michaud, H. W. Kerr, and D. C. Weckman, "Temporal pulse shaping and solidification cracking in laser welded Al-Cu alloys," Art. no. CONF-950682-, Dec. 1996, Accessed: Jul. 19, 2021. [Online]. Available:

https://www.osti.gov/biblio/442935-temporal-pulse-shaping-solidification-cracking-laser-welded-al-cu-alloys

[122] H. Lee, C. H. J. Lim, M. J. Low, N. Tham, V. M. Murukeshan, and Y.-J. Kim, "Lasers in additive manufacturing: A review," *International Journal of Precision Engineering and Manufacturing-Green Technology*, vol. 4, no. 3, pp. 307–322, Jul. 2017, doi: 10.1007/s40684-017-0037-7.

[123] W. Schulz, G. Simon, H. M. Urbassek, and I. Decker, "On laser fusion cutting of metals," *J. Phys. D: Appl. Phys.*, vol. 20, no. 4, pp. 481–488, Apr. 1987, doi: 10.1088/0022-3727/20/4/013.

[124] "Schuöcker: High power lasers in production engineering.... - Google Scholar." https://scholar.google.com/scholar_lookup?title=High%20Power%20Lasers%20in%20Production%20Engineering&publication_year=1999&author=D.%20Schu%C3%B6cker (accessed Jul. 20, 2021).

[125] J. W. Kim, B. S. Jang, Y. T. Kim, and K. S. Chun, "A study on an efficient prediction of welding deformation for T-joint laser welding of sandwich panel PART I : Proposal of a heat source model," *International Journal of Naval Architecture and Ocean Engineering*, vol. 5, no. 3, pp. 348–363, Sep. 2013, doi: 10.2478/IJNAOE-2013-0138.

[126] W. J. Suder and S. W. Williams, "Investigation of the effects of basic laser material interaction parameters in laser welding," *Journal of Laser Applications*, vol. 24, no. 3, p. 032009, Aug. 2012, doi: 10.2351/1.4728136.

[127] T. Heeling and K. Wegener, "The effect of multi-beam strategies on selective laser melting of stainless steel 316L," *Additive Manufacturing*, vol. 22, pp. 334–342, Aug. 2018, doi: 10.1016/j.addma.2018.05.026.

[128] G. E. Bean, D. B. Witkin, T. D. McLouth, D. N. Patel, and R. J. Zaldivar, "Effect of laser focus shift on surface quality and density of Inconel 718 parts produced via selective laser melting," *Additive Manufacturing*, vol. 22, pp. 207–215, Aug. 2018, doi: 10.1016/j.addma.2018.04.024.

[129] J. Metelkova, Y. Kinds, K. Kempen, C. de Formanoir, A. Witvrouw, and B. Van Hooreweder, "On the influence of laser defocusing in Selective Laser Melting of 316L," *Additive Manufacturing*, vol. 23, pp. 161–169, Oct. 2018, doi: 10.1016/j.addma.2018.08.006.

[130] T. T. Roehling *et al.*, "Modulating laser intensity profile ellipticity for microstructural control during metal additive manufacturing," *Acta Materialia*, vol. 128, pp. 197–206, Apr. 2017, doi: 10.1016/j.actamat.2017.02.025.

[131] T. T. Roehling *et al.*, "Controlling grain nucleation and morphology by laser beam shaping in metal additive manufacturing," *Materials & Design*, vol. 195, p. 109071, Oct. 2020, doi: 10.1016/j.matdes.2020.109071.

[132] M. J. Matthews *et al.*, "Spatial modulation of laser sources for microstructural control of additively manufactured metals," *Procedia CIRP*, vol. 74, pp. 607–610, 2018, doi: 10.1016/j.procir.2018.08.077.

[133] R. Shi, S. A. Khairallah, T. T. Roehling, T. W. Heo, J. T. McKeown, and M. J. Matthews, "Microstructural control in metal laser powder bed fusion additive manufacturing using laser beam shaping strategy," *Acta Materialia*, vol. 184, pp. 284–305, Feb. 2020, doi: 10.1016/j.actamat.2019.11.053.

[134] F. Fetzer, M. Sommer, R. Weber, J.-P. Weberpals, and T. Graf, "Reduction of pores by means of laser beam oscillation during remote welding of AlMgSi," *Optics and*

Lasers in Engineering, vol. 108, pp. 68–77, Sep. 2018, doi: 10.1016/j.optlaseng.2018.04.012.

[135] S. Li, G. Mi, and C. Wang, "A study on laser beam oscillating welding characteristics for the 5083 aluminum alloy: Morphology, microstructure and mechanical properties," *Journal of Manufacturing Processes*, vol. 53, pp. 12–20, May 2020, doi: 10.1016/j.jmapro.2020.01.018.

[136] A. Haeusler, A. Schürmann, C. Schöler, A. Olowinsky, A. Gillner, and R. Poprawe, "Quality improvement of copper welds by laser microwelding with the usage of spatial power modulation," *Journal of Laser Applications*, vol. 29, no. 2, p. 022422, May 2017, doi: 10.2351/1.4983505.

[137] L. H. Shah, F. Khodabakhshi, and A. Gerlich, "Effect of beam wobbling on laser welding of aluminum and magnesium alloy with nickel interlayer," *Journal of Manufacturing Processes*, vol. 37, pp. 212–219, Jan. 2019, doi: 10.1016/j.jmapro.2018.11.028.

[138] N. Islam, J. Schanz, D. Kolb, and H. Riegel, "Improvement of Surface Quality and Process Area Rate in Selective Laser Melting by Beam Oscillation Scan Technique," *J. of Materi Eng and Perform*, May 2021, doi: 10.1007/s11665-021-05665-9.

[139] H. Yang, G. Jing, P. Gao, Z. Wang, and X. Li, "Effects of circular beam oscillation technique on formability and solidification behaviour of selective laser melted Inconel 718: From single tracks to cuboid samples," *Journal of Materials Science & Technology*, vol. 51, pp. 137–150, Aug. 2020, doi: 10.1016/j.jmst.2019.09.044.

[140] J. V. Gordon *et al.*, "Defect structure process maps for laser powder bed fusion additive manufacturing," *Additive Manufacturing*, vol. 36, p. 101552, Dec. 2020, doi: 10.1016/j.addma.2020.101552.

[141] E. Wycisk, A. Solbach, S. Siddique, D. Herzog, F. Walther, and C. Emmelmann, "Effects of Defects in Laser Additive Manufactured Ti-6Al-4V on Fatigue Properties," *Physics Procedia*, vol. 56, pp. 371–378, Jan. 2014, doi: 10.1016/j.phpro.2014.08.120.

[142] P. Edwards and M. Ramulu, "Fatigue performance evaluation of selective laser melted Ti–6Al–4V," *Materials Science and Engineering: A*, vol. 598, pp. 327–337, Mar. 2014, doi: 10.1016/j.msea.2014.01.041.

[143] P. N. Anyalebechi, "Analysis of the effects of alloying elements on hydrogen solubility in liquid aluminum alloys," *Scripta Metallurgica et Materialia*, vol. 33, no. 8, pp. 1209–1216, Oct. 1995, doi: 10.1016/0956-716X(95)00373-4.

[144] K. V. Yang *et al.*, "Porosity formation mechanisms and fatigue response in Al-Si-Mg alloys made by selective laser melting," *Materials Science and Engineering: A*, vol. 712, pp. 166–174, Jan. 2018, doi: 10.1016/j.msea.2017.11.078.

[145] G. K. L. Ng, A. E. W. Jarfors, G. Bi, and H. Y. Zheng, "Porosity formation and gas bubble retention in laser metal deposition," *Appl. Phys. A*, vol. 97, no. 3, pp. 641–649, Nov. 2009, doi: 10.1007/s00339-009-5266-3.

[146] S. K. Dinda, J. M. Warnett, M. A. Williams, G. G. Roy, and P. Srirangam, "3D imaging and quantification of porosity in electron beam welded dissimilar steel to Fe-Al alloy joints by X-ray tomography," *Materials & Design*, vol. 96, pp. 224–231, Apr. 2016, doi: 10.1016/j.matdes.2016.02.010.

[147] H. Shipley *et al.*, "Optimisation of process parameters to address fundamental challenges during selective laser melting of Ti-6Al-4V: A review," *International Journal of Machine Tools and Manufacture*, vol. 128, pp. 1–20, May 2018, doi: 10.1016/j.ijmachtools.2018.01.003.

[148] S. Leuders *et al.*, "On the mechanical behaviour of titanium alloy TiAl6V4 manufactured by selective laser melting: Fatigue resistance and crack growth performance," *International Journal of Fatigue*, vol. 48, pp. 300–307, Mar. 2013, doi: 10.1016/j.ijfatigue.2012.11.011.

[149] A. Gasper, "Spatter and powder evolution in laser powder bed fusion of Nickel-based superalloys," p. 291.

[150] M. Tang, P. C. Pistorius, C. Montgomery, and J. Beuth, "Build Rate Optimization for Powder Bed Fusion," *J. of Materi Eng and Perform*, vol. 28, no. 2, pp. 641–647, Feb. 2019, doi: 10.1007/s11665-018-3647-5.

[151] M. Tang, P. C. Pistorius, and J. L. Beuth, "Prediction of lack-of-fusion porosity for powder bed fusion," *Additive Manufacturing*, vol. 14, pp. 39–48, Mar. 2017, doi: 10.1016/j.addma.2016.12.001.

[152] E. Louvis, P. Fox, and C. J. Sutcliffe, "Selective laser melting of aluminium components," *Journal of Materials Processing Technology*, vol. 211, no. 2, pp. 275–284, Feb. 2011, doi: 10.1016/j.jmatprotec.2010.09.019.

[153] V. Laurent, D. Chatain, C. Chatillon, and N. Eustathopoulos, "Wettability of monocrystalline alumina by aluminium between its melting point and 1273 K," *Acta Metallurgica*, vol. 36, no. 7, pp. 1797–1803, Jul. 1988, doi: 10.1016/0001-6160(88)90248-9.

[154] R. Lin, H. Wang, F. Lu, J. Solomon, and B. E. Carlson, "Numerical study of keyhole dynamics and keyhole-induced porosity formation in remote laser welding of Al alloys," *International Journal of Heat and Mass Transfer*, vol. 108, pp. 244–256, May 2017, doi: 10.1016/j.ijheatmasstransfer.2016.12.019.

[155] S. M. H. Hojjatzadeh *et al.*, "Pore elimination mechanisms during 3D printing of metals," *Nat Commun*, vol. 10, no. 1, p. 3088, Dec. 2019, doi: 10.1038/s41467-019-10973-9.

[156] S. Tammas-Williams, P. J. Withers, I. Todd, and P. B. Prangnell, "Porosity regrowth during heat treatment of hot isostatically pressed additively manufactured titanium components," *Scripta Materialia*, vol. 122, pp. 72–76, Sep. 2016, doi: 10.1016/j.scriptamat.2016.05.002.

[157] C. Weingarten, D. Buchbinder, N. Pirch, W. Meiners, K. Wissenbach, and R. Poprawe, "Formation and reduction of hydrogen porosity during selective laser melting of AlSi10Mg," *Journal of Materials Processing Technology*, vol. 221, pp. 112–120, Jul. 2015, doi: 10.1016/j.jmatprotec.2015.02.013.

[158] A. A. Martin *et al.*, "Dynamics of pore formation during laser powder bed fusion additive manufacturing," *Nat Commun*, vol. 10, no. 1, p. 1987, Apr. 2019, doi: 10.1038/s41467-019-10009-2.

[159] J. Eggers, "Nonlinear dynamics and breakup of free-surface flows," *Rev. Mod. Phys.*, vol. 69, no. 3, pp. 865–930, Jul. 1997, doi: 10.1103/RevModPhys.69.865.

[160] M. Simonelli *et al.*, "A Study on the Laser Spatter and the Oxidation Reactions During Selective Laser Melting of 316L Stainless Steel, Al-Si10-Mg, and Ti-6Al-4V," *Metall and Mat Trans A*, vol. 46, no. 9, pp. 3842–3851, Sep. 2015, doi: 10.1007/s11661-015-2882-8.

[161] Q. Guo *et al.*, "Transient dynamics of powder spattering in laser powder bed fusion additive manufacturing process revealed by in-situ high-speed high-energy x-ray imaging," *Acta Materialia*, vol. 151, pp. 169–180, Jun. 2018, doi: 10.1016/j.actamat.2018.03.036.

[162] A. R. Nassar, M. A. Gundermann, E. W. Reutzel, P. Guerrier, M. H. Krane, and M. J. Weldon, "Formation processes for large ejecta and interactions with melt pool formation in powder bed fusion additive manufacturing," *Scientific Reports*, vol. 9, no. 1, 2019, doi: 10.1038/s41598-019-41415-7.

[163] M. J. Matthews, G. Guss, S. A. Khairallah, A. M. Rubenchik, P. J. Depond, and W. E. King, "Denudation of metal powder layers in laser powder bed fusion processes," *Acta Materialia*, vol. 114, pp. 33–42, Aug. 2016, doi: 10.1016/j.actamat.2016.05.017.

[164] X. Li, C. Zhao, T. Sun, and W. Tan, "Revealing transient powder-gas interaction in laser powder bed fusion process through multi-physics modeling and high-speed synchrotron x-ray imaging," *Additive Manufacturing*, vol. 35, p. 101362, Oct. 2020, doi: 10.1016/j.addma.2020.101362.

[165] C. Zhao *et al.*, "Bulk-Explosion-Induced Metal Spattering During Laser Processing," *Phys. Rev. X*, vol. 9, no. 2, p. 021052, Jun. 2019, doi: 10.1103/PhysRevX.9.021052.

[166] P. Mercelis and J. Kruth, "Residual stresses in selective laser sintering and selective laser melting," *Rapid Prototyping Journal*, vol. 12, no. 5, pp. 254–265, Jan. 2006, doi: 10.1108/13552540610707013.

[167] J. P. Kruth, L. Froyen, J. Van Vaerenbergh, P. Mercelis, M. Rombouts, and B. Lauwers, "Selective laser melting of iron-based powder," *Journal of Materials Processing Technology*, vol. 149, no. 1, pp. 616–622, Jun. 2004, doi: 10.1016/j.jmatprotec.2003.11.051.

[168] B. Vrancken, R. Wauthle, J.-P. Kruth, and J. Humbeeck, "Study of the influence of material properties on residual stress in selective laser melting," *24th International SFF Symposium - An Additive Manufacturing Conference, SFF 2013*, pp. 393–407, Jan. 2013.

[169] L. A. Parry, "Investigation of Residual Stress in Selective Laser Melting," p. 289.

[170] T. Mukherjee, V. Manvatkar, A. De, and T. DebRoy, "Mitigation of thermal distortion during additive manufacturing," *Scripta Materialia*, vol. 127, pp. 79–83, Jan. 2017, doi: 10.1016/j.scriptamat.2016.09.001.

[171] A. S. Wu, D. W. Brown, M. Kumar, G. F. Gallegos, and W. E. King, "An Experimental Investigation into Additive Manufacturing-Induced Residual Stresses in 316L Stainless Steel," *Metall and Mat Trans A*, vol. 45, no. 13, pp. 6260–6270, Dec. 2014, doi: 10.1007/s11661-014-2549-x.

[172] N. C. Levkulich, S. L. Semiatin, J. E. Gockel, J. R. Middendorf, A. T. DeWald, and N. W. Klingbeil, "The effect of process parameters on residual stress evolution and distortion in the laser powder bed fusion of Ti-6Al-4V," *Additive Manufacturing*, vol. 28, pp. 475–484, Aug. 2019, doi: 10.1016/j.addma.2019.05.015.

[173] Z. Xiao *et al.*, "Study of residual stress in selective laser melting of Ti6Al4V," *Materials & Design*, vol. 193, p. 108846, Aug. 2020, doi: 10.1016/j.matdes.2020.108846.

[174] S. Kou, *Welding metallurgy*, 2nd ed. Hoboken, N.J: Wiley-Interscience, 2003.

[175] H. L. Wei, J. Mazumder, and T. DebRoy, "Evolution of solidification texture during additive manufacturing," *Sci Rep*, vol. 5, no. 1, p. 16446, Dec. 2015, doi: 10.1038/srep16446.

[176] J. D. Hunt, “Steady state columnar and equiaxed growth of dendrites and eutectic,” *Materials Science and Engineering*, vol. 65, no. 1, pp. 75–83, Jul. 1984, doi: 10.1016/0025-5416(84)90201-5.

[177] W. Kurz, B. Giovanola, and R. Trivedi, “Theory of microstructural development during rapid solidification,” *Acta Metallurgica*, vol. 34, no. 5, pp. 823–830, May 1986, doi: 10.1016/0001-6160(86)90056-8.

[178] A. Prasad *et al.*, “Towards understanding grain nucleation under Additive Manufacturing solidification conditions,” *Acta Materialia*, vol. 195, pp. 392–403, Aug. 2020, doi: 10.1016/j.actamat.2020.05.012.

[179] M. Gäumann, S. Henry, F. Cléton, J.-D. Wagnière, and W. Kurz, “Epitaxial laser metal forming: analysis of microstructure formation,” *Materials Science and Engineering: A*, vol. 271, no. 1, pp. 232–241, Nov. 1999, doi: 10.1016/S0921-5093(99)00202-6.

[180] M. Rappaz, S. A. David, J. M. Vitek, and L. A. Boatner, “Analysis of solidification microstructures in Fe-Ni-Cr single-crystal welds,” *Metallurgical Transactions A*, vol. 21, no. 6, pp. 1767–1782, 1990, doi: 10.1007/BF02672593.

[181] S. Kou and Y. Le, “Nucleation Mechanisms and Grain Refining of Weld Metal,” p. 9.

[182] N. Coniglio and C. E. Cross, “Initiation and growth mechanisms for weld solidification cracking,” *International Materials Reviews*, vol. 58, no. 7, pp. 375–397, Sep. 2013, doi: 10.1179/1743280413Y.0000000020.

[183] J. H. Martin, B. D. Yahata, J. M. Hundley, J. A. Mayer, T. A. Schaedler, and T. M. Pollock, “3D printing of high-strength aluminium alloys,” *Nature*, vol. 549, no. 7672, pp. 365–369, 2017, doi: 10.1038/nature23894.

[184] C. M. Gourlay and A. K. Dahle, “Dilatant shear bands in solidifying metals,” *Nature*, vol. 445, no. 7123, pp. 70–73, Jan. 2007, doi: 10.1038/nature05426.

[185] M. Yang, L. Wang, and W. Yan, “Phase-field modeling of grain evolutions in additive manufacturing from nucleation, growth, to coarsening,” *npj Comput Mater*, vol. 7, no. 1, pp. 1–12, Apr. 2021, doi: 10.1038/s41524-021-00524-6.

[186] E. Herderick, “Additive Manufacturing of Metals: A Review,” p. 13.

[187] P. C. Collins, D. A. Brice, P. Samimi, I. Ghamarian, and H. L. Fraser, “Microstructural Control of Additively Manufactured Metallic Materials,” *Annual Review of Materials Research*, vol. 46, no. 1, pp. 63–91, 2016, doi: 10.1146/annurev-matsci-070115-031816.

[188] K. N. Amato *et al.*, “Microstructures and mechanical behavior of Inconel 718 fabricated by selective laser melting,” *Acta Materialia*, vol. 60, no. 5, pp. 2229–2239, Mar. 2012, doi: 10.1016/j.actamat.2011.12.032.

[189] E. W. Hovig, A. S. Azar, F. Grytten, K. Sørby, and E. Andreassen, “Determination of Anisotropic Mechanical Properties for Materials Processed by Laser Powder Bed Fusion,” *Advances in Materials Science and Engineering*, vol. 2018, p. e7650303, Nov. 2018, doi: 10.1155/2018/7650303.

[190] L. Yuan, A. S. Sabau, D. StJohn, A. Prasad, and P. D. Lee, “Columnar-to-equiaxed transition in a laser scan for metal additive manufacturing,” *IOP Conf. Ser.: Mater. Sci. Eng.*, vol. 861, p. 012007, Jun. 2020, doi: 10.1088/1757-899X/861/1/012007.

[191] G. P. Dinda, A. K. Dasgupta, and J. Mazumder, “Texture control during laser deposition of nickel-based superalloy,” *Scripta Materialia*, vol. 67, no. 5, pp. 503–506, Sep. 2012, doi: 10.1016/j.scriptamat.2012.06.014.

[192] A. H. Pham, W. Yeh, S. Morito, and T. Ohba, “Selective growth of single-grain crystal in Al thin film by micron chevron-shaped laser beam scanning,” *Thin Solid Films*, vol. 672, pp. 100–103, Feb. 2019, doi: 10.1016/j.tsf.2019.01.023.

[193] R. R. Dehoff, M. M. Kirka, F. A. List, K. A. Unocic, and W. J. Sames, “Crystallographic texture engineering through novel melt strategies via electron beam melting: Inconel 718,” *Materials Science and Technology*, vol. 31, no. 8, pp. 939–944, Jun. 2015, doi: 10.1179/1743284714Y.0000000697.

[194] N. Raghavan, “Numerical modeling of heat-transfer and the influence of process parameters on tailoring the grain morphology of IN718 in electron beam additive manufacturing,” *Acta Materialia*, p. 12, 2016.

[195] N. Raghavan *et al.*, “Localized melt-scan strategy for site specific control of grain size and primary dendrite arm spacing in electron beam additive manufacturing,” *Acta Materialia*, vol. 140, pp. 375–387, Nov. 2017, doi: 10.1016/j.actamat.2017.08.038.

[196] A. Plotkowski *et al.*, “A stochastic scan strategy for grain structure control in complex geometries using electron beam powder bed fusion,” *Additive Manufacturing*, vol. 46, p. 102092, Oct. 2021, doi: 10.1016/j.addma.2021.102092.

[197] R. R. Dehoff *et al.*, “Site specific control of crystallographic grain orientation through electron beam additive manufacturing,” *Materials Science and Technology*, vol. 31, no. 8, pp. 931–938, Jun. 2015, doi: 10.1179/1743284714Y.0000000734.

[198] M. J. Matthews *et al.*, “Diode-based additive manufacturing of metals using an optically-addressable light valve,” *Opt. Express, OE*, vol. 25, no. 10, pp. 11788–11800, May 2017, doi: 10.1364/OE.25.011788.

[199] J. D. Roehling *et al.*, “Reducing residual stress by selective large-area diode surface heating during laser powder bed fusion additive manufacturing,” *Additive Manufacturing*, vol. 28, pp. 228–235, Aug. 2019, doi: 10.1016/j.addma.2019.05.009.

[200] E. Liverani, S. Toschi, L. Ceschini, and A. Fortunato, “Effect of selective laser melting (SLM) process parameters on microstructure and mechanical properties of 316L austenitic stainless steel,” *Journal of Materials Processing Technology*, vol. 249, pp. 255–263, Nov. 2017, doi: 10.1016/j.jmatprotec.2017.05.042.

[201] M. A. Ackers, O. M. D. M. Messé, and U. Hecht, “Novel approach of alloy design and selection for additive manufacturing towards targeted applications,” *Journal of Alloys and Compounds*, vol. 866, p. 158965, Jun. 2021, doi: 10.1016/j.jallcom.2021.158965.

[202] U. Scipioni Bertoli, A. J. Wolfer, M. J. Matthews, J.-P. R. Delplanque, and J. M. Schoenung, “On the limitations of Volumetric Energy Density as a design parameter for Selective Laser Melting,” *Materials & Design*, vol. 113, pp. 331–340, Jan. 2017, doi: 10.1016/j.matdes.2016.10.037.

[203] N. T. Aboulkhair, “Reducing porosity in AlSi10Mg parts processed by selective laser melting,” *Additive Manufacturing*, p. 10, 2014.

[204] D. Hann, J. Iammi, and J. Folkes, “Keyholing or Conduction? Prediction of Laser Penetration Depth,” *Lasers in Engineering*, vol. 22, pp. 309–317, Jan. 2011, doi: 10.1007/978-1-84996-432-6_63.

[205] J. Ye *et al.*, “Energy Coupling Mechanisms and Scaling Behavior Associated with Laser Powder Bed Fusion Additive Manufacturing,” *Adv. Eng. Mater.*, vol. 21, no. 7, p. 1900185, Jul. 2019, doi: 10.1002/adem.201900185.

[206] E. Soylemez, "High deposition rate approach of selective laser melting through defocused single bead experiments and thermal finite element analysis for Ti-6Al-4V," *Additive Manufacturing*, vol. 31, p. 100984, Jan. 2020, doi: 10.1016/j.addma.2019.100984.

[207] H. Ghasemi-Tabasi, J. Jhabvala, E. Boillat, T. Ivas, R. Drissi-Daoudi, and R. E. Logé, "An effective rule for translating optimal selective laser melting processing parameters from one material to another," *Additive Manufacturing*, vol. 36, p. 101496, Dec. 2020, doi: 10.1016/j.addma.2020.101496.

[208] J. C. Ion, H. R. Shercliff, and M. F. Ashby, "Diagrams for laser materials processing," *Acta Metallurgica et Materialia*, vol. 40, no. 7, pp. 1539–1551, Jul. 1992, doi: 10.1016/0956-7151(92)90097-X.

[209] M. Thomas, G. J. Baxter, and I. Todd, "Normalised model-based processing diagrams for additive layer manufacture of engineering alloys," *Acta Materialia*, vol. 108, pp. 26–35, Apr. 2016, doi: 10.1016/j.actamat.2016.02.025.

[210] G. Tapia and A. Elwany, "A Review on Process Monitoring and Control in Metal-Based Additive Manufacturing," *Journal of Manufacturing Science and Engineering*, vol. 136, no. 6, Oct. 2014, doi: 10.1115/1.4028540.

[211] D. L. Bourell, D. W. Rosen, and M. C. Leu, "The Roadmap for Additive Manufacturing and Its Impact," *3D Printing and Additive Manufacturing*, vol. 1, no. 1, pp. 6–9, Mar. 2014, doi: 10.1089/3dp.2013.0002.

[212] M. Mani, B. M. Lane, M. A. Donmez, S. C. Feng, and S. P. Moylan, "A review on measurement science needs for real-time control of additive manufacturing metal powder bed fusion processes," *International Journal of Production Research*, vol. 55, no. 5, pp. 1400–1418, Mar. 2017, doi: 10.1080/00207543.2016.1223378.

[213] S. Kleszczynski, "Error detection in laser beam melting systems by high resolution imaging," p. 14.

[214] P. Lott, H. Schleifenbaum, W. Meiners, K. Wissenbach, C. Hinke, and J. Bültmann, "Design of an Optical system for the In Situ Process Monitoring of Selective Laser Melting (SLM)," *Physics Procedia*, vol. 12, pp. 683–690, Jan. 2011, doi: 10.1016/j.phpro.2011.03.085.

[215] S. Clijsters, T. Craeghs, S. Buls, K. Kempen, and J.-P. Kruth, "In situ quality control of the selective laser melting process using a high-speed, real-time melt pool monitoring system," *Int J Adv Manuf Technol*, vol. 75, no. 5–8, pp. 1089–1101, Nov. 2014, doi: 10.1007/s00170-014-6214-8.

[216] H. Ki, J. Mazumder, and P. S. Mohanty, "Modeling of laser keyhole welding: Part II. simulation of keyhole evolution, velocity, temperature profile, and experimental verification," *Metall Mater Trans A*, vol. 33, no. 6, pp. 1831–1842, Jun. 2002, doi: 10.1007/s11661-002-0191-5.

[217] V. V. Semak, B. Damkroger, and S. Kempka, "Temporal evolution of the temperature field in the beam interaction zone during laser material processing," *Journal of Physics D: Applied Physics*, vol. 32, no. 15, pp. 1819–1825, 1999, doi: 10.1088/0022-3727/32/15/309.

[218] T. Craeghs, F. Bechmann, S. Berumen, and J.-P. Kruth, "Feedback control of Layerwise Laser Melting using optical sensors," *Physics Procedia*, vol. 5, pp. 505–514, Jan. 2010, doi: 10.1016/j.phpro.2010.08.078.

[219] V. Renken, A. von Freyberg, K. Schünemann, F. Pastors, and A. Fischer, "In-process closed-loop control for stabilising the melt pool temperature in selective

laser melting," *Prog Addit Manuf*, vol. 4, no. 4, pp. 411–421, Dec. 2019, doi: 10.1007/s40964-019-00083-9.

[220] C. Reiff, W. Bubeck, D. Krawczyk, M. Steeb, A. Lechler, and A. Verl, "Learning Feedforward Control for Laser Powder Bed Fusion," *Procedia CIRP*, vol. 96, pp. 127–132, Jan. 2021, doi: 10.1016/j.procir.2021.01.064.

[221] S. A. Shevchik, C. Kenel, C. Leinenbach, and K. Wasmer, "Acoustic emission for in situ quality monitoring in additive manufacturing using spectral convolutional neural networks," *Additive Manufacturing*, vol. 21, pp. 598–604, May 2018, doi: 10.1016/j.addma.2017.11.012.

[222] H. Yeung, B. Lane, and J. Fox, "Part geometry and conduction-based laser power control for powder bed fusion additive manufacturing," *Additive Manufacturing*, vol. 30, p. 100844, Dec. 2019, doi: 10.1016/j.addma.2019.100844.

[223] T. Phillips, S. Fish, and J. Beaman, "Development of an automated laser control system for improving temperature uniformity and controlling component strength in selective laser sintering," *Additive Manufacturing*, vol. 24, pp. 316–322, Dec. 2018, doi: 10.1016/j.addma.2018.10.016.

[224] T. Phillips, T. Ricker, S. Fish, and J. Beaman, "Design of a laser control system with continuously variable power and its application in additive manufacturing," *Additive Manufacturing*, vol. 34, p. 101173, Aug. 2020, doi: 10.1016/j.addma.2020.101173.

[225] R. J. Williams *et al.*, "In situ thermography for laser powder bed fusion: Effects of layer temperature on porosity, microstructure and mechanical properties," *Additive Manufacturing*, vol. 30, p. 100880, Dec. 2019, doi: 10.1016/j.addma.2019.100880.

[226] D. Axinte and J. Billingham, "Time-dependent manufacturing processes lead to a new class of inverse problems," *Proc Natl Acad Sci USA*, vol. 116, no. 12, pp. 5341–5343, Mar. 2019, doi: 10.1073/pnas.1900420116.

[227] A. Papacharalampopoulos, P. Stavropoulos, and J. Stavridis, "Adaptive Control of Thermal Processes: Laser Welding and Additive Manufacturing Paradigms," *Procedia CIRP*, vol. 67, pp. 233–237, Jan. 2018, doi: 10.1016/j.procir.2017.12.205.

[228] Q. Wang, P. (Pan) Michaleris, A. R. Nassar, J. E. Irwin, Y. Ren, and C. B. Stutzman, "Model-based feedforward control of laser powder bed fusion additive manufacturing," *Additive Manufacturing*, vol. 31, p. 100985, Jan. 2020, doi: 10.1016/j.addma.2019.100985.

[229] E. Stathatos and G.-C. Vosniakos, "Efficient temperature regulation through power optimization for arbitrary paths in Laser Based Additive Manufacturing," *CIRP Journal of Manufacturing Science and Technology*, vol. 33, pp. 133–142, May 2021, doi: 10.1016/j.cirpj.2021.03.008.

[230] M. A. Balbaa, A. Ghasemi, E. Fereiduni, M. A. Elbestawi, S. D. Jadhav, and J.-P. Kruth, "Role of powder particle size on laser powder bed fusion processability of AlSi10mg alloy," *Additive Manufacturing*, vol. 37, p. 101630, Jan. 2021, doi: 10.1016/j.addma.2020.101630.

[231] P. A. Cundall and O. D. L. Strack, "A discrete numerical model for granular assemblies," *Géotechnique*, vol. 29, no. 1, pp. 47–65, Mar. 1979, doi: 10.1680/geot.1979.29.1.47.

[232] C. Kloss, C. Goniva, A. Hager, S. Amberger, and S. Pirker, "Models, algorithms and validation for opensource DEM and CFD–DEM," *Progress in Computational Fluid*

Dynamics, an International Journal, vol. 12, no. 2–3, pp. 140–152, Jan. 2012, doi: 10.1504/PCFD.2012.047457.

[233] Y. Zhang and J. Zhang, "Modeling of solidification microstructure evolution in laser powder bed fusion fabricated 316L stainless steel using combined computational fluid dynamics and cellular automata," *Additive Manufacturing*, vol. 28, pp. 750–765, Aug. 2019, doi: 10.1016/j.addma.2019.06.024.

[234] E. J. R. Parteli and T. Pöschel, "Particle-based simulation of powder application in additive manufacturing," *Powder Technology*, vol. 288, pp. 96–102, Jan. 2016, doi: 10.1016/j.powtec.2015.10.035.

[235] Y. He, A. Hassanpour, and A. E. Bayly, "Linking particle properties to layer characteristics: Discrete element modelling of cohesive fine powder spreading in additive manufacturing," *Additive Manufacturing*, vol. 36, p. 101685, Dec. 2020, doi: 10.1016/j.addma.2020.101685.

[236] Z. Xiang, M. Zhang, R. Yan, Q. Yin, and K. Zhang, "Powder-spreading dynamics and packing quality improvement for laser powder bed fusion additive manufacturing," *Powder Technology*, vol. 389, pp. 278–291, Sep. 2021, doi: 10.1016/j.powtec.2021.05.036.

[237] H. Gu and L. Li, "Computational fluid dynamic simulation of gravity and pressure effects in laser metal deposition for potential additive manufacturing in space," *International Journal of Heat and Mass Transfer*, vol. 140, pp. 51–65, Sep. 2019, doi: 10.1016/j.ijheatmasstransfer.2019.05.081.

[238] W. Yuan, H. Chen, T. Cheng, and Q. Wei, "Effects of laser scanning speeds on different states of the molten pool during selective laser melting: Simulation and experiment," *Materials & Design*, vol. 189, p. 108542, Apr. 2020, doi: 10.1016/j.matdes.2020.108542.

[239] A. Hozoorbakhsh, M. Hamdi, A. A. D. M. Sarhan, M. I. S. Ismail, C.-Y. Tang, and G. C.-P. Tsui, "CFD modelling of weld pool formation and solidification in a laser micro-welding process," *International Communications in Heat and Mass Transfer*, vol. 101, pp. 58–69, Feb. 2019, doi: 10.1016/j.icheatmasstransfer.2019.01.001.

[240] W. Tan, N. S. Bailey, and Y. C. Shin, "Investigation of keyhole plume and molten pool based on a three-dimensional dynamic model with sharp interface formulation," *J. Phys. D: Appl. Phys.*, vol. 46, no. 5, p. 055501, Jan. 2013, doi: 10.1088/0022-3727/46/5/055501.

[241] W. Tan and Y. C. Shin, "Analysis of multi-phase interaction and its effects on keyhole dynamics with a multi-physics numerical model," *J. Phys. D: Appl. Phys.*, vol. 47, no. 34, p. 345501, Jul. 2014, doi: 10.1088/0022-3727/47/34/345501.

[242] A. Zakirov *et al.*, "Predictive modeling of laser and electron beam powder bed fusion additive manufacturing of metals at the mesoscale," *Additive Manufacturing*, vol. 35, p. 101236, Oct. 2020, doi: 10.1016/j.addma.2020.101236.

[243] C. Panwisawas *et al.*, "Keyhole formation and thermal fluid flow-induced porosity during laser fusion welding in titanium alloys: Experimental and modelling," *Acta Materialia*, vol. 126, pp. 251–263, Mar. 2017, doi: 10.1016/j.actamat.2016.12.062.

[244] C. Tang, "A numerical investigation on the physical mechanisms of single track defects in selective laser melting," *International Journal of Heat and Mass Transfer*, p. 12, 2018.

[245] A. Choudhury, K. Reuther, E. Wesner, A. August, B. Nestler, and M. Rettenmayr, "Comparison of phase-field and cellular automaton models for dendritic

solidification in Al–Cu alloy," *Computational Materials Science*, vol. 55, pp. 263–268, Apr. 2012, doi: 10.1016/j.commatsci.2011.12.019.

[246] "Geometrical effects on residual stress in selective laser melting," *Additive Manufacturing*, vol. 25, pp. 166–175, Jan. 2019, doi: 10.1016/j.addma.2018.09.026.

[247] D. ROSENTHAL, "Mathematical Theory of Heat Distribution during Welding and Cutting," *Welding Journal*, vol. 20, pp. 220–234, 1941.

[248] D. ROSENTHAL, "The Theory of Moving Sources of Heat and Its Application of Metal Treatments," *Transactions of ASME*, vol. 68, pp. 849–866, 1946.

[249] S. A. Khairallah *et al.*, "Controlling interdependent meso-nanosecond dynamics and defect generation in metal 3D printing," *Science*, vol. 368, no. 6491, pp. 660–665, May 2020, doi: 10.1126/science.aay7830.

[250] V. Vedachalam, "Discrete Element Modelling Of Granular Snow Particles Using LIGGGHTS," p. 105.

[251] N. V. Brilliantov, F. Spahn, J.-M. Hertzsch, and T. Pöschel, "Model for collisions in granular gases," *Phys. Rev. E*, vol. 53, no. 5, pp. 5382–5392, May 1996, doi: 10.1103/PhysRevE.53.5382.

[252] J. Abrahamson, "Fluent Theory Guide," p. 1072, 2021.

[253] J. U. Brackbill, D. B. Kothe, and C. Zemach, "A continuum method for modeling surface tension," *Journal of Computational Physics*, vol. 100, no. 2, pp. 335–354, Jun. 1992, doi: 10.1016/0021-9991(92)90240-Y.

[254] S. I. Anisimov and V. A. Khokhlov, *Instabilities in Laser-Matter Interaction*. CRC Press, 1995.

[255] A. E. Gheribi and P. Chartrand, "Temperature and oxygen adsorption coupling effects upon the surface tension of liquid metals," *Sci Rep*, vol. 9, no. 1, p. 7113, May 2019, doi: 10.1038/s41598-019-43500-3.

[256] M. Leitner, T. Leitner, A. Schmon, K. Aziz, and G. Pottlacher, "Thermophysical Properties of Liquid Aluminum," *Metall Mater Trans A*, vol. 48, no. 6, pp. 3036–3045, Jun. 2017, doi: 10.1007/s11661-017-4053-6.

[257] I. Yadroitsev, P. Krakhmalev, I. Yadroitsava, S. Johansson, and I. Smurov, "Energy input effect on morphology and microstructure of selective laser melting single track from metallic powder," *Journal of Materials Processing Technology*, vol. 213, no. 4, pp. 606–613, Apr. 2013, doi: 10.1016/j.jmatprotec.2012.11.014.

[258] A. D. Rakić, "Algorithm for the determination of intrinsic optical constants of metal films: application to aluminum," *Appl. Opt., AO*, vol. 34, no. 22, pp. 4755–4767, Aug. 1995, doi: 10.1364/AO.34.004755.

[259] D. Bergström, J. Powell, and A. F. H. Kaplan, "Absorptance of nonferrous alloys to Nd:YLF and Nd:YAG laser light at room temperature," *Appl. Opt., AO*, vol. 46, no. 8, pp. 1290–1301, Mar. 2007, doi: 10.1364/AO.46.001290.

[260] H. E. Bennett, M. Silver, and E. J. Ashley, "Infrared Reflectance of Aluminum Evaporated in Ultra-High Vacuum," *J. Opt. Soc. Am., JOSA*, vol. 53, no. 9, pp. 1089–1095, Sep. 1963, doi: 10.1364/JOSA.53.001089.

[261] J.-P. Kruth, J. Duflou, P. Mercelis, J. Van Vaerenbergh, T. Craeghs, and J. De Keuster, "On-line monitoring and process control in selective laser melting and laser cutting," *Proceedings of the 5th Lane Conference, Laser Assisted Net Shape Engineering*, no. 1, pp. 23–37, 2007.

[262] J.-H. Cho, D. F. Farson, J. O. Milewski, and K. J. Hollis, “Weld pool flows during initial stages of keyhole formation in laser welding,” *J. Phys. D: Appl. Phys.*, vol. 42, no. 17, p. 175502, Aug. 2009, doi: 10.1088/0022-3727/42/17/175502.

[263] Q. Tan *et al.*, “Inoculation treatment of an additively manufactured 2024 aluminium alloy with titanium nanoparticles,” *Acta Materialia*, vol. 196, pp. 1–16, Sep. 2020, doi: 10.1016/j.actamat.2020.06.026.

[264] Giuseppe Del Guercio *et al.*, “Cracking behaviour of high-strength AA2024 aluminium alloy produced by Laser Powder Bed Fusion,” *Yet to be Published*.

[265] S. Kou, “A criterion for cracking during solidification,” *Acta Materialia*, vol. 88, pp. 366–374, Apr. 2015, doi: 10.1016/j.actamat.2015.01.034.

[266] D. G. Eskin and L. Katgerman, “A Quest for a New Hot Tearing Criterion,” *Metall Mater Trans A*, vol. 38, no. 7, pp. 1511–1519, Jul. 2007, doi: 10.1007/s11661-007-9169-7.

[267] S. A. David and J. M. Vitek, “Correlation between solidification parameters and weld microstructures,” *International Materials Reviews*, vol. 34, no. 1, pp. 213–245, Jan. 1989, doi: 10.1179/imr.1989.34.1.213.

[268] “Hunt: Solidification and casting of metals - Google Scholar.” https://scholar.google.com/scholar_lookup?title=Solidification%20and%20Casting%20of%20Metals&pages=3-9&publication_year=1979&author=Hunt%2CJ.D.#d=gs_cit&u=%2Fscholar%3Fq%3Dinfo%3AK-OMinPDZvcJ%3Ascholar.google.com%2F%26output%3Dcite%26scirp%3D0%26hl%3Den (accessed Dec. 01, 2021).

[269] M. C. Flemings, “Solidification processing,” *Metall Mater Trans B*, vol. 5, no. 10, pp. 2121–2134, Oct. 1974, doi: 10.1007/BF02643923.

10 Appendices

10.1 Discrete element modelling script used for generating the initial powder bed configuration in LIGGGHTS

Script used to generate the LIGGGHTS initial powder bed configuration

```
####################Header for General commands####################
atom_style      granular        #Simulation of particles
boundary        f f f                   #fixed boundaries -> particles will be deleted if leaving the simulation box
units           si
communicate     single vel yes  #default
newton          off                             #default
###################System variables#############
#Definition of boundaries
variable xmin equal -2.55
variable xmax equal 2.55
variable ymin equal -2.55
variable ymax equal 2.55
variable zmin equal -0.05
variable zmax equal 5.0
#Definition of the timestep
variable dt equal 1e-5                  #timestep = 0.0001 second; Each iteration step represents 0.0001 seconds.

############## Specific variables for current simulation#################
variable natoms equal 2     #1 -> particle #2->hopper,frame and ground, lid, bed, recoater
####variable for material properties####
####Young Modulus####
variable  youngmodulus1   equal     1e8             #N/mm^2
variable  youngmodulus2   equal     1e8             #N/mm^2
####Poission ratio####
variable  poission1       equal     0.3
variable  poission2       equal     0.3
####variable for contact properties####
####coefficient of restitution####
variable  CoR11     equal     0.6
variable  CoR12     equal     0.6
variable  CoR21     equal     0.6
variable  CoR22     equal     0.6
####sliding friction coefficient####
variable  sf11      equal     0.3
variable  sf12      equal     0.36
variable  sf21      equal     0.36
variable  sf22      equal     0.0
####rolling friction coefficient####
variable  rf11      equal     0.8
variable  rf12      equal     0.8
variable  rf21      equal     0.8
variable  rf22      equal     0.8
####variable for particle################################################
#Number of particle radius
variable  nradii    equal     8

variable  radius1   equal     0.0075  #m
variable  radius2   equal     0.008   #m
variable  radius3   equal     0.009   #m
variable  radius4   equal     0.010   #m
variable  radius5   equal     0.011   #m
variable  radius6   equal     0.014   #m
variable  radius7   equal     0.018   #m
variable  radius8   equal     0.0225  #m
```

```
variable  frac1      equal     0.07
variable  frac2      equal     0.13
variable  frac3      equal     0.18
variable  frac4      equal     0.25
variable  frac5      equal     0.17
variable  frac6      equal     0.11
variable  frac7      equal     0.06
variable  frac8      equal     0.03
variable  density    equal     1000      #kg/m^3
####filling parameters#####################################

variable  filltime   equal     4                 #seconds
variable  fillmass   equal     180       #kg
variable  fillmassrate         equal     ${fillmass}/${filltime}         #kg/s
variable  fillsteps  equal     ${filltime}/${dt}               #Transform time to iteration steps

####settle time#####

variable  settletime           equal     3 #second
variable  settlesteps          equal     ${settletime}/${dt}                     #Transform time to iteration steps
####recoater blade 1 #####
variable  recoatervel1         equal     -0.4          #m/s
variable  recoatertime1        equal     0.5 #seconds
variable  recoatersteps1 equal         ${recoatertime1}/${dt}  #transform time to iteration steps
####recoater blade 2 #####
variable  recoatervel2         equal     0.1           #m/s
variable  recoatertime2        equal     14 #seconds
variable  recoatersteps2       equal     ${recoatertime2}/${dt}  #transform time to iteration steps
####discharge time 2 #####
variable  dischargetime2       equal     1 #seconds
variable  dischargesteps2 equal        ${dischargetime2}/${dt}     #Transform time to iteration steps
##########Definition of simulation box###################
region                 reg block ${xmin} ${xmax} ${ymin} ${ymax} ${zmin} ${zmax} units box
create_box             2 reg
neighbor 0.004 bin                     #default
neigh_modify           delay 0                 #default
################Definition of the contact models#######################
pair_style gran model hertz tangential history rolling_friction epsd2          #contact model
pair_coeff             * *                                     #default
timestep ${dt}
fix                    integrator all nve/sphere                       #default
fix                    gravi all gravity 9.81 vector 0.0 0.0 -1.0                      #gravity of 9.81 m/s^2 in negative z direction
#####################################Definition of Material properties#########################################

fix                    m1 all property/global youngsModulus peratomtype ${youngmodulus1} ${youngmodulus2}
fix                    m2 all property/global poissonsRatio peratomtype ${poission1} ${poission2}
fix                    m3 all property/global coefficientRestitution peratomtypepair ${natoms} 0.6 0.6 0.6 0.6
fix                    m4 all property/global coefficientFriction peratomtypepair ${natoms} ${sf11} ${sf12} ${sf21} ${sf22}
fix                    m5 all property/global coefficientRollingFriction peratomtypepair ${natoms} ${rf11} ${rf12} ${rf21} ${rf22}
#####################################Generation and Loading of the Geometry .stl#############################################
#fix                           silo      all mesh/surface file Silo.stl type 2  scale 0.001          #load mesh from STL file. Type 2 for geometry. Scale down to transform mm to meters
#fix                           lid       all mesh/surface file Lid.stl  type 2  scale 0.001
#fix                           ground    all mesh/surface file Ground.stl type 2  scale 0.001
#fix                           frame     all mesh/surface file Frame.stl  type 2  scale 0.001
fix                    bed    all mesh/surface file bed.stl       type 2  scale 0.001
fix                    recoater all mesh/surface file recoater.stl type 2 scale 0.001
```

```
fix                walls      all wall/gran model hertz tangential history rolling_friction epsd2 mesh
n_meshes 2 meshes bed recoater
####################################Generation and Insertion of the
particles#########################################
fix                pts1 all particletemplate/sphere 10487 atom_type 1 density constant ${density} radius
constant ${radius1}
fix                pts2 all particletemplate/sphere 11887 atom_type 1 density constant ${density} radius
constant ${radius2}
fix                pts3 all particletemplate/sphere 11897 atom_type 1 density constant ${density} radius
constant ${radius3}
fix                pts4 all particletemplate/sphere 11903 atom_type 1 density constant ${density} radius
constant ${radius4}
fix                pts5 all particletemplate/sphere 11909 atom_type 1 density constant ${density} radius
constant ${radius5}
fix                pts6 all particletemplate/sphere 11923 atom_type 1 density constant ${density} radius
constant ${radius6}
fix                pts7 all particletemplate/sphere 12097 atom_type 1 density constant ${density} radius
constant ${radius7}
fix                pts8 all particletemplate/sphere 12197 atom_type 1 density constant ${density} radius
constant ${radius8}
fix        pdd1 all particledistribution/discrete 32452867 ${nradii} pts1 ${frac1} pts2 ${frac2} pts3
${frac3} pts4 ${frac4} pts5 ${frac5} pts6 ${frac6} pts7 ${frac7} pts8 ${frac8}
fix                ins_mesh all mesh/surface/planar file Insertionsface.stl type 1 scale 0.001
fix        ins all insert/stream seed 86028157 distributiontemplate pdd1 &
     mass ${fillmass} massrate ${fillmassrate} overlapcheck yes all_in yes vel constant 0 0 -0.75 &
     insertion_face ins_mesh extrude_length 0.25

###############Dumping of the data for post-processing to visualize############
shell      mkdir post
#Definition of the dumptime
variable dumptime equal 0.04          # Every 0.05 s 1 image
variable dumpstep equal ${dumptime}/${dt}    #Transform to iteration steps

dump     dmpparticle all custom/vtk ${dumpstep} post/particles_*.vtk id type x y z vx vy vz fx fy fz radius
mass
#dump    dmpground all mesh/stl ${dumpstep} post/Ground*.stl ground
#dump    dmpsilo all mesh/stl ${dumpstep} post/Silo*.stl silo
#dump    dmpframe all mesh/stl ${dumpstep} post/Frame*.stl  frame
#dump    dmplid all mesh/stl ${dumpstep} post/Lid*.stl lid
dump    dmpbed all mesh/stl ${dumpstep} post/Bed*.stl bed
dump     dmprecoater all mesh/stl ${dumpstep} post/Recoater*.stl recoater

#####################################RUN the simulation
filling#####################################################
run         ${fillsteps}
unfix      ins
##########RUN the simulation settling##############################

run         ${settlesteps}
#####RUN the recoater blade 1 ##########################

#fix        MoveRecoater1     all move/mesh mesh recoater linear ${recoatervel1} 0. 0.
#run ${recoatersteps1}
#unfix MoveRecoater1
###############RUN the recoater blade 2 ################

#fix        MoveRecoater2     all move/mesh mesh recoater linear ${recoatervel2} 0. 0.
#run ${recoatersteps2}
#unfix MoveRecoater2
####################RUN the simulation  Outflow 2 ####################
#run        ${dischargesteps2}
```

10.2 ANSYS Fluent custom user defined functions

10.2.1 Heat source model

```
DEFINE_DPM_SCALAR_UPDATE(RayTracing, c, t, initialize, tp)
{
	c = P_CELL(tp);
	t = P_CELL_THREAD(tp);
	real x[ND_ND];

	/* variables for polimi */
	real multiplyer = 1.0;
	real ramp_time = 0.0;
	real limiter = 1.0;
	real rate = 0.0;
	real time = fmod(CURRENT_TIME, exposure_timep);
	real time2 = fmod(CURRENT_TIME, e_d_time);

	/* variables for gaussian laser */
	real laser_position = laser_vel * CURRENT_TIME;
	real laser_power_mod;
	real laserm2;
	real xp, yp, fp;

	/* variables for fresnel equation */
	double complex index = index_metal;
	double complex cnums;
	double complex cdems;
	double complex cnump;
	double complex cdemp;
	double complex Spol;
	double complex Ppol;
	double complex rf;
	real Ab;
	real cos_angle;
	real sin_angle;

	real norm[ND_ND];
	real nonorm[ND_ND];
	real inc[ND_ND];
	real refl[ND_ND];
	real normal_velocity;

	/* polimi modulation parameters */
	if (ramping_process != 0)
	{
		if (ramping_process == 1)
		{
			ramp_time = exposure_timep;
			rate = limiter / ramp_time;
			if (time < ramp_time)
			{
				multiplyer = rate * time;
			}
			else
			{
				multiplyer = limiter;
			}
		}
		if (ramping_process == 2)
		{
			ramp_time = exposure_timep;
			rate = limiter / ramp_time;
			if (time < ramp_time)
			{
```

```
                    multiplyer = 1 - (rate * time);
                }
                else
                {
                    multiplyer = limiter;
                }
        }
        if (ramping_process == 3)
        {
                ramp_time = exposure_timep / 2;
                rate = limiter / ramp_time;
                if (time < ramp_time)
                {
                    multiplyer = rate * time;
                }
                else if (time > (exposure_timep - ramp_time))
                {
                    multiplyer = (rate * exposure_timep) - (rate * time);
                }
                else
                {
                    multiplyer = limiter;
                }
        }
        if (ramping_process == 4)
        {
                if (time < (exposure_timep / 2))
                {
                    multiplyer = 1.0;
                }
                else if (time > (exposure_timep / 2))
                {
                    multiplyer = 0;
                }
        }
}

/* pulsed laser modulation, decides the laser position during the laser pass */
if (pulsed_laser == 1)
{
        laser_position = (floor((CURRENT_TIME) / e_d_time) + 1.0) * point_distance;

        if (time2 < (e_d_time - jump_delay))
        {
                multiplyer = 1.0;
        }
        else if (time2 >= (e_d_time - jump_delay))
        {
                multiplyer = 0;
        }
}

/* laser irradiance in W/m2 is calculated */
C_CENTROID(x, c, t);
laser_power_mod = (laser_power * multiplyer) + laser_base;
fp = (2.0 * laser_power_mod) / (M_PI * SQR(laser_spot_rad));
xp = SQR(x[0] - laser_position - init_x);
yp = SQR(x[1] - 0.0);
laserm2 = fp * exp((-2.0 * (xp + yp)) / SQR(laser_spot_rad));

C_LASER_POWER_MOD(c, t) = laser_power_mod;

/* inital particle power in watts is given */
if (initialize)
{
        TP_BEAM_WATTS(tp) = laserm2;
```

```
                TP_IN_PARTICLE(tp) = 0.0;
                TP_BOUNCES(tp) = 0.0;
                C_LASERM2_START(c, t) = laserm2;
                C_ENERGY_IN(c, t) = (laserm2 * SQR(cell_size)) / C_VOLUME(c, t);
        }

        /* this part deletes the particle if it travels inside a particle */
        if (C_VOLUME_FRACTION(c, t) == 1.0 && C_VMAG(c, t) == 0.0)
        {
                TP_IN_PARTICLE(tp) += 1.0;
        }

        if (TP_IN_PARTICLE(tp) > 4.0)
        {
                MARK_PARTICLE(tp, P_FL_REMOVED);
                P_DIAM(tp) = 0.0;
                return;
        }

        /* free surface finder */
        C_FREE_SURFACE(c, t) = 0.0;

        if (laserm2 > 1.0)
        {
                if ((C_VMAG(c, t) > 90000.0) && (C_VOLUME_FRACTION(c, t) > 0.1))
                {
                        C_FREE_SURFACE(c, t) = 1.0;

NV_D(norm, =, C_NSURFACE_NORM_X(c, t), C_NSURFACE_NORM_Y(c, t), C_NSURFACE_NORM_Z(c, t));
NV_D(nonorm, =, C_SURFACE_NORM_X(c, t), C_SURFACE_NORM_Y(c, t), C_SURFACE_NORM_Z(c, t));
                        NV_V(inc, =, TP_VEL(tp));
                        normal_velocity = NV_DOT(inc, norm);
                        if (normal_velocity >= 0.0)
                        {
                                return;                 /* particle is coming from the phase side
*/
                        }
                        normal_velocity *= 2.0;
                        NV_VS(inc, -=, norm, *, normal_velocity);

                        cos_angle = ((NV_DOT(inc, nonorm)) / (NV_MAG(inc) * NV_MAG(nonorm)));
                        sin_angle = (sqrt(1.0 - SQR(cos_angle)));
                        cnums = cos_angle - csqrt((cpow(index, 2)) - (cpow(sin_angle, 2)));
                        cdems = cos_angle + csqrt((cpow(index, 2)) - (cpow(sin_angle, 2)));
cnump = (cpow(index, 2) * cos_angle) - csqrt(cpow(index, 2) - (cpow(sin_angle, 2)));
cdemp = (cpow(index, 2) * cos_angle) + csqrt(cpow(index, 2) - (cpow(sin_angle, 2)));
                        Spol = (cpow(cabs(cnums / cdems), 2));
                        Ppol = (cpow(cabs(cnump / cdemp), 2));
                        rf = (0.5 * Spol) + (0.5 * Ppol);
                        Ab = 1.0 - rf;

                        C_CELL_WATTSM2(c, t) += TP_BEAM_WATTS(tp) * Ab;
                        TP_BEAM_WATTS(tp) -= TP_BEAM_WATTS(tp) * Ab;

                        TP_BOUNCES(tp) += 1.0;
                        NV_V(TP_VEL(tp), =, inc);
                }
        }
        else
        {
                C_CENTROID(x, c, t);
                if (x[2] > (substrate_height + 20e-6))
                {
                        MARK_PARTICLE(tp, P_FL_REMOVED);
                        P_DIAM(tp) = 0.0;
                }
```

```
	}
}
```

10.2.2 Momentum equations

```
DEFINE_SOURCE(x_mom, c, t, dS, eqn)
{
	Thread* g, * w;
	g = THREAD_SUB_THREAD(t, 0);
	w = THREAD_SUB_THREAD(t, 1);
	real source = 0.0;
	real recoil_pressure = 0.0;
	real marangoni_flow = 0.0;
	real D;
	real T = C_T(c, t);
	D = (2.0 * C_R(c, t)) / ((C_R(c, g) + C_R(c, w)));

	if (C_VMAG(c, t) != 0)
	{
		if (T > boiling_temp)
		{
			recoil_pressure = (0.54 * 101000.0 * exp((latent_vap * molar_mass * (T - boiling_temp)) / (8.314 * T * boiling_temp))) * C_VOF_NX(c, t);
		}
		if (C_LIQUID_FRAC(c, t) > 0)
		{
			marangoni_flow = temp_surface_tension * (C_TEMP_G_X(c, t) - (C_VOF_NX(c, t) * (ND_DOT(C_VOF_NX(c, t), C_VOF_NY(c, t), C_VOF_NZ(c, t), C_TEMP_G_X(c, t), C_TEMP_G_Y(c, t), C_TEMP_G_Z(c, t)))));
		}
	}

	source = (recoil_pressure + marangoni_flow) * C_VMAG(c, t) * D;
	dS[eqn] = 0.0;

	C_X_MOM_SOURCE(c, t) = fabs(source);
	C_RECOIL_PRESSURE_X(c, t) = recoil_pressure;
	C_MARANGONI_FLOW_X(c, t) = marangoni_flow;

	return source;
}
```

10.2.3 Define Adjust

```
DEFINE_ADJUST(var_allocation, domain)
{
#if !RP_HOST

	Thread* t;
	Thread** pt;
	cell_t c;
	int phase_domain_index = 0;
	Domain* pDomain = DOMAIN_SUB_DOMAIN(domain, phase_domain_index);
	real x[ND_ND];
	real max_metal_temp1 = 0.0;
	real max_metal_temp1_max;
	real surface_normal_out[3];
	CX_Cell_Id* cx_cell;
	real vol_mush;
	real vol_mush_global;

	/* allocation of memory for gradients */
	{
		Alloc_Storage_Vars(pDomain, SV_VOF_RG, SV_VOF_G, SV_NULL);
		Scalar_Reconstruction(pDomain, SV_VOF, -1, SV_VOF_RG, NULL);
```

```
        Scalar_Derivatives(pDomain, SV_VOF, -1, SV_VOF_G, SV_VOF_RG, Vof_Deriv_Accumulate);
}
{
        Alloc_Storage_Vars(domain, SV_T_RG, SV_T_G, SV_NULL);
        T_derivatives(domain);
        Free_Storage_Vars(domain, SV_T_RG, SV_NULL);
}

mp_thread_loop_c(t, domain, pt)
        if (FLUID_THREAD_P(t))
        {
                Thread* ppt = pt[phase_domain_index];
                begin_c_loop(c, t)
                {
                C_VOF_SURF_AREA_X(c, t) = C_VOF_G(c, ppt)[0];
                C_VOF_SURF_AREA_Y(c, t) = C_VOF_G(c, ppt)[1];
                C_VOF_SURF_AREA_Z(c, t) = C_VOF_G(c, ppt)[2];
                C_VOLUME_FRACTION(c, t) = C_VOF(c, ppt);
                C_VMAG(c, t) = ND_MAG(C_VOF_SURF_AREA_X(c, t), C_VOF_SURF_AREA_Y(c, t),
                C_VOF_SURF_AREA_Z(c, t));
                C_AREA(c, t) = C_VOLUME(c, t) * NV_MAG(C_VOF_G(c, ppt));

                C_VOF_NX(c, t) = C_VOF_G(c, ppt)[0] / NV_MAG(C_VOF_G(c, ppt)); /* nx */
                C_VOF_NY(c, t) = C_VOF_G(c, ppt)[1] / NV_MAG(C_VOF_G(c, ppt)); /* ny */
                C_VOF_NZ(c, t) = C_VOF_G(c, ppt)[2] / NV_MAG(C_VOF_G(c, ppt)); /* nz */

                C_TEMP_G_X(c, t) = C_T_G(c, t)[0];      /*  temp_g_x */
                C_TEMP_G_Y(c, t) = C_T_G(c, t)[1];      /*  temp_g_y */
                C_TEMP_G_Z(c, t) = C_T_G(c, t)[2]       /*  temp_g_z */

                C_LIQUID_FRAC(c, t) = C_LIQF(c, ppt);

                NV_VS(surface_normal_out, =, C_VOF_G(c, ppt), *, -1.0);

                C_SURFACE_NORM_X(c, t) = surface_normal_out[0];
                C_SURFACE_NORM_Y(c, t) = surface_normal_out[1];
                C_SURFACE_NORM_Z(c, t) = surface_normal_out[2];

                C_NSURFACE_NORM_X(c,    t)      =       surface_normal_out[0]       /
        NV_MAG(surface_normal_out);
                C_NSURFACE_NORM_Y(c,    t)      =       surface_normal_out[1]       /
        NV_MAG(surface_normal_out);
                C_NSURFACE_NORM_Z(c,    t)      =       surface_normal_out[2]       /
        NV_MAG(surface_normal_out);

                C_PERCENT_DONE(c, t) = ((laser_vel * CURRENT_TIME) / track_length) * 100.0;

/* G&R module where temperature gradients and solidification rates are assignined */
                if (C_LIQUID_FRAC(c, t) > 0.0 && C_VOLUME_FRACTION(c, t) > 0.1)
                {
                C_G_TGRAD(c, t) = fabs(ND_MAG(C_TEMP_G_X(c, t), C_TEMP_G_Y(c, t),
                C_TEMP_G_Z(c, t)));
                C_R_SOLID(c, t) = fabs(laser_vel * (C_TEMP_G_X(c, t) / C_G_TGRAD(c, t)));
                C_GR(c, t) = C_G_TGRAD(c, t) * C_R_SOLID(c, t);
                C_GDIVR(c, t) = C_G_TGRAD(c, t) / C_R_SOLID(c, t);

                C_STRAINRATE(c, t) = CTE * C_G_TGRAD(c, t) * C_R_SOLID(c, t);
                }

                /* max metal temperature */
                if (C_VOLUME_FRACTION(c, t) > 0.5)
                {
                if (C_T(c, t) > max_metal_temp1 || max_metal_temp1 == 0.0)
                {
                max_metal_temp1 = C_T(c, t);
                }
```

```
                }

                if (C_VOLUME_FRACTION(c, t) > 0.2 && C_LIQUID_FRAC(c, t) > 0.0)
                {
                        C_TEMP_TAG(c, t) = 1.0;
                }

                if (C_VOLUME_FRACTION(c, t) > 0.1)
                {
                        if ((C_LIQUID_FRAC(c, t) > 0.0) && (C_LIQUID_FRAC(c, t) < 1.0))
                        {
                                vol_mush += C_VOLUME(c, t) * C_VOLUME_FRACTION(c, t);
                        }
                }
        }
        end_c_loop(c, t)
}
Free_Storage_Vars(pDomain, SV_T_RG, SV_VOF_RG, SV_VOF_G, SV_NULL);
Free_Storage_Vars(domain, SV_T_G, SV_NULL);

if (gauss_iv == 1)
{
        int curr_ts;
        curr_ts = N_TIME;

        if (last_ts != curr_ts)
        {
                last_ts = curr_ts;
                CX_Cell_Id* cx_cell;

                real P[3];
                real P_Cell[3];

                P[0] = spot_point1[0];
                P[1] = spot_point1[1];
                P[2] = spot_point1[2];
                spot_point1_templ = 11.0;

                domain_table = CX_Start_ND_Point_Search(domain_table, TRUE, -1);
                cx_cell = CX_Find_Cell_With_Point(domain_table, P, 0.0);
                if (cx_cell)
                {
                        c = RP_CELL(cx_cell);
                        t = RP_THREAD(cx_cell);
                        C_CENTROID(P_Cell, c, t);
                        spot_point1_templ = C_T(c, t);
                }

                real P1[3];
                real P1_Cell[3];

                P1[0] = spot_middle[0];
                P1[1] = spot_middle[1];

                spot_middle_templ = 11.0;
                real iv_pulsed = 2e19;
                real iv_power = 2000.0;
                real t_target, density, Cp;

                spot_middle_templ = PRF_GRHIGH1(max_metal_temp1);

                int i = 0.0;
                for (i = ((substrate_height + 60e-6) / 1e-6); i > 0; i--)
                {
                        P1[2] = (double)i * 1e-6 + 1e-8;
```

```
                                cx_cell = CX_Find_Cell_With_Point(domain_table, P1, 0.0);
                                if (cx_cell)
                                {
                                        c = RP_CELL(cx_cell);
                                        t = RP_THREAD(cx_cell);
                                        C_CENTROID(P1_Cell, c, t);

                                        if ((C_VMAG(c, t) > 90000.0) && (C_VOLUME_FRACTION(c,
t) > 0.5))
                                        {
                                                t_target = htarget - spot_middle_templ;
                                                if (t_target < 0.0)
                                                {
                                                        t_target = 0.0;
                                                }

                                                density = ((-(densy1 - densy2) / (demox1 -
                                                demox2)) * C_T(c, t)) + densc1;
                                                Cp = (((cpy1 - cpy2) / (demox11 - demox22)) *
                                                C_T(c, t)) + cpc1;

                                                iv_pulsed = (density * Cp * t_target) /
CURRENT_TIMESTEP;
                                                iv_power = (iv_pulsed * C_VOLUME(c, t) * M_PI *
                                                SQR(laser_spot_rad)) / (2.0 * C_AREA(c, t));

                                                if (iv_power > max_power)
                                                {
                                                        iv_power = max_power;
                                                }

                                                break;
                                        }
                                }
                        }

                        /* global summations for all partitions */
                        spot_point1_tempg = PRF_GRHIGH1(spot_point1_templ);
                        magic_power = PRF_GRLOW1(iv_power);
                        magic_powerm3 = PRF_GRLOW1(iv_pulsed);

                        if (magic_power > max_power)
                        {
                                magic_power = max_power;
                        }
                }
                domain_table = CX_End_ND_Point_Search(domain_table);
        }


        if (gauss_iv == 0)
        {
                max_metal_temp1_max = PRF_GRHIGH1(max_metal_temp1);
        }

        vol_mush_global = PRF_GRSUM1(vol_mush);

        /* loop to assign the max metal temperature so that it can be measured in the console */
        mp_thread_loop_c(t, domain, pt)
                if (FLUID_THREAD_P(t))
                {
                        Thread* ppt = pt[phase_domain_index];
                        begin_c_loop(c, t)
                        {
                                if (gauss_iv == 0)
                                {
```

```
                                        C_MAX_METAL_TEMP(c, t) = max_metal_temp1_max;
                                }

                                if (gauss_iv == 1)
                                {
                                        C_MAGIC_POWERM(c, t) = magic_power;
                                        C_MAGIC_POWERM3(c, t) = magic_powerm3;
                                        C_MAX_METAL_TEMP(c, t) = spot_middle_templ;
                                        C_POINT1(c, t) = spot_point1_tempg;
                                }

                                C_VOL_MUSH(c, t) = vol_mush_global;

                        }
                        end_c_loop(c, t)
                }
        Free_Storage_Vars(pDomain, SV_T_RG, SV_VOF_RG, SV_VOF_G, SV_NULL);
        Free_Storage_Vars(domain, SV_T_G, SV_NULL);
#endif
}
```

10.2.4 Patching

```
DEFINE_INIT(patching, domain)
{
#if !RP_HOST
        Thread* t, ** pt;
        cell_t c;
        real x[ND_ND];
        int num = 1239;
        int i = 1;
        int aa, bb, cc;
        real sphere_radius, disx, disy, disz;
        real location[3];
        real sphere_centre[3];
mp_thread_loop_c(t, domain, pt)
        {
                if (FLUID_THREAD_P(t))
                {
                        begin_c_loop(c, t)
                        {
                                C_VOF(c, pt[0]) = 0.0;

                                C_LASER_POWER_MOD(c, t) = 0.0;
                                C_LASERM2_START(c, t) = 0.0;
                                C_CELL_WATTSM2(c, t) = 0.0;
                                C_POINT1(c, t) = 0.0;
                                C_TEMP_TAG(c, t) = 0.0;
                                C_RTXNF(c, t) = 0.0;
                                C_OPTIBEAM(c, t) = 0.0;

                                spot_middle[0] = iv_start;
                                spot_middle[1] = 0.0;
                                spot_middle[2] = substrate_height;

                                spot_point1[0] = iv_start;
                                spot_point1[1] = 0.0;
                                spot_point1[2] = substrate_height;

                                spot_middle_templ = 10.0;
                                spot_point1_templ = 10.0;

                                magic_power = 0.1;
                                magic_powerm3 = 0.1;

                                C_CENTROID(x, c, t);
```

```
                                        if (x[2] < substrate_height)
                                        {
                                                C_VOF(c, pt[0]) = 1.0;
                                        }
                                        else
                                        {
                                                for (i = 0; i < num; i++)
                                                {
                                                        sphere_centre[0] = x_coordinates[i];
                                                        sphere_centre[1] = y_coordinates[i];
                                                        sphere_centre[2]        =        z_coordinates[i]        +
increase_pbf_height;
                                                        sphere_radius        =        radius_sphere[i]        -
reduce_p_radius;

                                                        for (aa = -2; aa < 3; aa++)
                                                        {
                                                                for (bb = -2; bb < 3; bb++)
                                                                {
                                                                for (cc = -2; cc < 3; cc++)
                                                                {
                                                                C_CENTROID(x, c, t);
                                                                location[0] = x[0] + (((double)aa / 4) *
cell_size);
                                                                location[1] = x[1] + (((double)bb / 4) *
cell_size);
                                                                location[2] = x[2] + (((double)cc / 4) *
cell_size);

                                                                disx        =        fabs(location[0]        -
sphere_centre[0]);
                                                                disy        =        fabs(location[1]        -
sphere_centre[1]);
                                                                disz        =        fabs(location[2]        -
sphere_centre[2]);

                                                                if    (ND_MAG(disx,    disy,    disz)    <
sphere_radius)
                                                                {
                                                                if (C_VOF(c, pt[0]) < 1)
                                                                {
                                                                C_VOF(c, pt[0]) += 0.008;
                                                                }
                                                                }
                                                                }
                                                                }
                                                        }
                                                }
                                        }
                                C_VOF(c, pt[1]) = 1.0 - C_VOF(c, pt[0]);
                                end_c_loop(c, t)
                        }
                }
                Message0("\n Initialised LPBF");
                Message0("\n Type: %d ", gauss_iv);
                Message0("\n Pulsed: %d ", pulsed_laser);
                Message0("\n LaserPower: %g", laser_power);
                Message0("\n LaserBase: %g", laser_base);
                Message0("\n LaserVel: %g", laser_vel);
                Message0("\n PD: %g", point_distance);
                Message0("\n ET: %g", exposure_time);
                Message0("\n LaserSpot: %g", laser_spot_rad);
                Message0("\n InitX: %g", init_x);
                Message0("\n TrackLength: %g", track_length);
                Message0("\n CellSize: %g", cell_size);
```

```
        Message0("\n SubstrateHeight: %g", substrate_height);
        Message0("\n Ramping: %d", ramping_process);
        Message0("\n PeakDistance: %g", peak_distance);
        Message0("\n LaserPower: %g", laser_power);
        Message0("\n LVAP: %g", latent_vap);
        Message0("\n MM: %g", molar_mass);
        Message0("\n Boiling: %g", boiling_temp);
        Message0("\n ST: %g", surface_tension);
        Message0("\n TST: %g", temp_surface_tension);
        Message0("\n Viscosity: %g", viscosity);

#endif
}
```

10.2.5 Submission of HPC Job

To submit the file for the HPC, the case file is first prepared, initialised, and then saved, so that a case (.cas.h5) and data (.dat.h5) file are located in the working directory, along with the UDF file, journal file and submission file. The journal file is similar to below:

```
/file/read-case "LPBF_01.cas.h5"
/file/read-data "LPBF_01.dat.h5"
/solve/dual-time-iterate 50000 6
```

Where the first line reads the case file, the second reads the data file, and the last line starts the calculation for 50,000 timesteps running with 6 iterations for each timestep. The batch file then submits the file to the HPC queue, and is similar too:

```
#!/bin/bash
#SBATCH --time=120:00:00
#SBATCH --job-name=RTX_MS2
#SBATCH --partition=defq
#SBATCH --nodes=7
#SBATCH --ntasks-per-node=40
#SBATCH --mem=50g

module load ansys-uon/v211

FLUENTNODEFILE=$(mktemp)
scontrol show hostnames > $FLUENTNODEFILE
echo "Running on nodes:"
cat $FLUENTNODEFILE
/software/ansys_inc/v211/fluent/bin/fluent -t280 3ddp -cnf="$FLUENTNODEFILE" -
gu -i jor.jou > LPBF_log
```

Where the job run time, partition name, number of nodes, memory are selected. The defq partition corresponds to the general nodes for calculations on the HPC. The ANSYS Fluent module is then loaded, and the program is loaded with 280 cores, and the jor.jou (journal file) file is executed, starting the simulation. LPBF_log is the log file for the simulation.

10.3 Matlab post processing script for plotting ANSYS Fluent data

```
%% AA2024pc
%{
% columns:
% 1. cell number
% 2. x
% 3. y
% 4. z
% 5. x-velocity
% 6. y-velocity
% 7. z-velocity
% 8. temperature
% 9. x-G
% 10. y-G
% 11. z-G
% 12. (?) always 0
% 13. G
% 14. R
% 15. Above melting?
% 16. Strain Rate
% 17. Mushy zone volume
% 18. Ignore
% 19. Strain Rate model
% 20. Metal-liquid-fraction
% 21. Metal-vof
%}

clear all, close all, clc
file_list=dir('aa2024pc/*');
files=file_list(3:end,:);
mastertest_name=files(1).name;
mastertest_test=importdata(mastertest_name,' ',1);
[~,order_m]=sortrows(round(mastertest_test.data(:,[2 4]),8),'Ascend');
mastertest_test.data=mastertest_test.data(order_m,:);
master_gen_info=mastertest_test.data(:,1:4);
ndompts=size(mastertest_test.data,1); step=2*10^(-6);
ntimesteps=size(files,1);
metal_vof_time=zeros(ndompts,ntimesteps);
T_time=zeros(ndompts,ntimesteps);
G_time=zeros(ndompts,ntimesteps);
R_time=zeros(ndompts,ntimesteps);

% Init. materials properties
scheil_data=load('AA2024_scheil.txt');
T_liquidus=scheil_data(1,2);
T_solidus=scheil_data(end,2);
alfa=24*10^(-6);

TIMES=[[14:14:14000]];
TIMES=TIMES(1:ntimesteps);
% Save variables I need in time and space
for ii=1:length(files)
  current_file=files(ii).name;
```

```
  test=importdata(current_file,' ',1);
  [~,order_c]=sortrows(round(test.data(:,[2 4]),8),'Ascend');
  test.data=test.data(order_c,:);
  metal_vof_time(:,ii)=test.data(:,21);
  T_time(:,ii)=test.data(:,8);
  G_time(:,ii)=test.data(:,13);
  R_time(:,ii)=test.data(:,14);
end
% Evaluate cooling rate and strain rate
Tdot_time=(T_time(:,2:end)-T_time(:,1:(end-1)))/(14*10^(-6));
strainrate_time=Tdot_time*alfa;

dlmwrite('aa2024c_metal_vof_time.txt',metal_vof_time);
dlmwrite('aa2024c_T_time.txt',T_time);
dlmwrite('aa2024c_G_time.txt',G_time);
dlmwrite('aa2024c_R_time.txt',R_time);
dlmwrite('aa2024c_Tdot_time.txt',Tdot_time);
dlmwrite('aa2024c_strainrate_time.txt',strainrate_time);
dlmwrite('aa2024c_sorted_x_z.txt',master_gen_info(:,[2 4]));
clear all, close all, clc

%% AA2024p
clear all, clc
file_list=dir('aa2024p/*');
files=file_list(3:end,:);
mastertest_name=files(1).name;
mastertest_test=importdata(mastertest_name,' ',1);
[~,order_m]=sortrows(round(mastertest_test.data(:,[2 4]),8),'Ascend');
mastertest_test.data=mastertest_test.data(order_m,:);
master_gen_info=mastertest_test.data(:,1:4);
ndompts=size(mastertest_test.data,1); step=2*10^(-6);
ntimesteps=size(files,1);
metal_vof_time=zeros(ndompts,ntimesteps);
T_time=zeros(ndompts,ntimesteps);
G_time=zeros(ndompts,ntimesteps);
R_time=zeros(ndompts,ntimesteps);

% Init. materials properties
scheil_data=load('AA2024_scheil.txt');
T_liquidus=scheil_data(1,2);
T_solidus=scheil_data(end,2);
alfa=24*10^(-6);

TIMES=[[14:14:14000]];
TIMES=TIMES(1:ntimesteps);
% Save variables I need in time and space
for ii=1:length(files)
  current_file=files(ii).name;
  test=importdata(current_file,' ',1);
  [~,order_c]=sortrows(round(test.data(:,[2 4]),8),'Ascend');
  test.data=test.data(order_c,:);
  metal_vof_time(:,ii)=test.data(:,21);
  T_time(:,ii)=test.data(:,8);
  G_time(:,ii)=test.data(:,13);
  R_time(:,ii)=test.data(:,14);
end
% Evaluate cooling rate and strain rate
Tdot_time=(T_time(:,2:end)-T_time(:,1:(end-1)))/(14*10^(-6));
strainrate_time=Tdot_time*alfa;

dlmwrite('aa2024_metal_vof_time.txt',metal_vof_time);
dlmwrite('aa2024_T_time.txt',T_time);
dlmwrite('aa2024_G_time.txt',G_time);
dlmwrite('aa2024_R_time.txt',R_time);
dlmwrite('aa2024_Tdot_time.txt',Tdot_time);
dlmwrite('aa2024_strainrate_time.txt',strainrate_time);
```

```
dlmwrite('aa2024_sorted_x_z.txt',master_gen_info(:,[2 4]));
clear all, close all, clc

%% Post-Post Process - DATA IN
% Load the aa2024pc data
metal_vof_time_pc=load('aa2024c_metal_vof_time.txt');
T_time_pc=load('aa2024c_T_time.txt');
G_time_pc=load('aa2024c_G_time.txt');
R_time_pc=load('aa2024c_R_time.txt');
Tdot_time_pc=load('aa2024c_Tdot_time.txt');
strainrate_time_pc=load('aa2024c_strainrate_time.txt');
xz_pc=load('aa2024c_sorted_x_z.txt');

% Load the aa2024p data
metal_vof_time_p=load('aa2024_metal_vof_time.txt');
T_time_p=load('aa2024_T_time.txt');
G_time_p=load('aa2024_G_time.txt');
R_time_p=load('aa2024_R_time.txt');
Tdot_time_p=load('aa2024_Tdot_time.txt');
strainrate_time_p=load('aa2024_strainrate_time.txt');
xz_p=load('aa2024_sorted_x_z.txt');

% evaluate times for both datasets
TIMES=[14:14:14000]';
nt_pc=size(T_time_pc,2);
nt_p=size(T_time_p,2);
times_pc=TIMES(1:nt_pc);
times_p=TIMES(1:nt_p);

[X,Z]=meshgrid([0:1:800]*10^(-6),[0:1:300]*10^(-6));

%% Post-Post Process - PLOT
% here you need to select a datatoplot, remember to change the xz values
% and the metal_fit values according to the material (p or pc) you are
% plotting
time_index=34;
datatoplot=strainrate_time_pc;
datatoplot2=T_time_pc;
datatoplot(metal_vof_time_pc(:,time_index)<=0.4,time_index)=300;
YLIM=3e7; % change according to the variable
datatoplot_fit=fit(xz_pc,datatoplot(:,time_index),'linearinterp');
datatoplot_fit2=fit(xz_pc,datatoplot2(:,time_index),'linearinterp');
metal_fit=fit(xz_pc,metal_vof_time_pc(:,time_index),'linearinterp');scheil=load('AA2024_scheil.txt');

T_solidus=scheil(end,2);
T_liquidus=scheil(1,2);figure()

surf(X,Z,datatoplot_fit(X,Z),'EdgeColor','none')
hold on
contour3(X,Z,YLIM+datatoplot_fit2(X,Z),YLIM+[T_solidus T_liquidus],'k-','linewidth',1)
hold on
contour3(X,Z,YLIM+metal_fit(X,Z),YLIM+[0.5 0.5],'w-','linewidth',1)
box on
axis equal
xlabel('x [m]','FontSize', 24)
ylabel('z [m]','FontSize', 24)
set(gca,'FontSize',24, 'TickDir','out')
ylim([100e-6 225e-6])
xlim([200e-6 400e-6])
view([0 0 1])
% colormap(flipud(jet))
colormap(jet)
caxis([-100 100])
colorbar('FontSize', 24)
c = colorbar;
c.Label.String = 'Temperature [K]';
```

```
c.Label.FontSize=24;
```

*****